The UV Environment for Prebiotic Chemistry: Connecting Origin-of-Life Scenarios to Planetary Environments

The UV Environment for Prebiotic Chemistry: Connecting Origin-of-Life Scenarios to Planetary Environments

A dissertation presented

by

Sukrit Ranjan

to

The Department of Astronomy

in partial fulfillment of the requirements

for the degree of

Doctor of Philosophy

in the subject of

Astronomy & Astrophysics

Harvard University

Cambridge, Massachusetts

April 2017

Dissertation Advisor: Professor Dimitar D. Sasselov Sukrit Ranjan

The UV Environment for Prebiotic Chemistry: Connecting Origin-of-Life Scenarios to Planetary Environments

Abstract

Recent laboratory studies of prebiotic chemistry (chemistry relevant to the origin of life) are revolutionizing our understanding of the origin of life (abiogenesis) on Earth just as telescopes capable of searching for life elsewhere are coming online. This thesis sits at the intersection of these revolutions. I examine prebiotic chemical pathways postulated to be relevant to the origin of life and identify the environmental conditions they require to function. I compare these environmental requirements to what was available on Earth and other planets, and use the comparison to 1) improve studies of the origin of life on Earth and 2) explore the implications for the inhabitability of other worlds.

Multiple lines of evidence suggest UV light may have played a critical role in the synthesis of molecules relevant to abiogenesis (prebiotic chemistry), such as RNA. I show that UV light interacts with prebiotic chemistry in ways that may be sensitive to the spectral shape and overall amplitude of irradiation. I use radiative transfer models to constrain the UV environment on early Earth (3.9 Ga). I find that the surface UV is insensitive to much of the considerable uncertainty in the atmospheric state, enabling me to constrain the UV environment for prebiotic chemistry on early Earth. Some authors have suggested Mars as a venue for prebiotic chemistry. Therefore, I explore plausible UV spectral fluences on Mars at 3.9 Ga. I find that the early Martian UV environment is comparable to Earth's under conventional assumptions about the

atmosphere. However, if the atmosphere was dusty or SO_2 levels were high, UV fluence would have been strongly suppressed. Intriguingly, despite overall attenuation of UV fluence, SO_2 preferentially attenuates destructive FUV radiation over prebiotically-useful NUV radiation, meaning high-SO_2 epochs may have been more clement for the origin of life. Better measurements of the spectral dependence of prebiotic photoprocesses are required to constrain this hypothesis. Finally, I calculate the UV fluence on planets orbiting M-dwarfs. I find that UV irradiation on such planets is low compared to Earth. Laboratory studies are required to understand whether prebiotic processes that worked on Earth can function on low-UV M-dwarf planets.

In addition to UV light, the most promising pathways for the prebiotic synthesis of RNA require reduced sulfidic anions. I show that prebiotically-relevant levels of such anions derived from volcanically-outgassed SO_2 should be robustly available on early Earth, and that episodes of high volcanism may be especially clement for these prebiotic pathways. However, H_2S-derived anions are much less common, and prebiotic chemistry which invokes them must rely on alternate, localized sources.

My work 1) provides initial conditions for laboratory studies of prebiotic chemistry, 2) constrains the inhabitability of Mars and planets orbiting M-dwarfs, and 3) demonstrates the need for laboratory studies to characterize the sensitivity of putative prebiotic chemistry to environmental conditions, e.g the spectral shape and amplitude of UV irradiation. All software associated with these studies, including models and data inputs, are publicly available for validation and extension.

Contents

Acknowledgments

First and foremost, I thank my advisor, Dimitar Sasselov, without whose guidance, insight, and unwavering support this thesis would not have been possible. Dimitar showed me the importance of pursuing your curiosity wherever it might lead, even if the path lies outside traditional divisional boundaries. I thank Robin Wordsworth, for letting a rotation in his group evolve into an ongoing exploration of just how interesting planetary atmospheres can be. I thank my research exam advisors, David Charbonneau and Jean-Michel Désert, for teaching me the value of care and discipline in research, and Martin Elvis and Jose Luis Galache, for fun romps in asteroid science. I thank Karin Oberg, for her guidance as my mentor and TAC chair, Jack Szostak for numerous discussions on organic and prebiotic chemistry, and David Catling, for flying out to Boston to offer his insight as external examiner. I thank Phil Sadler, Ruth Murray-Clay and Avi Loeb for their advice.

I thank my fellow students, for their companionship and scientific insight along this journey. In particular, I thank Zach Berta-Thompson and Sarah Rugheimer for taking me under their wings when I ventured into new fields, and Anjali Tripathi and Zachary Slepian for emergency BibTeX help when I needed it most. I thank Li Zeng, Laura Schaefer, Chris Magnani, Zoe Todd, Elisabeth Newton, Courtney Dressing, Jason Dittmann, Hannah Diamond-Lowe, Ragnhild Lunnan, Lauranne Lanz, Stephen Portillo, Lauren Woolsey, Tanmoy Laskar, Jane Huang, Bekki Dawson, Robert Harris, Max Moe, Nathan Sanders, Bence Beky, Katherine Rosenfeld, Josh Suresh, Chris Faesi, Marion Dierickx, Doug Ferrer, Meredith Macgregor, Ryan Loomis, Dawn Graninger, Alexa Hart, Kushal Mehta, Petri Savolainen, Sophia Dai, Tana Joseph, Katie Auchettl, James

Matthews, Ruth Angus, and Sharon Rapaport Miller for shared laughter and stolid solidarity on the way. I thank my peers from outside the department, including Eddie Schwieterman, Siddharth Hegde, Chester (Sonny) Harman, Peter Gao, Michael Chaffin, Alessondra Springmann, Mary Knapp, and Tony Jia.

I thank my friends, for laughter, for fun, and for support. In particular, I thank the Order of the Lepton. Nicole Berdy, Caroline Morley, Scott Morrison, Elizabeth Maroon, and Melodie Kao: Captain Gravity is ever in your debt. I thank the Honeybear Synchrotron Club: Krista Shapton, Shilpa Ahuja, Amna Chadhry, and Geoff Chung (honorary member). I thank the friends with whom I was lucky enough to share Cambridge, including Enrique Cintron, Stephanie Schmit, Fangfei Shen, Bobby Fortanely, Christina Jaworsky, Viral Modi, Daniel Pillon, Liz Chhouk, Jennifer Hogan, Blair Simon, Hayk Yegoryan, Sandhya Ramakrishnan, Priya Ramaswamy, Andrew Jones, Cristen Jones, Jillian James, Adam Kuang, Tess Grynoch, Paul Weaver, Elaina Chai, Lauren Chai, Vrajesh Modi, Jareth Holt, Simeon Bird, Zavisa Dogic, Kim Scott, Andie Rossi, and Ted Steiner.

I thank the staff at the CfA, without whom nothing would get done. In particular, I thank Peg Herlihy, Donna Adams, and Robb Scholten; Jaime Villanueva, Kelly Moreno, Christine Benoit, Sara Yorke, and Amanda Preston; Mike Capone and the CF team; Maria McEachern and Wolbach library staff. I thank Niti Seth at the BSC, for enlightening conversations.

I thank influential teacher-mentors, especially Sara Seager, Max Tegmark, Jim Elliott, and Lynne Zielinski (Z). The inspiration you sparked burns in me still.

I thank my family, who have loved and unhesitatingly supported me on the journey

to become the first scientist in our family. I especially thank my mother, Sangeeta Prasad, for the trip to Nehru Planetarium in 1997 that launched me on this path, and my Nanaji, Kamta Prasad, for being an academic role model. I thank my fiance, Kate Alexander, for her affection, for her encouragement, and for being my rock when I need it most. I'm glad we found each other.

To Z, and to Joel, Carl, David, Sam, Stan and the rest of G.A.D.G.E.T.,

who showed me the sky is NOT the limit.

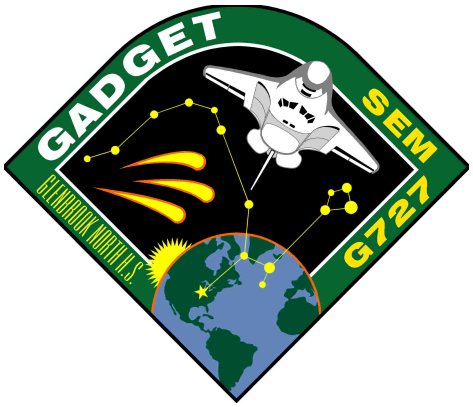

Ad astra*, my friends.*

Chapter 1

Introduction

1.1 Overview

> "And if the force of nature remains the same,
> To throw the wandering elements to and fro,
> In the same way as here, it must be admitted,
> There are other worlds in other parts of the universe,
> And other races of men and of wild beasts"
> – Lucretius, *On the Nature of Things*, c. 1st century B.C.E.[1]

Since antiquity, humans have wondered how life began on Earth and whether it exists on other worlds, and since ancient times, we have recognized that the two questions are linked. Are there other habitable worlds, and do the same natural laws that lead to the origin of life on Earth prevail there as well? If so, then it seems almost hubris to think that we are alone in the universe.

Recent advances are revolutionizing our efforts to answer these age-old questions.

[1] Translation of Sisson (2003)

Telescopic observations are revealing a cornucopia of potentially habitable worlds, suggesting that potential venues for the emergence of Earthlike life are abundant. At the same time, we are experiencing dramatic advances in our understanding of the origin of life (abiogenesis) on Earth. Might the processes that lead to life on Earth operate elsewhere in the cosmos? If so, which planets are most favorable for their operation, and hence likely to experience abiogenesis events of their own? This thesis presents work in service of these questions.

1.2 The Search for Life on Other Worlds

> "For it is impossible that a rational being fairly vigilant, can imagine that these innumerable worlds, manifest as like to our own or yet more magnificent, should be destitute of similar and even superior inhabitants; for all are either suns or the sun doth diffuse to them no less than to us those most divine and fertilizing rays..."
> – Giordano Bruno, *On the Infinite Universe and Worlds*, 1584[2]

1.2.1 The Search for Life Within Our Solar System

Since the discovery of the Solar System, scholars have speculated about life inhabiting its worlds (Sullivan 1964; Shklovskii & Sagan 1966). Best-known is the case of Mars: in the late 19th century, what turned out to be optical artifacts in observations of Mars were interpreted as artificial canals, and evidence of an indigenous civilization (Lowell 1906), an idea which caught the popular imagination (e.g., Burroughs 1917). This theory was resoundingly falsified by the 1965 Mariner 4 mission (Leighton et al. 1965), which

[2]From translation of Singer (1950)

revealed a barren world studded with impact craters and no signs of any life. Subsequent missions revealed Mars to be cold, desiccated, and blasted by radiation. Surveys of the remaining planets and moons one-by-one revealed worlds with harsh conditions incompatible with complex life as we know it.

However, while planets in the solar system are inhospitable for complex life, they are not wholly incompatible with microbial life, which can tolerate a far broader range of conditions. The paradigm for life detection in the solar system quickly evolved to focus on these simpler, more robust lifeforms. The discovery of extremophiles energized this approach by revealing that microbes could tolerate a far broader range of conditions than had previously been thought possible, dramatically expanding the potential habitats for life (Cavicchioli 2002). Scientists hypothesized that life might survive in the the clouds of Venus, the subsurface of Mars, or in the ice-shielded oceans of outer moons like Europa or Enceladus (Morowitz & Sagan 1967; McKay 1997; Shapiro & Schulze-Makuch 2009).

The prospects for extraterrestrial life in the solar system were further strengthened by the realization that while the other planets are hostile environments today, they need not always have been so: atmospheric modelling suggests that Venus could have been habitable (i.e. not in a runaway greenhouse) as recently as 715 Ma (Way et al. 2016), and there is robust geological evidence for surficial liquid water on Mars in the Noachian era (4.1-3.7 Ga), consistent with clement surface conditions (e.g., Squyres et al. 2004, Grotzinger et al. 2015). Weiss et al. (2000) demonstrated that the interior of meteorites transferred from Mars to Earth never heated to temperatures above 40° C, suggesting microbes in meteorite interiors could journey from one planet to the other without being sterilized by heat. This discovery strengthened the case for extraterrestrial life in the solar system, since one could now envision that terrestrial life could be seeded to other

worlds – or that life from another world could jump-start terrestrial life (Worth et al. 2013; Benner & Kim 2015).

Today, the world's space agencies, especially NASA, maintain active programs towards searching for evidence of extraterrestrial life, past or present, in the solar system. Mars is a particular focus of these programs, because of evidence for past and present liquid water (Squyres et al. 2004; Grotzinger et al. 2015; Ojha et al. 2015), because of the worlds in our solar system it harbors surficial conditions least hostile to life, and because of its comparative accessibility due to proximity and environmental factors [3] (McKay 1997). Results from the life-detection experiments on the Viking missions were inconclusive (e.g., Klein 1999). Claims of microbial microfossils in Martian meteorites were shown to be overinterpreted, with a ready abiotic explanation (McKay et al. 1996; Martel et al. 2012). Detections of methane on Mars have been cited as evidence of a biosphere; however, both these detections and their interpretation have been strongly challenged in the literature (Krasnopolsky et al. 2004; Mumma et al. 2009; Zahnle et al. 2011; Webster et al. 2015; Zahnle 2015). Astrobiological investigations of Mars today, e.g, those to be conducted with the Mars 2020 rover, are focused on characterizing its past habitability, and for searching for fossil evidence of past life (Mustard et al. 2013); future missions may one day directly search for extant life in potentially hospitable refuges on the planet, such as the potentially warm subsurface (Boston et al. 1992).

Beyond Mars, other intriguing astrobiological targets include the icy moons of the outer planets which host subsurface liquid water oceans thanks to tidal heating, such as Europa and Enceladus. Astrobiologists hypothesize life might exist in such

[3]Mars is a much easier environment for probes to operate than, say, Venus.

environments, perhaps nourished by hydrothermal vents or chemical gradients (Shapiro & Schulze-Makuch 2009). The Europa Clipper mission will advance characterization of the history and habitability of Europa, and may even be able to sample material from Europa's plumes for evidence of organic matter (Pappalardo et al. 2015). Titan, with its thick atmosphere and abundance of organics has also been cited as a target of astrobiological interest (Shapiro & Schulze-Makuch 2009). None of these objects have yet shown remotely-detectable evidence of biological activity; therefore, in-situ observations may be necessary to detect or falsify life on these worlds.

1.2.2 An Abundance of Potentially Habitable Exoplanets

The discovery of exoplanets (Latham et al. 1989; Mayor & Queloz 1995) opened up a new avenue in the search for extraterrestrial life. Prior to the discovery of exoplanets, astrobiology was limited to searching for life on objects in the solar system, a limited sample which includes no objects with habitability comparable to Earth. The discovery of exoplanets opened up the prospects of drastically increasing the sample to search for evidence of life, including the tantalizing possibility of the discovery of true Earth analogs well-suited to the evolution and existence of life as we know it.

This hope has been stunningly borne out by exoplanet searches over the past two decades. Statistical analyses of ground-based and spaced-based exoplanet surveys, especially transit searches from the Kepler mission, suggest planets similar in size and instellation (bolometric stellar irradiation) to Earth are common, and that billions of such planets exist in our galaxy (Petigura et al. 2013; Dressing & Charbonneau 2015; Burke et al. 2015). Planets similar in size to Earth ($< 1.6R_{\oplus}$) are expected to be rocky

(Rogers 2015) and are termed "terrestrial" planets, and planets similar in instellation to Earth are thought to have surface temperatures compatible with stable surface liquid water and are termed "habitable zone" planets (Kasting et al. 1993; Kopparapu 2013). Terrestrial, habitable-zone worlds may therefore provide clement environments for life as we know it, and hence are prime astrobiological targets. One such world has been discovered orbiting Proxima Centauri B (the closest star to the Sun; Anglada-Escudé et al. 2016), and 3-4 more such objects have recently been discovered around the late M-dwarf TRAPPIST-1 (Gillon et al. 2017). Future surveys like the Transiting Exoplanet Survey Satellite (TESS) and MEarth are expected to find even more such objects, and we may expect to discover a sample of tens of worlds with size and instellation consistent with Earth-analog conditions over the next decade. (Berta et al. 2013; Sullivan et al. 2015).

1.2.3 Prospects for Exoplanet Biosignature Search

Excitingly, this cornucopia of worlds is being discovered just as telescopes with the capacity to search them for evidence of life are coming on-line. Techniques like transmission and emission spectroscopy and ground-based high-resolution spectroscopy have been used to chararcterize the atmospheres of of planets much larger than Earth (Charbonneau et al. 2002, 2005; Knutson et al. 2007; Snellen et al. 2010; Deming et al. 2013; Ranjan et al. 2014; Kreidberg et al. 2014), and are now being used to study the atmospheres of more Earth-sized worlds (de Wit et al. 2016). The dominant paradigm for the remote search for life is telescopic detection of biosignature gases, i.e. combinations

of atmospheric gases thought to require a biogenic source or sink[4] (Lovelock 1965; Sagan et al. 1993; Seager et al. 2013). Other remotely-detectable signatures of life have also been proposed, including vegetation spectral signatures (Seager et al. 2005) and signatures of technological civilizations (Lin et al. 2014; Lingam & Loeb 2017). The James Webb Space Telescope (JWST; expected launch: 2018) and the ground-based Extremely Large Telescopes (ELTs; expected first light: mid-2020s) may be able to search the atmospheres of favorable targets for evidence of life (Rodler & López-Morales 2014; Batalha et al. 2015), meaning that within the next 10-15 years, we may finally answer the millennia-old question of whether we are alone in the universe.

1.2.4 Challenges For Exoplanet Biosignature Search

Searching the atmospheres of terrestrial habitable-zone exoplanets for biosignatures will be at the limits of the abilities of even next-generation instruments like JWST and the ELTs (Seager 2014; Rodler & López-Morales 2014; Batalha et al. 2015; Meadows et al. 2016). Biosignature seaches with these instruments will require huge investments of tens to hundreds of hours of scarce observation time, distributed over timescales comparable to the telescope lifetime. These challenges mean we may expect to characterize at most 3 terrestrial habitable-zone planets with JWST (Cowan et al. 2015). We may speculate a similar level of investment from the ELTs. By contrast, the TESS mission alone is expected to discover 48 ± 7 planets with radius $R < 2R_\oplus$ and instellation S $0.2S_\oplus < S < 2S_\oplus$, i.e. with size and instellation comparable[5] to the Earth (Sullivan

[4]e.g. the combination of CH_4 and O_2 in the terrestrial atmosphere (Sagan et al. 1993)

[5]Instellations of $2S_\oplus$ are firmly within the runaway greenhouse limit according to the work of Kopparapu (2013). However, Kopparapu (2013) neglect clouds, and Yang et al.

et al. 2015), and other surveys (e.g., HARPS, CARMENES, MEarth, TRAPPIST, CHEOPS, PLATO) will continue to deliver even more.

We therefore face the challenge of how to select just a few objects for biosignature search from a sample of tens of objects. Biosignature search will be challenging even for far-future[6] missions like HabEx and LUVOIR (Mennesson et al. 2016; Crooke et al. 2016; Robinson et al. 2016), so near-term technological development alone will not fully solve this problem. Observational constraints will aid target selection; for example, targets orbiting nearby stars are easier to study regardless of technique. However, even when selecting for bright (i.e. nearby) host stars, TESS alone is expected to discover > 10 objects with size and instellation comparable to Earth orbiting stars with apparent magnitude $I_c \leq 12$ (Sullivan et al. 2015), and other surveys will continue to discover even more (e.g., Anglada-Escudé et al. 2016), meaning further selection criteria are still required. Habitability constraints will help as well: if life as we know it cannot survive on an exoplanet, it is not a compelling target for biosignature searches. However, it is difficult to strongly rule on the habitability of a planet; for example, recent analyses of the habitability of Proxima Centauri b concluded that the planet could be habitable or inhabitable, depending on its evolutionary history (Barnes et al. 2016; Meadows et al. 2016).

A further challenge is the potential ambiguity of biosignatures, and in particular the dominant biosignature gas paradigm: spectrally searching the atmospheres of

(2013) find that including cloud feedback permits tidally-locked planets orbiting M-dwarfs (the only HZ objects TESS can detect) to be habitable at up to twice the insolations derived from cloud-free studies.

[6]Expected advent: 2030s or later

exoplanets for gases or combinations of gases that must be attributed to biology. This paradigm is appealing because even primitive biospheres can generate atmospheric biosignatures, because atmospheric biosignatures are remotely detectable, and because this paradigm has been previously used to remotely detect evidence of life on Earth, via Galileo lookback observations (Sagan et al. 1993). However, combinations of gases that are due to life on Earth may not necessarily have a biological origin on other planets with different conditions, i.e. the biosignature gas paradigm is vulnerable to false positives. For example, the oxic gases O_2 and O_3 have been considered strong biosignatures, because of their strong spectral signatures and their uniquely biological origin on modern Earth (Kaltenegger et al. 2002; Des Marais et al. 2002; Léger et al. 2011). However, exoplanets are very diverse; a broad range of surface conditions and planetary states are possible, and it transpires that in some regions of parameter space, terrestrial planets can abiotically build up O_2 and O_3 (Hu et al. 2012; Wordsworth & Pierrehumbert 2014; Harman et al. 2015; Gao et al. 2015). Observational discriminants can identify abiotic oxygen production in some of these cases (e.g., production of O_2 from CO_2 dissociation on planets orbiting M-dwarfs; Schwieterman et al. 2016), but not others (e.g. production of O_2 from H_2O dissociation on planets with low noncondensible gas inventories; Wordsworth & Pierrehumbert 2014). Similarly, CH_4 in the presence of atmospheric O_2 is normally considered a robust biosignature, due to the instability of reduced CH_4 in oxidized atmospheres (Sagan et al. 1993); however, infall of carbonaceous micrometeorites can generate false-positive levels of CH_4, especially in young systems or systems undergoing Late Heavy Bombardment (LHB)-like events (Court & Sephton 2012). Biosignature false negatives as also possible (Reinhard et al. 2017).

Given the diversity of planetary environments and the ambiguity inherent in remote

biosignature searches, it seems likely that the detection of life on another world will be a probabilistic statement, evaluating the detected signal in the context of a number of priors. Assessing the probability that a putative biosignature detection is a signpost of life will involve folding in a number of prior probability assumptions, such as the prior probability that the planetary parameters are within ranges that can generate a false positive[7]. The habitability of this putative exoplanet can provide another prior: if life as we know it could not survive there, it is difficult to argue the plausibility of a biogenic interpretation to a putative biosignature. However, as demonstrated by the case study of Proxima Centauri b, habitability evaluations can be ambiguous, especially when they are sensitive to assumptions as to planetary evolution, which are unconstrained (Barnes et al. 2016; Meadows et al. 2016).

1.2.5 Connection to Prebiotic Chemistry

To date, most evaluations of potential astrobiological targets focus on their *habitability*, i.e. their clemency for life as we know it to survive (e.g, O'Malley-James & Kaltenegger 2016, Shields et al. 2016a, Meadows et al. 2016). Such work has typically focused on the availability of liquid water (e.g., Shields et al. 2016b, Ribas et al. 2016), but has also explored other parameters like the surface radiation environment (Segura et al. 2005; Rugheimer et al. 2015; Thomas et al. 2015). However, comparatively little work has been done on the favorability of planets for origin-of-life events to occur and for native biospheres to arise, a metric which I term *inhabitability*. This is natural; direct measurements are possible of the tolerance limits of modern life, whereas few firm

[7]C.f. Harman et al. 2015's study of abiotic oxygenation of M-dwarf planets

constraints are available on the origin of life. However, this situation is changing. Recent advances in origin-of-life studies[8], especially in the field of prebiotic chemistry (chemistry related to the origin of life), have begun to hint towards environmental requirements for the origin of life.

A major theme of this thesis is identifying these emergent environmental requirements for the origin of life, and translating them into criteria to assess the inhabitability of planetary environments. Our efforts are analogous to past work which translated the observation that life as we know it requires liquid water into a habitability criterion, and used this criterion to gauge the habitability of planetary bodies inside and outside our solar system (e.g., Kasting et al. 1993). Such inhabitability criteria can help prioritize target selection for biosignature searches: all else being equal, objects which had environmental conditions clement for prebiotic chemistry are more compelling targets for biosignature search than objects that did not. Similarly, inhabitability criteria can be used to provide priors in analyses of putative biosignatures: all else being equal, a biotic interpretation for a given biosignature, whether atmospheric or in-situ, is more likely on objects which had environmental conditions clement for the origin of life than objects that did not. In this, inhabitability criteria play a role analogous to habitability criteria, such as the liquid water requirement. However, inhabitability criteria are likely to be more restrictive than habitability criteria, because modern life has evolved sophisticated techniques to survive hostile environmental conditions (c.f. extremophiles; see Rothschild & Mancinelli 2001, Canganella & Wiegel 2011) that would not have been available to the earliest life (Cockell et al. 2016). As such, inhabitability criteria have the potential to offer stronger constraining power than habitability criteria.

[8]See Sections 1.3.4-1.3.5

1.3 Prebiotic Chemistry: History and Recent Advances

1.3.1 Prebiotic Chemistry: A Brief History

For millennia, the dominant paradigm for abiogenesis in the European scholarly tradition was the theory of spontaneous generation. This theory held that life could spontaneously arise from nonlife, and cited a number of everyday examples as support, e.g., the spontaneous appearance of living maggots from nonliving meat. The first blow to this theory was struck by in 1668 by Francesco Redi, an Italian physician who demonstrated that if meat was isolated in sterile conditions, maggots did not spontaneously arise, and gave the causative mechanism as fly eggs instead (Srinivasan 1976). However, spontaneous generation was surprisingly resilient, and it was not until the comprehensive experiments of the French scientist Louis Pasteur in 1862 that spontaneous generation was completely refuted[9] (Srinivasan 1976).

While spontaneous generation persisted in the scientific mainstream until the late 19th century, scientists by this date had already begun to probe alternative scenarios for the origin of life. The abiotic synthesis of urea by Wohler (1828) demonstrated that compounds previously thought to be of exclusively biological origin could arise from comparatively simple chemical reactions, and scientists began to explore the idea that abiotic chemical reactions might have lead to the origin of biologically important molecules, and even life. Perhaps the most famous articulation of this paradigm was put

[9]The same experiments also showed the existence of microorganisms.

forward by Charles Darwin in an 1871 letter to his colleague Hooker:

> "It is often said that all the conditions for the first production of a living organism are now present, which could ever have been present. But if (& oh what a big if) we could conceive in some warm little pond with all sorts of ammonia & phosphoric salts,light, heat, electricity &c present, that a protein compound was chemically formed, ready to undergo still more complex changes, at the present day such matter would be instantly devoured, or absorbed, which would not have been the case before living creatures were formed." [10]

The hypothesis articulated by Darwin was prescient: its essence, that aqueous chemical reactions driven by a source of free energy could lead to the production of biological molecules capable of undergoing further complexification, e.g., via Darwinian evolution, remains at the heart of the dominant modern paradigm of the origin of life (Follmann & Brownson 2009). The study of the chemical processes that might have lead to this origin event is known as "prebiotic chemistry".

While the core paradigm of prebiotic chemistry has remained unchanged since Darwin's day, the theory of prebiotic chemistry (i.e., how to execute this paradigm) has evolved substantially. Notably, Oparin and Haldane pointed out that Earth's early atmosphere was anoxic and hence that prebiotic chemistry likely occurred under reducing conditions. Oparin and Haldane suggested that atmospheric and photolytic reactions in reducing conditions could help generate a rich population of organic molecules, which could accumulate in aqueous reservoirs and undergo further complexification until life arose. This is the "primordial soup" model for the origin of life (Oparin 1924; Haldane 1929; Shapiro 1987; McCollom 2013).

[10] Accessed via `https://www.darwinproject.ac.uk/letter/DCP-LETT-7471.xml`, 3/20/2017; see also Follmann & Brownson (2009)

1.3.2 Miller-Urey Syntheses

The primordial soup model received dramatic experimental support with the landmark Miller-Urey experiment, which demonstrated the robust and diverse synthesis of a broad range of amino acids (protein monomers) simply by putting a reducing mix of gases in contact with an aqueous reservoir and a source of free energy in the form of "lightning", i.e. a spark discharge system (Miller 1953). This result is remarkable because it suggests the building blocks of life may be synthesized simply by combining their raw ingredients with a source of free energy under anoxic conditions.

The Miller-Urey experiment assumed a highly reducing mix of gases, matching then-current thinking regarding the state of Earth's early atmosphere. Later work pointed out that UV photolysis and strong emission of relatively oxidizing gases like SO_2 and CO_2 by volcanoes should mean that the early Earth's atmosphere was much more weakly reducing than assumed by Miller & Urey. Initial challenges in replicating the Miller-Urey results under more oxidizing conditions were overcome by Cleaves et al. (2008), who pointed out that oxidation during the sampling process was interfering with measurements of the results. Miller-Urey-style synthesis appears to be a robust source of amino acids over a broad range of possible atmospheric states, and has also proven robust to the choice of free energy source and to local conditions; such nondirected syntheses have even been shown to function in conditions corresponding to space (Bernstein et al. 2002; Caro & Dartois 2013; McCollom 2013). Work by Oró & Kimball (1961) lead to the discovery that similar syntheses could also abiotically produce nucleobases. Combined with the well-known formose reaction for the syntheses of sugars (Butlerow 1861), it seemed as though simple prebiotic pathways existed that could robustly account for the

origin of most of the essential constituents of life, leading to a very simple picture of prebiotic chemistry, i.e. simply that combining the molecular ingredients of life in the presence of free energy might be sufficient to synthesize the building blocks of life.

1.3.3 Key Challenges Faced by Prebiotic Chemistry & The RNA World

However, this rosy picture hid a number of key challenges faced by prebiotic chemistry prior to 2009. Some of these challenges relate to the origin of the proteins: Miller-Urey style syntheses can generate a broad range of amino acids, but they can generate only about half of the amino acids used by life. Further, these syntheses are nonselective: Miller-Urey style syntheses generate many of the amino acids that life used, but also many of the amino acids that life does not (Ferris 1987; Johnson et al. 2008; Parker et al. 2011). Lastly, no plausible prebiotic pathway for protein polymerization is known, meaning there is no mechanism known by which the amino acid products of Miller-Urey reactions could have been prebiotically assembled into proteins.

But perhaps the most critical problems were faced by the synthesis of the ribonucleotides, the monomers of ribonucleic acid (RNA). A ribonucleotide is composed of a 5-carbon ribose sugar, connected to a phospate group and a nucleotide. We can envision plausible geochemical origins for phospate (Yamagata et al. 1991; Orgel 2004), and the nucleobases can be synthesized locally or delivered from space (Oró & Kimball 1961; LaRowe & Regnier 2008; Barks et al. 2010; Callahan et al. 2011; Burton et al. 2012; Nuevo et al. 2012; Menor-Salván & Marín-Yaseli 2013). However, sugar synthesis is a problem. The mechanism typically invoked for the prebiotic synthesis of the sugars, the

formose reaction, is a homologation reaction: it works by joining smaller sugars together into larger sugars, starting from a feedstock of formaldehyde (1-carbon sugars). The problem with this reaction is that it is nonselective: it generates a whole range of sugars, meaning that the biotically-useful ribose is generated only in small yield. Moreover, it does not terminate: it assembles larger and larger sugars until the organic feedstocks have been transformed into biotically-useless tar: the so-called "asphaltization problem" (Benner et al. 2012). Even if one assumes a ready source of the short sugars useful to biology, assembling the constituents into a ribonucleotide remains a challenge. The N-glycosdic (C-N) bond connecting the sugar to the nucleobase is very high energy and consequently extremely hard to form without either invoking a catalyst, which would not have been available in a prebiotic context, or delivering enough energy to destroy the molecular subunits. In other words, even if all the pieces are available, there is no known mechanism to assemble them into a ribonucleotide. These challenges have confronted prebiotic chemistry for decades, and in the case of the formose reaction for more than a century.

The challenges in synthesizing the ribonucleotides were especially disappointing given the otherwise promising RNA world hypothesis, i.e. the hypothesis that a self-replicating RNA polymer was the first life. This hypothesis was motivated by the discovery of ribozymes, i.e. the realization that in addition to information-bearing functions, RNA could perform the catalytic functions that were previously assumed to be the exclusive domain of the proteins. This discovery meant that proteins were potentially unnecessary to the origin of life, and may have been incorporated along with other molecules at a later stage (Gilbert 1986; Orgel 2004; Sankaran 2016). The RNA world received dramatic support when it was discovered that ribosomes were

made of RNA, i.e. that RNA catalyzes its own replication (Ban et al. 2000; Nissen et al. 2000; Steitz & Moore 2003). This hypothesis is appealing because it explains the intermediate role RNA plays in the "Central Dogma" of modern biology, the ancient nature of ribozymes (Cech 2009), the reason RNA is found in all organisms, and because it eliminates the need for prebiotic origin and co-evolution of proteins with nucleic acids, offering a potentially simpler path to abiogenesis (Orgel 2004; McCollom 2013). While other models for the origin of life do exist (e.g., Yu et al. 2013), the RNA world remains a dominant hypothesis. In this context, the failure to discover a plausible abiotic pathway to the ribonucleotides represented a critical barrier to abiogenesis and a key challenge to the RNA world hypothesis.

1.3.4 Recent Breakthroughs in Prebiotic Chemistry & Environmental Requirements

The past decade has witness dramatic progress on these decades-old problems in prebiotic chemistry, especially related to the synthesis of ribonucleotides. Powner et al. (2009) demonstrated the first plausibly prebiotic synthesis of the activated pyrimidine ribonucleotides[11] uridine monophospate (UMP) and cytidine monophospate (CMP), two of the four monomers of RNA. The key innovation of Powner et al. (2009) was to sidestep the problem of forming the N-glycosidic bond by instead starting with a C-N bond and building the rest of the of the ribonucleotide around it, similar to the approach pioneered by Sanchez & Orgel (1970) (McCollom 2013). Work is ongoing to further improve the prebiotic plausibility of this pathway, and to derive a prebiotic pathway to the purine

[11]Activated nucleotides are amenable to polymerization; see, e.g., Ferris et al. (1996)

ribonucleotides, (Powner et al. 2010; Xu et al. 2016).

A key requirement of the Powner et al. (2009) pathway are the 2- and 3-carbon sugars glycolaldehyde and glyceraldehyde. Ritson & Sutherland (2012) demonstrated a pathway for the selective synthesis of glycolaldehyde and glyceraldehyde from HCN and formaldehyde, which are thought to have been prebiotically available though mechanisms like impactor delivery or atmospheric chemistry (Zahnle 1986; Chyba & Sagan 1992; Cleaves 2008). As such, the work of Ritson & Sutherland (2012) represents a potential solution to the century-old problem of selective prebiotic synthesis of short, biologically useful sugars[12]. Patel et al. (2015) built on these earlier breakthroughs by deriving a reaction network that can can generate precursors[13] for each of the 4 major classes of biomolecule from common feedstock molecules and chemical pathways. Taken together, these discoveries are sometimes colloquially referred to as the "Sutherland" pathways, for the PI of the team which has lead many of these discoveries. The Sutherland pathways comprise major progress towards the understanding abiogenesis in general and the origin of ribonucleotides in particular, and constitute a new paradigm in in prebiotic chemistry (Ruiz-Mirazo et al. 2014; Higgs & Lehman 2015; Springsteen 2015; Šponer et al. 2016).

The Sutherland pathways are unified in their requirement for UV light. This requirement is noteworthy, given that UV light is often viewed as a stressor for abiogenesis (Sagan 1973; Cleaves & Miller 1998). However, the Sutherland pathways critically require UV light to proceed. In the Powner et al. (2009) pathway for the prebiotic synthesis of pyrimidine ribonucleotides, UV light amplifies the population of the

[12]See Section 1.3.3 for details

[13]In addition to pyrimidine ribonucleotides and short sugars, the network can generate lipid precursors and 11 of the 20 biogenic amino acids

target biotic pyrimidine ribonucleotides by destroying the abiotic stereoisomers generated by the thermal chemistry, and drives the production of UMP by photohydration and deamination of CMP. In the Ritson & Sutherland (2012) and Patel et al. (2015) pathways, UV light drives the production of cyanogen and of solvated (aquated) electrons, which are critical to the reductive prebiotic chemistry they invoke in their pathways.

In addition to the key role UV light plays in the only known pathways for the abiotic synthesis of the RNA monomer and its precursor sugars, other lines of evidence suggest an important role for UV light for the origin of life on Earth. First, the Sutherland pathways are not alone in invoking UV light. UV light has been invoked in pathways for phenomena as diverse as the origin of chirality (Rosenberg et al. 2008), the synthesis of amino acid precursors (Sarker et al. 2013), and the polymerization of RNA (Mulkidjanian et al. 2003). Second, the biogenic nucleotides are highly stable to UV irradiation compared to molecules with similar thermal properties, suggesting they emerged in a UV-rich environment; this is consistent with our understanding of surface conditions on the early Earth (Cockell 2000a; Ranjan & Sasselov 2017). Third, on a theoretical level, high-energy radiation like light is capable of directly altering the electronic states of molecules, permitting it to irreversibly alter the entropic states of molecular systems (Pascal 2012). Effecting such changes thermally requires temperatures of thousands of degrees Kelvin coupled to a quenching mechanism to preserve the changes in state; lightning and impacts can provide such temperatures, but they deliver $\sim 1000\times$ less energy to the surface of early Earth compared to UV photons, suggesting a niche role in comparison to UV (Ferris & Chen 1975).

1.3.5 Connection to Planetary Environment

Prebiotic pathways generally require specific feedstocks and environmental conditions to function. These requirements couple prebiotic chemistry to the planetary context, offering a threefold opportunity. First, we can ask if the conditions required by a putative prebiotic pathway were available on ancient Earth, and if so how broadly; this permits us to assess the prebiotic plausibility of this pathway (i.e., how likely is it that this pathway could have operated on early Earth). Second, we can compare the environmental conditions that would have been available on the early Earth to their simulation in the laboratory, isolate the differences that might impact the fidelity of the simulation, and use this evaluation to improve laboratory studies of prebiotic chemistry. Finally, we can ask if the environmental requirements for key prebiotic pathways would have been satisfied on different planets, e.g. early Mars or planets orbiting M-dwarfs. This permits us to gauge the clemency of different planetary environments for prebiotic chemistry and the origin of life, and hence their value as astrobiological targets: the inhabitability criteria discussed in Section 1.2.5.

In this thesis, we exploit this opportunity. We explore environmental requirements for putative prebiotic chemistry, and use them to constrain the plausibility of these pathways, improve their simulations in the laboratory, and explore the implications for the inhabitability of other worlds. We focus especially on UV light, because of its key role in prebiotic chemistry like the Sutherland pathways (Powner et al. 2009; Ritson & Sutherland 2012; Patel et al. 2015; Xu et al. 2016), the empirical evidence that the nucleotides emerged in a UV-rich environment (Rios & Tor 2013; Beckstead et al. 2016; Pollum et al. 2016), and because theoretical arguments suggest that it can effect chemical

change in ways that other sources of free energy cannot (Pascal 2012; Rapf & Vaida 2016). We also begin to explore the availability of reduced sulfidic anions in aqueous solution, which are emerging as key requirements for promising prebiotic pathways (Patel et al. 2015).

1.4 Thesis Summary

The fundamental goal of this thesis is to help understand how planetary conditions influence prebiotic chemistry, with the objectives of improving our understanding of the origin of life on Earth, and using this improved understanding to enhance our search for life elsewhere. As such, this thesis sits at the intersection of origins-of-life studies and astrobiology, and its results are applicable to both disciplines. The method we employ is to to identify emergent environmental requirements for putative prebiotic chemistry, compare them to what was available on Earth and on other worlds, and use the comparison to 1) improve laboratory studies of terrestrial prebiotic chemistry, 2) rule on the terrestrial plausibility of putative prebiotic pathways, and 3) understand how favored these pathways would have been on other worlds, and explore the implications for planetary inhabitability.

Chapter 1 presents an overview of this thesis, and provides background and motivation for this work. Chapters 2-5 focus on the UV environment. Chapter 2 focuses on comparing UV sources used in laboratory studies of prebiotic chemistry to the surficial and aqueous UV environment on a fiducial prebiotic Earth, and exploring the implications for laboratory studies of prebiotic chemistry. Chapters 3, 4, and 5 constrain the UV environments on early Earth, early Mars, and on planets orbiting M-dwarfs, and

explore the implications for prebiotic chemistry on these worlds. Chapter 6 explores the availability of reduced sulfidic compounds in aqueous solution on early Earth, and discusses the implications for laboratory studies of prebiotic chemistry. Chapter 7 summarizes our findings and identifies avenues for further work.

Chapter 2

Influence of the UV Environment on the Synthesis of Prebiotic Molecules

This thesis chapter originally appeared in the literature as:

S. Ranjan and D. Sasselov, *Astrobiology*, 16, 1, 2016.

Abstract

Ultraviolet (UV) radiation is common to most planetary environments, and could play a key role in the chemistry of molecules relevant to abiogenesis (prebiotic chemistry). In this work, we explore the impact of UV light on prebiotic chemistry that might occur in liquid water on the surface of a planet with an atmosphere. We consider effects including atmospheric absorption, attenuation by water, and stellar variability to constrain the UV input as a function of wavelength. We conclude that the UV environment would be characterized by broadband input, and wavelengths below 204 nm and 168 nm would be

shielded out by atmospheric CO_2 and water, respectively. We compare this broadband prebiotic UV input to the narrowband UV sources (e.g. mercury lamps) often used in laboratory studies of prebiotic chemistry, and explore the implications for the conclusions drawn from these experiments. We consider as case studies the ribonucleotide synthesis pathway of Powner et al (2009) and the sugar synthesis pathway of Ritson et al (2012). Irradiation by narrowband UV light from a mercury lamp formed an integral component of these studies: we quantitatively explore the impact of more realistic UV input on the conclusions that can be drawn from these experiments. Finally, we explore the constraints solar UV input places on the buildup of prebiotically important feedstock gasses like CH_4 and HCN. Our results demonstrate the importance of characterizing the wavelength dependence (action spectra) of prebiotic synthesis pathways to determine how pathways derived under laboratory irradiation conditions will function under planetary prebiotic conditions.

2.1 Introduction

Ultraviolet (UV) light plays an important role in the chemistry of prebiotic molecules. UV photons are energetic enough to affect the electronic structure of molecules by dissociating bonds, ionizing molecules, or exciting molecules into higher-energy states. These effects can degrade biologically important molecules, creating environmental stress and impeding abiogenesis (Sagan 1973; Cockell 2000b). However, these same properties mean that UV light is an ideal candidate as a source of energy for Miller-Urey style synthesis of prebiotic molecules (Sagan & Khare 1971; Chyba & Sagan 1992; Pestunova et al. 2005). UV light has been invoked in prebiotic chemistry as diverse as

the origin of chirality (Rosenberg et al. 2008), the synthesis of amino acids (Sarker et al. 2013), and the formation of ribonucleotides (Powner et al. 2009). Due to the greater fractional output of the young Sun in the UV compared to the modern Sun (Ribas et al. 2010; Claire et al. 2012), as well as the absence of biogenic UV-shielding O_2 and O_3 in the prebiotic terrestrial atmosphere, UV light is expected to have been a ubiquitous component of the prebiotic environment. Ferris & Chen (1975) estimate that for an ozone-free prebiotic atmosphere, UV light with $\lambda < 300$ nm contributed three orders of magnitude more energy than electrical discharges or shockwaves to the surface of the early Earth. UV light may have been the most abundant source of energy available for prebiotic chemistry.

Many experimental studies of prebiotic chemistry have sought to include the effects of UV irradiation. A large number of them are concerned with formation of prebiotic molecules on interstellar ices and cometary surfaces (see, e.g., Bernstein et al. 2000). Such studies usually use lamps or synchrotron sources in ultrahigh vacuum, and the UV output is below $\lambda < 160$ nm (see, e.g., Bernstein et al. 2002 and Öberg et al. 2009).

Prebiotic chemistry experiments in aqueous solution also often use UV lamps, because they are safe, stable and affordable UV sources. However, their output is often characterized by narrowband emission at specific wavelengths: for example, mercury lamps with primary emission at 254 nm are commonly used as proxies for prebiotic solar UV input (See, e.g., Balavoine et al. 1974; Ferris & Chen 1975; Kuzicheva & Gontareva 2001; Guillemin et al. 2004; Pestunova et al. 2005; Ferris et al. 2005; Powner et al. 2007; Simonov et al. 2007; Guzman & Martin 2008; Barks et al. 2010). However, solar UV input in that wavelength range is characterized by broadband emission. Many photoprocesses involving biological molecules are wavelength-dependent (e.g., Matsunaga

et al. 1991); hence, conclusions drawn from simulations conducted using monochromatic UV light may not hold true under more realistic conditions. In addition, solar UV input also shapes atmospheric photochemistry, which may impact the availability of reactants for some of these prebiotic pathways, as well as the energy deposited at the surface.

In this work, we explore the impact of UV light on prebiotic chemistry in liquid water on planetary environments corresponding to the young Earth, and the implications for laboratory simulations. Therefore, we consider effects including atmospheric absorption, attenuation by water, and stellar variability, to estimate the UV input as a function of wavelength in prebiotically important environments. We compare these estimates to the output of UV lamps, and discuss the implications for laboratory studies like the ribonucleotide synthesis pathway of Powner et al. (2009) and the sugar synthesis pathway of Ritson & Sutherland (2012). We selected these two experiments as our case studies because they comprise the core part of a recently developed prebiotic chemistry network for the common origin of RNA, proteins, and lipid precursors (Patel et al. 2015). Irradiation by narrowband UV light from an Hg lamp formed an integral component of these studies: we quantitatively explore their viability under more realistic UV input. Finally, we determine the constraints solar UV input places on the buildup of prebiotically important feedstock gasses like CH_4 and HCN.

2.2 Background

2.2.1 UV Light and Prebiotic Chemistry

In this subsection, we review the impact of UV light on prebiotic chemistry. By "prebiotic chemistry", we refer to the chemistry of small molecules, principally those containing C, H, N, O, P, or S, relevant to the origin of life. We focus on small molecules because large, complex molecules like proteins are not expected to be abundant prior to abiogenesis. We focus on molecules containing C, H, N, O, P, and S because those elements are the building blocks of life as we know it. We also include the chemistry of mineral catalysts which may be relevant to prebiotic chemistry. An example of a potentially relevant molecule is hydrogen cyanide, which may be a source of fixed nitrogen for organic molecules (Zahnle 1986). An example of a potentially relevant catalyst is the mineral montmorillonite ($(Na,Ca)_{0.33}(Al,Mg)_2(Si_4O_10)(OH)_2 \cdot nH_2O$), which has been shown to promote polymerization of nucleotides (Ferris et al. 1996).

UV light directly impacts the chemistry of small molecules. UV light can break molecular bonds (photolysis), produce secondary electrons (photoionization), and excite molecules out of the ground state (photoexcitation). All three of these mechanisms can affect prebiotic chemistry. We discuss the importance of each mechanism in the following.

Many evaluations of the role of UV light in prebiotic chemistry focus on photolysis of molecular bonds, stressing the potential of UV light to destroy populations of prebiotically interesting molecules. Photolyzed molecules can also recombine to form substances toxic to biological life today; for example, photolyzed water fragments

can produce toxic hydrogen peroxide, H_2O_2(Alizadeh & Sanche 2012). From this perspective, UV light is considered a biological stressor, and many disfavor high-UV environments from a habitability perspective (Sagan 1973; Cockell 2000b). However, UV photolysis may also play a role in promoting prebiotic chemistry. For example, Sagan & Khare (1971) rely on UV photolysis of H_2S to produce superthermal H atoms which collisionally provide activation energy for reactions involving hydrocarbons, such as dissociation of CH_4 for participation in subsequent reactions. Bond dissociation energies for prebiotically interesting molecules vary, but are often contained in the range 1-10 eV (23-230 kcal/mol), corresponding to photons of wavelengths $\lambda = 120 - 1200$ nm. For example, the dissociation energy of the C=C bond in the alkene C_2H_4 is 7.55 eV (171 kcal/mol, $\lambda = 164$ nm), and the bond dissociation energy of the H-OH bond in water is 5.15 eV (119 kcal/mol, $\lambda = 240$ nm)(Blanksby & Ellison 2003).

Absorption of UV light can photoionize molecules, release free electrons (termed secondary electrons) into the surrounding medium. Photoionization of liquid H_2O begins at low efficiencies at 6.0-6.5 eV and increases to 100% efficiency at 11.7 eV (270. kcal/mol, $\lambda = 106$ nm) (Mozumder 2002; Bernas et al. 1997), while benzene, the simplest aromatic hydrocarbon, photoionizes at 9.3 eV (214 kcal/mol, $\lambda = 130$ nm) at 350K (Lias & Ausloos 1978). Production of secondary electrons generates free radicals which can interact chemically with other compounds in the system. This can lead to detrimental effects for biological systems. For example, secondary electrons can induce strand breaks in DNA and damage proteins (Alizadeh & Sanche 2012). However, photoionization can also drive relevant prebiotic chemistry. For example, Ritson & Sutherland (2012) rely on photoionization of cyanocuprates to drive their synthesis pathway for simple sugars. Generation of secondary electrons by photoionization may also help explain the

origin of chirality in biomolecules. Rosenberg et al. (2008) demonstrate generation of chiral excesses at the 10% level in butanol via selective bond cleavage by spin-polarized electrons from a substrate. They suggest spin-polarized electrons generated by UV light incident on magnetic substrates as a potential mechanism for the origin of chirality.

UV light can excite molecules (photoexcitation), promoting electrons from the ground state to a higher energy state. Excited molecules can decay to the ground state via flourescence (emission of photon from excited state to ground) or phosphorescence (emission of photons over multiple transitions through lower-energy excited states on the way to ground). Excited molecules can also dissipate this energy vibrationally or collisionally. These pathways can transfer energy to other molecules, "sensitizing" them for further interactions. Finally, excited molecules can return to their ground states by rearranging their electronic orbitals (undergoing chemical changes), including breakage of the bond corresponding to the excited electron. An example of such a process is the hydration and deamination of the nucleobase cytosine into uracil. Under exposure to UV light, water is taken up by photoexcited cytosine to form a photohydrate. This photohydrate is unstable, and decays in part to uracil, releasing ammonia in the process (Peng & Shaw 1996). This is the mechanism for generation of uracil in the synthesis pathway discovered by Powner et al. (2009). Another example of photoexcitation-induced chemistry is the formation of thymine-thymine dimers in DNA (Matsunaga et al. 1991). Through such mechanisms, photoexcitation can influence prebiotic chemistry.

2.2.2 UV Light and the RNA World

A major theory for the origin of life is the RNA world hypothesis (Gilbert 1986; McCollom 2013). Under this hypothesis, RNA was the original autocatalytic information-bearing molecule, with enzymatic functions being accomplished by short RNAs. Eventually, proteins supplanted RNA as enzymes due to greater diversity of monomers, and DNA supplanted RNA as an information-bearing molecule due to greater stability. This model is appealing because it resolves the metabolism/genetics first debate by leveraging RNA's ability to fulfill both catalytic, structural and genetic roles, and it explains the origins of RNA's intermediary role in the modern "Central Dogma" of molecular biology. While other models for the origin of life do exist (see e.g., Yu et al. 2013), the RNA world remains a dominant hypothesis (Copley et al. 2007). Recent work, in particular that of Powner et al. (2009) and Ritson & Sutherland (2012), have furnished key steps toward a plausible prebiotic synthesis of RNA. In this subsection, we discuss the pathways discovered by these studies and their interaction with UV light.

Powner et al. (2009) Pathway for Synthesis of Activated Pyrimidines

A key challenge with the RNA world hypothesis is how the comparatively complex RNA molecule originated (McCollom 2013). Powner et al. (2009) achieved a remarkable step forward with their synthesis of the activated pyrimidine ribonucleotides cytosine and uracil under prebiotically plausible conditions. This pathway is the first plausible candidate for the synthesis of activated ribonucleotides, and potentially fills in a missing

step in the road to abiogenic RNA[1].

A key ingredient of the Powner et al. (2009) pathway is irradiation with UV light. UV irradiation, by a lamp with primary emission at 254 nm, plays two key roles in this pathway. First, UV irradiation destroys a number of competing pyrimidine molecules generated by the synthesis pathway. Indeed, the exceptional photostability of the pyrimidine ribonucleotides might in part explain why these particular pyrimidines were selected by evolution for incorporation into an informational polymer. Second, UV light is required to photoactivate ribocytidine to enable a partial conversion to ribouridine via hydration and deamination.

Ritson & Sutherland (2012) Pathway for Synthesis of Simple Sugars

Irradiation by UV light is also a necessary element of a companion synthesis mechanism to the Powner et al. (2009) pathway, the Ritson & Sutherland (2012) synthesis of the two- and three-carbon sugars glycolaldehde and glyceraldehyde from the one-carbon sugar formaldehyde and hydrogen cyanide (HCN). These sugars are required for the synthesis of the the pentose sugar ribonucleotide backbone in the Powner et al. (2009) process. Previously, the mechanism generally invoked to explain the prebiotic formation of sugars was the formose reaction, whereby formaldehyde polymerizes to form longer sugars. However, the formose reaction is nondiscriminate, meaning that it produces not only glycoldehyde and glyceraldehyde but also longer sugars as well as structural isomers of the sugars. Additionally, the polymerization tends to run away, generating

[1]Ferris et al. (1996) demonstrate mechanisms by which activated nucleotides can polymerize to form nucleic acids.

longer and longer chains until the products form an insoluble tar, useless to prebiotic chemistry (McCollom 2013; Ritson & Sutherland 2012). By contrast, the Ritson & Sutherland (2012) pathway uses a much more selective Kiliani-Fischer synthesis that generates a small number of products, including glycolaldehyde and glyceraldehyde in solution, available for further chemistry.

Ritson & Sutherland (2012) suggest that their synthesis relies on production of solvated electrons and protons via photoionization of the photocatalytic transition-metal cyanide complex tricyanocuprate (I) ($Cu(CN)_3{}^{2-}$). Cyanocuprates of this type can be generated from solvated Cu^+ and CN^- ions, for example via reaction of copper sulfides with cyanide solution (Patel et al. 2015). Under irradiation from a mercury lamp with primary emission at 254 nm, tricyanocuprate (I) photoionizes to tricyanocuprate (II), releasing a solvated electron on the way. This electron transfer triggers a cycle during which HCN is reduced, initiating the Kiliani-Fischer synthesis. Efforts to achieve this effect via pulse radiolysis (exposure to a beam of accelerated electrons) were unsuccessful due to generation of additional radicals which lead to a proliferation of reaction products. This suggests UV irradiation is required for this pathway.

Banerjee et al. (2014) suggest an alternate mechanism underlying the photoredox synthesis of simple sugars discovered by Ritson & Sutherland (2012). They conducted theoretical calculations to suggest that instead of photoionizing electrons from tricyanocuprate (I) to reduce HCN, the UV input excites the transition metal complex from its ground S_0 state to its excited S_1 state. The S_1 state then decays to the triplet T_1 state via intersystem crossing. This state favorably binds HCN. The resulting molecular complex can then relax by dissociation to HCN^- and tricyanocuprate (II), from which point the cycle can proceed. This mechanism is appealing because it avoids generating

free radicals, which (due to their high reactivity) might impair the selectivity of the reaction process.

The Ritson & Sutherland (2012) and Banerjee et al. (2014) photoredox pathways differ significantly in their wavelength dependence on the input UV energy. The Ritson & Sutherland (2012) process simply calls for the photoionization of the tricyanocuprate (I) complex. This process should proceed with approximately equal quantum efficiency for input photons with energy exceeding the ionization energy of tricyanocuprate (I). If the ionization energy of tricyanocuprate (I) is E_0, then for $\lambda < \lambda_0 = hc/E_0$ the pathway should proceed; for $\lambda > \lambda_0$, it should not. By contrast, the Banerjee et al. (2014) pathway requires the excitation of tricyanocuprate from S_0 to S_1, which then decays to a reactive triplet state via intersystem crossing. Banerjee et al. (2014) calculate this initial excitation occurs upon the absorption of photons with energies corresponding to a wavelength of 265 nm. Under the Banerjee et al. (2014) mechanism, the quantum efficiency of the process should peak at 265 nm.

2.3 Results

As discussed in Section 2.2, UV radiation has a key influence on prebiotic chemistry, and many experiments that seek to replicate prebiotic conditions have sought to incorporate it into their studies. However, many if not most of these studies have used narrowband UV lamps whose emission spectra are characterized by line emission. In this section, we provide estimates of the UV input in environmental conditions relevant to prebiotic chemistry and compare them to narrowband lamp input. We review factors including stellar output and activity, atmospheric attenuation, and aqueous shielding of UV flux.

We also consider the constraints furnished by UV input on buildup of feedstock gases relevant to prebiotic chemistry. Our objective is to furnish guidance to experimentalists seeking to better simulate the prebiotic environment in laboratory settings.

2.3.1 Solar UV Output in the Prebiotic Era

The dominant source of UV light in the prebiotic era, as today, was the Sun. The young Sun around the era of abiogenesis was as much as 30 % dimmer and significantly more active than the Sun today. Studies of the star κ^1 Ceti, which is a proxy for the 3.7-4.1 Ga Sun, show that despite being less luminous than the modern Sun overall, κ^1 Ceti's emission exceeds solar emission for wavelengths shorter than 170 nm by $\gtrsim 10 - 15\%$ (Ribas et al. 2010). This is due to a higher level of magnetic activity powered by a more rapidly rotating stellar dynamo. Based on observations of this solar analog, we expect the young Sun to have delivered far more of its energy in the UV wavelengths than does the Sun today. As an initial estimate of the young Sun's luminosity, we turn to the model of Claire et al. (2012), which uses data from the Sun and solar analogs to calibrate wavelength and time-dependent scalings for the modern Sun's emission spectrum. The net data product is a model for the solar spectrum through time. For purposes of our study, we choose 3.9 Ga as the era of abiogenesis. This period coincides with the end of the Late Heavy Bombardment (LHB) and is consistent with available geological and fossil evidence for early life (see Section 2.6 for details).

Effect of Stellar Variability

Shortwave UV flux ($\lambda < 170$ nm) is formed in the upper solar atmosphere, which is composed of high-temperature plasma sensitive to phenomena such as stellar activity and flares (Ribas et al. 2010). As the young Sun formed a larger fraction of its emission from shortwave radiation (Cnossen et al. 2007), this argues that the young Sun should have had stronger fractional variations in UV output than the present day. What level of variability might we expect, and how might this variability affect biologically relevant molecules?

We can obtain an initial estimate of young Sun UV variability by using the modern Sun as a proxy for the young Sun. Since we expect the young Sun to have been more variable than the modern Sun, this estimate can be interpreted as a lower bound on the young Sun's variability. Thuillier et al. (2004) present composite spectra of the Sun synthesized from multiple data sources during the ATLAS 1 (March 1992) and ATLAS 3 (November 1993) space shuttle missions. These spectra correspond to moderately high (ATLAS 1) and low (ATLAS 3) periods of solar activity, and the epochs of observation "span half of the solar cycle amplitude in terms of the MgII and F10.7 indices" (Thuillier et al. 2004). These data are accurate to 4% for the data spanning $\lambda = 122 - 400$ nm. Figure 2.1a presents the ratio between these two measured spectra. UV variability is higher at shorter wavelengths due to greater relative emission from the hot outer atmosphere of the Sun. Line variability reaches as high as 20% at sampling of 0.05 nm over the temporal and wavelength range presented, but the highest-variability lines are also the short-wavelength ($\lambda < 200$ nm) lines most strongly screened by atmospheric absorbers like CO_2 and H_2O. For most of the unshielded $\lambda > 200$ nm region variability is

less than 5%. However, the Mg II k and h lines at 279.6 and 280.3 nm (Ayres & Linsky 1980) are variable at the 11% and 8% levels respectively, and these are not strongly shielded by expected atmospheric absorbers. Since the ATLAS 1 and 3 periods spanned only about half the amplitude of the solar cycle as measured by the Mg II index, over the full solar cycle we may expect variance at levels as high as 20% in these lines. We note these lines are comparatively narrow, with the entire Mg II line complex having a width of ~ 2 nm.

(a) Ratio of composite solar reference spectra from Thuillier et al. (2004) corresponding to the ATLAS 1 (moderately-high activity) and ATLAS 3 (low activity) mission.

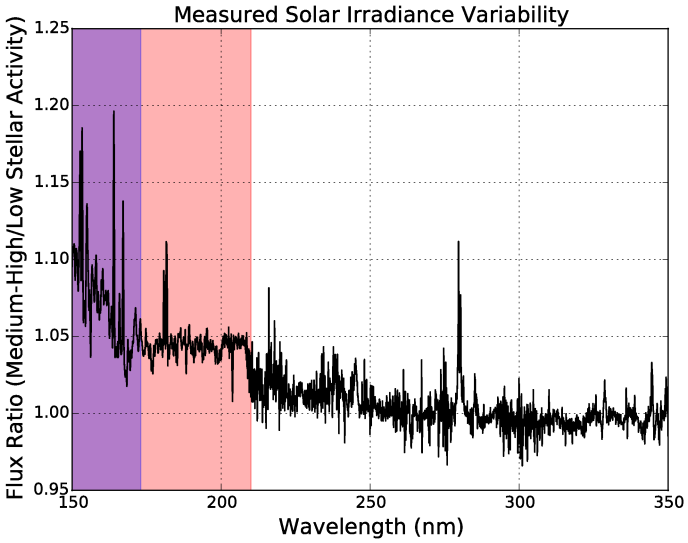

(b) Ratio of model spectra of flaring and non-flaring young Sun derived by Cnossen et al. (2007) for $\lambda = 150 - 300$ nm.

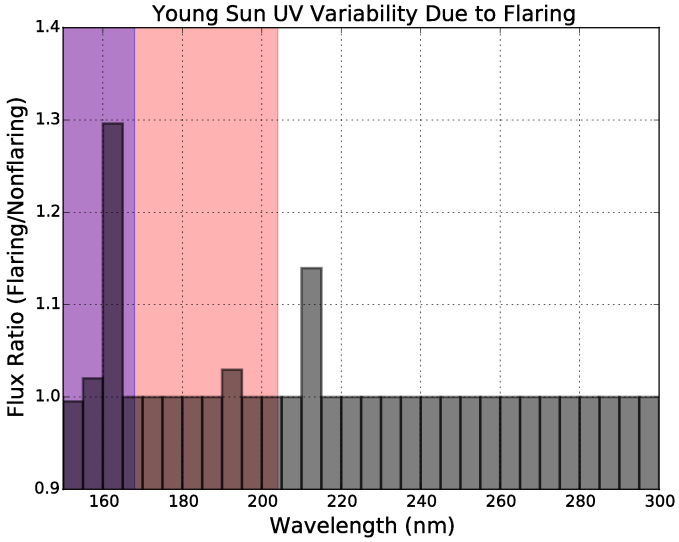

Figure 2.1: Two estimates for variability in the emission spectrum of the young Sun. Shaded in red is the region of the spectrum shielded by the prebiotic atmosphere. Shaded in purple is the region of the spectrum shielded by a 1μm layer of water. The impact of flux variations in these regions will be damped by atmospheric and aqueous attenuation.

We obtain a second estimate of the UV variability of the young Sun by considering the effects of a flare on the stellar spectrum, as modeled by Cnossen et al. (2007). Cnossen et al. (2007) estimate the emission spectra of the young Sun in flaring and non-flaring states. To do so, they divide the emission of the 4-3.5 Ga Sun into components due to the photosphere and the outer-atmosphere (corona+chromosphere). Cnossen et al. (2007) estimate photospheric emission by scaling the emission of the modern Sun by 75%. To estimate the emission due to the outer atmosphere, Cnossen et al. (2007) use the young solar analog κ^1 Ceti. κ^1 Ceti is a $M_\star = 1.04 m_\odot$, [Fe/H]=0.10 ± 0.05, $T = 0.4 - 0.8$ Gyr analog to the 3.7-4.1 Ga Sun (Ribas et al. 2010). Cnossen et al. (2007) use UV and X-ray observations of κ^1 Ceti to derive an emission model for the outer atmosphere of the star. Adding this outer-atmosphere component to the previously derived photospheric component yields an estimate of the UV spectrum of the 3.7-4.1 Ga non-flaring Sun. To estimate the UV spectrum of the flaring Sun, they scale a solar flare to κ^1 Ceti to form a new emission model for the outer atmosphere, and proceed as before. Figure 2.1b presents the Cnossen et al. (2007) ratio between the flaring and non-flaring young Sun models. For wavelengths shorter than 150 nm, chromospheric/coronal emission dominates, and there exist differences in flux that exceed a factor of 100. However, wavelengths shorter than 210 nm are shielded by atmospheric absorption, muting their impact on terrestrial prebiotic chemistry. For wavelengths longer than 210 nm, photospheric emission dominates, and variability is again low. The maximum UV variability at wavelengths longer than 200 nm is found in the 210-215 nm bin, which displays variability at the 14% level.

We sought to obtain a quantitative estimate of the impact of variability on prebiotic chemistry. We noted that the variable Mg II h and k lines are nearly coincident with

absorption peaks of some ribonucleotides (see Figure 2.2). Absorption of UV photons by ribonucleotides, can drive a variety of chemistry, ranging from photodegradation to photohydration/degradation. To gain a quantitative estimate of the potential photochemical impact of the variability of the Mg II h and k lines on the absorption of UV photons by ribonucleotides, we compute the difference in the rate of ribonucleotide photon absorption for the low and medium-high Thuillier et al. (2004) solar spectra. We weight these composite spectra with the absorption spectra corresponding to ribocytidine (at pH=7.9 and 2.5) and ribouridine (at pH=7.6 and 3.2), taken from Voet et al. (1963)[2]. We integrate these weighted spectra across the photochemically relevant 200-300 nm, and compare the resulting photoabsorption rates. Integrated across the $\lambda = 200 - 300$ nm UV window, the variation in photoabsorption rate is $\leq 0.4\%$ for all ribonucleotides, with the variation ranging from 0.09% (ribocytidine, pH=2.5) to 0.4% (ribocytidine, pH=7.9). Note that our data cover only half of the solar cycle amplitude; hence, we can expect that over a full solar cycle, we would see twice the variation in photoabsorption rates. The change in ribonucleotide UV photoabsorption rate due to the solar cycle as measured from the modern sun is small ($< 0.65\%$) in the broadband ($\lambda = 200 - 300$ nm), though in narrowband (0.05 nm) it can change by as much as 11%(Mg II line).

We perform a similar analysis with the Cnossen et al. (2007) young sun flare models. We convolve their flaring and non-flaring models against the ribonucleotide absorption spectra from Voet et al. (1963). Integrated across $\lambda = 200 - 300$ nm, the variations in photoabsorption rates are $0.2 - 0.3\%$, with the minimum and maximum variation again

[2]Note this procedure implicitly assumes an optically thin solution of ribonucleotides. At sufficiently high concentrations the solution will be optically thick and essentially all incident flux will be absorbed

corresponding to ribocytidine at pH=2.5 and 7.9, respectively. As with solar cycle-driven variation in UV output, flare-driven variations in UV output can affect the ribonucleotide UV photoabsorption rate by up to 14% in a narrow band (5 nm), but integrated across $\lambda = 200 - 300$ nm variation in photoabsorption rates falls $< 1\%$.

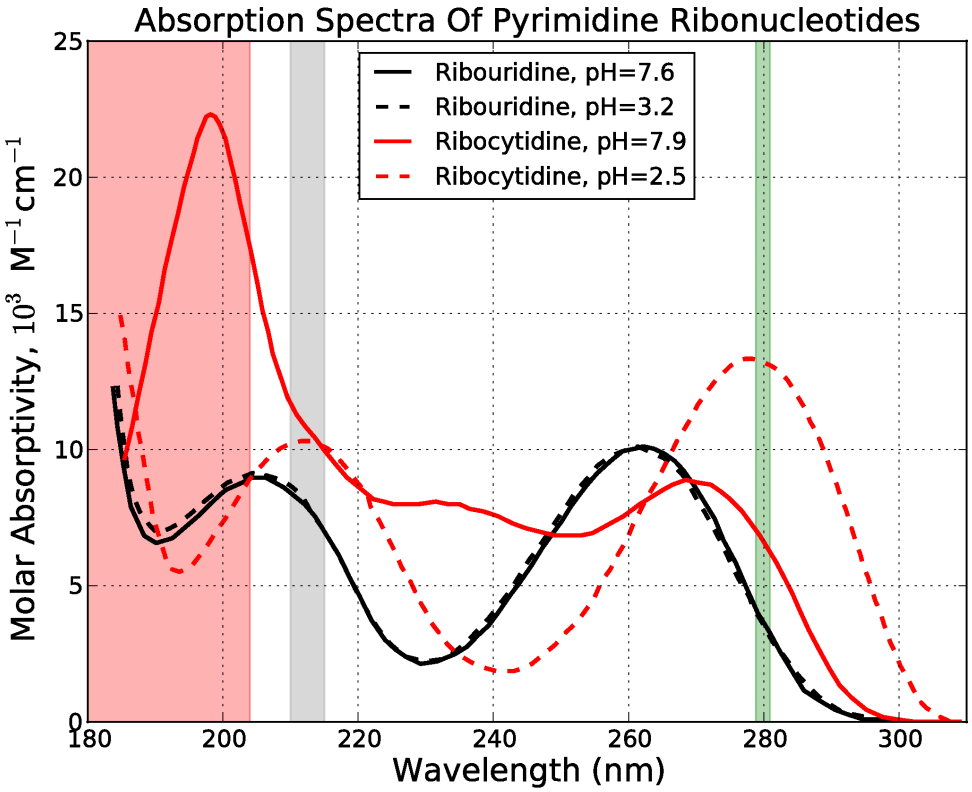

Figure 2.2: Absorption spectrum of pyrimidine ribonucleotides at different pHs, taken from Voet et al. (1963). Shaded in red is the region of the spectrum shielded by the prebiotic atmosphere. Shaded in grey is the region of the spectrum corresponding to the 210-215 nm variability feature due to flaring from the work of Cnossen et al. (2007). Shaded in green is the region of the spectrum corresponding to the Mg II k, h line complex identified from the data of Thuillier et al. (2004).

Overall, UV variability in the $\lambda > 204$ nm region of the emission spectrum of the young Sun that is relatively unshielded by atmospheric absorbers (especially CO_2) is low, usually at the level of a few percent or less. UV variability within individual features can vary at the level of tens of percent, but these features are generally narrow, muting their effect on the total UV power being received by the Earth.

2.3.2 Attenuation of UV Light By Aqueous Environments

Prebiotic chemistry, both on Earth and in space (e.g. on meteorite progenitors, see Glavin et al. 2012) is thought to have occurred in an aqueous environment. In this section, we explore attenuation of incident UV flux by water.

For the absorption spectrum of water in the UV, we draw upon the data presented in Segelstein (1981), compiled in Querry et al. (1991), and made available online by Jonasz (2007). This work aggregated previous measurements of the absorption coefficient $\kappa(\lambda)$ of liquid water near standard conditions from $10^1 - 10^{10}$ nm, and confirmed their validity with an electron sum rule calculation. Figure 2.3 presents the UV spectrum of the 3.9 Ga Sun derived from the models of Claire et al. (2012) filtered through varying depths of water. Water absorption rises sharply at wavelengths shorter than 173 nm, with 1 μm of water enough to reduce stellar flux by a factor of 10 or more for $\lambda < 168$ nm. 1 μm of water is enough to extinguish transmission by 6 orders of magnitude at $\lambda = 160$ nm, while 78 m of water is required to extinguish flux at wavelengths $\lambda = 300$ nm by an equivalent amount. This high level of absorption is due to a broad, strong absorption band (peaking at 65 nm) corresponding to a superposition of transitions associated with the photoionization and photodissociation of water (Wozniak & Dera

2007). For example, incident photons with wavelength 180 nm and shorter have enough energy to promote the $1b_1 \rightarrow 4a_1$ orbital transition, dissociating water to OH+H; for more details, see Mota et al. (2005) and Wozniak & Dera (2007). The implication is that even a thin film of water on an asteroid is enough to shield mineral chemistry from XUV flux ($\lambda < 168$ nm), but midrange UV flux ($\lambda > 168$ nm) can readily penetrate. For comparison, the fatty acid vesicles studied as model systems for protocell membranes in work like Mansy et al. (2008) and Hanczyc et al. (2003) are of order 100 nm (0.1 μm) in size.

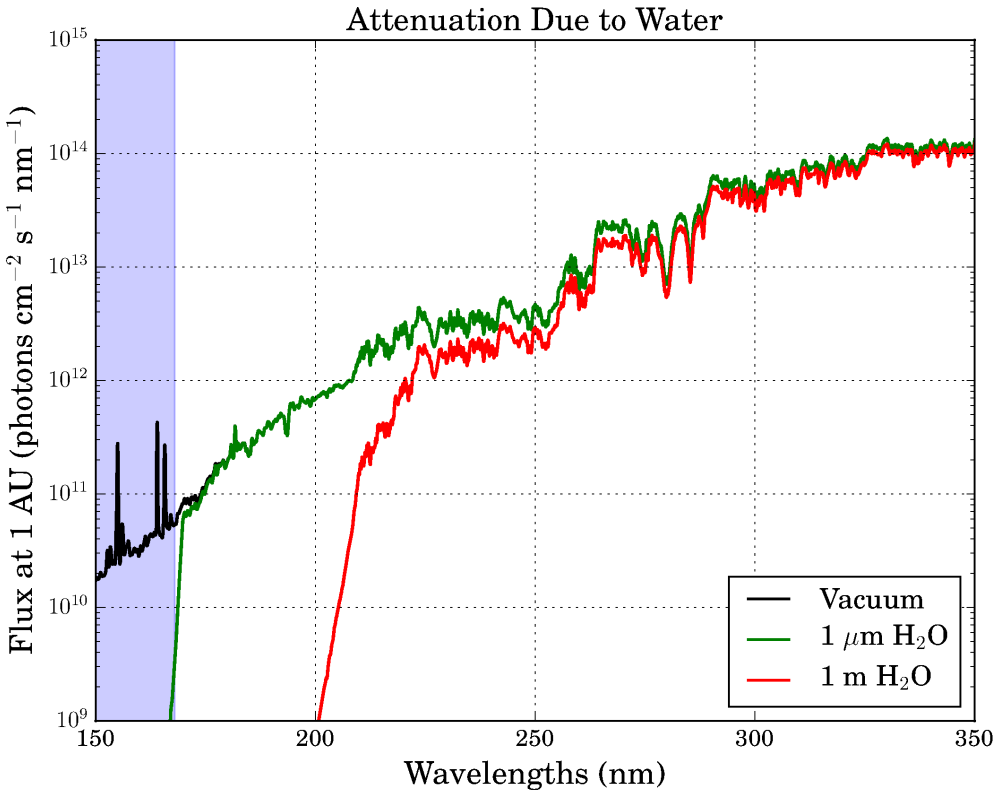

Figure 2.3: Attenuation of UV spectrum of 3.9 Ga sun through water layers of varying thickness. The spectral region shielded by water absorption is shaded in blue.

The results described above are for pure water. Prebiotic synthesis requires solutes as input for chemical reactions. We use modern seawater as a guide to approximate how dissolved constituents might affect the absorption of a water layer. 96-97% of seawater molecules are H_2O. The remaining 3-4 % of molecules are dominated by dissolved salts, but also suspended organic and inorganic particulates and dissolved bioresidue ("Gelbstoff") (Wozniak & Dera 2007; Jonasz & Fournier 2007). The addition of salts causes increased absorption in the far-ultraviolet, as well as enhanced scattering due to variations in refractive index due to salt concentration variations (Jonasz & Fournier 2007; Cleaves & Miller 1998). Bioresidue ("Gelbstoff") also absorbs in the UV, but in pre-abiogenesis waters it would not be present. Scattering due to suspended particulates is also an important effect in seawater, with particle sizes ranging from roughly 0.01-1000 μm (Jonasz & Fournier 2007). In general, inorganic suspensions are weak absorbers in the UV (Wozniak & Dera 2007). In summary, inorganic dissolved and suspended minerals have the effect of enhancing UV attenuation; hence the transmitted UV flux presented here should be interpreted as an upper bound to prebiotic conditions.

2.3.3 Attenuation of UV Light by the Terrestrial Atmosphere

Estimating the UV input on the terrestrial surface requires computing the attenuation of UV flux due to the atmosphere. As Earth in the prebiotic era would lack the biogenic oxygen and ozone that play a dominant role in UV attenuation in modern Earth's atmosphere, we are unable to use the modern Earth's atmosphere as a proxy for the young Earth's, and must instead estimate an atmospheric model from available information.

Constraints on the Prebiotic Atmosphere

Relatively little is known about the Earth's atmosphere in the prebiotic ($\sim$ 3.9 Ga) era. Synthesizing what constraints exist (see Section 2.7), we find that what evidence we have points to an N_2-CO_2 dominated atmosphere, with a high enough concentration of greenhouse gases (e.g. CO_2, CH_4) to sustain liquid surface water. Volcanogenic gases such as SO_2 may also have been important constituents during periods of high volcanic activity, and for a warm planet water vapor would also be an important atmospheric constituent. We therefore focus on these four gases as the major absorbers to consider when estimating UV flux to the planetary surface.

We note that Wolf & Toon (2010) have suggested the possibility of hydrocarbon hazes in providing planetary greenhouse warming, similar to what is seen on Titan today. Such hazes could act as UV shields. However, the formation of such hazes requires high CH_4 production rates, corresponding to a CH_4/CO_2 abundance ratio of $\gtrsim 0.1$ (DeWitt et al. 2009). Given the absence of biogenic production and lack of significant volcanic production of CH_4 based on the redox state of the mantle, such CH_4 production rates are unlikely. We consequently do not focus on hydrocarbon hazes in estimating atmospheric attenuation of UV light.

Attenuation Due to The Prebiotic Atmosphere

To estimate atmospheric attenuation due to the prebiotic atmosphere, we use the atmospheric model of Rugheimer et al. (2015). This model uses a coupled radiative-convective model that includes the effects of climate, photochemistry, and radiative transfer. This model uses stellar input equivalent to the Sun at an age of 3.9 Ga as

modeled by the Sun Through Time project (Claire et al. 2012), squarely within the 3.5-4.3 Ga age range of plausible abiogenesis. It assumes an overall atmospheric pressure of 1 bar and atmospheric mixing ratios of 0.9, 0.1, and 1.65×10^{-6} for N_2, CO_2, and CH_4, respectively. It also assumes modern abiotic outgassing rates of gases such as SO_2 and H_2S, and includes humidity (water vapor). Hence, the model includes the four key absorbers identified in the previous section. The nitrogen partial pressures adopted in the model are consistent with the constraints measured by Marty et al. (2013) for the 3.5 Ga Earth. The high CO_2 abundance relative to the present day is consistent with an atmosphere dominated by volcanic outgassing. The trace methane level is adopted from Kaltenegger et al. (2007). When iterated to convergence, this model indicates a surface temperature above freezing, indicating consistency with the constraints from zircon which suggests at least transient surface liquid water on Earth during this era.

Figure 2.4 presents the attenuation of the UV flux of the 3.9 Ga sun due to the primordial atmospheric model of Rugheimer et al. (2015). Compared to the present day, the prebiotic Earth would have received much more > 204 nm radiation due to the absence of UV-shielding oxygen. The planetary surface would still have been shielded from extremely shortwave radiation due to atmospheric CO_2: this fiducial atmosphere by a factor of 10 or more for wavelengths shorter than 204 nm. These results are consistent with the prebiotic atmosphere study of Cnossen et al. (2007). High surface UV is also consistent with the findings of Farquhar et al. (2001) that the primitive Earth was exposed to high UV.

Figure 2.4 also presents the attenuation of the surficial solar flux due to a 1 m water layer. For surface water layers of thickness ≥ 1 meter, UV light with wavelengths up to 224 nm are additionally shielded out, meaning that for water layers with depth ≥ 1

m, UV light at wavelengths less than 224 nm is not relevant to prebiotic chemistry. For water column depths < 1 m, attenuation of UV at wavelengths shorter than 200 nm is dominated by atmospheric absorption. At the 254 nm wavelength range probed by mercury lamps, the attenuation due to this fiducial prebiotic atmosphere is equivalent to that provided by 127 cm of liquid water. Hence water absorption dominates the UV environment at 254 nm at depths greater than 127 cm (e.g. in the deep ocean).

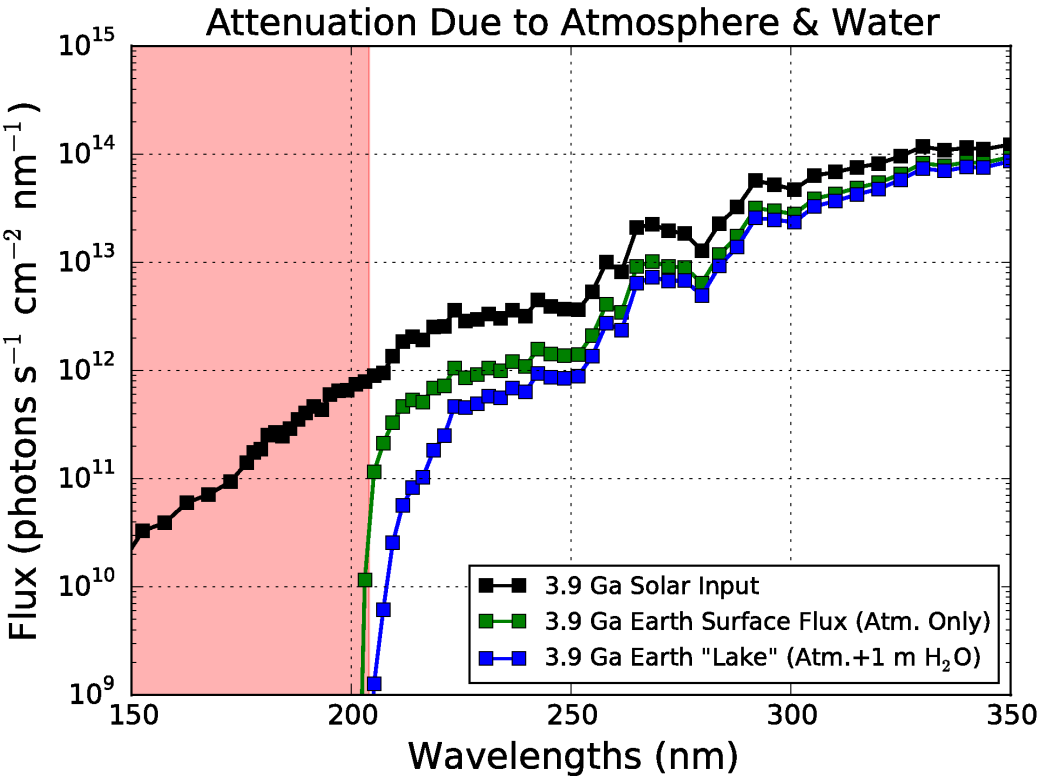

Figure 2.4: Attenuation of the 3.9 Ga solar UV spectrum due to the atmosphere modeled by Rugheimer et al. (2015), corresponding to the surface UV flux. Also shown is the surface flux attenuated by 1 m of water, corresponding to a surficial lake. The spectral region shielded by atmospheric absorption (primary CO_2 is shaded in red.

This atmospheric model assumes modern levels of volcanogenic input of SO_2 and

H_2S. It is plausible that volcanism levels, and hence SO_2 and H_2S abundances, were at least transiently higher on the young Earth (see e.g. Kaltenegger & Sasselov 2010. Higher SO_2 and H_2S levels could significantly impact the surface UV environment because these gases are better UV shields than CO_2 (see Figure 2.5).

We are not aware of existing empirical constraints on SO_2 and H_2S levels at 3.9 Ga. We can place a theoretical upper limit on the abundance of SO_2 by the work of Halevy et al. (2007), who explored potential sulfur cycle chemistry on Mars. Their work suggested that at SO_2 levels of $10^{-6} - 10^{-4}$, SO_2 starts supplanting CO_2 as the controlling agent for temperature, precipitation, weathering, and aquatic reservoir pH chemistry, i.e. a sulfur cycle starts dominating over the carbon cycle. We take 10^{-4} as the upper bound on SO_2 level at 3.9 Ga. We constrain H_2S levels by assuming the $[H_2S]/[SO_2]$ outgassing ratio to be the same as the present day value. Halmer et al. (2002) find the annual volcanic SO_2 and H_2S fluxes to the atmosphere to be $15 - 21 \times 10^{12}$ g and $1.5 - 37.1 \times 10^{12}$ g, respectively, corresponding to an $[H_2S]/[SO_2]$ ratio of .29-9.9. We therefore adopt an upper bound of 10^{-3} on H_2S levels at 3.9 Ga.

For $\lambda = 200 - 300$ nm, $\sigma_{SO_2}/\sigma_{CO_2} = 3 \times 10^6$. At an SO_2 levels of 10^{-4}, $[SO_2]/[CO_2] = 10^{-3}$. At this SO_2 level, attenuation from SO_2 would outpace extinction from CO_2 by 3 orders of magnitude. Similarly, integrated from 200-300 nm, $\sigma_{H_2S}/\sigma_{CO_2} = 2 \times 10^6$. At an H_2S level of 10^{-3}, this corresponds to extinction from H_2S outpacing extinction from CO_2 by 4 orders of magnitude. It is difficult to confidently describe the impact of epochs of high volcanism on the UV surface environment, given the uncertainties in SO_2/H_2S levels as well as secondary photochemical effects, e.g formation of UV-shielding hazes (Tian et al. 2010; Wolf & Toon 2010). Further modeling, using a framework capable of accounting for high SO_2 cases, is required. However, it

seems plausible that episodes of high volcanism may be low-UV epochs in the young Earth's history.

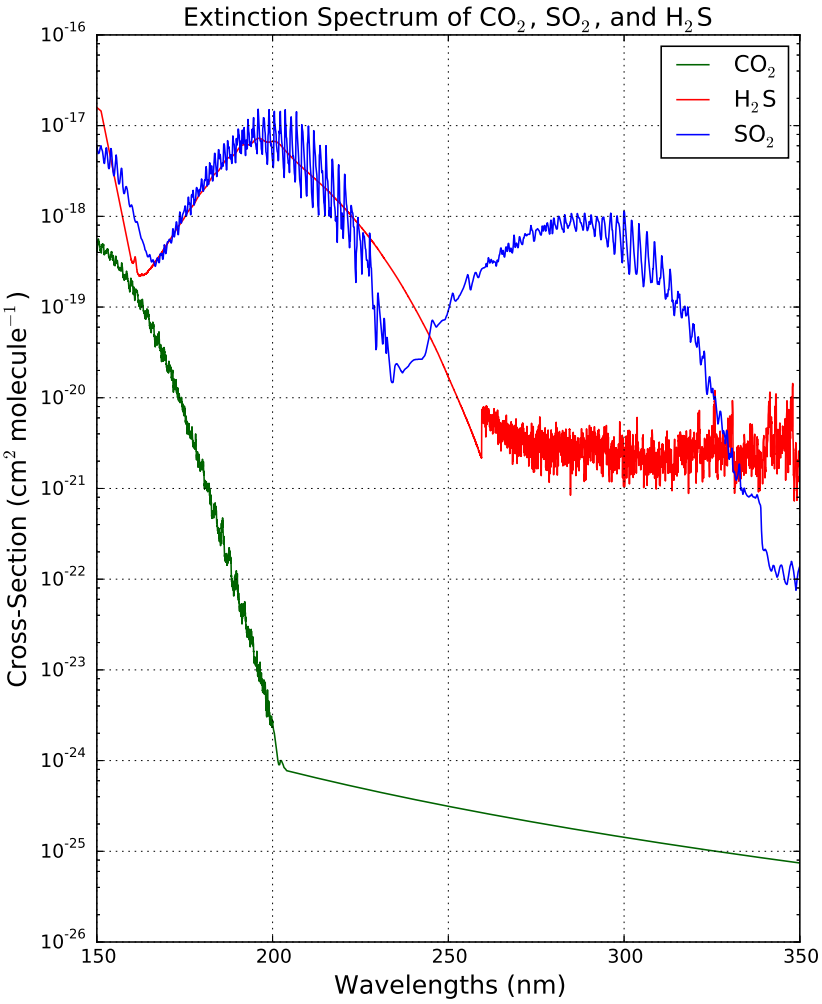

Figure 2.5: UV extinction cross-sections of SO_2, H_2S, and CO_2. Section 2.10 describes the sources of these cross-sections..

2.3.4 CO_2 Shielding of Prebiotic Feedstock Gases From Photolysis

Theoretical and experimental explorations of prebiotic chemistry often assume the availability of feedstock gases, substances which may plausibly have been present in the prebiotic era which furnish biologically useful forms of elements useful for prebiotic chemistry. Examples include CH_4 as a source of reduced carbon, and HCN as a source of reduced nitrogen (Zahnle 1986).

One fundamental constraint on the abundance of such substances is photolysis. UV photolysis can destroy these compounds as they are formed, preventing them from being available to participate in prebiotic chemistry. UV attenuation from high CO_2 atmospheres, like the 0.1 bar CO_2 atmosphere invoked in Rugheimer et al. (2015), may be capable of shielding these gases from photolysis. However, such high CO_2 atmospheric models are ad hoc models: the CO_2 level is assumed. Effects such as the carbon cycle may present geophysical sinks not considered in these models, that may make high CO_2 levels impossible to sustain. We adopt such ad hoc models because they are the best guess we have at conditions at 3.9 Ga. However, from the point of view of understanding what feedstock gases are plausibly accessible for prebiotic chemistry, it behooves us to consider how sensitive the abundance of some of these gases is to the CO_2 level.

In this section, we estimate the levels of CO_2 required to quench direct photolysis of the prebiotic feedstock gases methane and HCN. These molecules are often included in prebiotic chemistry studies, and photolysis is a major sink for both. We conduct this study by estimating the abundance of these gases under equilibrium conditions using a simple 1 source/1 sink model, and computing the CO_2 column density required to

attenuate incoming UV flux to the point at which their abundances can build up to varying levels.

We assume the source of methane/HCN to be abiotic geochemical fluxes, and we assume the sink to be UV photolysis. To gain traction on the problem, we assume an isothermal atmosphere of ideal gases in hydrostatic equilibrium. Following Rugheimer et al. (2015), we take our young Earth atmosphere to be N_2/CO_2 dominated with a surface pressure of 1 bar. We assume the mixing ratio of the feedstock gas under consideration to remain constant until a heigh z_0, whereupon it goes to zero. Lastly, we assume the feedstock gas population to be optically thin, i.e. we ignore self-shielding. This means our estimates will be upper bounds on the amount of CO_2 required to permit a given methane/HCN level. We take our top-of-atmosphere input ϕ_0 to be the UV spectrum of the 3.9 Ga sun computed from the models of Claire et al. (2012), spanning a wavelength range of 1-300 nm at 0.1 nm resolution. We obtain our CO_2 cross-sections $\sigma_{CO_2}(\lambda)$from Huestis & Berkowitz (2010), who compile CO_2 cross-sections at 300 K from 0.12-201.6 nm. Section 2.8 presents the detailed calculations used to compute these estimates. The code used to implement these calculations is available at `https://www.cfa.harvard.edu/~sranjan/www/RanjanSasselov2015/`

We emphasize that these calculations are not intended as realistic models of the early Earth's atmosphere. Rather, they are intended to estimate the column density of CO_2, N_{CO_2}, that is required to quench photolysis to the degree required to build up the surficial partial pressure of a given feedstock gas to a level P_{gas}. We emphasize that achieving this CO_2 level does not automatically imply that the gas will build up to this degree; rather, if CO_2 levels build up to or past N_{CO_2}, the constraint of photolysis on feedstock gas buildup to P_{gas} is removed, though other constraints might remain.

CO_2 shielding of CH_4 from Photolysis

Methane is important to prebiotic chemistry. Methane constitutes a reservoir of reduced carbon potentially useful to the synthesis of prebiotically interesting molecules (see e.g. Zahnle 1986, Ferris & Chen 1975). Indeed, early prebiotic chemistry studies, including the Miller-Urey experiment, were conducted in reduced gas mixes with methane as a major constituent (Kasting & Brown 1998a). CH_4 levels indirectly control the local oxidation state, affecting the prebiotic chemistry that can proceed. The buildup of methane is limited by photolytic processes, both direct photolysis as well as interaction with O and OH radicals (whose production is also dominated by photolysis) (Rugheimer et al. 2015). CO_2 shielding can protect methane lower in the atmosphere from photodestruction.

We estimate the column density of CO_2, N_{CO_2}, required to shield CH_4 buildup to a level P_{CH_4} by the formalism presented in Section 2.8. We choose $z_0 = 50$ km because the model of Rugheimer et al. (2015) shows a fall-off in CH_4 mixing ratio at this altitude. We take the rate of supply of methane to the atmosphere, S, to be equal to the present-day abiotic atmospheric flux of methane. Emmanuel & Ague (2007) estimate the present-day abiotic flux of methane to the atmosphere from serpentinization at mid-ocean ridges, volcanic emission, and other geothermal sources to be $S \sim 2.3 Mt/y = 7.3 \times 10^4 g/s = 2.7 \times 10^{27} s^{-1}$. For comparison, for a 1 $M_\oplus$, 1 $R_\oplus$ planet, Guzmán-Marmolejo et al. (2013) estimate a maximum abiotic methane production rate of $9.2 \times 10^4 g/s$, which is consistent with the Emmanuel & Ague (2007) estimate to 26%. We adopt the Emmanuel & Ague (2007) estimate for S. We obtain our methane cross-sections from Au et al. (1993), who provide cross-sections from 5.6-165 nm for 298 K methane. The methane cross-section data set the limits of the wavelength

range considered in this calculation; i.e., we calculated photolysis due to absorptions in the range of 5.6-165 nm.

We evaluate $P_{CH_4}(z = 0)$ for various values of N_{CO_2}, holding all other parameters constant. We find that CO_2 column densities of 1.04×10^{20} cm^{-2}, 2.59×10^{20} cm^{-2}, and 4.87×10^{20} cm^{-2} are required to removed photolytic constraints on methane surface pressures of 10^{-9} bar, 10^{-6} bar, and 10^{-3} bar, respectively. Under our assumption of an isothermal atmosphere in hydrostatic equilibrium, these column densities correspond via the formula $P_{CO_2} = N_{CO_2} \times kT/H$ to shielding CO_2 partial pressures at $z = z_0 = 50$ km of 5.03×10^{-6} bar, 1.25×10^{-5} bar, and 2.35×10^{-5} bar, respectively. Note that this calculation implicitly assumes all attenuation of the solar signal occurs for $z > z_0$; hence the CO_2 surface pressures estimated here are upper bounds. For $N_{CO_2}(z = 50\text{km}) \geq 7.46 \times 10^{20}$ cm^{-2} ($P_{CO2}(z = 50\text{km}) > 3.60 \times 10^{-5}$ bar), $P_{CH_4}(z = 0) \geq 1$ bar. As this exceeds the total pressure of the atmosphere, this indicates that past this column density of CO_2 shielding, photolysis is no longer a constraint on CH_4 abundance. $P_{CO2} = 3.60 \times 10^{-5}$ bar at $z_0 = 50$ km of altitude corresponds to a surface partial pressure of CO_2 of 1.49×10^{-2} bar. Hence, a surface partial pressure of CO_2 of 0.015 bar is required to shield CH_4 from photolysis up to an altitude of $z_0 = 50$ km. On the other hand, if we are willing to restrict CH_4 to the bounds of the modern troposphere ($z_0 \approx 17$ km), then a CO_2 surface partial pressure of only 2.77×10^{-4} bar is required to remove photolytic constraints on CO_2 buildup. If we further restrict CH_4 to the bottom 1 km of the atmosphere, then a CO_2 surface partial pressure of 3.60×10^{-5} bar will suffice to shield the CH_4. Table 2.1 summarizes these findings. At even 10^{-4} bar levels, CO_2 is able to shield CH_4 in the troposphere from photolysis. Hence, under our assumptions, we may expect photolysis to not be a constraint on the participation of

CH_4 in chemistry in the lower atmosphere for a wide range of CO_2 surface pressures.

Table 2.1:: CO_2 levels required to remove constraint of photolysis on buildup of CH_4 for varying values of z_0.

	$z_0 = 50$ km	$z_0 = 17$ km	$z_0 = 1$ km
N_{CO_2} (cm^{-2})	7.46×10^{20}	7.41×10^{20}	6.63×10^{20}
$P_{CO_2}(z = z_0)$ (bar)	3.60×10^{-5}	3.57×10^{-5}	3.19×10^{-5}
$P_{CO_2}(z = 0)$ (bar)	1.49×10^{-2}	2.77×10^{-4}	3.60×10^{-5}

CO_2 shielding of HCN from Photolysis

Like methane, HCN is a key feedstock gas for prebiotic chemistry. HCN provides a biologically accessible source of reduced nitrogen (Zahnle 1986). Its presence has been invoked for a variety of prebiotic chemistry studies (see e.g., Ritson & Sutherland 2012, Ferris & Hagan 1984, Orgel 2004).

Following Section 2.3.4, we estimate the column density of CO_2, N_{CO_2}, required to shield HCN buildup to a level P_{HCN} by the formalism presented in Section 2.8. Following Zahnle (1986), we take the rate of supply of HCN to the atmosphere, S, to be equal to $0.1\times$ the methane flux. We adopt the same value for the methane flux as in Section 2.3.4, hence $S \sim 2.7 \times 10^{26} s^{-1}$. We obtain our HCN cross-sections from Nuth & Glicker (1982), who provide cross-sections from 100.5-299.5 nm. Based on Lee (1980), we assume that all absorptions lead to photolysis.

Unlike methane, which in the UV absorbs only at wavelengths shorter than 165 nm (Romanzin et al. 2005), HCN absorbs until 190 nm. Due to higher solar output and

reduced CO_2 shielding at these longer wavelengths, HCN absorbs orders of magnitude more photons than CH_4 and suffers a concomitant increase in photolysis rates. As a result, much higher levels of CO_2 are required to shield equivalent amounts of HCN. Indeed, while the column density of CO_2 required to shield CH_4 from photolysis up to an altitude of $z_0 = 50$ km corresponds to a CO_2 surface pressure of 0.015 bar, the amount of CO_2 shielding required to remove photolytic constraints on HCN at this altitude would correspond to 4.75 bars of CO_2 at the surface – far exceeding the 0.1 bar of surface CO_2 assumed in our ad hoc model atmosphere.

However, if we restrict HCN to the bounds of the modern troposphere ($z_0 \approx 17$ km), absorption corresponding to a much lower surface pressure of CO_2 is required to shield HCN from photolysis. At $z_0 = 17$ km, CO_2 column densities of 2.30×10^{20} cm^{-2}, 4.78×10^{22} cm^{-2}, and 1.37×10^{23} cm^{-2} are required to removed photolytic constraints on HCN surface pressures of 10^{-9} bar, 10^{-6} bar, and 10^{-3} bar, respectively. For $N_{CO_2} > 2.35 \times 10^{23}\mathtt{cm}^{-2}$, $P_{HCN} > 1$ bar, indicating the photolytic constraint on HCN has been lifted. This corresponds to $P_{CO_2}(z = 17\text{km}) = 1.11 \times 10^{-2}$ bar, and $P_{CO_2}(z = 0) = 8.81 \times 10^{-2}$. Table 2.2 summarizes the level of CO_2 required to remove the constraint of photolysis on HCN up until different heights z_0. Overall, while very high (> 1 bar) levels of CO_2 are required to shield HCN from photolysis at high altitudes ($z_0 = 50$ km), CO_2 levels of ≈ 0.1 bar are adequate to remove photolytic constraints on HCN in the troposphere (up to $z_0 = 17$ km), and levels of 0.01 bar can shield HCN below $z_0 = 1$ km. Compared to CH_4, much higher levels of CO_2 are required to shield HCN from photolysis, and photolysis constrains HCN to be lower in the atmosphere than CH_4. Under our assumptions, surface CO_2 levels corresponding to our ad-hoc prebiotic atmospheric model (0.1 bar) are adequate to shield HCN in the troposphere

from photolysis.

Table 2.2:: CO_2 levels required to remove constraint of photolysis on buildup of HCN for varying values of z_0.

	$z_0 = 50$ km	$z_0 = 17$ km	$z_0 = 1$ km
N_{CO_2} (cm^{-2})	2.38×10^{23}	2.35×10^{23}	2.05×10^{23}
$P_{CO_2}(z = z_0)$ (bar)	1.15×10^{-2}	1.13×10^{-2}	9.89×10^{-3}
$P_{CO_2}(z = 0)$ (bar)	4.75	8.76×10^{-2}	1.12×10^{-2}

2.4 Discussion

2.4.1 Lessons for Laboratory Simulations

The prebiotic UV environment, both in space and on the terrestrial surface, is likely characterized by broadband UV exposure. On the ground, the terrestrial atmosphere will shield UV radiation shortward of 204 nm. However, there remains high UV throughput at wavelengths longer than 204 nm, even with additional shielding from layers of water as much as a meter thick. Sites of relevant prebiotic chemistry in space will lack this atmospheric shielding. However, even micron-thick layers of water will shield out UV radiation shortward of 168 nm.

This yields a few immediate lessons for prebiotic chemistry simulations involving UV light. For simulations of prebiotic chemistry on Earth, wavelengths shorter than 204 nm are not accessible. Lamps which operate at such wavelengths should therefore

not be used as UV sources in prebiotic simulations. For example, ArF eximer lasers (193 nm)(e.g., Pestunova et al. 2005), and Hg lamps with strong emission at the 184.9 nm line (e.g., Ferris & Chen 1975) are disfavored for use in simulations of surficial or near-surficial prebiotic chemistry. Similarly, for studies of aqueous chemistry on bodies not shielded by an atmosphere, lamps with emission shortward of 168 nm are disfavored.

More generally, energy is delivered to the prebiotic environment along a broad UV band. Experiments which use narrow-band lamps risk under-activating chemical pathways with photoactivation curves that are not coincident with the lamp emission peaks, while over-activating pathways whose photoactivation curves are coincident with lamp emission. As such, broadband UV sources such as Xenon arc-discharge lamps should be favored over narrowband sources in prebiotic chemistry. Such broadband sources should be fitted with filters to remove $\lambda < 204$ nm and $\lambda < 168$ nm radiation, as appropriate.

Estimates of UV variability derived from the modern Sun and from flare models of κ^1 Ceti suggest that narrowband variability is low, generally on the order of a few percent or less and never more than $\sim 20\%$. Integrated from 200-300 nm, this corresponds to a $< 1\%$ variance in the number of photons absorbed by biomolecules such as ribonucleotides. Based on these data, we argue that stellar UV variability is a less crucial phenomenon to consider when designing laboratory studies of prebiotic chemistry.

In addition to the differences in the shape of the input UV spectrum, UV lamps provide higher intensity radiation than would have been accessible at the planetary surface. For example, the lamp apparatus used in Powner et al. (2007) and Powner et al. (2009) can be expected to deliver 6×10^{15} photons/s/cm^2 to the sample integrated

across its 254 nm emission feature. In comparison, we expect the surficial solar input to have delivered 4×10^{13} photons/s/cm^2 from 250-260 nm, and 1×10^{15} photons/s/cm^2 from 200-300 nm. Hence we expect the lamp to deliver 1-2 orders of magnitude more flux to the sample than the natural environment. This difference has in the past been dismissed under the argument that increasing the UV flux serves simply to accelerate the UV photochemistry to timescales more readily accessible in the laboratory. However, care must be taken in the interpretation of such studies to ensure that nonlinearities at lower fluence levels (e.g., due to backreactions) do not disrupt the pathway. One way to probe such effects is to measure reaction rate as a function of fluence level and verify linearity down to natural fluence levels.

2.4.2 Narrowband vs. Broadband Input

We have demonstrated that the natural prebiotic environment was characterized by broadband UV input, as compared to the narrowband input provided by sources like mercury lamps. However, the question remains as to the impact of using narrowband lamps instead of more realistic natural input: are narrowband sources viable proxies for prebiotic UV flux? We explore this question through the case studies of the Powner et al. (2009) and Ritson & Sutherland (2012) pathways.

Implications for Powner et al. (2009) Process

The Powner et al. (2009) pathway for synthesis of activated pyrimidine ribonucleotides was derived under narrowband 254 nm emission from a mercury lamp. In this section, we explore whether this pathway can proceed under our modeled prebiotic UV input.

UV light impacts the Powner et al. (2009) pathway in two ways. One is a relatively straightforward photohydration and deamination of cytosine, which is the mechanism for production of uracil. The second way is by destroying competitor pyrimidine nucleosides and nucleotides generated by the phosporylation reaction. Non-biogenic pyrimidine molecules generated along with the biogenic ribonucleotides photolyzed at higher rates than the biogenic molecules, amplifying the population of biogenic molecules over time. However, this phenomenon was observed only at 254 nm. It is unknown whether at different wavelengths competitor molecules might have higher survivability than the ribonucleotides, negating the amplification mechanism used in this pathway. It has been argued that the biogenic nucleobases emerged as informational polymers because of exceptional stability to UV radiation (see, e.g., Mulkidjanian et al. 2003). Under this hypothesis, ribocytidine and ribouridine are more photostable than competitor molecules across all wavelengths, in which case 254 nm radiation would be a good proxy for prebiotic UV input. However, this hypothesis has not been proven. It remains possible that at other wavelengths, other competitor molecules might emerge as more stable than ribouridine and ribocytosine. In this case, 254 nm radiation would be a poor proxy for prebiotic UV input. Empirical measurements of nucleotide photostability as a function of wavelength are required to differentiate between these possibilities.

We illustrate this quantitatively with a numerical experiment. Powner et al. (2009) found irradiation to enhance the population of the biogenic β form of the molecule relative to the α form also produced previously in the synthesis pathway. This implies that the photolysis rate of the β form should be less than that of the α form. We compute photolysis rates for the α (non-biogenic) and β (biogenic) stereoisomers of ribocytidine as a function of wavelength under irradiation by 1) a Pen-Ray mercury lamp

of the type used by Powner et al. (2009) and 2) under modeled natural prebiotic input. To do so, we must define action spectra for photolysis of each of these molecules. These action spectra can be computed as the product of absorption spectra (fraction of incident photons absorbed) and quantum efficiency functions (QEF, fraction of absorbed photons leading to photolysis). We assume that both forms of the ribocytidine molecule share the same absorption spectrum since they share similar chromophores, which we represent by the absorption spectrum of pH=7.9 ribocytidine measured by Voet et al. (1963). For comparison, the Powner et al. (2009) experiments were conducted at pH=6.5. As the QEF for photolysis of α and β are not available, we assume functional forms for them. We represent the QEF of β ribocytidine photolysis by a flat line at 0.4, and the QEF of α ribocytidine photolysis by a step function with value 0.6 between 250 and 260 nm, and 0.2 elsewhere. We emphasize that these QEFs are not physically motivated, and should not be taken to be representative of the true QEFs. Rather, they are constructed to illustrate the point that QEFs may exist that permit β ribocytidine to be more stable than the α form at wavelengths accessed by the mercury lamp, but not at other wavelengths.

Figure 2.6 presents the formation of the phototolysis rate calculation. We represent the prebiotic flux with the emergent surface spectrum computed by Rugheimer et al. (2015), corresponding to the radiation environment on the surface following attenuation by the atmosphere. We represent the lamp flux by the emission spectrum of a Pen-Ray 90-0012-01 UVP mercury lamp emitting 4.4×10^4 erg/s/cm^2 at a distance of 1.9 cm integrated across the 254 nm line. We compute the fraction of incident flux absorbed as a function of wavelength via the molar absorptivities from Voet et al. (1963); we assume a path length of 0.53 cm and a nucleotide concentration of 20 mM, chosen to accord with

the experimental setup of Powner et al. (2009). At this concentration and path length, the absorption spectrum is optically thick across most of the wavelength range under consideration, implying the photolysis rate should depend only weakly on the spectral absorbance. We consider fluxes from 200-303 nm, chosen to encompass the 200-300 nm region of photochemical interest while avoiding truncating the wavelength bins of our computed prebiotic UV spectrum.

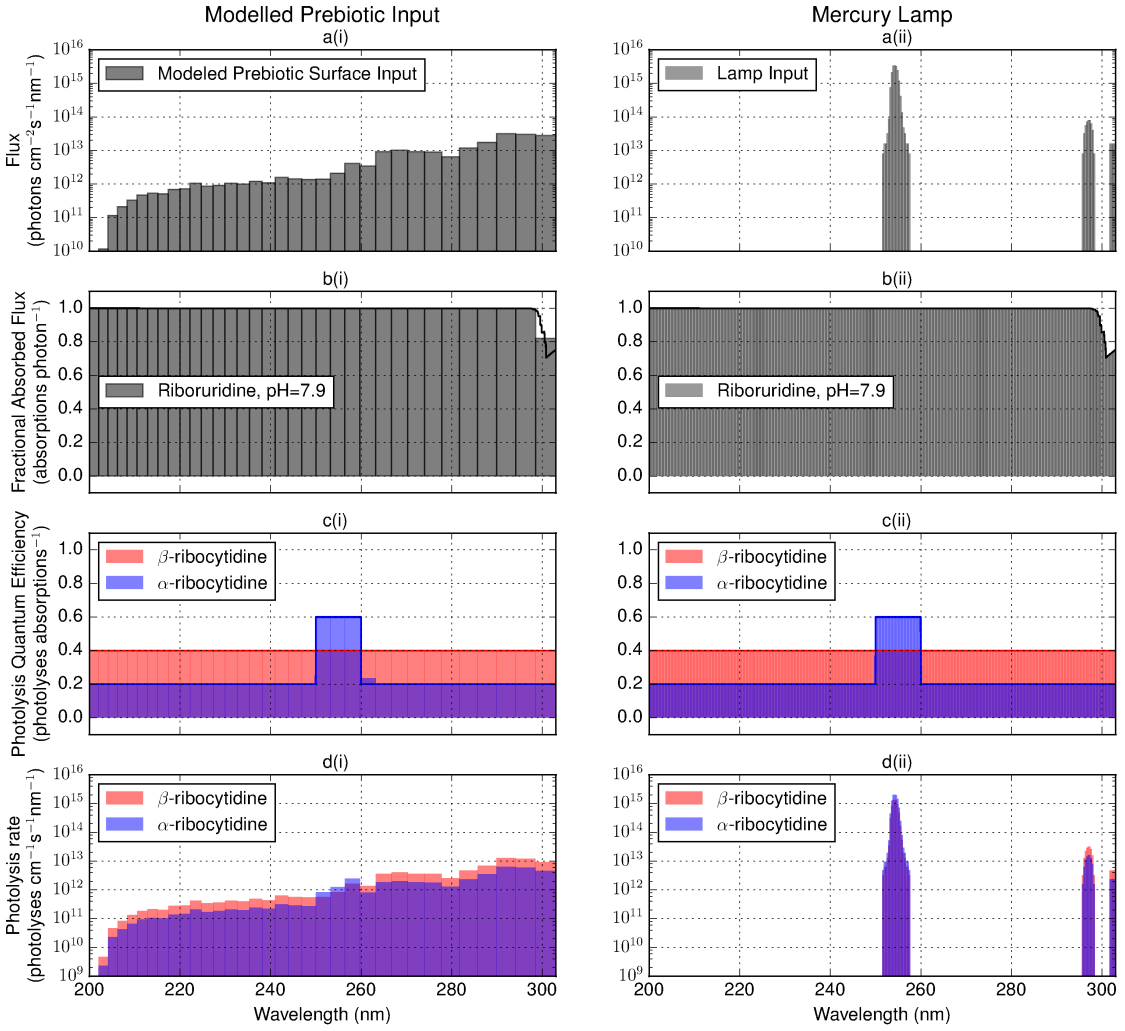

Figure 2.6: (a) Incident flux, (b) fraction of incident flux absorbed, (c) assumed QEF of photolysis for β (biogenic) and α (nonbiogenic) ribocytidine. Panel (d) presents photolysis rate for each stereoismer under irradiation by (i) prebiotic flux and (ii) mercury lamp flux, formed by convolving panels (a), (b) and (c).

We convolve the two different incident flux distributions agains the absorption spectrum and the assumed quantum efficiency curves to derive photoreaction rates as a

function of wavelength. Figure 2.6 shows each of these input curves and the product of their convolution. Integrating over wavelength, we find that under these assumed QEFs, αribocytidine has a 47% higher photolysis rate under irradiation by lamp flux than β-ribocytidine, yielding the stability advantage to the biogenic β stereoisomer observed in the Powner et al. (2009) experiment. However, under irradiation by prebiotic UV input, α ribocytidine photolyzes at a rate 46% lower than β ribocytidine, meaning that under prebiotic input, the nonbiogenic stereoisomer would be amplified relative to the biogenic. This numerical experiment demonstrates that there exist QEFs consistent with the Powner et al. (2009) laboratory experiments which would nonetheless cause the reaction pathway to fail under exposure to a fully realistic prebiotic UV environment. These results highlight the importance of employing realistic simulations of UV environments when conducting prebiotic chemistry studies. Additionally, it is important to characterize the wavelength dependence of the action spectra of the underlying photoprocesses of these pathways, e.g. by repeating the experiment at different irradiation wavelengths using tunable UV sources and measuring yield. Measuring these action spectra permits characterization of the underlying photochemistry, enabling extrapolation from laboratory results to prebiotic settings.

Implications for Ritson & Sutherland (2012) Process

The Ritson & Sutherland (2012) process also relies on narrowband mercury lamp emission at 254 nm. In this section, we explore how how irradiation under our modeled natural prebiotic UV input would affect this process.

There are two presently postulated mechanisms by which UV light reduces HCN

to drive the Ritson & Sutherland (2012) pathway. The first is the hypothesis outlined by Ritson & Sutherland (2012) whereby UV light photoionizes an electron from tricyanocuprate (I). In this case, any incident radiation at wavelengths shorter than a critical wavelength λ_c will drive this synthesis, where λ_c corresponds to a photon with energy equal to the work function of tricyanocuprate (I). Empirically, we know $\lambda_c \gtrsim 254$ nm, since the reaction proceeded under action of 254 nm radiation. Alternately, Banerjee et al. (2014) suggest that the pathway is driven by UV excitement of tricyanocuprate (I) from the S_0 to the S_1 state. The energy difference between these states is calculated to correspond to 265 nm; consequently, 265 nm radiation should be much more efficient than 254 nm radiation at promoting this transition, and the Ritson & Sutherland (2012) experiments may underestimate the reaction rate. As the models suggest that both $\lambda > 254$ and $\lambda \approx 265$ nm radiation are abundant on the surface of the primeval Earth, the Ritson & Sutherland (2012) pathway should function regardless of photochemical mechanism; however, depending on the nature of the mechanism, the difference between lamp and primeval input may drive significant differences in reaction rate. We note that two reductions are required to produce a single molecule of product.

To explore this question quantitatively, we again conduct a simple numerical experiment to that done in Section 2.4.2. We again represent the two UV light sources by the Rugheimer et al. (2015) surficial emergent spectrum and a Pen-Ray Hg lamp radiating 4.4×10^4 erg/cm2/s integrated across the 254 nm line at a distance of 1.9 cm. We again consider fluxes from 200-303 nm, chosen to encompass the 200-300 nm region of photochemical interest while avoiding truncating the wavelength bins of our computed prebiotic UV spectrum. We compute the fraction of incident flux absorbed by $Cu(CN)_3^{2-}$(I) as a function of wavelength assuming a path length of 1 cm and a

$Cu(CN)_3^{2-}$(I) concentration of 6 mM, chosen to accord with the experimental setup of Ritson & Sutherland (2012). We obtained the spectral molar absorption of $Cu(CN)_3^{2-}$(I) from Magnani (2015) (see also Section 2.9). At this concentration and path length, the absorption spectrum is optically thick across most of the wavelength range under consideration, implying the photolysis rate should depend only weakly on the spectral absorbance. Lastly, we represent the QEF of the photoionization-driven mechanism postulated by Ritson & Sutherland (2012) as a step function valued at 1 for $\lambda < \lambda_c$ nm and 0 otherwise, and the QEF of the photoexcitation-driven mechanism postulated by Banerjee et al. (2014) by a Gaussian with amplitude 1, centered at 265 nm, with width σ_c. We convolved these emission spectra, absorption curve, and QEFs together to determine the HCN photoreduction rate as a function of wavelength. We explored a range of values for λ_c and σ_c. Figures 2.7a and 2.7b show the dependence of the integrated photoreduction rate on λ_c and σ_c.

(a) Integrated HCN photoreduction rate (200-303 nm) under lamp and modeled prebiotic UV input as a function of λ_c (the threshold value for the assumed step function QEF).

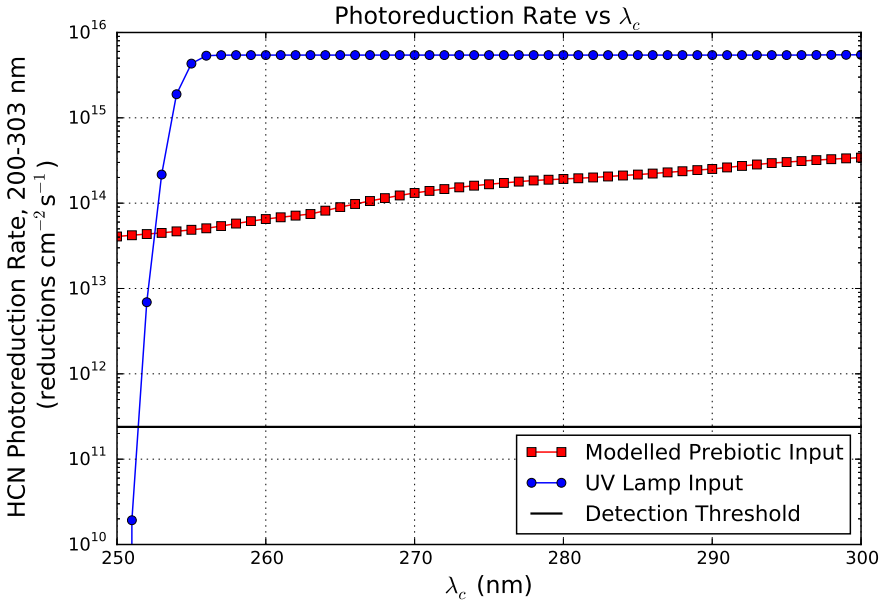

(b) Integrated HCN photoreduction rate (200-303 nm) under lamp and modeled prebiotic UV input as a function of σ_c (the standard deviation of the assumed Gaussian profile for the reaction QEF).

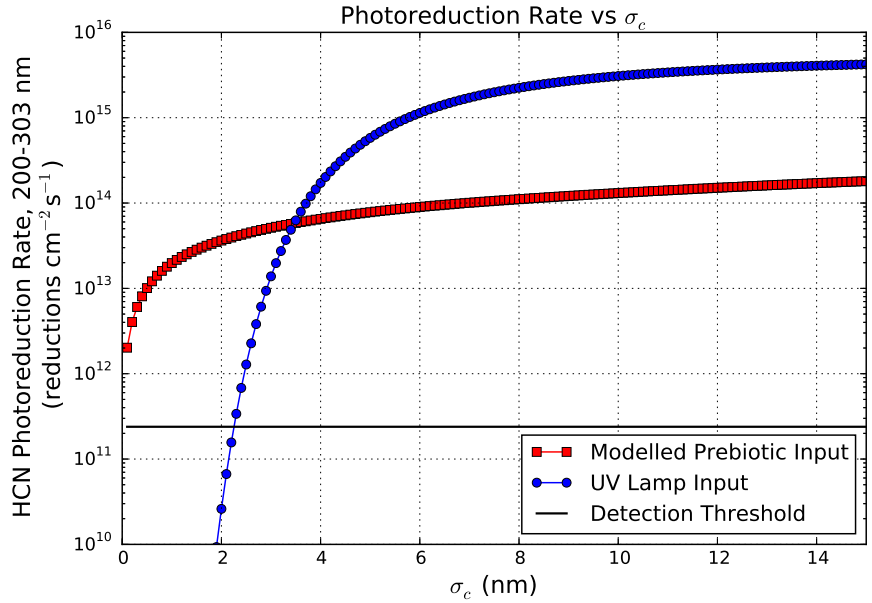

Figure 2.7: Dependence of HCN photoreduction rate on λ_c and σ_c. Also plotted is the minimum photoreduction rate required to generate a detectable quantity of product assuming 7 hour integration, 10 μL sample, and 50 picomol detection threshold.

Figure 2.7a shows the integrated HCN photoreduction rate under exposure to lamp and model prebiotic spectra as a function of λ_c. The lamp photoreduction rate increases rapidly as λ_c increases from 251 to 257 nm, corresponding to the mercury emission line. The photoreduction rate then levels off, reflecting the minimal flux produced outside the emission line. By contrast, the prebiotic photoproduction rate increases monotonically with λ_c as more and more of the absorbed flux is usefully exploited. The lamp photoreduction rate is greater than the prebiotic photoreduction rate even at $\lambda_c = 300$. This is because the irradiance from the UV lamp at the distance we have modeled here (1.9 cm) is larger in amplitude than the prebiotic flux. A dimmer lamp or larger irradiance distance will lead to lower lamp fluxes and hence photoreduction rates.

Figure 2.7b shows the integrated photoreduction rate under exposure to lamp and model prebiotic spectra as a function of σ_c. For values of $\sigma_c < 3.4$ nm, the lamp photoreduction rate is less than the prebiotic photoreduction rate. This reflects the displacement between the 254 nm emission of the lamp and the 265 nm center of the QEF. However, for $\sigma_c > 3.4$ nm, the wings of the QEF are wide enough to capture adequate lamp flux to exceed the photoproduction rate under prebiotic UV input. This is a function of both the wavelength dependence of the action spectrum as well as the greater amplitude of UV flux emanating from the lamp.

Also plotted in both figures is the experimental detection threshold, the photoreduction rate required to generate a detectable quantity of product. The detection threshold is dependent on the laboratory setup and experimental technique used to measure the photoreduction rate, as well as the experimental integration time. The example plotted here is based on an experimental setup which requires 50 picomols

of product to be present in 10 μL samples for an LCMS detection[3]. We assume an integration period of 7 hours for the example presented here, corresponding to the integration period used in Ritson & Sutherland (2012). Under these assumptions, a detectable quantity of product is generated for a wide range of λ_c and σ_c. This suggests experimental measurements of the action spectrum of this photoprocess should be tractable.

Figure 2.8 shows the photoreduction rate calculation for $\lambda_c = 257.$ nm and $\sigma_c = 3.65$ nm. At these values, the photoreduction rates under exposure to the lamp emission spectrum are equal under both mechanisms. However, under prebiotic emission, the Gaussian QEF yields photoreduction rates 69 times higher than the step function QEF. The HCN photoreduction rate can vary by two orders of magnitude depending on whether lamp or realistic prebiotic flux are used! This numerical experiment illustrates the importance of characterizing action spectra of prebiotic photoprocesses, to enable extrapolation from laboratory to prebiotic contexts.

[3]C. Magnani & Anders Bjorkbom, personal communication, 05/15/2015.

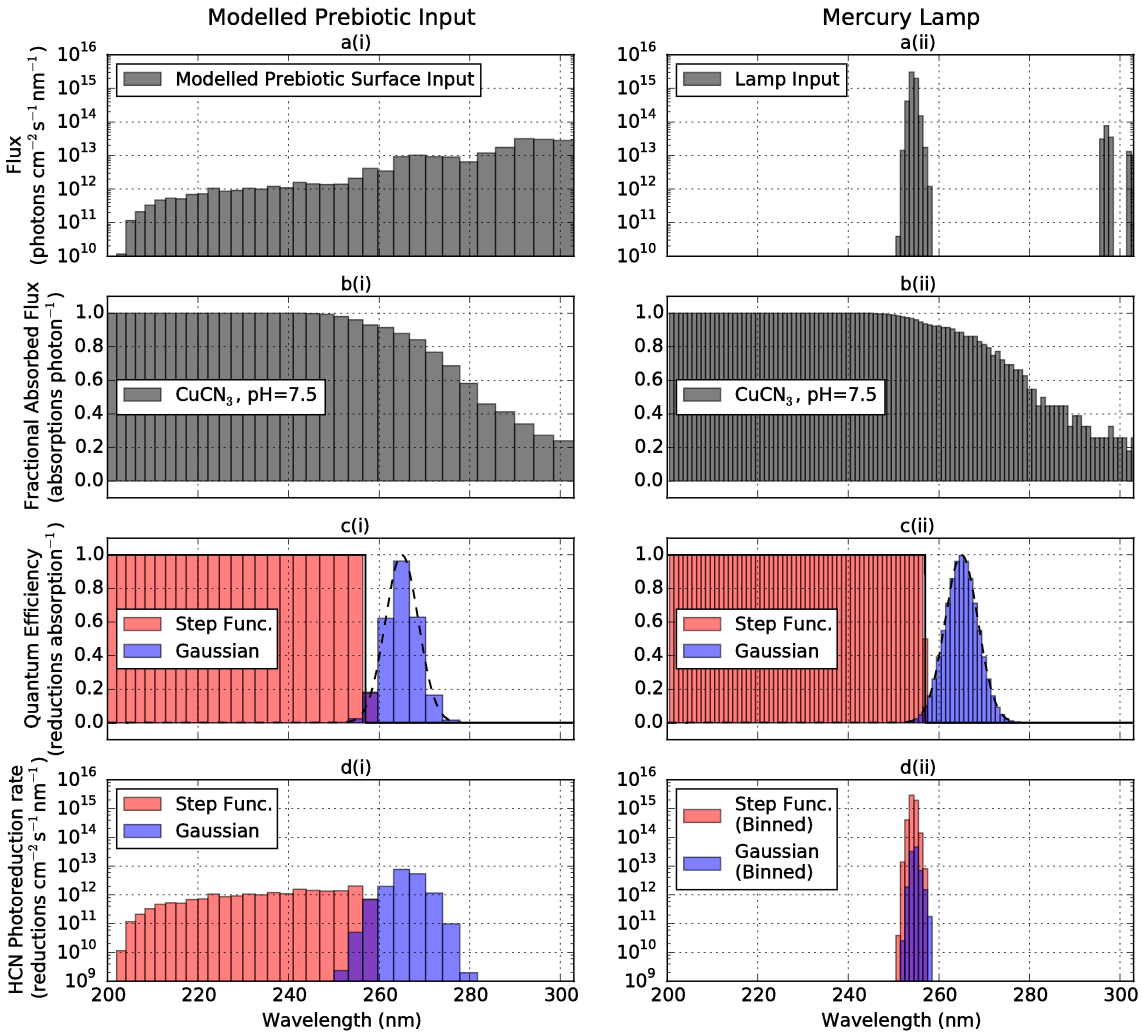

Figure 2.8: (a) Incident flux, (b) fraction of incident flux absorbed, (c) assumed Gaussian and step function QEFs of HCN photoreduction by tricyanocuprate. Panel (d) presents photoreduction rate for the two assumed QEFs under irradiation by (i) prebiotic flux and (ii) mercury lamp flux, formed by convolving panels (a), (b) and (c).

2.5 Conclusions

The prebiotic UV environment was exposed to high levels of UV radiation relative to the present day. The surface of the young Earth would had been exposed to much more UV light than the modern Earth, due to lack of UV-shielding O_2 and O_3. However, the shortest wavelength radiation remained blocked by environmental constituents. Micron-thick films of water can extinct UV flux with $\lambda < 168$ nm, suggesting that even on bodies such as asteroids and comets such short wavelengths are not relevant to prebiotic chemistry. On Earth, attenuation of solar UV flux due to atmospheric carbon dioxide means that UV inputs with $\lambda < 204$ nm was sharply attenuated. However, UV flux with $\lambda > 204$ nm would have been readily available. It is possible that SO_2 absorption during epochs of high volcanism may have been comparable or even exceeded that due to CO_2; future work should self-consistently include SO_2 absorption at varying levels in estimating atmospheric UV attenuation.

These findings bear lessons for efforts to simulate prebiotic photochemistry in laboratory settings. First, UV sources emitting radiation with $\lambda < 168$ nm, such as 158 nm flourine lasers, should not be used to simulate aqueous prebiotic chemistry in any situation. For surficial chemistry on the prebiotic earth, sources should emit at wavelengths $\lambda > 204$ nm; sources like ArF eximer lasers which emit at 193 nm, or Hg lamps calibrated for primary emission at 184.9 nm, should not be used. Second, broadband UV sources are favored over narrowband sources like UV lamps. Sources able to incorporate the effects of solar atomic lines and molecular absorption, like tunable UV lasers, would provide an even higher-fidelity simulation of the UV environment. Tunable sources will also enable simulation of phenomena such as solar activity, which

may influence photochemistry. However, based on proxies for the young Sun such as κ^1 Ceti and the modern Sun, the variation in UV output of the young Sun may have been comparatively modest, corresponding to a $< 1\%$ variation in ribonucleotide photoabsorption rates integrated over 200-300 nm. This suggests variations in UV output driven solar variability are not crucial drivers of prebiotic chemistry. Third, there can be significant differences (1-2 orders of magnitude) between natural UV fluence levels and those generated by UV lamps. The often-higher fluence levels of UV lamps can make the timescales of photochemistry-driven processes more tractable to laboratory study, but such studies should take care when extrapolating from high-fluence regimes to natural conditions. Sensitivity studies characterizing the dependence of reaction rate on fluence level can help with such extrapolations.

Simulations of prebiotic chemistry often rely on the availability of feedstock gases such as HCN and CH_4. A key constraint on the availability of these gases is UV photolysis, which would have been higher in the prebiotic era due to higher UV throughput in the atmosphere. Atmospheric CO_2 can shield such gases from photolysis, depending on its atmospheric levels. For CH_4, $N_{CO_2} > 7.46 \times 10^{20}$ cm^{-2} is enough to remove photolytic constraints on CH_4 abundance. Under our assumptions of a uniform isothermal atmosphere in equilibrium, achieving this level of shielding at $z = 50$ km requires a CO_2 surface pressure of 1.49×10^{-2} bar, with lower CO_2 levels being required the deeper one goes into the atmosphere. CO_2 surface pressures of $> 2.77 \times 10^{-4}$ bar will remove photolytic constraints on tropospheric ($z < 17$ km)CH_4. The more photoactive HCN requires more shielding: $N_{CO_2} > 2.35 \times 10^{23}$ cm^{-2} is required to lift photolytic constraints up to an altitude of 50 km, corresponding to a staggering 4.75 bars of CO_2 required at the surface. If HCN is sequestered in the troposphere, then 8.76×10^{-2} bar

of CO_2 is adequate to remove the photolytic constraint.

The work of Ritson & Sutherland (2012) and Powner et al. (2009) towards prebiotic synthesis of RNA provide case studies into the relevance of accurately reproducing the UV environment. The Ritson & Sutherland (2012) pathway for the controllable synthesis of simple sugars uses UV light to reduce HCN using tricyanocuprate (I) as an electron donor. Two theoretical mechanisms have been outlined whereby this is accomplished. We have demonstrated that under both mechanisms, narrowband 254 nm mercury lamp radiation is an acceptable proxy for prebiotic UV flux with the caveat that, depending on the underlying mechanism, reaction rates measured under narrowband lamp radiation may conceivably be different from those measured under irradiation corresponding to the prebiotic environment by multiple orders of magnitude.

The Powner et al. (2009) pathway for the synthesis of activated ribonucleotides uses UV light in two steps. The most crucial of these is the amplification of ribocytidine and ribouridine relative to other products of the synthesis reaction due to differential UV photolysis. The wavelength dependence of this relative photostability advantage is not known for this set of molecules. It is plausible that photolysis rates will vary as a function of molecule and wavelength. We have demonstrated that it is possible for there to exist photolysis quantum efficiency curves such that the Powner et al. (2009) process proceeds in laboratory settings but not in a radiation environment corresponding to the surface of the young Earth. Further experimental work, e.g. replicating the experiment under broadband or tunable laser UV input, is required to fully validate this pathway.

In general, our work suggests the importance of characterizing the action spectra (wavelength dependence) of UV-sensitive chemical pathways thought relevant to prebiotic

chemistry. Determining these action spectra enables the extension of laboratory studies to the natural prebiotic environment. Further, these action spectra can be used to determine the viability of proposed chemical pathways on alien planetary environments, e.g. exoplanets. Characterizing the action spectra of prebiotic pathways is crucial to understanding whether mechanisms hypothesized to have lead to abiogenesis on Earth could also operate on other planets.

Acknowledgements

We thank C. Magnani for many discussions and his sharing his measurement of the tricyanocuprate absorption spectrum with us. We thank S. Rugheimer for sharing her prebiotic atmosphere models and insight with us. We thank M. Powner for sharing insights on the photochemistry underlying the pathways in his work with us, as well as further discussions and his feedback on our manuscript. We additionally thank I. Ribas for kindly sharing his spectrum of κ^1 Ceti and his insight upon request, I. Cnossen for sharing her young Sun models, C. Y. Wu for sharing his methane cross-section data, V. Vuitton for sharing her compilation of HCN cross-sections, and E. Schwieterman for help with absorption spectra of atmospheric absorbers. We thank D. Zubarev, D. Ritson, K. Zahnle, R. Wordsworth, F. Tian, J. Delano, S. Harman, A. Bjorkbom, A. Glenday, and A. Fahrenbach for instructive discussions. We thank L. Schaefer and an anonymous reviewer for comments which substantially improved this manuscript.

This research has made use of NASA's Astrophysics Data System Bibliographic Services, and the MPI-Mainz UV-VIS Spectral Atlas of Gaseous Molecules.

S. R. and D. D. S. gratefully acknowledge support from the Simons Foundation, grant no. 290360.

2.6 Appendix A: Constraints on the Era of Abiogenesis

This Appendix presents the literature review underlying our decision to choose 3.9 Ga as the time period relevant to abiogenesis.

Based on evidence such as the discovery of fossilized microorganisms (microfossils) (Javaux et al. 2010) and microbially induced sedimentary structures (MISS) generated by microbial mats (Noffke et al. 2006), life was established by 3.2 Ga. Reports of putative stromatolites[4] (Buick 2007; Hofmann et al. 1999), MISS (Noffke et al. 2013), and potentially biogenic carbon and sulfur fractionation (Buick 2007) are suggestive of life being established by 3.5 Ga. Carbon fractionation arguments have been used to argue for life as early as 3.7 Ga, but this is still debated (Ohtomo et al. 2014; Buick 2007). For purposes of this work, therefore, we constrain the era of abiogenesis to have been earlier than 3.5 Ga.

Upper bounds on the era of abiogenesis suffer from even more paucity of information. Surface liquid water existed as early as 4.3 Ga (Mojzsis et al. 2001; Catling & Kasting 2007). Another constraint on the era of abiogenesis may come from the Late Heavy Bombardment (LHB). From 4.1-3.8 Ga, the Earth experienced a high flux of

[4]Laminated sedimentary structures that trace microbial activity

extraterrestrial impactors (Deamer 2007), peaking sharply 3.9 Ga (Chapman et al. 2007). Maher & Stevenson (1988) argue that bombardment would have sterilized the planetary surface and would have heated the oceans, potentially to uninhabitable levels. Sleep et al. (1989) go further, arguing that LHB impacts could vaporize the oceans. However, Abramov & Mojzsis (2009) incorporate better cratering records and new Solar System dynamical and terrestrial lithospheric models to conclude that the 3.9 Ga peak of the LHB may not have entirely sterilized life. We cannot therefore state with certainty that the LHB sterilized the Earth. Consequently, abiogenesis may have occurred as early as 4.3 Ga

Hence, the range of ages potentially relevant to prebiotic chemistry is 3.5-4.3 Ga. We choose 3.9 Ga as it lies squarely in the middle of this range and postdates the LHB, hence avoiding planetary sterilization concerns.

2.7 Appendix B: The 3.9 Ga Terrestrial Environment

This Appendix summarizes available constraints on the prebiotic atmosphere at 3.9 Ga.

Evidence from zircon samples demonstrate the existence of surface liquid water starting 4.3 Ga ago (Mojzsis et al. 2001; Catling & Kasting 2007). This means that the surface temperature had to be above the freezing point of water. This is a key constraint as the young Sun was as much as 30% fainter compared to the present day. In order to maintain surface liquid water an enhanced greenhouse effect due to higher levels of CO_2 is typically invoked (Kasting 1993, 2014).

The atmosphere in the prebiotic era was likely dominated by volcanic outgassing

from high-temperature magmas. The Earth's interior had differentiated by 4.4 Ga, meaning that the composition of the mantle was set by this date (Catling & Kasting 2007). Delano (2001) study Cr and V abundance in ancient volcanic rocks to show that the redox state of volcanic rocks and hence the mantle has not changed since 3.6 Ga, and likely since 3.9 Ga [5]. Since the redox state controls speciation of H-C-O-S elements, this fact implies that primordial volcanic outgassing of H-C-O-S elements from T>1300K magma was dominated by H_2O, CO_2, and SO_2, with $\leq 1\%$ contributions of H_2 and CO. Trail et al. (2011) extend this constraint by studying incorporation of Ce into ancient zircons. Their analysis suggests that the redox state of the mantle has been unchanged to within measurement error since 4.3 Ga, and conclude that volcanic outgassing was dominated by H_2O, CO_2, SO_2, and N_2, consistent with Delano (2001). Zolotov & Shock (2000) give the relative abundances of H_2O, CO_2, and SO_2 in an quartz-fayalite-magnetite (QFM) buffer, which approximates the terrestrial mantle, as a function of temperature. For T$> 1000°C$, the abundances of H_2O, CO_2, and SO_2 are roughly independent of temperature; for T$= 1200°C$, the mole fractions of H_2O, CO_2, and SO_2 are 0.54, 0.31, and 0.15, respectively. It is generally assumed that gases are given off by magmas in the same proportions as they were dissolved (J. Delano, private communication July 9 2014). Despite its high production rate, SO_2 is not expected to be a major component of the atmosphere due to its tendency to photolyze or be oxidized into rock. However, during periods of high volcanism it is plausible for SO_2 to build up to the level of hundreds of parts per million (ppm) (Kaltenegger & Sasselov 2010). Therefore, particularly on the more active primordial Earth, SO_2 may have at least

[5]The paucity of high-quality samples makes it challenging to draw fully robust conclusions for >3.6 Ga, though what data exists is suggestive.

transiently been an important component of the planetary atmosphere.

Molecular nitrogen (N_2) is another key component of the terrestrial atmosphere, and may have been delivered by impacting planetismals (Kasting 2014). Factors affecting nitrogen abundance in the prebiotic era include production rates from planetismals, which would have been higher on the young Earth. However, atmospheric shock heating of nitrogen in a nonreducing (e.g. N_2/CO_2) atmosphere can also convert N_2 to NO, which can be geochemically fixed and removed from the atmosphere (Summers et al. 2012). Goldblatt et al. (2009) argue that the nitrogen reservoirs in the mantle are subducted, not primordial, and that crustal nitrogen accumulated with the continents; based on these and the utility of high N_2 levels for greenhouse warming to solve the Faint Young Sun paradox, they argue that primordial N_2 levels were as much as 2-3 times the present level of 0.79 bar. However, Marty et al. (2013) use N_2/Ar fluid inclusions in 3.5 Ga quartz crystals to demonstrate that N_2 pressures and isotopic composition at this time were, similar to present-day levels (0.5-1.1 bar).

In summary, existing evidence is suggestive of an N_2/CO_2-dominated atmosphere with sufficient concentration of greenhouse gases (e.g. CO_2, CH_4) to support liquid water on the surface. During epochs of high volcanism, volcanogenic gases (especially SO_2) may also have formed an important constituent of the atmosphere. If the young Earth were warm, water vapor would also be a significant atmospheric constituent.

2.8 Appendix C: Derivation of Photolytic Constraints on Feedstock Gas Buildup

In this section, we derive the equilibrium surface partial pressure of a feedstock gas X, assuming the sole sink to be photolysis. As discussed in Section 2.3.4, we assume an isothermal atmosphere of ideal gases in hydrostatic equilibrium dominated by 0.9 bar N_2 and 0.1 bar CO_2, with total surface pressure 1 bar. We assume the mixing ratio of the feedstock gas under consideration to remain constant until a height z_0, whereupon it goes to zero. Lastly, we assume the feedstock gas population to be optically thin. We take our top-of-atmosphere input ϕ_0 to be the UV spectrum of the young solar analog κ^1 Ceti from Ribas et al. (2010) which extends from 93-300 nm. We obtain our CO_2 cross-sections $\sigma_{CO2}(\lambda)$from Huestis & Berkowitz (2010), who compile CO_2 cross-sections at 300 K from 0.12-201.6 nm.

Let the rate of supply of methane to the atmosphere to be S. Let the rate of removal of X from the atmosphere due to photolysis be B. Then B satisfies

$$d^2B = d\lambda dV n_X(r)\sigma_X(\lambda)\phi(\lambda)\cos(\Phi)$$

where n_X is the number density of X, $\sigma_X(\lambda)$ is the cross-section of X as a function of wavelength, $\phi(\lambda)$ is the emergent flux irradiating the X population, r is the distance from the planet center, and Φ is the zenith angle of the irradiating flux. Then

$$B = \int d\lambda \int dV n_X(r)\sigma_X(\lambda)\phi(\lambda)\cos(\Phi)$$
$$= \left[\int d\lambda \sigma_X(\lambda)\phi(\lambda)\right]\left[\int_0^{2\pi} d\theta \int_0^{\pi/2} d\Phi \sin(\Phi)\cos(\Phi) \int_{R_\oplus}^{R_\oplus + z_0} dr r^2 n_X(r)\right],$$

$z_0/R_\oplus << 1$, so changing variables to $z = R - R_\oplus$, we can write

$$B = \left[\int d\lambda \sigma_X(\lambda)\phi(\lambda)\right]\left[2\pi \times \frac{1}{2}\right]\left[\int_{R_\oplus}^{R_\oplus + z0} dr r^2 n_X(r)\right]$$
$$\approx \pi R_\oplus^2 \left[\int d\lambda \sigma_X(\lambda)\phi(\lambda)\right]\left[\int_0^{z0} dz n_X(z)\right]$$

Under our assumptions of an isothermal atmosphere composed of ideal gases in hydrostatic equilibrium, we can compute:

$$\int_0^{z0} dz n_X(z) = \int_0^{z0} dz \frac{P_X(z=0)}{kT} exp(-z/H)$$
$$= \frac{P_X(z=0)}{kT} \times H(1 - \exp(-z_0/H)),$$

where the scale height $H = (kT)/(\mu g)$, μ is the mean molecular mass of the atmosphere, g is the acceleration due to gravity, and T is the temperature of the atmosphere. For a 0.1 bar CO_2, 0.9 bar N_2 atmosphere, $\mu = 29.6$ amu. We take $T = 290K$, the surface temperature computed in the model of Rugheimer et al. (2015). Then H=8.3 km, comparable to H=8.5 km for the modern Earth.

Let the input flux at the top of the atmosphere be $\phi_0(\lambda)$. Then

$$\phi(\lambda) = \phi_0(\lambda)\exp(-\tau_{CO2}(\lambda))$$
$$= \phi_0(\lambda)\exp(-N_{CO2}\sigma_{CO2}(\lambda)$$

where N_{CO2} is the column density of CO_2 shielding X. We can then compute the quantity

$$b_X = \int_{93\text{nm}}^{165\text{nm}} d\lambda \sigma_X(\lambda)\phi(\lambda)]$$

For $N_{CO_2} = 1.4 \times 10^{21}$ cm^{-2}, $b_{CH_4} = 3.1 \times 10^{-27}\mathbf{s}^{-1}$, for example.

Combining these relations, we may write:

$$\begin{aligned} S =& B \\ S =& \Pi R_{\oplus}^2 b[\frac{P_X(z=0)}{kT} \times H(1-\exp(-z_0/H))] \\ \rightarrow P_X(z=0) =& \frac{kTS}{\pi R_{\oplus}^2 bH(1-\exp(-z_0/H))} \end{aligned}$$

2.9 Appendix D: Collection of $Cu(CN)_3^{2-}$ Absorption Spectrum

The absorption spectrum of tricyanocuprate (I) used in this paper was taken from Magnani (2015), an undergraduate thesis. While the content of this thesis is currently being prepared for publication, this material is not yet peer-reviewed and publicly available. Hence, with permission of the author, we briefly excerpt here a description of the techniques used to collect this spectrum. We emphasize that credit for this work must go to Magnani (2015) and their forthcoming paper.

The absorption spectra in this study were collected using a Starna quartz cuvette (1 cm cube) mounted in a UV-Vis spectrometer (Ultraspec 3100 Pro, Amersham Biosciences). First, an absorption spectrum was taken of a blank consisting of 2.5 mL of

pure deionized water. Then, a $Cu(CN)_3^{2-}$ solution was prepared by combining a stock solution of 0.2 mM CuCN with a 1.1 equivalent of CN^-. A spectrum of this solution was taken using the UV-Vis spectrometer and quartz cuvette. Additional spectra were taken of the complex as 0.1 equivalents of cyanide were added, up until a total of 5 equivalents of the original 0.2 mM CuCN solution. Additionally, a spectrum of a 0.89 mM CN^- solution formed by dissolving KCN in deionized degassed water was collected, allowing the determination of the absorption spectrum of pure CN^-. The same cuvette was used for all absorption experiment for consistency. Finally, the blank was differenced from the other spectra to subtract out background absorption due to water, the cuvette, and oxygen in the air.

The titration of CuCN by CN demonstrated that as CN concentration increased, the solution spectrum increasingly resembled the spectrum of pure CN^-. This indicates that the additional CN was being partitioned preferentially into solution as opposed to into the tricyanocuprate complex. Therefore, we chose to use the spectrum corresponding to the solution formed by combining of 0.2 mM CuCN with just 1.1 equivalent of CN^- to represent the spectrum of the tricyanocuprate (I) complex; we term this the "base solution". The tricyanocuprate species dominates the spectrum because the dicyanocuprate species is not photoactive and the tetracyanocuprate species is not thermodynamically favored at neutral pH (Horváth et al. 1984).

The base solution was prepared by combining a stock solution of 0.2 mM CuCN with a 1.1 equivalent of CN^{-1}, resulting in a solution containing 0.2 mM Cu^+ and 0.42 mM CN^-. Assuming all the CN^- goes into the tricyanocuprate complex, this corresponds to a 0.14 mM solution of tricyanocuprate (I). However, the partitioning between the CN^- in solution versus in the tricyanocuprate complex is not known. Hence, 0.14 mM

represents an upper limit on the tricyanocuprate (I) concentration.

We computed the molar absorptivities via the absorbance formula $A/(d \times C) = e$, where A is the absorbance, e is the molar absorptivity ($M^{-}1cm$), d is the path length in cm, and C is the concentration of the solution in M. $A = \log_{10}(I_0/I)$, where I_0 is the intensity incident on the cuvette and I is the transmitted intensity. A is reported by the UV-Vis spectrometer, the cuvette dimensions set $d = 1$ cm and we took $C = 0.14$ mM. As 0.14 mM is an upper bound for C, this means that the values we compute for e are lower bounds.

Ritson & Sutherland (2012) report they formed their tricyanocuprate complex by adding 30 mg KCN (65.12g/mol) and 2 mg CuCN (89.56 g/mol) to 2.2 mL of water and titrating with an unspecified amount of 1M HCl to reach neutral pH. The amount of HCl solution added cannot exceed 1.3 mL as the total volume of the cuvette used in their experiment was 3.5 mL. This corresponds to a total of 2.23×10^{-5} mol Cu^{+} and 4×10^{-4} mol CN^{-}. Assuming all the Cu goes into the complex, which seems reasonable given that [Cu]<<3[CN], this corresponds to a tricyanocuprate concentration of $(2.23 \times 10^{-5}\text{mol})/(2.2 - 3.5\text{mL})$=6-12 mM. As even using the lower of these values and our lower bounds for e the absorption spectrum is saturated at the Ritson & Sutherland (2012) concentration of 6 mM (see Figure 2.8), the use of our lower bounds for e has minimal impact on our results.

2.10 Appendix E: Extinction Cross-Sections

This Appendix specifies the sources of the extinction cross-sections for the gases used in Figure 2.5 (Section 2.3.3). We used laboratory measurements of cross-sections where available, and assumed extinction was due to Rayleigh scattering otherwise. Unless otherwise stated, all measurements were collected near room temperature (295-298 K) and 1 bar of atmospheric pressure, and the digitized data files of the empirical measurements are collected from the MPI-Mainz UV/Vis Spectral Atlas.

2.10.1 CO_2

We take empirically measured cross-sections shortward of 201.6 nm from Huestis & Berkowitz (2010). Huestis & Berkowitz (2010) review existing measurements of extinction cross-sections for CO_2, and aggregate the most reliable ones into a single spectrum ($<$ 1 nm resolution). They test their composite spectrum with an electron-sum rule, and find it to agree with the theoretical expectation to 0.33%. From 201.75-300 nm, the measurements of Shemansky (1972) provide coverage. However, the resolution of these data ranges from 0.25 nm from 201.75-203.75 nm, to 12-25 nm from 210-300 nm. Further, Shemansky (1972) finds that essentially all extinction at wavelengths longer than 203.5 nm is due to Rayleigh scattering (Ityaksov et al. 2008 derive similar results) . Therefore, we adopt the measurements of Shemansky (1972) from 201.75-203.75 nm, and take Rayleigh scattering to describe CO_2 extinction at longer wavelengths.

We compute the Rayleigh scattering cross-section of CO_2 using the formalism of Vardavas & Carver (1984): $\sigma = 4.577 \times 10^{-21} \times KCF \times [A(1 + B/\lambda^2)]/\lambda^4$, where λ is in

μ m and KCF is the King correction factor, where $KCF = (6 + 3\delta)/(6 - 7\delta)$, where δ is the depolarization factor. This approach accounts for the wavelength dependence of the index of refraction but assumes a constant depolarization factor. We take the values of the coefficients A and B from Keady & Kilcrease (2000), and the depolarization factor of $\delta = 0.0774$ from Shemansky (1972).

2.10.2 SO_2

From 106.1-403.7 nm, we take the cross-sections for SO_2 extinction from the compendium of SO_2 cross-sections of Manatt & Lane (1993) (0.1 nm resolution). Manatt & Lane (1993) evaluate extant UV cross-sections for SO_2 extinction, and aggregate the most reliable into a single compendium covering this wavelength range at 293 $\pm$ 10 K.

2.10.3 H_2S

We take empirically measured cross-sections of H_2S shortward of 159.465 nm from the dipole (e,e) spectroscopy measurements of Feng et al. (1999) ($<$ 10 nm resolution). From 159.465-259.460 nm, we take the cross-sections for H_2S extinction from the gas cell absorption measurements of Wu & Chen (1998) (0.06 nm resolution), as recommended by Sander et al. (2011). From 259.460-370.007 nm, we take the gas cell absorption measurements of Grosch et al. (2015) (0.018 nm resolution). Many of the cross-sections reported in the Grosch et al. (2015) dataset are negative, corresponding to an increase in flux from traversing an gas-filled cell. These cross-sections are deemed unphysical and removed from the dataset. Further, the Grosch et al. (2015) dataset shows a great deal of high-resolution structure that is not relevant to our analysis. We use an 11-point

mean boxcar filter to smooth the data we take from the Grosch et al. (2015) datatset.

Chapter 3

Constraints on the Early Terrestrial Surface UV Environment Relevant to Prebiotic Chemistry

This thesis chapter is in press as:

S. Ranjan and D. Sasselov. Accepted to *Astrobiology* on 1 December 2016.

Abstract

The UV environment is a key boundary condition to abiogenesis. However, considerable uncertainty exists as to planetary conditions and hence surface UV at abiogenesis. Here, we present two-stream multi-layer clear-sky calculations of the UV surface radiance on Earth at 3.9 Ga to constrain the UV surface fluence as a function of albedo, solar zenith

angle (SZA), and atmospheric composition.

Variation in albedo and latitude (through SZA) can affect maximum photoreaction rates by a factor of > 10.4; for the same atmosphere, photoreactions can proceed an order of magnitude faster at the equator of a snowball Earth than at the poles of a warmer world. Hence, surface conditions are important considerations when computing prebiotic UV fluences.

For climatically reasonable levels of CO_2, fluence shortward of 189 nm is screened out, meaning that prebiotic chemistry is robustly shielded from variations in UV fluence due to solar flares or variability. Strong shielding from CO_2 also means that the UV surface fluence is insensitive to plausible levels of CH_4, O_2, and O_3. At scattering wavelengths, UV fluence drops off comparatively slowly with increasing CO_2 levels. However, if SO_2 and/or H_2S can build up to the $\geq 1 - 100$ ppm level as hypothesized by some workers, then they can dramatically suppress surface fluence and hence prebiotic photoprocesses.

H_2O is a robust UV shield for $\lambda < 198$ nm. This means that regardless of the levels of other atmospheric gases, fluence $\lesssim 198$ nm is only available for cold, dry atmospheres, meaning sources with emission $\lesssim 198$ (e.g. ArF eximer lasers) can only be used in simulations of cold environments with low abundance of volcanogenic gases. On the other hand, fluence at 254 nm is unshielded by H_2O and is available across a broad range of N_{CO_2}, meaning that mercury lamps are suitable for initial studies regardless of the uncertainty in primordial H_2O and CO_2 levels

3.1 Introduction

Ultraviolet (UV) light plays a key role in prebiotic chemistry (chemistry relevant to the origin of life). UV photons are energetic enough to affect the electronic structure of molecules by dissociating bonds and ionizing and exciting molecules. These properties mean that UV light can destroy molecules important to abiogenesis (Sagan 1973), but also that UV light can power photochemistry relevant to the synthesis of prebiotically important molecules. UV light has been invoked in prebiotic chemistry as diverse as the origin of chirality (Rosenberg et al. 2008), the synthesis of amino acid precursors (Sarker et al. 2013), and the polymerization of RNA (Mulkidjanian et al. 2003). Most recently, UV light has been shown to play a key role in the first plausible prebiotic synthesis of the activated pyrimidine ribonucleotides (Powner et al. 2009), the synthesis of glycolaldehyde and glyceraldehyde (Ritson & Sutherland 2012), and a reaction network generating precursors for a range of prebiotically important molecules including lipids, amino acids, and ribonucleotides (Patel et al. 2015).

Simulating UV-sensitive prebiotic chemistry in laboratory contexts requires understanding what the prebiotic UV environment was like, both in overall fluence level and in wavelength dependence. Prebiotic chemistry on Earth is generally assumed to have occurred in aqueous solution at the surface of the planet or at hydrothermal vents deep in the ocean. UV-dependent prebiotic chemistry could not have occurred too deep in the ocean due to attenuation from water, and so must have occurred near the surface. Therefore, in order to understand the fidelity of laboratory simulations of UV-sensitive prebiotic chemistry, it is important to understand what the prebiotic UV environment at the planetary surface was like.

In the present study, we use a two-stream multi-layer radiative transfer model to constrain the prebiotic UV environment at the surface. We calculate the surface radiance as a function of solar zenith angle (SZA), surface albedo (A), and atmospheric composition. We convolve the calculated surface radiance spectra against action spectra corresponding to two different simple photochemical reactions (one a stressor, the other a eustressor) that may have been important during the era of abiogenesis, and integrate the result to compute the biologically effective dose rate (BED) and estimate the impact of these parameters on prebiotic chemistry. Previous work (e.g., Cockell 2002, Cnossen et al. 2007, Rugheimer et al. 2015) has ignored the effect of SZA and albedo; we demonstrate that taken together, these factors can lead to variations in BED of more than an order of magnitude. Earlier analyses have focused on "case studies" for the atmospheric composition; we step through the plausible[1] range of abundances of CO_2, H_2O, CH_4, SO_2, H_2S, O_2, and O_3 to constrain the impact of varying levels of these gases on the surface UV environment.

In Section 3.2, we discuss previous work on this topic, and available constraints on the prebiotic atmosphere. In Section 3.3, we describe our radiative transfer model and its inputs and assumptions. In Section 3.4, we describe the tests we performed to validate our model. Section 3.5 then presents and discusses the results obtained through use of our model and the implications for the prebiotic UV environment, and Section 3.6 summarizes our findings.

[1]As well as some deemed implausible, to explore parameter space

3.2 Background

3.2.1 Previous Work

Recognizing the relevance of UV fluence to life (though mostly in the context of a stressor), previous workers have placed constraints on the surface UV environment of the primitive Earth. In this section, we present a review of some recent work on this topic, and discuss how our work differs from them.

Cockell (2002) calculate the UV flux received at the surface of the Earth at 3.5 Ga using a monolayer delta-Eddington approach to radiative transfer, assuming a solar zenith angle SZA= 0° (i.e. the sun directly overhead)[2], for an atmosphere composed of 0.7 bar N_2 and 40 mb and 1 bar of CO_2, as well as an atmosphere with a sulfur haze. Cockell (2002) found the surface UV flux to be spectrally characterized by a cutoff at $>$ 190 nm imposed by CO_2. They further found the surface UV flux for non-hazy primordial atmospheres to be far higher than for the modern day due to a lack of UV-shielding oxygen and ozone, with hazes potentially able to provide far higher attenuation.

Cnossen et al. (2007) calculate the UV flux received at the surface of the earth at 4-3.5 Ga at SZA= 0°. To calculate atmospheric radiative transfer, they partition the atmosphere into layers. They compute absorption using the Beer-Lambert Law. To account for scattering, they calculate the flux scattered in each layer and assume half of it proceeds up, and half proceeds down. They iterate this process to the surface. They explore the effect of atmospheric composition on surface flux, assuming an N_2-CO_2

[2]Cockell (2002) does not specific the albedo assumed

dominated atmosphere with levels of CO_2 varying from 0.02-1 bar, levels of CH_4 spanning 1 order of magnitude, and levels of O_3 spanning 5 orders of magnitude. Cnossen et al. (2007) found that atmospheric attenuation prevented flux at wavelengths shorter than 200 nm from reaching the surface in all the case studies they considered. In all cases, they found the surface flux to be far higher than on modern Earth, again due to lack of UV-shielding oxic molecules. They further found that the surface flux was insensitive to variation in CH_4 and O_3 concentration at the levels they considered, and that the wavelength cutoff from CO_2 rendered the surface flux insensitive to H_2O level. Cnossen et al. (2007) also use observations of a flare on an analog to the young Sun, κ Ceti, to estimate the impact of solar variability on the surface UV environment; they find the effect to be minor due to strong atmospheric attenuation.

Rugheimer et al. (2015) use a coupled climate-photochemistry model to compute radiative transfer through, among others, an atmosphere corresponding to the Earth at 3.9 Ga. Their model assumes and atmospheric pressure of 1 bar. It assumes atmospheric mixing ratios of 0.9, 0.1, and 1.65×10^{-6} for N_2, CO_2, and CH_4, respectively, coupled with modern abiotic outgassing rates of gases such as SO_2 and H_2S, and iterates to photochemical convergence. They report the resulting actinic fluxes (spherically integrated radiances) at the bottom of the atmosphere. Rugheimer et al. (2015) reiterated the findings of previous workers that overall far more UV flux reached the surface of the primitive Earth compared to the modern day, with a cut-off at 200 nm due to shielding from CO_2 and H_2O.

Our work builds on these previous efforts. Like Rugheimer et al. (2015), we employ a two-stream multilayer approximation to radiative transfer, which consequently accounts for multiple scattering. Proper treatment of scattering is crucial in studies of the anoxic

primitive Earth because of the uncovering of an optically thick yet scattering-dominated regime due to the absence of oxic shielding. For example, for a 0.9 bar N_2/0.1 bar CO_2 atmosphere of the kind considered by Rugheimer et al. (2015), the N_2 column density is 1.88×10^{25} cm^2 and the CO_2 column density is 2.09×10^{24} cm^2. At 210 nm, the Rayleigh scattering cross-section due to N_2 is 2.9×10^{-25} cm^{-2} and the Rayleigh scattering cross-section due to CO_2 is 6.8×10^{-25} cm^{-2}, corresponding to a scattering optical depth of $\tau = 6.8 > 1$. This optically thick scattering regime is shielded on Earth by strong O_2/O_3 absorption, but is revealed under anoxic prebiotic conditions. In this regime, scattering interactions and reflection from the surface become common, and self-consistent calculation of the upward and downward scattered fluence becomes important. We argue that consequently the radiative transfer formalism of Cnossen et al. (2007) is inappropriate, because it implicitly neglects multiple-scattering; it also ignores coupling between the upward and downward streams, and implicitly assumes an albedo of zero. Such an approximation may be reasonable on the modern Earth, where the scattering regime is confined to the optically thin region of the atmosphere by O_2 and O_3, meaning there are few scattering events and limited backscatter of reflected radiation. However, it is inappropriate for the anoxic prebiotic Earth where much of the prebiotically critical 200-300 nm regime is both scattering and optically thick, especially when treating cases with high albedo (e.g. snowfields).

Like Cnossen et al. (2007) and Cockell (2002), we explore multiple atmospheric compositions. However, we treat variations in the abundance of each gas independently, in order to isolate each gas's effect individually, and explore a broader range of gases and abundances. We also explore the effects of albedo and zenith angle, which these earlier works did not.

Finally, Cnossen et al. (2007) and Cockell (2002) reported the surface flux. However, as pointed out by Madronich (1987), the flux "describes the flow of radiant energy though the atmosphere, while the [intensity] concerns the probability of an encounter between a photon and a molecule". The distinction is often academic from a laboratory perspective, since in such studies the zenith angle of the source is often 0, meaning that the flux and spherically-integrated radiance[3] are identical. However, the flux can deviate significantly from the radiance in a planetary context (see, e.g., Madronich 1987). Rugheimer et al. (2015) report the actinic flux (i.e. the integral over the unit sphere of the radiance field; see Madronich 1987) at the bottom-of-atmosphere (BOA). This quantity, however, includes the upward diffuse reflection from the planet, which a molecule lying on the surface would not be not exposed to. We instead report what we term the *surface radiance*, which is the integral of the radiance field at the planet surface, integrated over the hemisphere defined by positive elevation (i.e. that part of the sky not blocked by the planet surface). Figure 3.1 demonstrates the difference between the surface flux, the BOA actinic flux, and the surface radiance for the model atmosphere of Rugheimer et al. (2015), with a surface albedo corresponding to fresh snow and SZA=60°.

[3]Also known as intensity; see Liou 2002, page 4

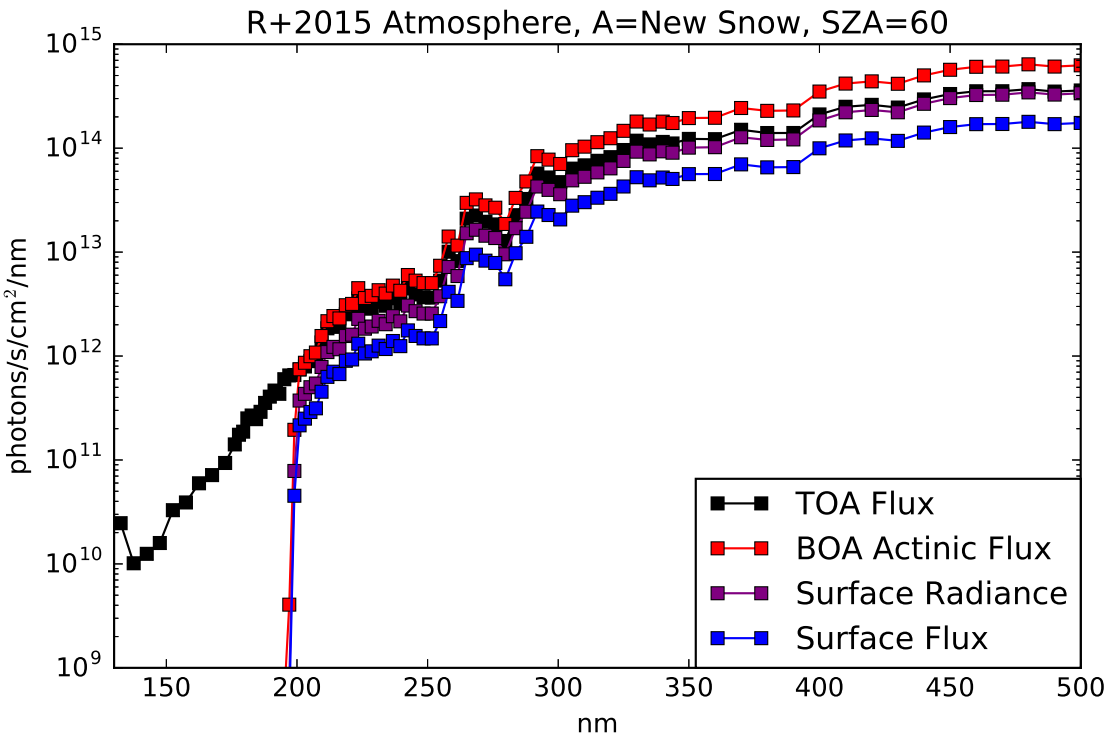

Figure 3.1: TOA (top-of-atmosphere) solar flux, surface flux, BOA actinic flux, reported by Rugheimer et al. (2015)) and surface radiance for a planet with an atmosphere corresponding to that calculated by Rugheimer et al. (2015) for the 3.9 Ga Earth, with an albedo corresponding to fresh snow and a solar zenith angle of 60°. In this example, these quantities can vary by up to a factor of 3.6, despite being for identical physical conditions and having the same units. In this paper, we report the surface radiance.

3.2.2 Constraints on the Composition of the Atmosphere at 3.9 Ga

In this section, we briefly summarize available constraints on the terrestrial atmosphere at $\sim$ 3.9 Ga. A more detailed discussion is available in our earlier paper (Ranjan &

Sasselov 2016, Appendix B).

Measurements of oxygen isotopes in zircons suggest the existence of a terrestrial hydrosphere by 4.4 Ga, usually interpreted as evidence that liquid water was stable at Earth's surface (Mojzsis et al. 2001; Wilde et al. 2001; Catling & Kasting 2007). Since the Sun was 30% less luminous in this era (the "Faint Young Sun Paradox"), an enhanced greenhouse effect, e.g. through higher levels of CO_2, is usually invoked (Kasting 1993; Wordsworth et al. 2013a; Kasting 2014). The initial nebular atmosphere is thought to have been lost soon after planet formation, and the subsequent atmosphere is thought to have been dominated by volcanic outgassing from high-temperature magmas. Measurements of ancient volcanic rocks suggest that the redox state of the Earth's mantle, and hence the gas speciation from magma melts, has not changed since 4.3 Ga (Trail et al. 2011; Delano 2001), suggesting that an outgassed atmosphere would be dominated by CO_2, H_2O, and SO_2, with H_2S also being delivered. Measurements of N_2/Ar fluid inclusions in 3.5 Ga quartz crystals (Marty et al. 2013) have been used to demonstrate that N_2 was also a major atmospheric constituent, established at levels of 0.5-1.1 bar by 3.5 Ga (comparable to the present day). SO_2 and H_2S are not expected to have persisted at high levels in the atmosphere due to their tendency to photolyze and/or oxidize; however, it has been suggested that during epochs of high volcanism volcanogenic reductants could exhaust the surface oxidant supply, permitting transient buildup of gases vulnerable to oxidation, e.g. SO_2, to the 1-100 ppm level (Kaltenegger & Sasselov 2010). O_2 and its by-product O_3 are thought to have been rare due to strong sinks from volcanogenic reductants coupled with a lack of the biogenic oxygen source. This low-oxygen hypothesis is reinforced by measurements of mass-independent fractional of sulfur in rocks from >2.45 Ga (Farquhar et al. 2000), which suggests atmospheric

UV throughput was high and oxygen/ozone content was low in the atmosphere prior to 2.45 Ga (Farquhar et al. 2001; Pavlov & Kasting 2002), and measurements of Fe and U-Th-Pb isotopes from a 3.46 Ga chert, which are consistent with an anoxic ocean (Li et al. 2013).

In summary, available geological constraints are suggestive of an atmosphere at 3.9 Ga with N_2 levels roughly comparable to the modern day, with sufficient concentration of greenhouse gases (e.g. CO_2) to support surface liquid water. O_2 (and hence O_3) levels are thought to have been low. If the young Earth were warm, water vapor would have been an important atmospheric constituent. During epochs of high volcanism, reducing volcanogenic gases (e.g. SO_2) may also have been important constituents of the atmosphere.

3.3 Surface UV Radiation Environment Model

We use the two-stream approximation to compute the radiative transfer of UV radiation through the Earth's atmosphere. We choose this method to follow and facilitate intercomparison with past work on this subject (e.g., Cockell 2002, Rugheimer et al. 2015). We follow the treatment of Toon et al. (1989), and we use Gaussian quadrature to connect the diffuse radiance (intensity) to the diffuse flux since Toon et al. (1989) find Gaussian quadrature to be more accurate than the Eddington and hemispheric mean closures at solar (shortwave) wavelengths. We do not include a pseudo-spherical correction because the largest SZA we consider is 66.5°, and radiative transfer studies for the modern Earth suggest the pseudo-spherical correction is only necessary for SZA$>$ 75° (Kylling et al. 1995).

While we are most interested in radiative transfer from 100-400 nm due to the prebiotically interesting 200-300 nm range (Ranjan & Sasselov 2016), our code can model radiative transfer out to 900 nm. The 400-900 nm regime where the atmosphere is largely transparent is useful because it enables us to compare our models against other codes (e.g., Rugheimer et al. 2015) and observations (e.g. Wuttke & Seckmeyer 2006) which extend to the visible. We include both solar radiation and blackbody thermal emission in our source function and boundary conditions. Planetary thermal emission is negligible at UV wavelengths for habitable worlds: we include it because the computational cost is modest, and because it may be convenient to those wishing to adapt our code to exotic scenarios where the planetary thermal emission is not negligible compared to instellation at UV wavelengths. We note as a corollary that this makes our model insensitive to the temperature profile and surface temperature.

Our code includes absorption and scattering due to gaseous N_2, CO_2, H_2O, CH_4, SO_2, H_2S, O_2, and O_3. We do not include extinction due to atmospheric particulates or clouds, hence our results correspond to clear-sky conditions. Laboratory studies suggest that $[CH_4]/[CO_2] \geq 0.1$ is required to trigger organic haze formation (DeWitt et al. 2009). Such levels of CH_4 are unlikely to be obtained in the absence of biogenic CH_4 production (Guzmán-Marmolejo et al. 2013), hence organic hazes of the type postulated by Wolf & Toon (2010) are not expected for prebiotic Earth. Modern terrestrial observations suggest that clouds typically attenuate UV fluence by a factor of $\leq 5\times$ under even fully overcast conditions (Cede et al. 2002; Calbó et al. 2005). Since our work focuses on the potential of atmospheric and surficial features to drive $\gtrsim 10\times$ changes in surface UV, we might expect our conclusions to be only weakly sensitive to the inclusion of clouds. However, clouds on early Earth may have been thicker or had different radiative

properties from modern Earth. Further work is required to constrain the potential impact of particulates and clouds on the surface UV environment of prebiotic Earth, and the results presented in this paper should be considered upper bounds.

We take the top-of-atmosphere (TOA) flux to be the solar flux at 3.9 Ga at 1 AU, computed at 0.1 nm resolution from the models of Claire et al. (2012). Claire et al. (2012) use measurements of solar analogs at different ages to calibrate a model for the emission of the sun through its history. We choose 3.9 Ga as the era of abiogenesis because it coincides with the end of the Late Heavy Bombardment (LHB) and is consistent with available geological and fossil evidence for early life (see, e.g., Ohtomo et al. 2014; Buick 2007; Noffke et al. 2013; Hofmann et al. 1999; Noffke et al. 2006; Javaux et al. 2010). Since two-stream radiative transfer is monochromatic, we integrate spectral parameters (solar flux, extinction and absorption cross-sections, and albedos) over user-specified wavelength bins, and compute the two-stream approximation for each bin independently. We use linear interpolation in conjunction with numerical quadrature to perform these integrals. Our wavelength bin sizes vary depending on the planned application, but in general range from 1-10 nm.

We set the extinction cross-section of the gases in our model equal to laboratory or observational measurements from the literature when available, and equal to the scattering cross-section when not [4]. We assume all scattering is due to Rayleigh scattering, and compute the Rayleigh scattering cross-section for all our molecules. Where total extinction cross-section measurements lie below the Rayleigh scattering prediction, we set the total extinction cross-sections to the Rayleigh value and the

[4] i.e. we assumed no absorption where we lacked constraints

absorption cross-section to zero. This formalism implicitly trusts the Rayleigh scattering calculation over the reported cross-sections; we adopt this step because at such low cross-sections, the measurements are more difficult and the error higher. For example, several datasets reported negative cross-sections in such regimes, which are unphysical. The extinction cross-section measurements and Rayleigh scattering formalism used in our model are described in Section 3.7.

Two-stream radiative transfer models require the partitioning of the atmosphere into N homogenous layers, and requires the user to specify the optical depths (τ_i), single-scattering albedo (ω_{0_i}), and asymmetry parameter g_i across each layer ($0 \leq i \leq N-1$), as well as the solar zenith angle (SZA) θ_0 and the albedo of the planet surface A. Inclusion of blackbody emission further requires the planetary surface temperature T_{surf} and the temperature at the layer boundaries, T_j ($0 \leq i \leq N$). Since we consider only Rayleigh scattering, $g_i = 0$ for all i. We compute ω_{0_i} by computing the molar-concentration-weighted scattering and total extinction cross-sections for the atmosphere in each homogenous layer, σ_{scat_i} and σ_{tot_i}, and taking their ratio: $\omega_{0_i} = \sigma_{scat_i}/\sigma_{tot_i}$. For reasons of numerical stability, we set the maximum value[5] of ω_{0_i} to be $1 - 1 \times 10^{-12}$. Finally, we compute the the optical depth $\tau_i = d_i \times \sigma_{tot_i} \times n_i$, where d_i is the thickness of each layer and n_i is the number density of gas molecules in each layer. d_i and N are chosen by the user. Unless otherwise stated, we followed the example of Segura et al. (2007) and Rugheimer et al. (2015) (their 3.9 Ga Earth case) and partitioned the atmosphere into 64 1-km thick layers. T_j, n_i, and the molar

[5]We previously followed Rugheimer et al. (2015) and imposed a maximum on ω_{0_i} of $1 - 1 \times 10^{-3}$, but we found that for thick, highly scattering atmospheres (e.g. multibar CO_2 atmospheres), this comparatively low upper limit on ω_{0_i} led to spurious absorption at purely scattering wavelengths

concentration of the gases are also specified by the user; they may be self-consistently specified through a climate model. θ_0 and A are free parameters. We explored both fixed values of A (see, e.g., Rugheimer et al. (2015)) as well as values of A corresponding to different physical surface media; see Section 3.8 for details.

We make the following modifications to the Toon et al. (1989) formalism. First, while Toon et al. (1989) adopt a single albedo for the planetary surface for both diffuse and direct streams, we allow for separate values for the diffuse and direct albedos (Coakley 2003). We use the direct albedo when computing the reflection of the direct solar beam at the surface, and the diffuse albedo for the reflection of the downwelling diffuse flux from the atmosphere off the surface. Section 3.8 discusses the albedos used in more detail.

The Toon et al. (1989) two-stream formalism provides the upward and downward diffuse flux in each layer of the model atmosphere as a function of optical depth of the layer, $F_i^{\uparrow}(\tau)$ and $F_i^{\downarrow}(\tau)$, where τ is the optical depth within the layer. From these quantities, we can compute the net flux at any point in the atmosphere, $F_{net_i}(\tau) = F_i^{\uparrow}(\tau) - F_i^{\downarrow}(\tau) - F_{dir}(\tau_{c_i} + \tau)$, where $F_{dir}(\tau) = \mu_0 \pi F_s \exp(-\tau/\mu_0)$ [6], $\mu_0 = \cos(\theta_0)$ and θ_0 is the solar zenith angle, πF_s is the solar flux at Earth's orbit, and τ_{c_i} is the cumulative optical depth from the TOA to the top of layer i. We can similarly compute the mean intensity J via $4\pi J = (1/\mu_1)(F^{\uparrow} + F^{\downarrow}) + F_{dir}/\mu_0$. We can also calculate the surface radiance $I_{surf} = F_N^{\downarrow}/\mu_1 + F_{dir}(\tau_{c_N})/\mu_0$, where $F_N^{\downarrow}$ and τ_{c_N} are the downward diffuse flux and the cumulative optical depth at the bottom edge of the $(N-1)$th layer, respectively. In Gaussian quadrature for the $n = 1$ (two-stream) case,

[6] via Beer-Lambert law

$\mu_1 = 1/\sqrt{3}$ (Toon et al. 1989; Liou 2002, 1974).

For each run of our model, we verify that the total upwelling flux at TOA $F^{\uparrow}(0)$ was less than or equal to the total incoming flux $F_{dir}(0)$ integrated over all UV/visible wavelengths, which is required for energy conservation since the Earth is a negligible emitter at these wavelengths. The code and auxiliary files associated with this model are available at: `https://github.com/sukritranjan/ranjansasselov2016b`.

3.4 Model Validation

In this section, we describe our efforts to test and validate our radiative transfer model. We describe tests of physical consistency in the pure absorption and scattering limiting cases, comparisons of our model to published radiative transfer calculations, and the efficacy of our model at recovering published measurements of surficial UV radiance and irradiance.

3.4.1 Tests of Model Physical Consistency: The Absorption and Scattering Limits

We describe here tests of the physical consistency of our model in the limits of pure absorption and pure scattering. We use the atmospheric model (composition and T/P profile) of Rugheimer et al. (2015) described in Section 3.4.2, and evaluate radiative transfer through this atmosphere in these two limiting cases. This atmospheric model includes an optically thick regime ($\tau > 1$)from 130-332.5 nm and an optically thin regime ($\tau < 1$) from 332.5-855 nm. For each of these limiting cases, we evaluate radiative

transfer corresponding to a range of albedos and solar zenith angles. We evaluate uniform albedos of 0, 0.20, and 1, corresponding to the extrema of possible albedo values and the albedo assumed by Rugheimer et al. (2015). We evaluate solar zenith angles of 0°, 60° and 85°, corresponding to extremal values of the possible solar zenith angle along with the value corresponding to the Rugheimer et al. (2015) findings. We choose 85° as our limit instead of 90° since the plane-parallel approximation breaks down when the Sun is sufficiently close to the horizon.

Pure Absorption Limit

As noted by Toon et al. (1989), in the limit of a purely absorbing atmosphere, the diffuse flux should vanish and the surface flux should reduce to the direct flux. In exploring the pure absorption limit, we cannot set $\omega_0 = 0$ as under Gaussian quadrature γ_2=0 for $\omega_0 = 0$, leading to a singularity when evaluating Γ under the Toon et al. (1989) formalism. We tried values for ω_0 ranging from 10^{-3} to 10^{-10} for the $A = 0.20$, $\theta_0 = 60°$ case. For all values of ω_0, we found the diffuse surface flux to be highly suppressed relative to the direct TOA flux. For $\omega_0 = 10^{-5}$, the diffuse flux was suppressed relative to the TOA flux by $\gtrsim 6$ orders of magnitude in each wavelength bin. The diffuse flux is also strongly suppressed relative to the direct surface flux, except at short wavelengths ($\lambda < 198$ nm) where extinction is so strong that that the diffuse layer blackbody flux dominates over the direct solar flux.

We evaluate the surface flux for $\omega_0 = 10^{-5}$ for a range of A and θ_0. Figure 3.2 presents the results. In all cases, the diffuse flux is highly suppressed relative to the TOA flux across all optical depths. Toon et al. (1989) report that while the pure absorption

limit is satisfied by two-stream approximations with Gaussian closure for $A = 0$, for $A > 0$ exponential instabilities may lead to anomalous behavior. We do not observe this phenomenon in our model. We conclude that our implementation of the two-stream algorithm passes the absorption limit test.

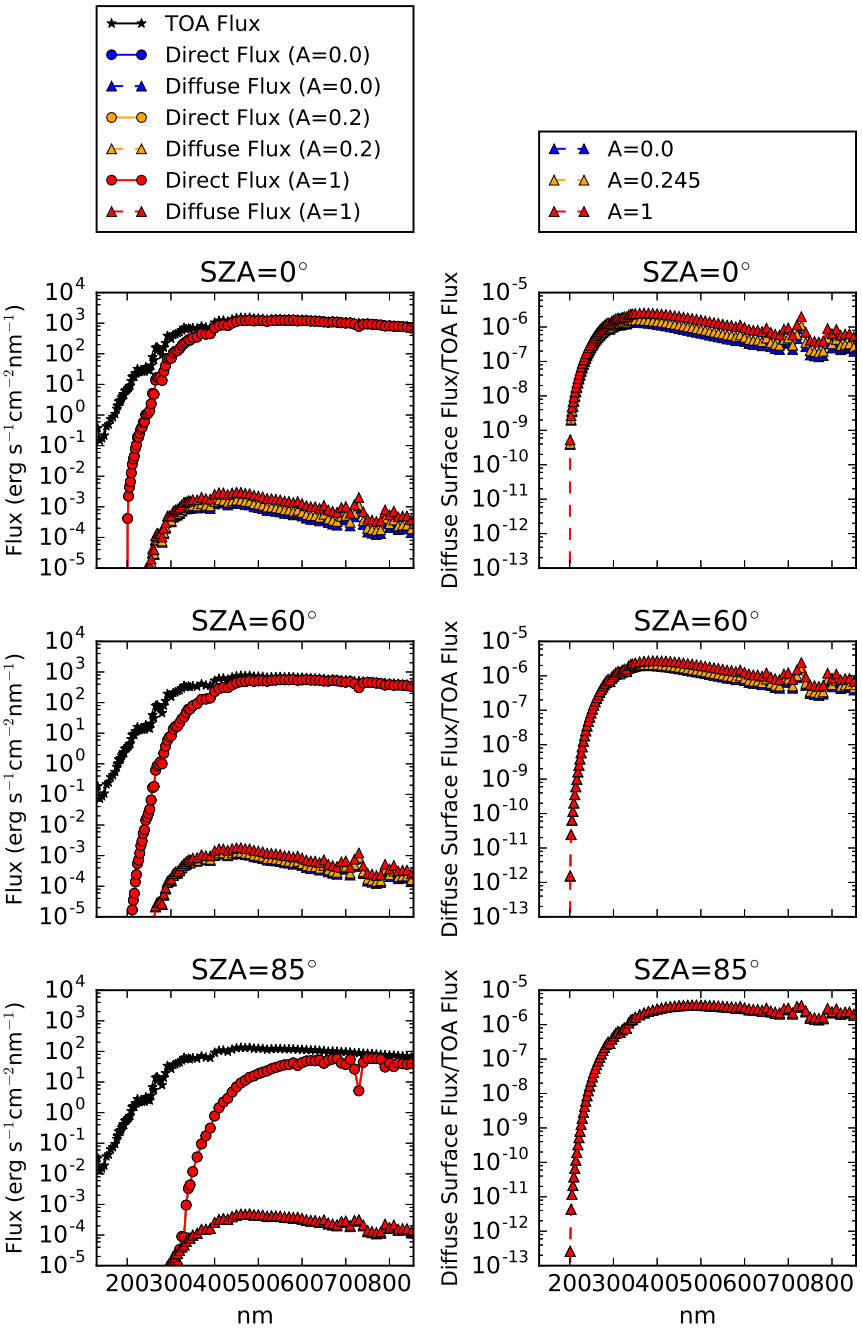

Figure 3.2: Direct, diffuse, and TOA fluxes (left-hand column) and diffuse flux at the surface normalized by TOA flux (right-hand column) for different solar zenith angles and surface albedos, for an atmosphere corresponding to the Rugheimer et al. (2015) 3.9 Ga Earth model with $\omega_0 = 10^{-5}$. The diffuse flux vanishes in this limit, as expected.

Pure Scattering Limit

In the limit of a purely scattering atmosphere ($\omega_0 = 1$), F_{net} should be a constant throughout the atmosphere at all wavelengths since radiation is neither absorbed nor emitted by the atmospheric layers (Liou 1973; Toon et al. 1989). In exploring this limit, we cannot set $\omega_0 = 1$: separate solutions are required for the fully conservative case (see e.g. Liou 1973). However, in practice we can set ω_0 arbitrarily close to 1 (Toon et al. 1989) and ensure that the net flux is constant throughout the atmosphere, or at least that its variations are small compared to the incident flux. We computed F_{net} at layer boundaries in the atmosphere for the $A = 0.20$, $\theta_0 = 60^\circ$ case, for values for ω_0 ranging from $1 - 10^{-3}$ to $1 - 10^{-12}$. For each wavelength bin, we computed the maximum deviation from the median net flux in the atmospheric column, and normalized this deviation to the incident flux. For $\omega_0 = 1 - 10^{-3}$, the variation of F_{net} from the median value ranged from 6×10^{-2} at short wavelengths to 7×10^{-5} at long wavelengths. The increase in deviation towards shorter wavelengths is expected because of the higher opacity at shorter wavelengths. Increasing ω_0 decreased the variation in F_{net}. For $\omega_0 = 1 - 10^{-7}$, the fractional deviation of F_{net} from the columnar median varied from 6×10^{-4} to 7×10^{-9}, and for $\omega_0 = 1 - 10^{-12}$, the deviation of F_{net} varied from 2×10^{-6} to 7×10^{-14}.

We compute the maximum deviation of F_{net} at the layer boundaries from the columnar median as a function of wavelength for $\omega_0 = 1 - 10^{-12}$ for a range of A and θ_0. Figure 3.3 presents the results. At optically thin wavelengths, larger albedos and zenith angles lead to higher deviations; we attribute this to higher levels of flux scattered into the more computationally difficult diffuse stream. At optically thick wavelengths, the

magnitude of the deviations is insensitive to the planetary albedo. We attribute this to the extinction of incoming flux higher in the atmosphere, meaning that surface properties have less impact on the flux profile. In the optically thick regime, smaller zenith angles lead to higher deviations. For all values of θ_0 and A considered here, the columnar deviation from uniformity is $< 3 \times 10^{-6}$ of incoming fluence across all wavelengths for $\omega_0 = 1 - 10^{-12}$, and the deviation decreases as ω_0 approaches 1 as expected.

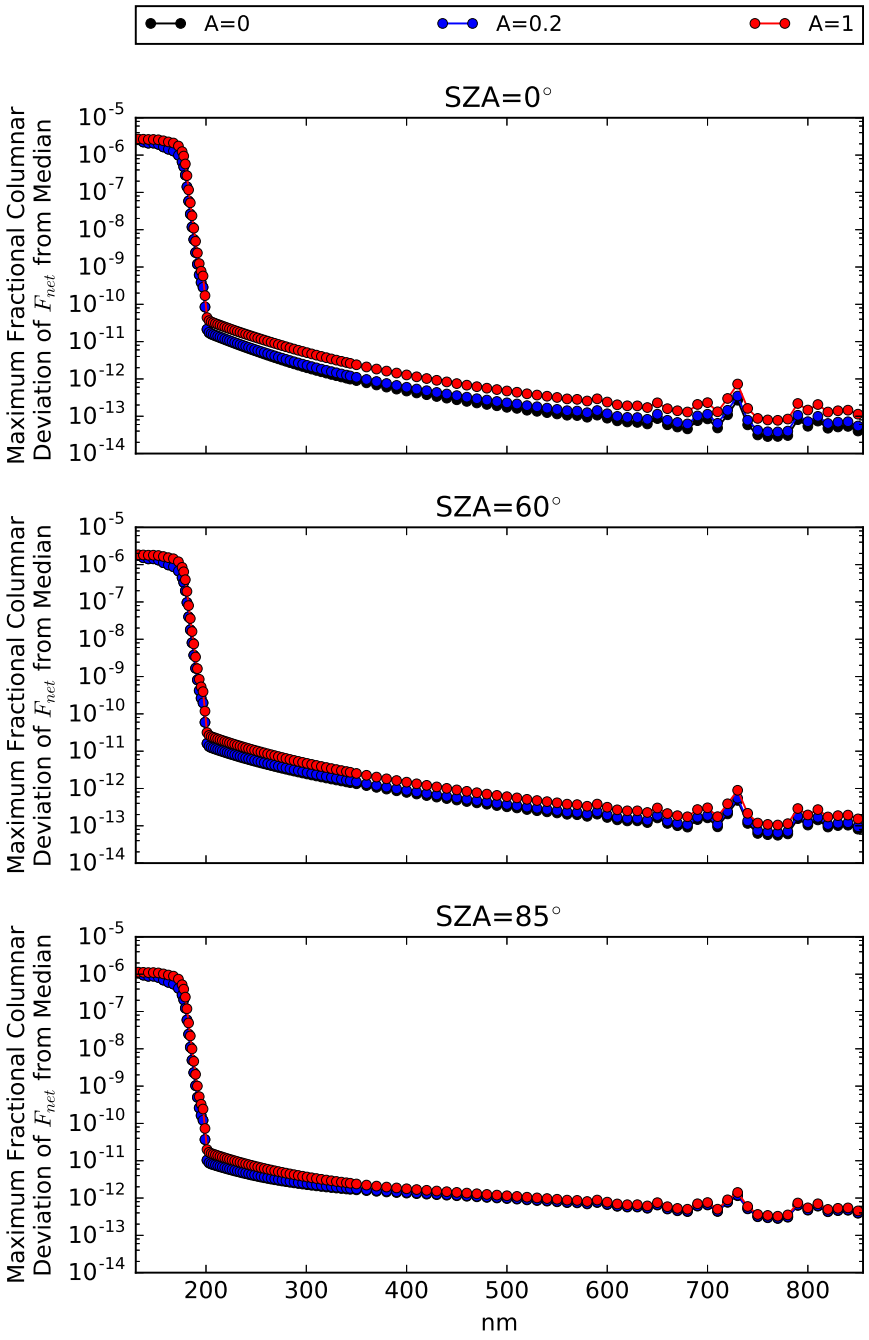

Figure 3.3: The maximum deviation of F_{net} from its median value in a given atmospheric column as a function of wavelength for an atmosphere corresponding to the Rugheimer et al. (2015) 3.9 Ga Earth model, with $\omega_0 = 1 - 10^{-12}$ and a variety of surface albedos and solar zenith angles. In the scattering limit, F_{net} approaches a constant value, with the variation in F_{net} decreasing as ω_0 approaches 1.

3.4.2 Reproduction of Results of Rugheimer et al. (2015)

In this section, we describe our efforts to recover the results of Rugheimer et al. (2015) with our code. Rugheimer et al. (2015) present a model for the total BOA actinic flux on the 3.9 Ga Earth orbiting the 3.9 Ga Sun[7] from 130-855 nm. They couple a 1D climate model (Kasting & Ackerman 1986; Pavlov et al. 2000; Haqq-Misra et al. 2008) and a 1D photochemistry model (Pavlov & Kasting 2002; Segura et al. 2005, 2007) and iterate to convergence. They assume an overall atmospheric pressure of 1 bar and atmospheric mixing ratios of 0.9, 0.1, and 1.65×10^{-6} for N_2, CO_2, and CH_4, respectively. For all other gases, their model assumes outgassing rates corresponding to modern terrestrial nonbiogenic fluxes.

When computing layer-by-layer radiative transfer, Rugheimer et al. (2015) include absorption due to O_3, O_2, CO_2, and H_2O, and Mie scattering due to sulfate aerosols. Rayleigh scattering is computed via an N_2-O_2 scattering law (Kasting 1982) that is scaled to include the effect of enhanced CO_2 scattering. Rugheimer et al. (2015) partition their atmosphere into 64 1-km layers and assume a solar zenith angle of 60°. As with our model, they compute the solar UV radiative transfer using a Toon et al. (1989) two-stream approximation with Gaussian quadrature closure. The surface albedo $A = 0.20$ is tuned to yield a surface temperature of 288K in the modern Earth/Sun system, to approximate the effect of clouds (Rugheimer et al. 2015).

We obtain the metadata[8] for an updated version of the 3.9 Ga Earth model of

[7]Figure 2, "Sun" curve

[8]That is, wavelength bins, mixing ratios as a function of altitude, atmospheric profile, and emergent spectra normalized to the TOA flux, i.e. $4\pi J_{N-1}/F_{\odot}$, where J_{N-1} is the

Rugheimer et al. (2015), courtesy of the authors. We use this metadata to run our radiative transfer model on the Rugheimer et al. (2015) atmospheric model. Figure 3.4 summarizes the results. The top row compares the incident flux at TOA (black) with the Rugheimer et al. (2015) results (red) and our model computations (blue, orange). The Rugheimer et al. (2015) results are not visible due to the close correspondence between our models. The bottom row gives the difference between our model and the Rugheimer et al. (2015) results, normalized to the TOA flux.

---

mean intensity in the middle of the lowest layer of their atmospheric model and $F_{\odot}$ is the flux of solar radiation incident on the TOA

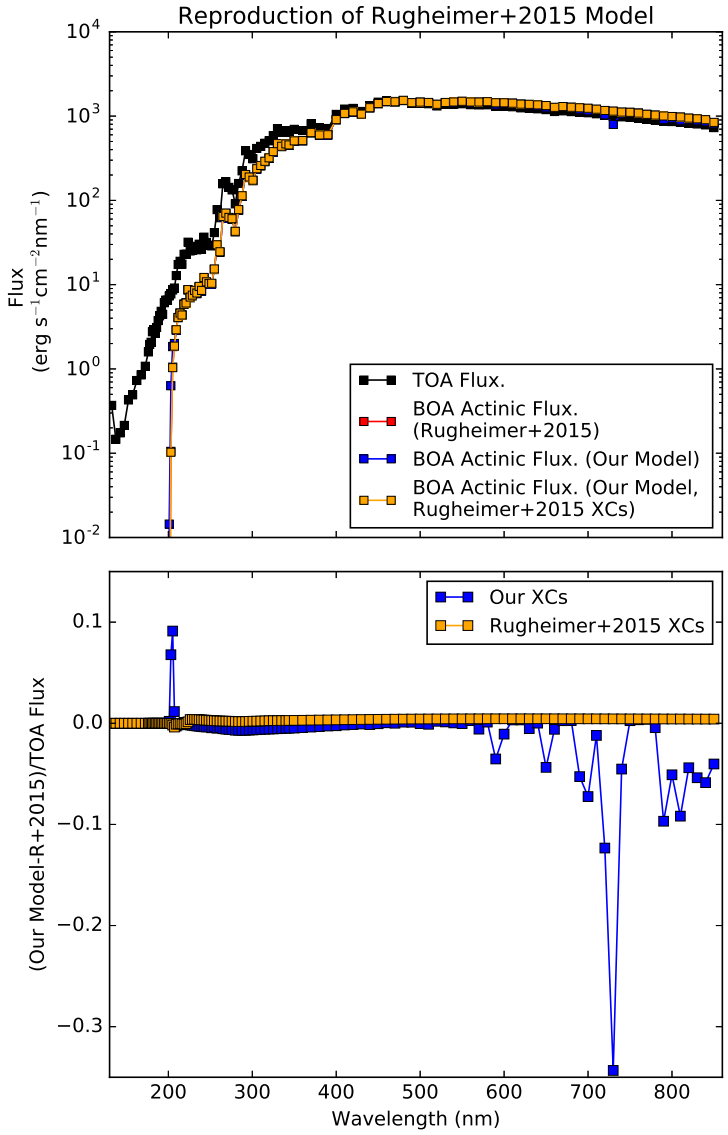

Figure 3.4: Comparison of the BOA actinic fluxes obtained with our radiative transfer model for the updated 3.9 Ga Earth atmosphere of Rugheimer et al. (2015), versus that computed by the authors themselves. The top shows the computed actinic fluxes and TOA flux, while the bottom shows the fractional difference between our models, normalized by the TOA flux. The difference between our and Rugheimer et al. (2015)'s results is driven by the use of different cross-section compilations; if we use the same cross-sections as Rugheimer et al. (2015) (orange curves), we agree with Rugheimer et al. (2015) to better than 0.45% of the TOA flux.

Our model reproduces the Rugheimer et al. (2015) results to within 34% of the of the TOA flux. Much of the difference between our model and Rugheimer et al. (2015)'s can be accounted for by differences in the absorption cross-sections we use. Our cross-section lists are more complete than Rugheimer et al. (2015); for example, our H_2O cross-section tabulation includes absorption at wavelengths longer than 208.3 nm, whereas Rugheimer et al. (2015) do not. Further, we include absorption due to SO_2 and CH_4, compute explicitly Rayleigh scattering on a gas-by-gas basis and include blackbody emission from atmospheric layers and the planetary surface, whereas Rugheimer et al. (2015) do not (though this last is not a significant factor given the paucity of planetary radiation at UV wavelengths).

If we run our model using the Rugheimer et al. (2015) cross-sections and scattering formalism and include only absorption due to O_2, O_3, CO_2, and H_2O, we arrive at the orange curve. This curve matches the Rugheimer et al. (2015) results to within 0.45% of the TOA flux. Our model, both with and without the Rugheimer et al. (2015) absorption, scattering, and emission formalism, can reproduce the scientific conclusions of Rugheimer et al. (2015) such as the 204 nm irradiance cutoff due to atmospheric CO_2. We conclude that our model is capable of reproducing the results of Rugheimer et al. (2015).

3.4.3 Comparison To Modern Earth Surficial Measurements

We describe here comparisons of our radiative transfer model calculations to surface measurements of UV reported in the literature.

Reproduction of Antarctic Diffuse Spectral Radiance Measurements

Wuttke & Seckmeyer (2006) report measurements of the diffuse spectral radiance (observed in the zenith direction) in Antartica. We compare our model to their measurements of the diffuse radiance collected under low-cloud conditions (since our model does not include scattering processes due to clouds). The measurement site was flat and uniformly covered by snow, and the solar zenith angle during the measurements was 51.2°. When running our model, we assume the same solar zenith angle, and take the albedo of the site to match fresh-fallen snow. We run our model at a spectral resolution matching the Wuttke & Seckmeyer (2006) measurements, i.e. from 280-500 nm at 0.25 nm resolution and from 501-1050 nm at 1 nm resolution. We run our model from 0-60 km of altitude, at 600 meter resolution (i.e. 100 layers evenly spaced in altitude), and assume a surface pressure of 1 bar. We assume composition and T/P profiles matching that of Rugheimer et al. (2013) for the modern Earth. In order to reproduce the Wuttke & Seckmeyer (2006) measurements, we are obliged to reduce the water abundance by a factor of 10 relative to the Rugheimer et al. (2013) models. This makes sense, since Antartica is a dry desert environment. Similarly, the Rugheimer et al. (2013) model has an ozone total column depth of 5.3×10^{18} cm^{-2} or 200 Dobson units (DU). For comparison, the Earth's typical ozone total column density is around 300 DU (Patel et al. 2002) and a column depth of 220 DU is considered to be the start point for an ozone hole[9]. It is therefore unsurprising that matching the observed diffuse radiance in Antarctica requires scaling up the ozone abundance of Rugheimer et al. (2013), by a factor of 1.25. While our simple model, which excludes trace absorbers, clouds and

[9]See, e.g., `http://ozonewatch.gsfc.nasa.gov/`

aerosols and is based on a globally averaged composition profile, cannot be expected to precisely replicate this measurement, we can reasonably expect it to identify major features of the modern surface UV environment.

Figure 3.5 presents the measured diffuse radiance observed by Wuttke & Seckmeyer (2006) and our model calculation smoothed by a 10-point moving average (boxcar) filter. Our code correctly replicated the major features of the modern terrestrial UV environment, such as the existence and location of the shortwave cutoff due to ozone. Figure 3.5 also presents the fractional difference between our model prediction and the measurement. The difference is within a factor of 2.2, and is highest in regions of strong atmospheric attenuation of UV. This accuracy is sufficient to distinguish between spectral regions of low and high ($> 100\times$) atmospheric attenuation, i.e. to identify the UV fluence that is suppressed by atmospheric absorbers (e.g., Section 3.5.3). It is similarly sufficient to identify order-of-magnitude-or-greater changes in dose rates due to varying columns of a given absorber (e.g., Section 3.5.7), particularly because the highest error occurs at the lowest throughput and hence has the least weight in the dose rate calculation. We conclude that our code is sufficiently accurate for the applications considered in this work.

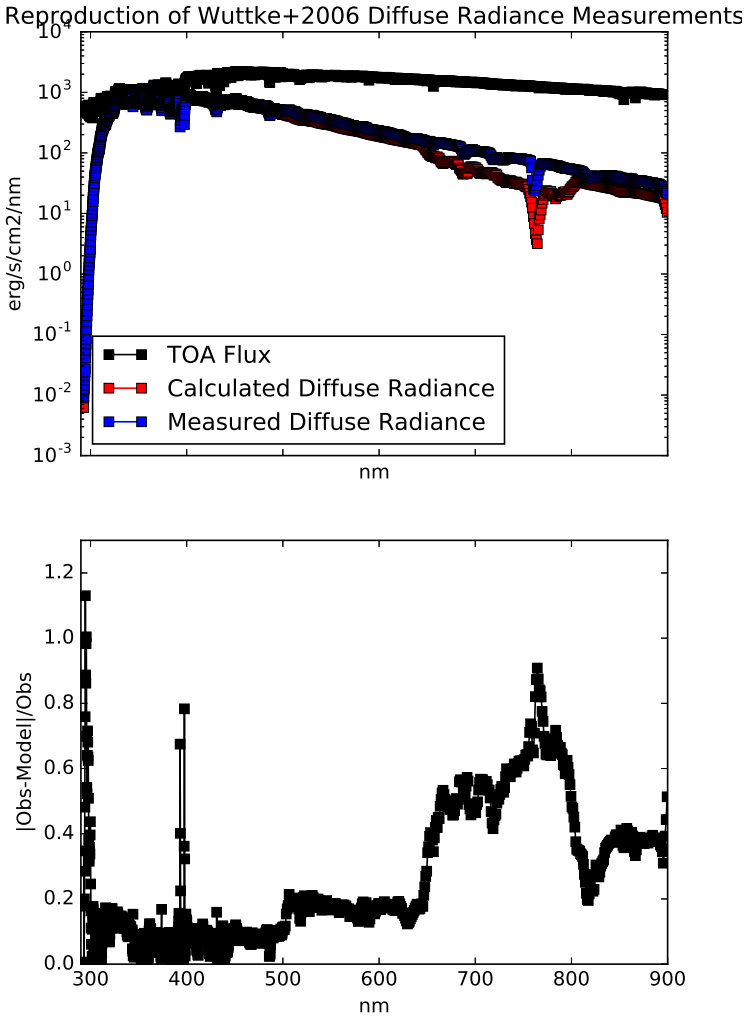

Figure 3.5: Top: Zenith diffuse radiance measurement by Wuttke & Seckmeyer (2006) in Antarctica, compared to the diffuse radiance calculated by our model for an atmosphere corresponding to the Rugheimer et al. (2013) modern Earth model, with the H_2O levels scaled down by a factor of 10 and the ozone column density scaled up by a factor of 1.25. Bottom: fractional difference between the measurements of Wuttke & Seckmeyer (2006) and our model calculation. Our code recovers key features of the terrestrial UV environment, such as the shortwave cutoff due to ozone.

Reproduction of Toronto Surface Flux Measurements

The World Ozone and UV Data Centre (WOUDC; `woudc.org`) compiles measurements of UV surface flux. We compare our radiative transfer model calculations to a measurement of the UV surface flux at Toronto from 292-360 nm on 6/21/2003 at 11:54:06 (solar time). We chose this measurement to compare to as it corresponded approximately to the data shown in Kerr & Fioletov (2008) (i.e. a measurement in Toronto at noon in summer). The solar zenith angle at time of measurement was 20.376°. We take the UV surface albedo to be 0.04, following the typical value suggested by Kerr & Fioletov (2008). We run our model from 292-360 nm at 0.5 nm resolution, matching the resolution of the measurements, from 0-60 km of altitude, at 600 meter vertical resolution. We assume a T/P profile and atmospheric composition profile matching that of Rugheimer et al. (2013) for the modern Earth. As in Section 3.4.3, we note that the Rugheimer et al. (2013) model has a total ozone column density of 200 Dobson units (DU), while the ozone column measured for this observation was 354 DU. We consequently scale our ozone mixing ratios by a factor of 1.77 to match the true column depth. As with Section 3.4.3, while we cannot expect our simple model to precisely replication the surface flux measurement, we can reasonably expect it to identify major features of the modern surface UV environment.

Figure 3.6 presents the measured UV flux compared to our model prediction, and the fractional difference between the two. Our model correctly replicates the shortwave UV cutoff due to ozone, which is characteristic of the modern surface UV environment. The relative difference between our model and the measurement is within a factor of 2.3, with the difference highest where the fluence is strongly suppressed This performance is

similar to that of our reproduction of Wuttke & Seckmeyer (2006), and is sufficient for the purposes of this paper.

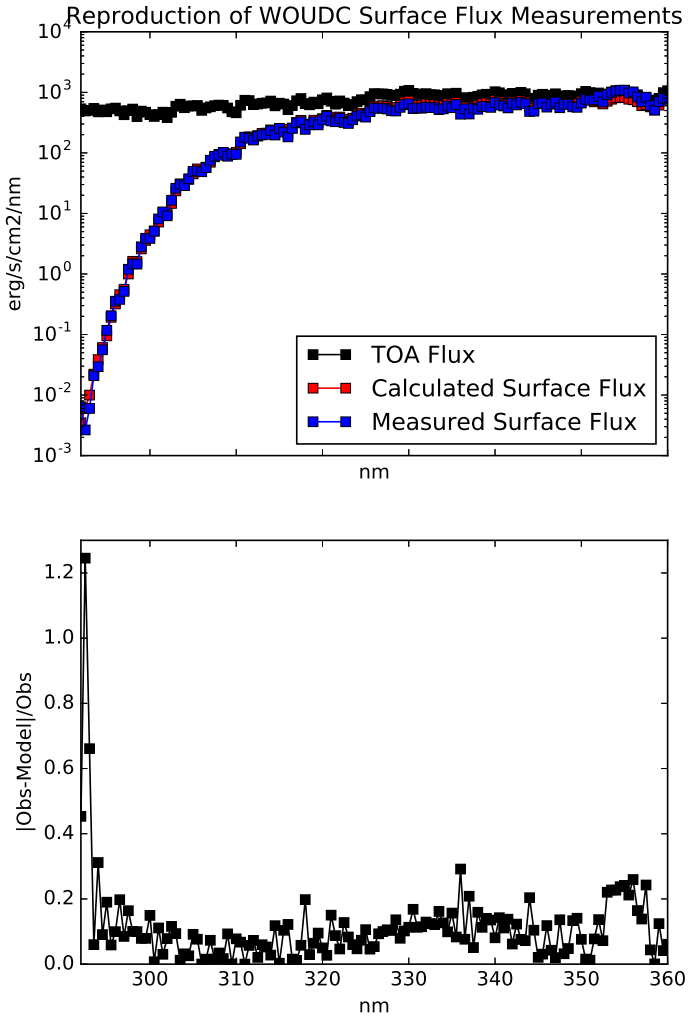

Figure 3.6: Top: Surface flux reported by a WOUDC station near summer noon in Toronto, compared to the surface flux calculated by our model for an atmosphere corresponding to the Rugheimer et al. (2013) modern Earth model with the ozone column density scaled up by a factor of 1.77. Bottom: fractional difference between the measurements and our model. Our code clearly identifies and locates the shortwave cutoff due to ozone.

3.5 Results and Discussion

In this section, we apply our two-stream radiative transfer model to the Rugheimer et al. (2015) 3.9 Ga Earth atmospheric model and variants. We explore the impact of albedo, zenith angle, and atmospheric composition on the surface radiance. We again note that unlike Rugheimer et al. (2015), we do not self-consistently calculate the photochemistry. Rather, we adopt ad-hoc values for these parameters to place bounds on the surface radiance environment. Our objective is to enable prebiotic chemists to correlate hypothesized prebiotic atmospheric composition (e.g. high levels of water vapor on a warm, wet young Earth) to the range of surficial UV environments that such gases would permit in a planetary context.

In calculating our models, we step from 100 to 500 nm of wavelength, at a resolution of 1 nm. This wavelength range includes the prebiotically crucial 200-300 nm range (Ranjan & Sasselov 2016) and the onsets of CO_2, H_2O, and CH_4 absorption. Unless stated otherwise, we assume the atmospheric composition and T/P profile calculated for the 3.9 Ga Earth by Rugheimer et al. (2015). We calculate radiative transfer in 1 km layers starting at the planet surface and ending at a high of 64 km, which corresponds to 7.7 scale heights for this atmosphere.

3.5.1 Action Spectra and UV Dose Rates

To quantify the impact of the surface radiation environments on prebiotic chemistry, we follow the example of Cockell (1999) in computing biologically weighted UV dose rates.

Specifically, we compute the biologically effective relative dose rate

$$D = (\int_{\lambda_0}^{\lambda_1} d\lambda A(\lambda) I_{surf}(\lambda))/(\int_{\lambda_0}^{\lambda_1} d\lambda A(\lambda) I_{space}(\lambda)),$$

where $A(\lambda)$ is an action spectrum, λ_0 and λ_1 are the limits over which $A(\lambda)$ is defined, $I_{surf}(\lambda)$ is the hemispherically-integrated total UV surface radiance, and $I_{space}(\lambda)$ is the the solar flux at the Earth's orbit. An action spectrum parametrizes the relative impact of radiation on a given photoprocess as a function of wavelength, with a higher value of A meaning that a higher fraction of the incident photons are being used in said photoprocess. Hence, D measures the relative rate of a given photoprocess for a single molecule at the surface of a planet, relative to in space at the location of the planet. If we compute the dose rate D_i corresponding to two UV surface radiance spectra $I_{surf,1}$ and $I_{surf,2}$ on a molecule that undergoes a photoprocess characterized by an action spectra A and find $D_1 > D_2$, we can say that the photoprocess encoded by A proceeds at a higher rate under $I_{surf,1}$ than $I_{surf,2}$.

Previous workers used the modern DNA damage action spectrum (Cockell 2002; Cnossen et al. 2007; Rugheimer et al. 2015) as a gauge of the level of stress imposed by UV fluence on the prebiotic environment. However, this action spectrum is based on studies of highly evolved modern organisms. Modern organisms have evolved sophisticated methods to deal with environmental stress, including UV exposure, that would not have been available to the first life. Further, this approach presupposes that UV light is solely a stressor, and ignores its potential role as a eustressor for abiogenesis.

In this work, we use the action spectra corresponding to the production of aquated electrons from photoionization of tricyanocuprate and to the cleavage of the N-glycosidic bond in uridine monophospate (UMP, an RNA monomer) to compute our biologically

effective doses. These processes are simple enough to have plausibly been in operation at the dawn of the first life, particularly in the RNA world hypothesis (Gilbert 1986; Copley et al. 2007; McCollom 2013)[10]. In the following sections, we discuss in more detail our rationale for choosing these pathways, and how we construct the action spectra associated with them.

Eustressor Pathway: Production of Aquated Electrons From Photoionization of $CuCN_3^{2-}$

Ritson & Sutherland (2012) outline a synthesis of glycolaldehyde and glyceraldehyde from HCN and formaldehyde. This pathway depends on UV light for the photoreduction of HCN mediated by the metallocatalyst tricyanocuprate ($CuCN_3^{2-}$, and Ritson & Sutherland (2012) hypothesize this photoreduction is driven by photoionization of the tricyanocuprate, generating aquated electrons (e_{aq}^-). Such aquated electrons are useful in a variety of prebiotic chemistry, participating generally in the reduction of nitriles to amines, aldehydes to hydroxyls, and hydroxyls to alkyls[11]; see Patel et al. (2015) for an example of a potential prebiotic reaction network that leverages aquated electrons in numerous reactions.

We define an action spectrum for the generation of aquated electrons from the irradiation of tricyanocuprate by multiplying the absorption spectrum of tricyanocuprate by the quantum yield (QY, number of e_{aq}^- produced per photon absorbed) of e_{aq}^- from

[10]The RNA world is the hypothesis that RNA was the original autocatalytic information-bearing molecule. Under this hypothesis, the problem of abiogenesis reduces to an abiotic synthesis of autocatalytic RNA polymers

[11]J. Szostak, private communication, 2/5/16

the system. We take our absorption spectrum from the work of Magnani (2015), via Ranjan & Sasselov (2016). The QY of e^-_{aq} production, $\Phi_{e^-_{aq}}$, is not known. Following Ritson & Sutherland (2012)'s hypothesis that e^-_{aq} production is driven by tricyanocuprate photoionization, we assume the QY to be characterized by a step function with $\Phi_{e^-_{aq}}(\lambda \leq \lambda_0) = \Phi_0$ and $\Phi_{e^-_{aq}}(\lambda > \lambda_0) = 0$ otherwise. We choose $\Phi_0 = 0.06$, consistent with the QY for tricyanocuprate measured by Horváth et al. (1984) at 254 nm. Empirically, we know $\lambda_0 > 254$ nm; to explore a range of possible λ_0, we consider $\lambda_0 = 254$ nm and $\lambda_0 = 300$ nm. The action spectrum is defined over the range $190 - 351$ nm, corresponding to the range of the absorption spectrum measured by Magnani (2015). As shorthand, we refer to this photoprocess under the assumption that λ_0 =X nm by CuCN3-X.

Stressor Pathway: Cleavage of N-Glycosidic Bond of UMP

UMP is a monomer of RNA, a key product of the Powner et al. (2009) pathway, and critical molecule for abiogenesis in the RNA-world hypothesis for the origin of life. Shortwave UV irradiation of UMP cleaves the glycosidic bond joining the nucleobase to the sugar (Gurzadyan & Görner 1994), destroying the biological effectiveness of this molecule. The reaction is difficult to reverse; indeed, the key breakthrough of the Powner et al. (2009) pathway was determining how to synthesize and incorporate this bond into the RNA monomers abiotically. Hence, this pathway represents a stressor for abiogenesis in the RNA-world hypothesis.

Glycosidic bond cleavage is not the only process operating in UMP at UV wavelengths. The (wavelength, QY) measured by Gurzadyan & Görner (1994) for glycosidic bond cleavage in UMP in anoxic aqueous solution are (193 nm, 4.3×10^{-3})

and (254 nm, $(2-3)\times10^{-5}$). By comparison, the (wavelength, QY) they measure for chromophore loss (a measure of unaltered UMP abundance, based on absorbance at 260 nm) are (193 nm, 4×10^{-2}) and (254 nm, 1.2×10^{-3}) – 1-2 orders of magnitude higher. The chromophore loss at 254 nm is well studied; for UMP, it is mostly due to photohydration, with a minor contribution from photodimer formation. The photohydration can be reversed with 90-100% efficiency via heating or lowering the pH (Sinsheimer 1954), whereas further UV light (especially shortward of 230 nm) can cleave the photodimers. Since these processes are reversible via dark reactions, the UMP in some sense is not fully "lost", unlike the glycosidic bond cleavage. We therefore argue the bond cleavage is more important than photohydration/photodimerization in measuring UV stress on UMP.

We define action spectra for the cleavage of the glycosidic bond in UMP by multiplying the absorption spectrum of UMP by the quantum yield for the process. We take the absorption spectra from the work of Voet et al. (1963), which gives the absorption spectra of UMP at pH=7.6. The QY of glycosidic bond cleavage as a function of wavelength has not been measured. To gain traction on this problem, we use the work of Gurzadyan & Görner (1994), which found the QY of N-glycosidic bond cleavage in UMP in neutral aqueous solution saturated with Ar (i.e. anoxic) to be 4.3×10^{-3} at 193 nm and $(2-3)\times10^{-5}$ for 254 nm. We therefore represent the QY curve as a step function with value 4.3×10^{-3} for $\lambda\leq\lambda_0$ and 2.5×10^{-5} for $\lambda>\lambda_0$. We consider λ_0 values of 193 and 254 nm, corresponding to the empirical limits from Gurzadyan & Görner (1994), as well as 230 nm, which corresponds to the end of the broad absorption feature centered near 260 nm corresponding to the $\pi-\pi^*$ transition and also to the transition to irreversible decomposition suggested by Sinsheimer & Hastings (1949).

As shorthand, we refer to this photoprocess under the assumption that λ_0 =Y nm by CuCN3-Y.

Figure 3.7 shows the action spectra considered in our study. Action spectra are normalized arbitrarily (see, e.g., Cockell 1999 and Rugheimer et al. 2015), hence they encode information about relative, not absolute, UV dose rate. We arbitrarily normalize these spectra to 1 at 190 nm.

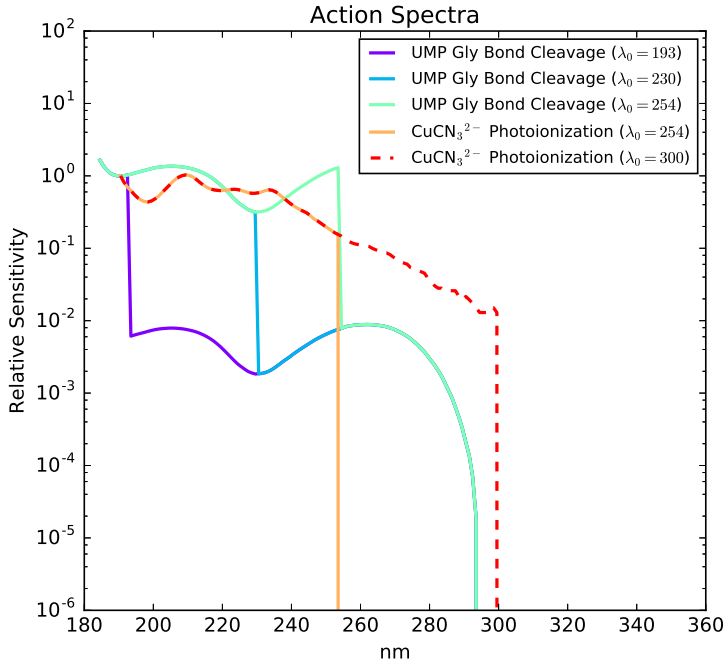

Figure 3.7: Action spectra for photolysis of UMP and photoionization of $CuCN_3^{2-}$, assuming a step-function form to the QE for both processes with step at $\lambda = \lambda_0$ The spectra are arbitrarily normalized to 1 at 190 nm.

3.5.2 Impact of Albedo and Zenith Angle On Surface Radiance & Prebiotic Chemistry

In this section, we quantify the impact of varying albedo and zenith angle on surface radiance, and on prebiotic chemistry as measured by our action spectra.

The atmospheric radiative transfer computed for the prebiotic (3.9 Ga) Earth by Rugheimer et al. (2015) assumed a spectrally uniform albedo of 0.20 and a solar zenith angle of 60°. However, much broader ranges of albedos and zenith angles are available in a planetary context. In this section, we explore the impact of different albedos (A)and solar zenith angles (SZA) on the surface radiance (azimuthally integrated) on the 3.9 Ga Earth.

We calculate the surface radiance at SZA= 0°, 48.2°, and 66.5°, for a range of different surface albedos. SZA= 0° is the smallest possible value for SZA and corresponds to the shorted possible path through the Earth's atmosphere. It is achieved at tropical latitudes. SZA= 48.2° corresponds to the insolation-weighed mean zenith angle on the Earth (Cronin 2014). SZA= 66.5° corresponds to the maximum zenith angle experienced at the poles (noon at the summer solstice)[12]. Our choices of zenith angle thus encapsulate the minimum possible zenith angles, and hence the shortest possible atmospheric path lengths, over the Earth's surface. As such, they may be understood as corresponding to the range of maximum possible UV surface radiances accessible at different latitudes on

[12]For simplicity, we assume here the modern terrestrial obliquity of 23.5°. We are not aware of any evidence suggesting terrestrial obliquity was much different at 3.9 Ga; in fact, dynamical modelling suggests that the Earth's obliquity is stabilized by the Moon (Laskar et al. 1993) so that it varies with an amplitude of only $\sim 1.3°$. Our results are insensitive to this magnitude of variation in obliquity

the Earth's surface. It is of course possible to achieve arbitrarily large zenith angles (and hence arbitrarily low surface radiances) anywhere on Earth through the diurnal cycle and through seasonal variations at polar latitudes.

When considering albedos, we consider fixed uniform albedos of 0, 0.2, and 1. Albedos of 0 and 1 correspond to the lowest and highest possible values of A, and hence the lowest and highest[13] surface radiance, respectively. The $A = 0.2$ case corresponds to the Rugheimer et al. (2015) base case. We also consider albedos corresponding to different physical surface environments, including ocean, tundra, desert, and old and new snow, including the dependence on z (see Section 3.8 for details). We consider this wide range of possible surface albedos because the climate state of the young Earth is minimally constrained by the available evidence, and climate states different than modern Earth are plausible. For example, Sleep & Zahnle (2001) argue for a cold, ice-covered Hadean/early Archaean climate, which would imply high-albedo conditions even at low latitudes.

Figure 3.8 presents the surface radiance computed for the Rugheimer et al. (2015) atmospheric model for these different zenith angles and surface albedos. The results match our qualitative expectations. Low albedo surfaces correspond to lower surface radiances, with spectral contrast ratios as high as a factor of 7.4 between the $A = 1$ and $A = 0$ cases for $\lambda > 204$ nm (i.e. the onset of the CO_2 cutoff, see Ranjan & Sasselov 2016). Similarly, small zenith angles correspond to higher surface radiances, with spectral contrast ratios as high as high as 4.1 between SZA$= 0^\circ$ and $z = 66.5^\circ$ for $\lambda > 204$ nm. Taken together, the effect is even stronger: for $\lambda > 204$ nm, the $A = 1$,

[13]By virtue of backscattering of the upward diffuse radiance

SZA= 0° case (the highest-radiance case in the parameter space we considered) has spectral contrast ratios as high as a factor of 30 with respect to the $A = 0$, SZA= 66.5° case (the lowest-radiance case considered in our parameter space). Using more physically motivated albedos, the spectral contrast ratio between a model with SZA= 0° and albedo corresponding to fresh snow (i.e. the brightest natural surface included in our model) and a model with SZA= 66.5° and albedo corresponding to tundra (i.e. the darkest natural surface included in our model) were as high as a factor of 21. This means that at some wavelengths, 21 times more fluence would have been available on the equator of a high-albedo snow-and-ice covered "snowball Earth" compared to the polar regions of a warmer world with tundra or open ocean at the poles, for identical planetary atmospheres.

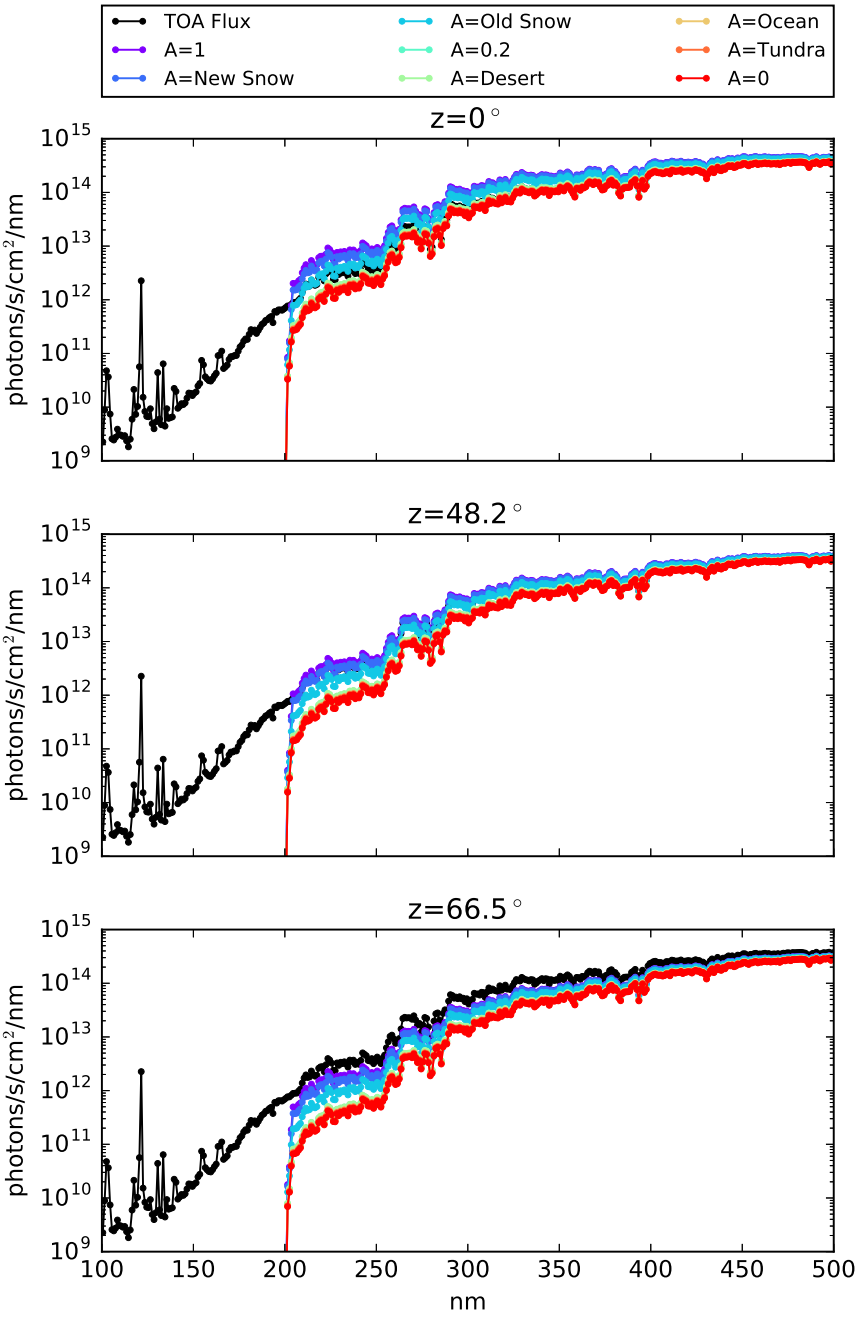

Figure 3.8: Surface radiance for the Earth at 3.9 Ga, assuming an atmosphere corresponding to the model of Rugheimer et al. (2015) and a range of solar zenith angles and surface albedos. Taken together, albedo and zenith angle can drive variations in spectral surface radiance as high as a factor of 20.6 for $\lambda > 204$ nm at 1 nm resolution.

Table 3.1:: Relative dose rates for prebiotic relevant photoprocesses as a function of solar zenith angle and surface albedo for the Rugheimer et al. (2015) 3.9 Ga Earth atmosphere. Abbreviations: T=Tundra, OS=Old Snow, NS=New Snow.

Zenith Angle	Albedo	UMP-193	UMP-230	UMP-254	CuCN3-254	CuCN3-300
66.5	Tundra	0.09	0.08	0.12	0.11	0.15
66.5	Ocean	0.10	0.09	0.12	0.11	0.15
66.5	Desert	0.11	0.10	0.13	0.13	0.17
66.5	OS	0.19	0.21	0.27	0.27	0.32
66.5	NS	0.25	0.36	0.43	0.44	0.47
0	Tundra	0.34	0.34	0.46	0.45	0.56
0	Ocean	0.35	0.34	0.47	0.45	0.56
0	Desert	0.39	0.39	0.53	0.51	0.63
0	OS	0.71	0.85	1.09	1.09	1.23
0	NS	0.99	1.47	1.73	1.79	1.85
66.5	NS/T	2.69	4.31	3.63	3.96	3.15
0	NS/T	2.88	4.38	3.72	4.02	3.34
0/66.5	Tundra	3.64	3.99	3.96	4.01	3.72
0/66.5	New Snow	3.89	4.05	4.06	4.07	3.95
0/66.5	NS/T	10.48	17.47	14.75	16.13	12.42

We note that, somewhat non-intuitively, for some values of albedo and zenith angle, surface radiances exceeding the incident TOA radiance are possible (see, e.g., the $A = 1$, SZA= 0° case in Figure 3.8). This is due to two factors. First, the downwelling diffuse radiance is enhanced by the backscatter of the upwelling diffuse radiance. Second, our flux conservation requirement coupled with our assumption of an isotropically scattering surface means that the upwelling radiance field is enhanced over the downwelling radiance field for low values of SZA and high values of A, meaning even more radiance is available to be backscattered. For a more thorough discussion of this phenomenon,

see Section 3.9. For a discussion of a similarly non-intuitive result for surface flux, see Shettle & Weinman (1970).

We quantify the impact of albedo and zenith angle from a biological perspective by computing the biologically effective relative dose rates D_i for the photoprocesses described in Section 3.5.1, for the hemispherically-integrated surface radiances corresponding to the different surface types and zenith angles considered in this study. These values are reported in Table 3.1. Variations in albedo can affect the biologically effective dose rates of UV by factors of 2.7-4.4, depending on the zenith angle and the action spectrum used to compute the dose rate. Variations in zenith angle can affect the biologically effective dose rate of UV by factors of 3.6-4.1, depending on the surface albedo and action spectrum. Taken together, variations in albedo and zenith angle can change the biologically effective dose of UV by factors of 10.5-17.5, depending on the action spectrum used to compute the dose rate. We conclude that local conditions like albedo and latitude could impact the availability of UV photons for prebiotic chemistry by an order of magnitude or more.

3.5.3 Impact of Varying Levels of CO_2 On Surface Radiance & Prebiotic Chemistry

In Ranjan & Sasselov (2016), we argued that shortwave UV light would have been inaccessible on the young Earth due to shielding from atmospheric CO_2. Specifically, we noted that atmospheric attenuation decreased fluence by a factor of 10 by 204 nm, with the damping increasing rapidly with the atmospheric cross-section (driven by CO_2) at shorter wavelengths. This shielding is important because it screens out

photons shortward of 200 nm that are expected to be harmful, while still permitting the potentially biologically useful flux in the $\gtrsim$ 200 nm range (see, e.g., Guzman & Martin 2008, Barks et al. 2010, Patel et al. 2015) to reach the planetary surface.

However, this argument is based on the models elucidated in Rugheimer et al. (2015). Rugheimer et al. (2015) assumed a CO_2 partial pressure at 3.9 Ga of 0.1 bar. This value is ad hoc: no direct geological constraints on CO_2 levels are available, and a variety of models with a wide range of CO_2 levels have been proposed that are consistent with the available climate constraints. Proposed CO_2 levels for the $\sim$ 3.9 Ga Earth range from 8×10^{-4} bar (Wordsworth et al. 2013a) to 7 bar Kasting (1987).

In this section, we examine the sensitivity of the shielding of UV shortwave fluence due to varying levels of CO_2 in the atmosphere. We compute radiative transfer through an atmosphere with varying levels of CO_2 and N_2 under irradiation by the 3.9 Ga Sun. We evaluate radiative transfer at (zenith angle, albedo) combinations of (SZA= 0°, A =fresh snow) and (SZA= 66.5°, A =tundra), corresponding to the extremal values of the range of plausible maximal surface radiances accessible on the Earth assuming present-day obliquities. We omit attenuation due to other gases in our model (H_2O, CH_4, etc) in order to isolate the influence of CO_2. We emphasize, therefore, that the UV throughputs we calculate should not be taken to correspond to the surface radiance plausibly expected on the 3.9 Ga Earth for a given CO_2 column, since they do not include attenuation from other gases and/or particulates/hazes that may have been present. Rather, these calculations represent the upper limits on surface radiance that are imposed by a given CO_2 column.

We assume a fixed background of N_2 gas, with column density $N_{N_2} = 1.88 \times 10^{25}$

cm^{-2}, corresponding to the 0.9 bar N_2 column assumed by the Rugheimer et al. (2015) atmospheric model. We choose this value for consistency with the model of Rugheimer et al. (2015), noting that it is also consistent with the deepest constraint on N_2 abundance in the Archaean, i.e. the finding of Marty et al. (2013) that pN_2 at 3-3.5 Ga was 0.5-1.1 bar based on analysis of fluid inclusions trapped in Archaean hydrothermal quartz samples. Since N_2 does not absorb at UV wavelengths longer than 108 nm (Huffman 1969; Chan et al. 1993b) and N_2 scattering is weak compared to e.g. CO_2 scattering, our results should be insensitive to the precise N_2 level.

We parametrize CO_2 abundance by scaling the CO_2 column calculated by Rugheimer et al. (2015) corresponding to 0.1 bar of CO_2, with total column density $N_{CO_2} = 2.09 \times 10^{24}$ cm^{-2}. We calculate the UV radiance through CO_2 columns equal to the Rugheimer et al. (2015) column scaled by factors in the range from $10^{-6} - 10^{3}$. To link these columns to CO_2 partial pressures, we employ the relation that the partial pressure of a well-mixed gas in an atmosphere is $p_i = g\bar{m}N_i$, where g is the acceleration due to gravity ($g = 981$ cm s^{-2} for Earth), $\bar{m}$ is the atmospheric mean molecular mass, and N_i is the column density of the gas. Figure 3.9 presents the UV surface radiances for atmospheres with $N_{N_2} = 1.88 \times 10^{25}$ cm^{-2}, and varying levels of CO_2. Table 3.2 presents the optical and atmospheric parameters associated with each model.

Table 3.2:: Atmospheric parameters defining the models shown in Figure 3.9. Also given are the mean molecular weight and surface partial pressures of CO_2 and N_2 associated with each model atmosphere. A background column density of $N_{N_2} = 1.88 \times 10^{25}$ cm^{-2} is assumed throughout. Each model atmosphere had radiative transfer computed for both (A=tundra, SZE=66.5°) and (A=fresh-fallen snow, SZE=0°).

N_{CO_2} (cm^{-2})	$\bar{m}$ (g)	pN_2 (bar)	pCO_2 (bar)	Note
0.00	4.65×10^{-23}	0.860	0.00	
2.09×10^{18}	4.65×10^{-23}	0.860	9.55×10^{-8}	
2.09×10^{19}	4.65×10^{-23}	0.860	9.55×10^{-7}	
2.09×10^{20}	4.65×10^{-23}	0.860	9.55×10^{-6}	
2.09×10^{21}	4.65×10^{-23}	0.860	9.55×10^{-5}	
1.87×10^{22}	4.65×10^{-23}	0.860	8.53×10^{-4}	Corresponds to Wordsworth et al. 2013a 2×PAL CO_2 model
2.09×10^{22}	4.66×10^{-23}	0.860	9.56×10^{-4}	
2.09×10^{23}	4.68×10^{-23}	0.865	9.61×10^{-3}	
1.26×10^{24}	4.82×10^{-23}	0.891	5.97×10^{-2}	Corresponds to von Paris et al. 2008 pCO_2 = 0.06 bar lower limit)
2.09×10^{24}	4.92×10^{-23}	0.909	0.101	
2.78×10^{24}	5.00×10^{-23}	0.923	0.136	Corresponds to Kasting 1987 pCO_2 = 0.2 bar lower limit
2.09×10^{25}	6.05×10^{-23}	1.12	1.24	
9.76×10^{25}	6.88×10^{-23}	1.27	6.58	Corresponds to Kasting 1987 pCO_2 = 7 bar upper limit
2.09×10^{26}	7.09×10^{-23}	1.31	14.6	
9.84×10^{26}	7.26×10^{-23}	1.34	70.1	Corresponds to volatilization of crustal carbon inventory of C as CO_2
2.09×10^{27}	7.28×10^{-23}	1.35	150	

To place these column densities in context, we compute the CO_2 columns associated with different climate models in the literature.

- Kasting (1987) calculate the range of CO_2 partial pressures required to sustain a plausible (i.e. consistent with an ice-free planet with liquid water oceans) climate on Earth throughout its history assuming a CO_2-H_2O greenhouse with 0.77 bar of N_2 as a background gas. Interpolating between model calculations, for 3.9 Ga the authors suggest a plausible CO_2 pressure range of $.2 - 7$ bar (calculated using a pure-CO_2 atmosphere equivalence). The lower limit corresponds to a surface temperature of 273K, whereas the upper point is interpolated between the CO_2 level required to sustain a temperature of 293K at 2.5 Ga, and the 10-bar limit for pCO_2 proposed by Walker (1985) at 4.5 Ga. This corresponds to CO_2 column density range of $2.79 \times 10^{24} - 9.76 \times 10^{25}$ cm^{-2}.

- If the requirement on global mean temperature is relaxed to 273 K from the > 278 K of Kasting (1987) (Haqq-Misra et al. 2008), von Paris et al. (2008) find only 0.06 bar of CO_2 is required at an insolation corresponding to 3.8 Ga (Gough 1981) in a CO_2-H_2O greenhouse with 0.77 bar of N_2 as a background gas. This corresponds to a CO_2 column density of 1.26×10^{24} cm $^{-2}$.

- More dramatically, Wordsworth et al. (2013a) model a N_2-H_2-CO_2 atmosphere, including the effects of collision-induced absorption (CIA) of N_2 and H_2 under the assumption of high levels of N_2 and H_2 relative to present atmospheric levels (PAL). By including N_2-H_2 CIA, for a solar constant of 75% the modern value (corresponding to 3.8 Ga using the methodology of Gough 1981) they are able to maintain global mean surface temperatures suitable for liquid water with dramatically lower CO_2 levels than H_2O-CO_2 greenhouses. For an atmosphere with $3\times$PAL N_2 and an H_2 mixing ratio of 0.1, only $2\times$ PAL of CO_2 (7.8×10^{-5} bar)is required, corresponding to 1.87×10^{22} cm^{-2}.

- Finally, as an extreme upper bound, we consider the observation of Kasting (1993) based on Ronov & Yaroshevsky (1969) and Holland (1978) that Earth has $\sim 10^{23}$ g of carbon stored in crustal carbonate rocks. If this entire carbon inventory were volatilized as CO_2, it would correspond to a CO_2 column of 9.84×10^{26} cm $^{-2}$.

We compute the surface radiance for N_2-CO_2 model atmospheres with N_{CO_2} corresponding to the CO_2 columns computed for the above literature models, with a fixed N_2 background of $N_{N_2} = 1.88 \times 10^{25}$ cm^{-2} as before. These models and the parameters associated with them are also shown in Figure 3.9 and Table 3.2.

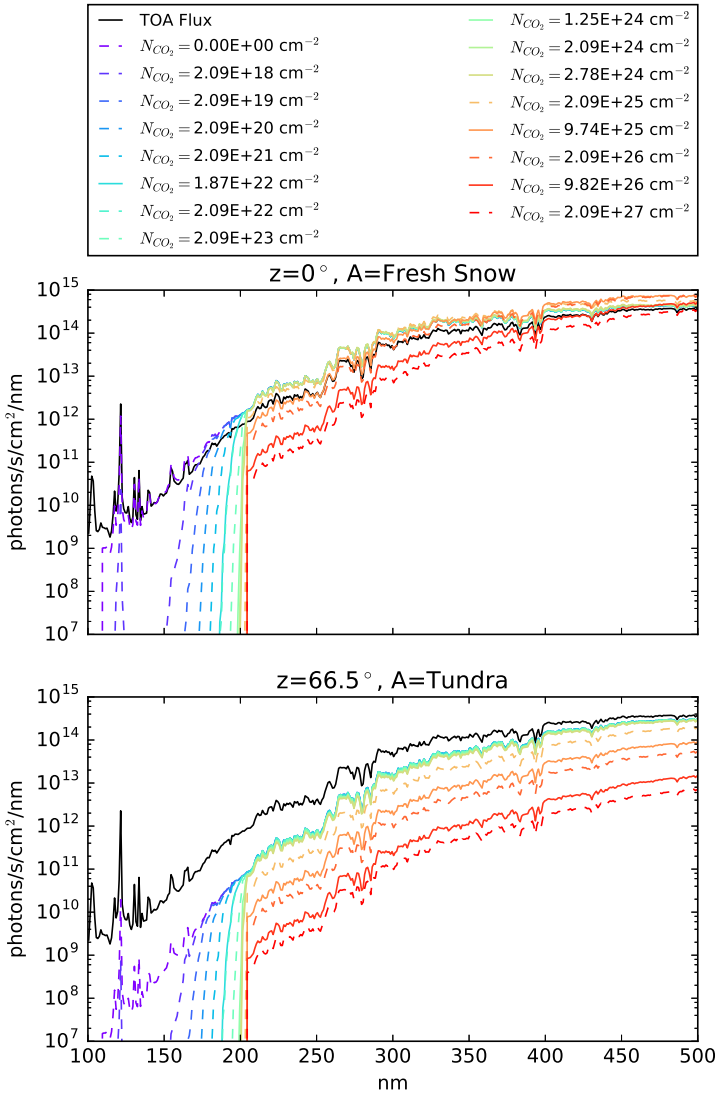

Figure 3.9: Surface radiances for an atmosphere with $N_{N_2} = 1.88 \times 10^{25}$ cm^{-2} and varying levels of CO_2, for surface albedo and solar zenith angle combinations of (tundra, 66.5°) and (new snow, 0°), corresponding to the range of maximum surface radiances available across the planetary surface. Solid lines correspond to CO_2 levels with motivation from climate models in the literature. The line corresponding to $N_{CO_2} = 2.09 \times 10^{24}$ cm^{-2} (i.e. the fiducial 0.1-bar CO_2 level in the Rugheimer et al. (2015) model) is highlighted with a thicker line.

Surface Radiance

An N_2-CO_2 atmosphere with even small amounts of CO_2 is enough to form a strong shield to extreme-UV (EUV) radiation. A column density as low as $N_{CO2} = 2.09 \times 10^{19}$ cm^{-2}, 10^{-5} of the Rugheimer et al. (2015) level, is enough to reduce the maximum possible surface radiance below 1% of the TOA flux for wavelengths shorter than 167 nm. In Ranjan & Sasselov (2016), we argued that variations in solar UV output due to variability and flaring would have minimal impact on prebiotic chemistry because most of the variability was confined to wavelengths shorter than 165 nm, and incoming photons at these wavelengths were strongly attenuated by both the atmosphere and water. Here, we have shown that this atmospheric shielding exists for atmospheres with $N_{CO2} \geq 2.09 \times 10^{19}$ cm^{-2}. In practice, this condition is satisfied by all climatologically plausible models for the 3.9 Ga Earth we are aware of. Therefore, even molecules that are removed from aqueous environments, e.g. through drying, are not expected to be vulnerable to solar UV variability for any plausible primitive atmosphere.

In Ranjan & Sasselov (2016), we argued that atmospheric CO_2 would have cut off fluence at wavelengths shorter than 204 nm, and hence that UV laboratory sources like ArF excimer lasers with primary emission at 193 nm were inappropriate for simulations of prebiotic chemistry. This was based on the assumption that $N_{CO2} = 2.09 \times 10^{24}$ cm^{-2}. However, lower CO_2 levels are plausible for the young Earth. The lowest CO_2 atmosphere model that we are aware of that is consistent with an ice-free Earth at 3.9 Ga is that of Wordsworth et al. (2013a), with $N_{CO2} = 1.87 \times 10^{22}$ cm^{-2}; at these levels, CO_2 extinction is enough to reduce the surface radiance shortward of 189 nm anywhere on Earth to less than 1% of the TOA flux, but longer-wavelength photons might have been accessible in

the absence of absorption from other species. Therefore, we revise our earlier statement: while photons shortward of 189 nm would have been inaccessible to prebiotic chemistry, photons longward of 189 nm might have been available if $N_{CO2} \leq 1.87 \times 10^{22}$ cm^{-2} and if there were no other major UV absorbers in the atmosphere (e.g., H_2O vapor, see Section 3.5.6). In such a regime, sources with primary emission in the 190-200 nm regime, like ArF eximer lasers, may be appropriate sources for prebiotic chemistry studies.

Kasting (1987) suggest a climatologically plausible upper limit of 7 bars of pure CO_2 at 3.9 Ga, interpolating between the upper bound of Walker (1985) at 4.5 Ga and the CO_2 level required to sustain $T \approx 293$ K at 2.5 Ga. This corresponds to $N_{CO_2} = 9.76 \times 10^{25}$ cm^{-2}. At this CO_2 level, surface fluences remain above 1% of that incident at the TOA at wavelengths > 210 nm even in the minimum fluence (low albedo, high zenith angle) case. Consequently, for CO_2 levels corresponding to mean temperatures similar to that of modern Earth, photons of wavelength $\lambda > 245$ nm would have been accessible on the 3.9 Ga Earth, provided no other major UV absorbers besides CO_2 (e.g. SO_2, H_2S) were present in the atmosphere. Therefore, the use of sources with primary emission at wavelengths longer than 210 nm, e.g., 254 nm Hg lamps, is appropriate for simulations of prebiotic chemistry assuming a climate similar to the present day (with the obvious caveat that monochromatic sources risk missing crucial wavelength-dependent processes, see, e.g., Ranjan & Sasselov 2016).

Overall, the UV surface fluence is relatively insensitive to the level of atmospheric CO_2. The conventional H_2O-CO_2-N_2 minimal greenhouses with pCO_2=0.06-0.2 bar ($N_{CO_2} = 1.26 - 2.78 \times 10^{24}$ cm^{-2}) (von Paris et al. 2008; Kasting 1987) feature virtually identical UV surface fluence environments. The surface fluence is suppressed only

modestly in the scattering regime ($\lambda > 204$ nm), even for optically thick atmospheres; for example, for $N_{CO2} = 2.09 \times 10^{27}$ cm^{-2}, the surface fluence is suppressed by $\lesssim 3$ orders of magnitude despite an optical depth of ~ 1000. This behavior is a consequence of the random walk photons undergo in highly scattering atmospheres, and illustrates the importance of accurately including the effects of multiple scattering when calculating radiative transfer in such atmospheres.

Biologically Effective Doses

Figure 3.10 presents the biologically effective dose rates for the photoprocesses considered in our study under irradiation by surface fluences corresponding to attenuation by different levels of CO_2, normalized by the dose rates corresponding to $N_{CO2} = 2.09 \times 10^{24}$ cm^{-2} (0.1 bar CO_2). With this normalization, a dose rate $D > 1$ means a higher dose rate than the 0.1 bar CO_2 case and hence a higher photoreaction rate, and $D < 1$ the opposite. Both the maximum radiance (A=new snow, $SZA = 0°$) and the minimum radiance (A=tundra, SZA= 66.5°) cases are presented.

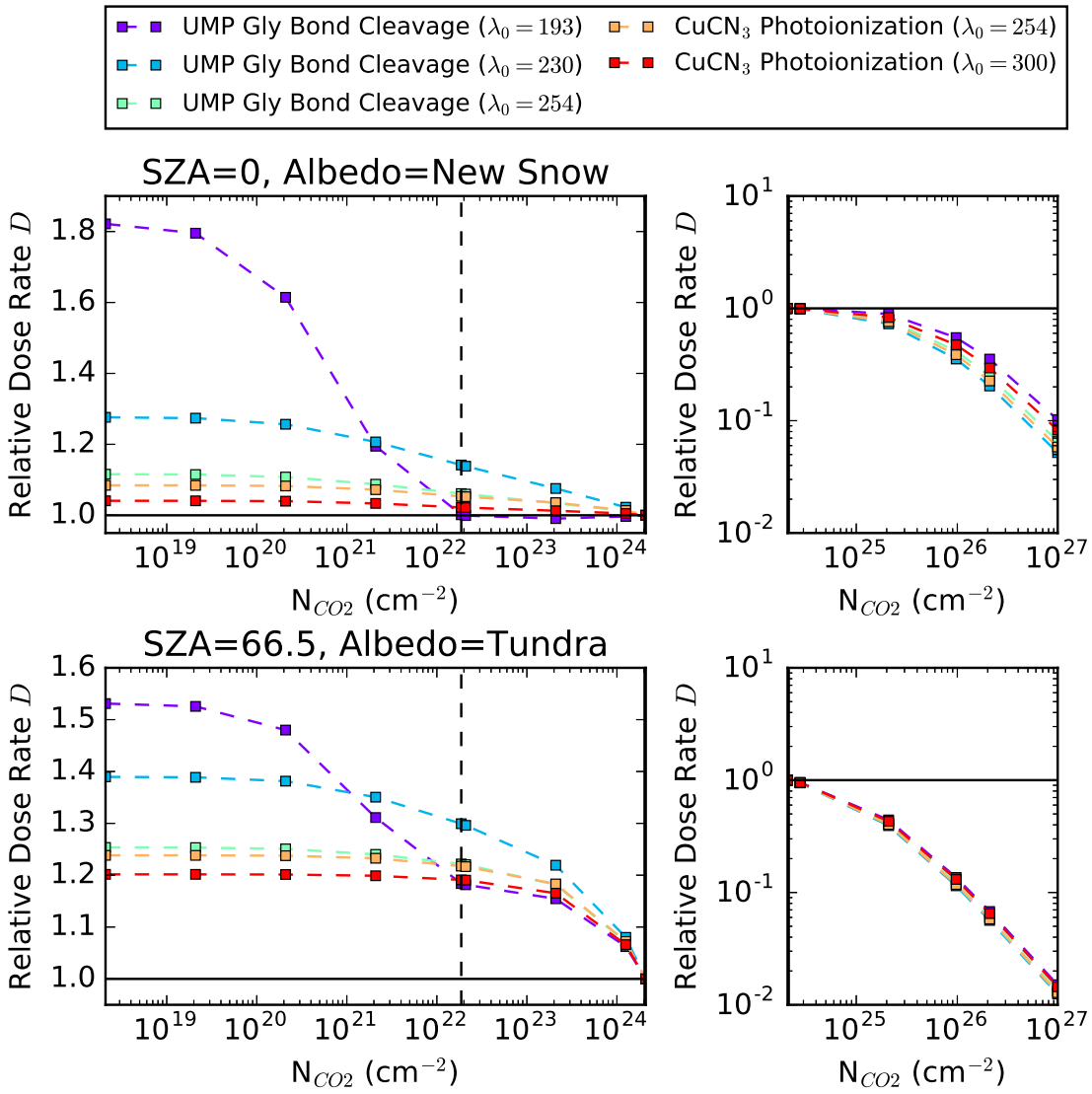

Figure 3.10: Biologically effective dose rates for UMP-X and CuCN3-Y as a function of N_{CO_2}, normalized to their values at $N_{CO2} = 2.09 \times 10^{24}$ cm^{-2}. The dashed line demarcates the level of CO_2 required by the climate model of Wordsworth et al. (2013a), the lowest proposed so far. The plot truncates at the CO_2 level corresponding to volatilization of all crustal carbonates as CO_2, an upper bound on plausible CO_2 levels.

For the minimum radiance case, we observe that the biologically effective dose rates uniformly decrease with increasing N_{CO2}, corresponding to uniforming decreasing fluence levels, as expected. $D_i > 1$ for $N_{CO2} < 2.09 \times 10^{24}$ cm^{-2} and $D_i < 1$ for $N_{CO2} > 2.09 \times 10^{24}$ cm^{-2}, meaning that both stressor and eustressor photoprocesses are slowed by increasing N_{CO2}.

In the maximum radiance case, the biologically effective dose rates generally also follow the same trend with N_{CO2}, i.e. decreasing as N_{CO2} increases. However, from $N_{CO2} = 2.09 \times 10^{23} - 10^{24}$ cm^{-2}, the dose rate of UMP-193 increases slightly, by 0.6%. This is because for $N_{CO2} \geq 2.09 \times 10^{23}$ cm^{-2}, photons shortward of $\lambda_0 = 193$ nm are effectively completely blocked from the surface, leaving only the longwave photons at the lower QY available to power the reaction. For high albedo surfaces, this longwave fluence increases slightly with N_{CO2} due to enhanced backscattering of reflected light from the surface by atmospheric CO_2[14], increasing slightly the effective dose. For $N_{CO2} > 2.09 \times 10^{24}$ cm^{-2}, this effect is overwhelmed by the overall decrease in fluence levels, and the UMP-193 dose rate returns to the general trend.

High levels of atmospheric CO_2 can suppress prebiotically relevant photoprocesses as measured by our action spectra. For $N_{CO2} = 9.84 \times 10^{26}$ cm^{-2}, corresponding to the volatilization of all CO_2 from crustal carbonates, the dose rates are suppressed by a factor of $10 - 100$ relative to the dose rates at $N_{CO2} = 2.09 \times 10^{24}$ cm^{-2}, depending on the surface conditions. UV-sensitive pathways relevant to prebiotic chemistry may be

[14]For low optical depth; at high optical depth (i.e. in the shortwave), so little fluence reaches the ground that this effect is lost. When ground reflection is turned off by setting the albedo to that of tundra (i.e. ≈ 0), while maintaining SZA=0, the radiance in all wavebands declines monotonically with N_{CO2}

photon-limited in high-CO_2 cases. If assuming a high-CO_2 atmosphere for UV-dependent prebiotic pathways, it may be important to characterize the sensitivity of the prebiotic pathways to fluence levels, to make sure that thermal backreactions will not retard the photoprocesses at low fluence levels.

Low levels of atmospheric CO_2 can modestly enhance prebiotically relevant photoprocesses as measured by our action spectra. For $N_{CO2} = 1.87 \times 10^{22}$ cm^{-2} (corresponding to the low-CO_2 model of Wordsworth et al. (2013a)), in the maximum radiance case the dose rates are $1.006 - 1.16$ of the dose rates at $N_{CO2} = 2.09 \times 10^{24}$ cm^{-2}. For the corresponding minimum radiance case, the dose rates are $1.19 - 1.31$ of the dose rates at $N_{CO2} = 2.09 \times 10^{24}$ cm^{-2}. If one allows CO_2 levels to decrease without regard for climatological or geophysical plausibility, higher dose rates are possible, but only to a point: assuming no CO_2 at all (only scattering from N_2), dose rates of 1.05-1.76 relative to the $N_{CO2} = 2.09 \times 10^{24}$ cm^{-2} base case are plausible (maximum radiance conditions). Hence, the variation in dose rate due to reducing CO_2 is less than a factor of 2. Pathways derived assuming attenuation from more conventional levels of CO_2 should function even with lower levels of CO_2 shielding.

Overall, across the range of possible CO_2 levels ($N_{CO2} \leq 9.84 \times 10^{26}$ cm^{-2}), the variation in biologically effective dose rates is < 2 orders of magnitude, for both stressor and eustressor pathways and all values of λ_0, assuming no other UV absorbers. Hence, as measured by these action spectra, UV-sensitive prebiotic photochemistry is relatively insensitive to the level of CO_2 in the atmosphere, assuming no other absorbers to be present.

3.5.4 Alternate shielding gases

In the previous section, we considered the constraints placed by varying levels of atmospheric CO_2 on the surficial UV environment. However, CO_2 is not the only plausible UV absorber in the atmosphere of the young Earth. Other photoactive gases that may have been present in the primitive atmosphere include SO_2, H_2S, CH_4 and H_2O. These gases have absorption cross-sections in the 100-500 nm range, and as such if present at significant levels could have influenced the surficial UV environment. O_2 and O_3, while expected to be scarce in the prebiotic era, are strongly absorbing in the UV, and might have an impact even at low abundances.

In this section, we explore the potential impact of varying levels of gases other than CO_2 on surficial UV fluence on the 3.9 Ga Earth. We consider each gas species G individually, computing radiative transfer through two-component atmospheres under insolation by the 3.9 Ga Sun, with varying levels of the photoactive gas G and a fixed column of N_2 as the background gas. We consider a range of column densities of G corresponding the levels computed in Rugheimer et al. (2015) scaled by factors of 10. Table 3.3 gives the abundance of each gas computed by Rugheimer et al. (2015).

As in the case of CO_2 (Section 3.5.3), we assume that G is well-mixed, and we omit attenuation due to other gases in order to isolate the effect of the specific molecule G. We evaluate radiative transfer for an (A, SZA) combination corresponding to (fresh snow, 0°) only; hence, the surface radiances we compute may be interpreted as planetwide upper bounds. We assume a fixed N_2 background with column density of $N_{N_2} = 1.88 \times 10^{25}$ cm^{-2}, corresponding to the 0.9 bar N_2 column in the Rugheimer et al. (2015) atmospheric model. We again emphasize that the UV throughput we calculate

should not be taken to correspond to the surface radiance plausibly expected on the 3.9 Ga Earth for a given column of G, since our calculations do not include attenuation from other gases that may have been present. Rather, these calculations represent the upper limits on surface radiance that are imposed by various levels of these gases.

The model metadata we secured from Rugheimer et al. (2015) do not include H_2S abundances. We estimate an upper bound on the H_2S abundances by assuming the relative abundance of H_2S compared to SO_2 traces their emission ratio from outgassing. Halmer et al. (2002) find the outgassing emission rate ratios of $[H_2S]/[SO_2]$=0.1-2 for subduction zone-related volcanoes and 0.1-1 for rift-zone related volcanoes for the modern Earth. Since the redox state of the mantle has not changed from 3.6 Ga and probably from 3.9 Ga (Delano 2001), we can expect the outgassing ratio to have been similar at 3.9 Ga. Therefore, we assign an upper bound to the H_2S column of 2× the SO_2 column.

Table 3.3:: Gas abundances in the Rugheimer et al. (2015) 3.9 Ga Earth model. The H_2S abundances listed are upper bounds estimated from SO_2 levels.

G	N_G (cm^{-2})	Molar Concentration
N_2	1.88×10^{25}	0.9
CO_2	2.09×10^{24}	0.1
H_2O	9.96×10^{22}	4.76×10^{-3}
CH_4	3.45×10^{19}	1.65×10^{-6}
SO_2	7.05×10^{14}	3.37×10^{-11}
O_2	5.66×10^{19}	2.71×10^{-6}
O_3	1.92×10^{15}	9.16×10^{-11}
H_2S *	$\leq 1.41 \times 10^{15}$	$\leq 6.7 \times 10^{-11}$

3.5.5 CH_4

Rugheimer et al. (2015) fix by assumption a uniform CH_4 mixing ratio of 1.65×10^{-6} throughout their 1-bar atmosphere, corresponding to $N_{CH_4} = 3.45 \times 10^{19}$ cm^{-2}. However, other authors have postulated a broad range of abundances for CH_4. Kasting & Brown (1998b) estimate a methane abundance of 0.5 ppm (mixing ratio of 5×10^{-7}) for a 1-bar N_2-CO_2 atmosphere assuming conversion of 1% carbon flux from mid-ocean ridges to CH_4 prior to the rise of life. Kasting (2014) echo this estimated mixing ratio for a CH_4 source of serpentinization of ultramafic rock with seawater at present-day levels, while Guzmán-Marmolejo et al. (2013) estimate serpentinization can drive CH_4 levels up to 2.1 ppmv. However, Kasting (2014) also note that methane production from impacts could have outpaced the supply from serpentinization multiple orders of magnitude, and could have sustained abiotic CH_4 levels up to 1000 ppmv. Shaw (2008) also postulates that such high CH_4 levels might be plausible, hypothesizing that conversion of dissolved carbon compounds to methane might have produced methane fluxes an order of magnitude higher than the present day, enough to sustain an atmosphere with sufficient methane to maintain a habitable climate. Such estimates correspond to a broad range of CH_4, from $N_{CH_4} = 9.83 \times 10^{18}$ cm^{-2} to $N_{CH_4} = 1.97 \times 10^{22}$ cm^{-2}. We consequently explore a range of CH_4 values corresponding to $10^{-2} - 10^{3}\times$ the Rugheimer et al. (2015) value, encompassing this range. Figure 3.11 shows the resultant spectra.

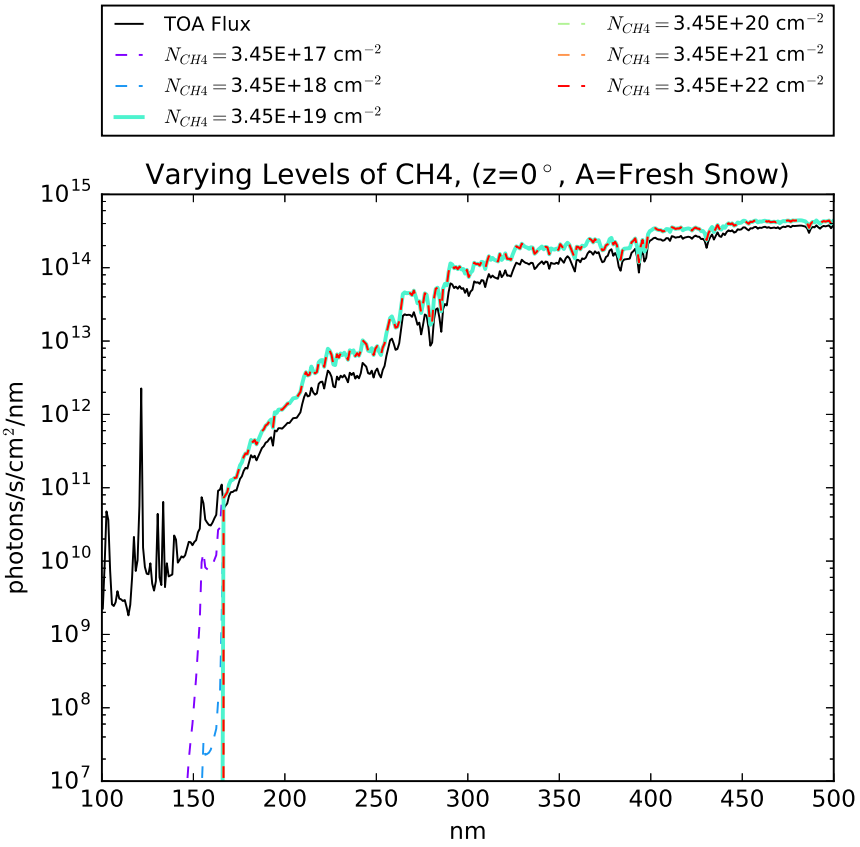

Figure 3.11: Surface radiances for an atmosphere with $N_{N_2} = 1.88 \times 10^{25}$ cm^{-2} and varying levels of CH_4, for a surface albedo corresponding to new snow and SZA=0°. The line corresponding to the CH_4 level assumed in the Rugheimer et al. (2015) model is presented as a solid, thicker line.

Absorption of UV light by CH_4 is negligible in an atmosphere with even trace amounts of CO_2, due to the extremely shortwave onset of absorption by CH_4 (165 nm). At CH_4 levels of $N_{CH_4} = 3.45 \times 10^{22}$ cm^{-2}, 3 orders of magnitude higher than those assumed in Rugheimer et al. (2015) and at the upper end of what has been

proposed in the literature, CH_4 extincts fluence shortward of 165 nm. A CO_2 level of $N_{CO_2} = 2.09 \times 10^{19}$ cm^{-2} is enough to extinct the fluence shortward of 167. This CO_2 level is 5 orders of magnitude less than the Rugheimer et al. (2015) value and 2 orders of magnitude less than the lowest level CO_2 suggested in the literature based on climatic constraints. We conclude that in an atmosphere with even trace amounts of CO_2, plausible levels of CH_4 do not further constrain the surface UV environment.

3.5.6 H_2O

There exist few constraints on primordial water vapor levels. The terrestrial water vapor profile is set by the temperature profile; evaporation rates and H_2O saturation pressures increase with temperature, meaning that a hot planet is likely to be steamier than a cold planet. Knauth (2005) use oxygen isotope data from cherts to argue that the ocean temperature was 328-358K (55-85°) at 3.5 Ga, though this is not universally accepted (Kasting 2010), in part due to the extraordinary inventory of greenhouse gases that would be required to sustain such high temperatures. By contrast, Rugheimer et al. (2015) computed a surface temperature of 293K for the Earth at 3.9 Ga.

The model of Rugheimer et al. (2015) corresponds to an atmosphere with an H_2O column density of $N_{H_2O} = 9.96 \times 10^{22}$ cm^{-2}. However, arbitrarily low H_2O abundances are possible depending on how cold the atmosphere and surface are. What of the upper limit? Kasting et al. (1984) computed among other parameters the H_2O mixing ratio for a planet with atmospheric composition matching the modern Earth under varying levels of insolation. In the case of 1.45× modern insolation, Kasting et al. (1984) compute a surface temperature of 384.2 K (greater than that suggested by Knauth (2005)), a

surface pressure of 2.481 bars, and H_2O volume mixing ratio of ~ 0.5. This corresponds to an atmosphere with a mean molecular mass of 3.89×10^{-23} g and an H_2O column of 3.25×10^{25} cm^{-2}.We interpret this value as an extreme upper limit for H_2O column density. We evaluate radiative transfer through N_2-H_2O atmospheres with total H_2O columns corresponding to $10^{-5} - 10^3$ of the Rugheimer et al. (2015) value, encompassing this upper bound. Figure 3.12 shows the resultant spectra.

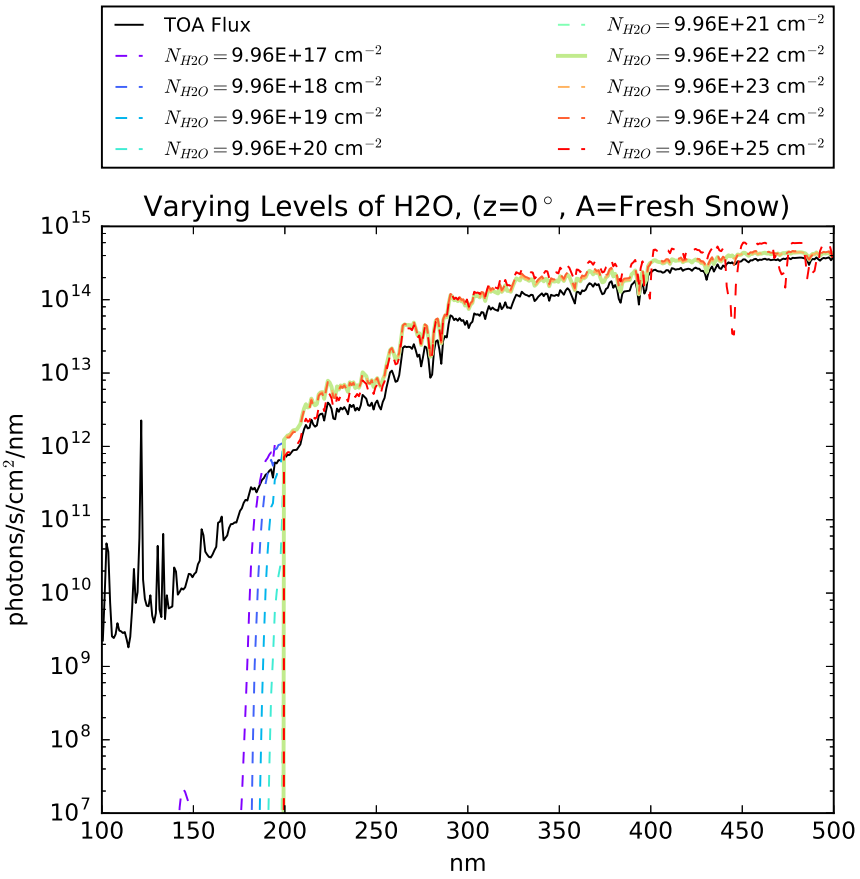

Figure 3.12: Surface radiances for an atmosphere with $N_{N_2} = 1.88 \times 10^{25}$ cm^{-2} and varying levels of H_2O, for a surface albedo corresponding to new snow and SZA=0°. The line corresponding to the H_2O level calculated in the Rugheimer et al. (2015) model is presented as a solid, thicker line.

H_2O is a robust UV absorber, with strong absorption for $\lambda_0 < 198$ nm. $N_{H_2O} = 9.96 \times 10^{21}$ cm^{-2} (0.1× the Rugheimer et al. (2015) level) is enough to block fluence for $\lambda_0 < 198$ nm; for comparison, $N_{CO_2} = 2.09 \times 10^{24}$ cm^{-2}, the fiducial Rugheimer et al. (2015) level, blocks fluence for $\lambda_0 < 201$ nm. Even in the absence of

attenuation from CO_2, attenuation from plausible levels of H_2O blocks deep UV flux with $\lambda < 198$ nm. Hence, no matter what the level of CO_2, fluence shortward of 198 nm would have been inaccessible to prebiotic chemistry, assuming warm enough surface temperatures to sustain $N_{H_2O} = 9.96 \times 10^{21}$ cm^{-2} of atmospheric water vapor.

Figure 3.13 presents the dose rates $D_i(N_{H_2O})/D_i(N_{CO_2} = 2.09 \times 10^{24}\mathtt{cm}^{-2})$, i.e. the biologically effective dose rates for UMP-193, -230, and -254, and CuCN3-254 and -300 as a function of N_{H_2O}[15] normalized by the corresponding dose rates calculated for an CO_2-N_2 atmosphere with 0.1 bar of CO_2. With this normalization, a value of $D_i/D_i(N_{CO_2} = 2.09 \times 10^{24}\mathtt{cm}^{-2}) > 1$ means that the given photoreaction is proceeding at a higher rate than for an atmosphere with $N_{CO_2} = 2.09 \times 10^{24}\mathtt{cm}^{-2}$. Across the range of N_{H_2O} considered here, the dose rates are similar (within a factor of 1.7) of the dose rates in the $N_{CO_2} = 2.09 \times 10^{24}\mathtt{cm}^{-2}$ case. We therefore argue that the constraints on UV imposed by H_2O are similar to those imposed by $N_{CO_2} = 2.09 \times 10^{24}\mathtt{cm}^{-2}$. Prebiotic chemistry studies derived assuming a surface radiance environment primarily shaped by $N_{CO_2} = 2.09 \times 10^{24}\mathtt{cm}^{-2}$ should be robust to the level of water vapor in the atmosphere.

[15]assuming an H_2O-N_2 atmosphere

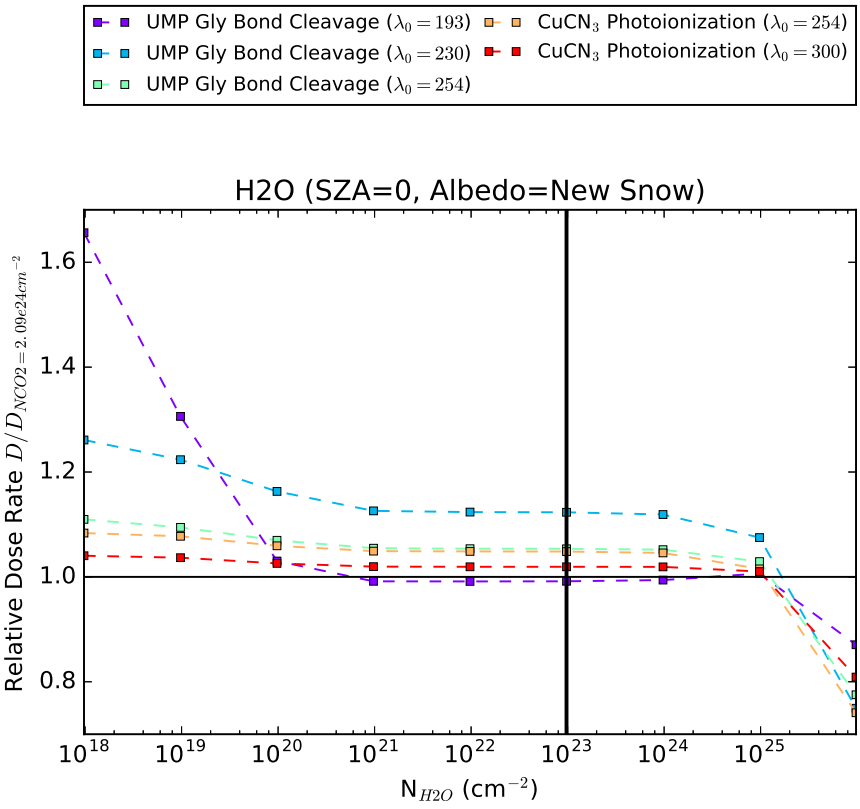

Figure 3.13: Biologically effective dose rates for UMP-X and CuCN3-Y as a function of N_{H_2O}, normalized to the dose rates at $N_{CO2} = 2.09 \times 10^{24}$ cm^{-2}. The solid line corresponds to the H_2O level of Rugheimer et al. (2015).

3.5.7 SO_2

SO_2 absorbs more strongly and over a much wider range than CO_2 (Figure 3.26). However, SO_2 is vulnerable to loss processes such as photolysis and reaction with oxidants (Kaltenegger & Sasselov 2010); consequently, SO_2 levels are usually calculated

to be very low on the primitive Earth. Assuming levels of volcanic outgassing at 3.9 Ga comparable to the present day, as did Rugheimer et al. (2015), SO_2 levels are low, with $N_{SO_2} = 7.05 \times 10^{14}$ cm^{-2} in the calculation of Rugheimer et al. (2015). At these levels, SO_2 does not significantly modify the surface UV environment (Figure 3.14).

However, relatively little is known about primordial volcanism. During epochs of high enough volcanism on the younger, more geologically active Earth, volcanic reductants might conceivably deplete the oxidant supply. While an extreme scenario, if it occurred, SO_2 might plausibly build up to the 1-100 ppm level (Kaltenegger & Sasselov 2010), at which point it might begin to supplant CO_2 as the controlling agent for the global thermostat [16] (c.f. the model of Halevy et al. 2007 for primitive Mars). Assuming a background atmosphere of 0.9 bar N_2 and 0.1 bar CO_2, this corresponds to column densities of $N_{SO_2} = 2.09 \times 10^{19} - 10^{21}$ cm^{-2}. We therefore explore a range of SO_2 values corresponding to $1 - 10^7\times$ the Rugheimer et al. (2015) value, encompassing this range. Figure 3.14 shows the resultant spectra. We considered lower SO_2 levels as well, but the resultant spectra were indistinguishable from the $1\times$ case and so are not shown.

[16]The outgassing-weathering-subduction feedback loop theorized to regulate planetary temperature.

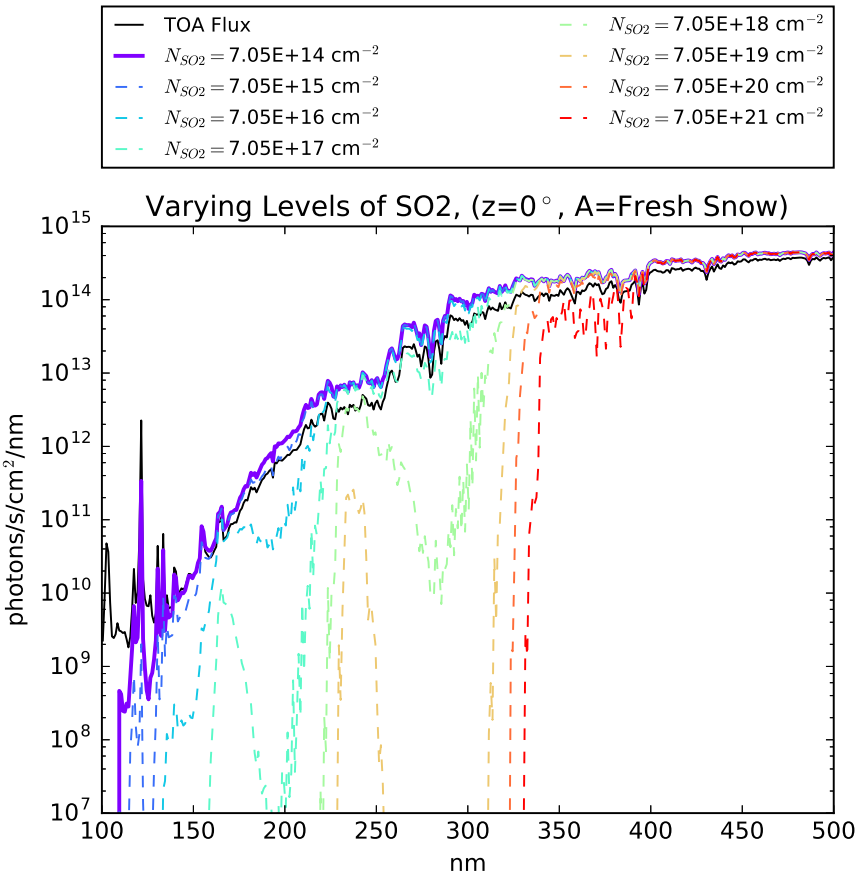

Figure 3.14: Surface radiances for an atmosphere with $N_{N_2} = 1.88 \times 10^{25}$ cm^{-2} and varying levels of SO_2, for a surface albedo corresponding to new snow and SZA=0°. The line corresponding to the SO_2 level calculated in the Rugheimer et al. (2015) model is presented as a solid, thicker line.

Such high SO_2 levels would be transient, and would subside with volcanism. But while they persisted, SO_2 could dramatically modify the surface UV environment. At $N_{SO_2} = 7.05 \times 10^{17}$ cm^{-2}, SO_2 starts to sharply reduce fluence at wavelengths $\lambda \lesssim 200$ nm. For $N_{SO_2} \geq 7.05 \times 10^{20}$ cm^{-2} ($\sim$ 36 ppm in the Rugheimer et al. 2015 model), all

fluence shortward of $\sim$ 327 nm is shielded out. Such levels of SO_2 would correspond to very low-UV epochs in Earth's history.

We quantify the impact of high SO_2 levels on UV-sensitive prebiotic chemistry by again convolving our surface radiance spectra for an SO_2-N_2 atmosphere against our action spectra and computing the BEDs as functions of N_{SO_2}. Figure 3.15 presents these values, normalized by the corresponding dose rates for the $N_{CO_2} = 2.09 \times 10^{24}\mathtt{cm}^{-2}$ case. As expected, higher levels of SO_2 reduce the BEDs. For $N_{SO_2} = 7.05 \times 10^{21}$ cm^{-2}, the BEDs are suppressed by over 60 orders of magnitude, implying the corresponding photoreactions would have been quenched. UV-dependent prebiotic chemistry could not function in such high-SO_2 epochs.

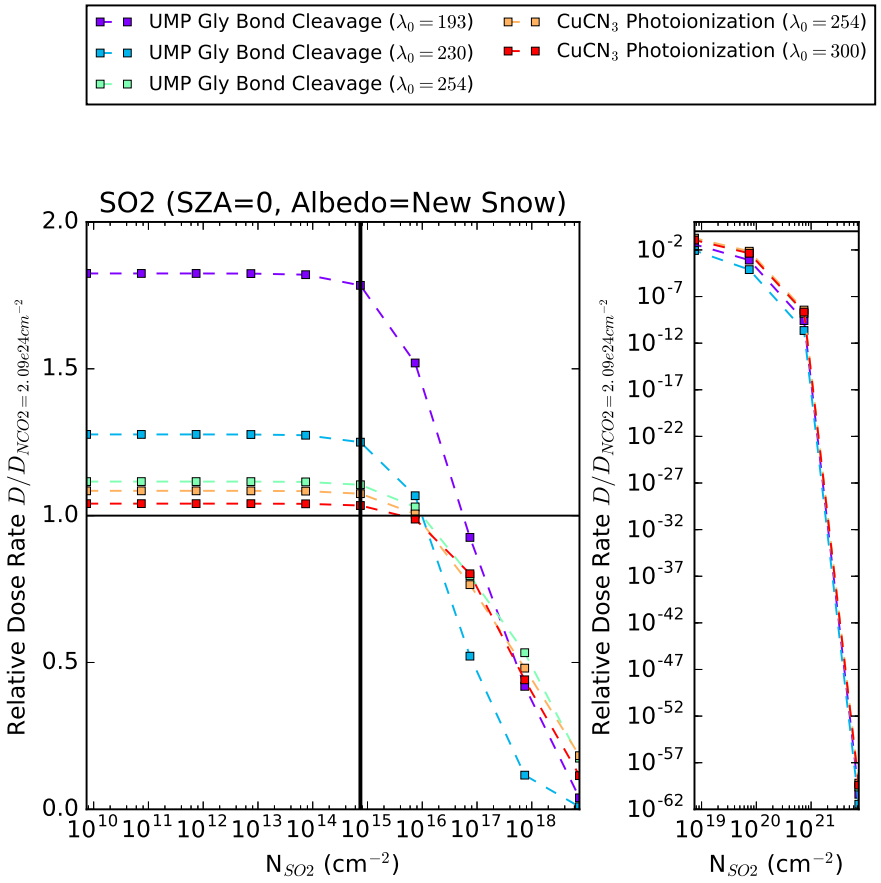

Figure 3.15: Biologically effective dose rates for UMP-X and CuCN3-Y as a function of N_{SO_2}, normalized to the dose rates at $N_{CO_2} = 2.09 \times 10^{24}$ cm^{-2}. The solid line corresponds to the SO_2 level of Rugheimer et al. (2015)

These BEDs do not fall off at the same rates. Figure 3.16 plots the ratio between UMP-X and CuCN3-Y, for all X and Y, as a function of N_{SO_2}. For $N_{SO_2} \geq 7.05 \times 10^{18}$ cm^{-2}, for all values of λ_0 the CuCN3 photoionization BEDs decrease at lower rates than the UMP glycosidic bond cleavage BEDs. For $N_{SO_2} \geq 7.05 \times 10^{19}$ cm^{-2}, the UMP-230 BED is suppressed two orders of magnitude more than the CuCN3-X BEDs, relative to

$N_{SO_2} \leq 7.05 \times 10^{15}$ cm^{-2}. Since the UMP-X BEDs measure a stressor for abiogenesis while CuCN3-X BEDs measure an eustressor for abiogenesis, one might argue that high-SO_2 environments present more clement environments for abiogenesis compared to low-SO_2 ones. However, these results are sensitive to the details of the action spectrum and photoprocess chosen. This is especially challenging given the paucity of data on the QY curves for these processes and the assumptions therefore required to construct them. Further, we have considered here only one stressor and eustressor photoprocess, whereas in reality there should have been many more photoprocesses. We therefore conclude that as measured solely by UMP-photolysis and cyanocuprate photoionization, high SO_2 epochs might have been more clement environments for abiogenesis, but further laboratory constraints on the action spectra of these processes are required to reduce the sensitivity of this statement to assumptions.

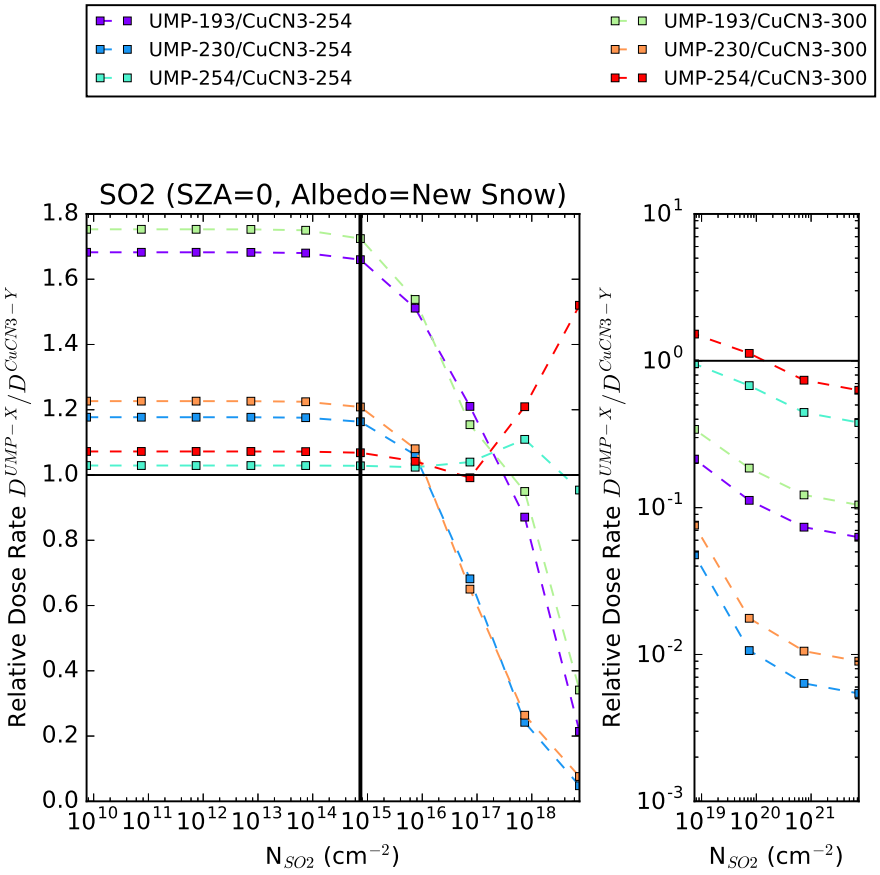

Figure 3.16: Ratio of biologically effective dose rates UMP-X/CuCN3-Y, for X=193, 230 and 254 nm and Y=254 and 300 nm, as a function of N_{SO_2}.

3.5.8 H_2S

H_2S shares similar properties to SO_2. Like SO_2, H_2S is a stronger and broader absorber in the UV than CO_2. Like SO_2, H_2S is primarily generated through outgassing from volcanic sources, and is lost from the atmosphere due to vulnerability to photolysis and reactions with oxidants. Consequently, H_2S is is not expected to have been a major

constituent of the prebiotic atmosphere.

Rugheimer et al. (2015) do not calculate an abundance for H_2S in their model. We estimate an upper bound on $N_{H_2S} \leq 2 \times N_{SO_2}$ by assuming that $[H_2S]/[SO_2]$ traces their relative outgassing ratios, which vary from 0.1-2 in the modern day (Halmer et al. 2002). The redox state of the terrestrial mantle has likely not changed since 3.9 Ga (Delano 2001; Trail et al. 2011), suggesting the proportion of outgassed gases from volcanogenic sources should not have changed either. Based on this reasoning, we assign an upper bound to N_{H_2S} in an atmosphere corresponding to the Rugheimer et al. (2015) model of 1.41×10^{15} cm^{-2}, corresponding to $2 \times N_{SO_2}$. We explore a range of H_2S values corresponding to $1 - 10^7\times$ this value, corresponding to the range of SO_2 values we explore. Figure 3.17 shows the resultant spectra. We considered lower SO_2 levels as well, but the resultant spectra were indistinguishable from the $1\times$ case and so are not shown.

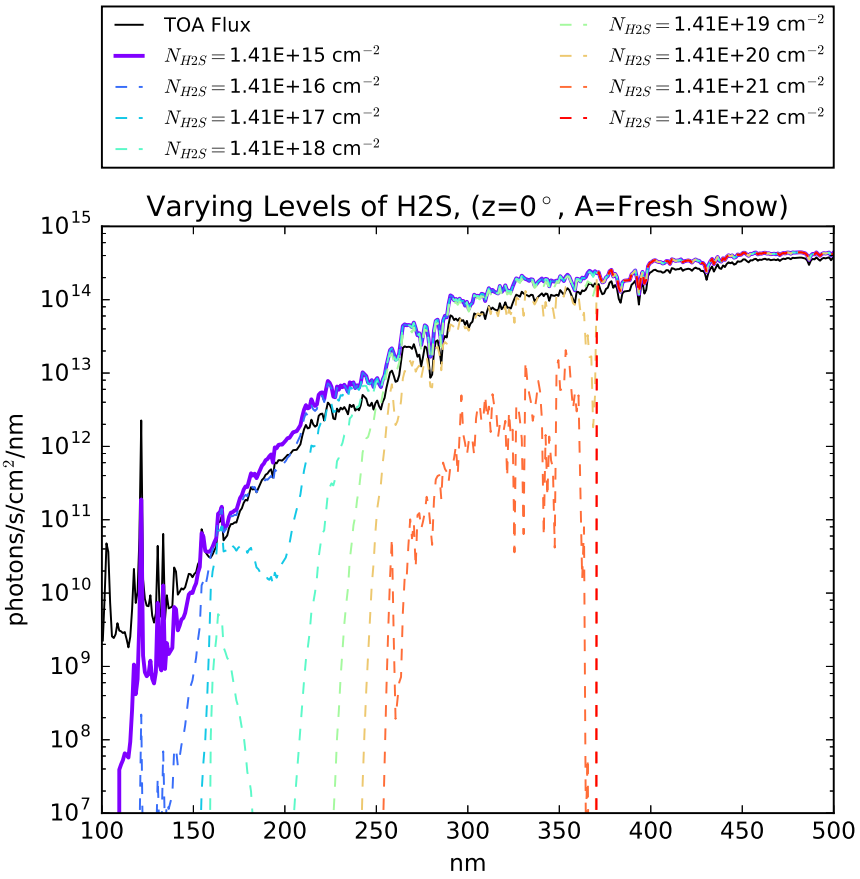

Figure 3.17: Surface radiances for an atmosphere with $N_{N_2} = 1.88 \times 10^{25}$ cm^{-2} and varying levels of H_2S, for a surface albedo corresponding to new snow and SZA=0°. The line corresponding to the 2×SO_2 level calculated in the Rugheimer et al. (2015) model is presented as a solid, thicker line.

For $N_{H_2S} = 1.41 \times 10^{15}$ cm^{-2}, H_2S has minimal impact on the surface UV environment. However, as with SO_2, epochs of high volcanism, possible on a younger Earth, might have depleted the oxidant supply, permitting the buildup of H_2 to higher levels. In this case, H_2S could have affected the surface UV environment. For

$N_{H_2S} \geq 1.41 \times 10^{19}$ cm^{-2}, H_2 suppresses the fluence at wavelengths shorter than 235 nm. For $N_{H_2S} \geq 1.41 \times 10^{22}$ cm^{-2}, fluence shortward of 369 nm is shielded out. This reduction in fluence results in the expected decrease in BED with N_{H_2S}, as shown in Figure 3.18. For $N_{H_2S} = 1.41 \times 10^{22}$ cm^{-2}, all dose rates are suppressed by $\gtrsim$11 orders of magnitude relative to the dose rates at $N_{H_2S} = 1.41 \times 10^{15}$ cm^{-2}. As with SO_2, high H_2S epochs in Earth's history would be low-UV epochs, and UV-sensitive prebiotic pathways might find themselves photon-starved.

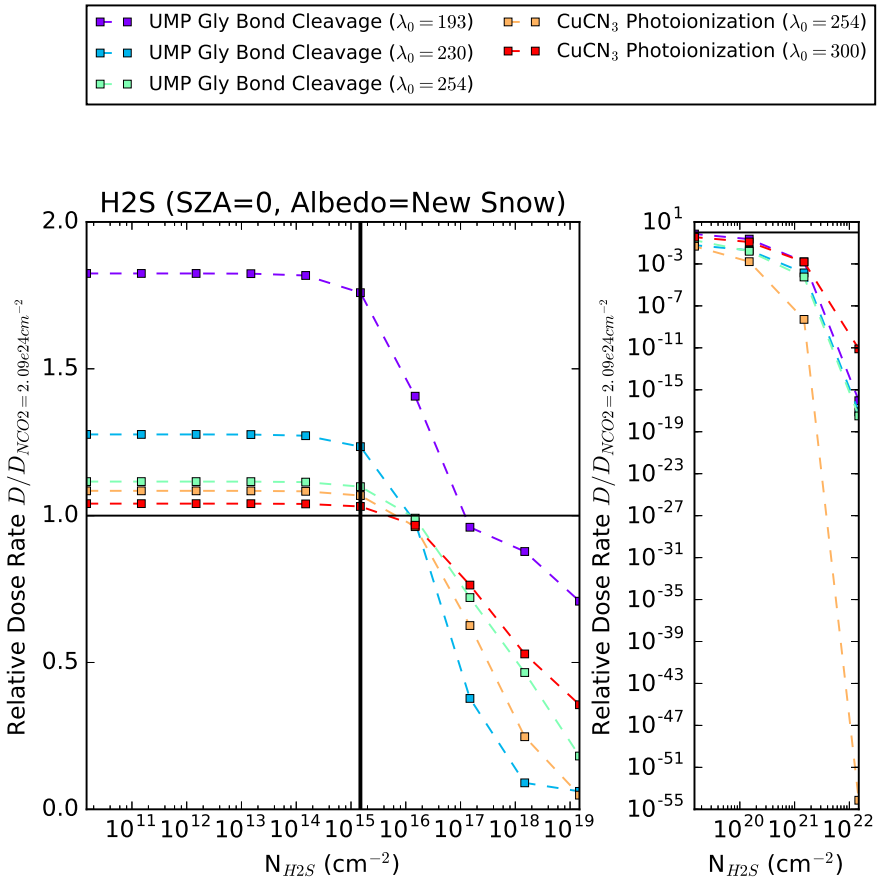

Figure 3.18: Biologically effective dose rates for UMP-X and CuCN3-Y as a function of N_{H_2S}, normalized to the dose rates at $N_{CO_2} = 2.09 \times 10^{24}$ cm^{-2}. The solid line corresponds to 2× the SO_2 level of Rugheimer et al. (2015).

Similarly as with SO_2, the various BED fall off at different rates with increasing N_{H_2S}. Figure 3.19 plots the ratio between UMP-X and CuCN3-Y, for all X and Y. The CuCN3-254 dose rate falls off faster than the other dose rates and the CuCN3-300 dose rate falls off slower. This is because H_2S absorbs much more strongly at $\lambda < 254$ nm than for $\lambda > 254$ nm. As presently defined, the CuCN3-254 dose rate can only utilize $\lambda < 254$

nm radiation, the UMP-X dose rates can make use of $\lambda > 254$ nm fluence but at a much lower efficiency, and the CuCN3-300 dose rate can fully utilize the $\lambda > 254$ nm radiation. Hence, $D_{UMP-X}/D_{CuCN3-254}$ increases with N_{H_2S} for all X, while $D_{UMP-X}/D_{CuCN3-300}$ decreases. Depending on the value of the CuCN3 photoionization step function, high H_2S environments may have been much more or much less clement environments for abiogenesis, as measured by the balance between glyocosidic bond cleave in UMP and aquated electron production from CuCN3 photoionization. We conclude that it is critical to further constrain empirically the action spectra of these photoprocesses in order to robustly use them to estimate the favorability of high-versus-low H_2S environments for abiogenesis.

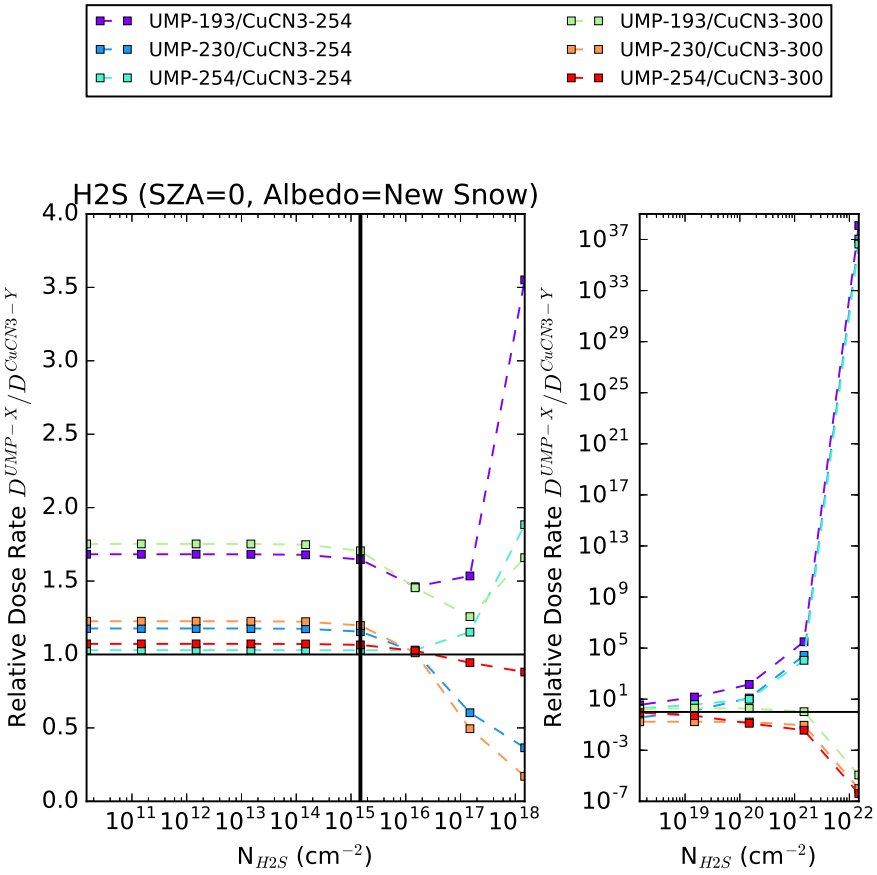

Figure 3.19: Ratio of biologically effective dose rates UMP-X/CuCN3-Y, for X=193, 230 and 254 nm and Y=254 and 300 nm, as a function of N_{H_2S}

3.5.9 O_2

O_2 is a robust UV shield. In the aphotosynthetic prebiotic era, O_2 is thought to have been generated from photolysis of CO_2 and H_2O, with sinks from reactions with reductants. Measurements of sulfur mass-independent isotope fractionation (SMIF) imply O_2 concentrations $< 1 \times 10^{-5}$ PAL prior to 2.3 Ga (Pavlov & Kasting 2002),

and Fe and U-Th-Pb isotopic measurements from a 3.46 Ga chert is consistent with an anoxic ocean during that era (Li et al. 2013). Rugheimer et al. (2015) calculate an O_2 abundance corresponding to $N_{O_2} = 5.66 \times 10^{19}$ cm^{-2}, consistent with the Pavlov & Kasting (2002) limit. We explore a range of O_2 columns corresponding to $10^{-5} - 10^{5}\times$ the Rugheimer et al. (2015) column. We note the O_2 columns exceeding the Rugheimer et al. (2015) column are disfavored by the SMIF modeling of Pavlov & Kasting (2002), and should therefore be taken as strictly illustrative. Figure 3.20 shows the resultant spectra.

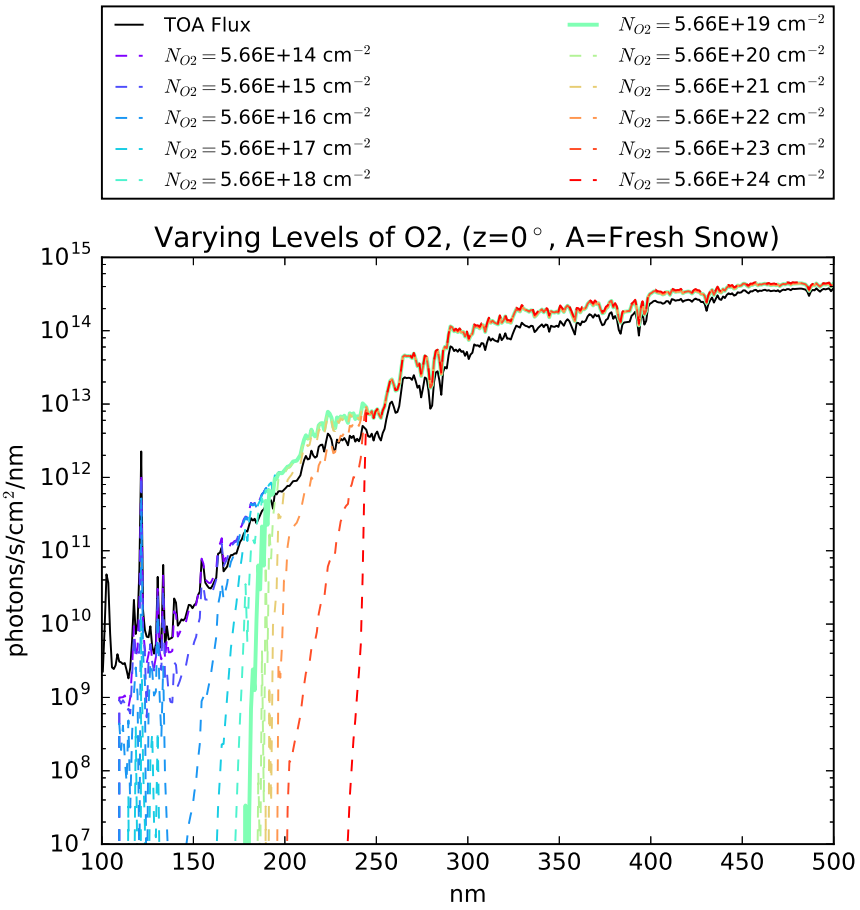

Figure 3.20: Surface radiances for an atmosphere with $N_{N_2} = 1.88 \times 10^{25}$ cm^{-2} and varying levels of O_2, for a surface albedo corresponding to new snow and SZA=0°. The line corresponding to the O_2 level calculated in the Rugheimer et al. (2015) model is presented as a solid, thicker line.

At the Rugheimer et al. (2015) level of $N_{O_2} = 5.66 \times 10^{19}$ cm^{-2}, O_2 blocks fluence at $\lambda < 183$ nm. $N_{CO_2} = 2.09 \times 10^{21}$ cm^{-2} is required to achieve a similar cutoff; $N_{CO_2} \geq 1.87 \times 10^{22}$ is expected based on the climate models we have found so far. Therefore, at the O_2 levels expected from photochemical models, O_2 does not further

constrain the surface UV environment assuming a climatically plausible CO_2 inventory. But, O_2 is a substantially stronger UV absorber than CO_2, and it is possible that in comparatively low-CO_2/high-O_2 scenarios, it could affect the surface UV environment. $N_{O_2} = 5.66 \times 10^{21}$ cm^{-2} of O_2 cuts off more fluence than $N_{CO_2} = 1.87 \times 10^{22}$ (the minimum proposed from climate models). Hence, at O_2 levels of $N_{O_2} \geq 5.66 \times 10^{21}$ cm^{-2}, O_2 may begin to have noticeable impact on the surface UV environment. However, it is unlikely that such high O_2 inventories were achieved at 3.9 Ga, given the strong reductant sink from vulcanogenic gases, the lack of a strong O_2 source, and the empirical constraint from SMIF. It is most likely that attenuation from O_2 would have been negligible compared to that from CO_2.

3.5.10 O_3

Similarly to O_2, O_3 is a well-known strong UV shield. It is generated from 3-body reactions involving photolysis of O_2 and hence its abundance is sensitive to O_2 levels, with sinks from photolysis and reactions with reducing gases. Rugheimer et al. (2015) estimate an O_3 column density of $N_{O_3} = 1.92 \times 10^{15}$ cm^{-2} for the 3.9 Ga Earth. At this level, O_3 does not significantly modify the surface UV environment. Figure 3.21 shows the surface radiance spectra for $N_{O_3} = 1.92 \times 10^{15} - 10^{18}$ cm^{-2}[17]. As the atmospheric O_3 inventory increases, so does its attenuation of UV fluence; at levels roughly comparable to the modern day ($N_{O_3} = 1.92 \times 10^{18}$ cm^{-2}), it suppresses the BEDs of the photoprocesses we consider by 2 orders of magnitude relative to $N_{CO_2} = 2.09 \times 10^{24}$ cm^{-2}. However,

[17]We considered lower O_3 levels as well, but the resultant spectra were indistinguishable from the $N_{O_3} = 1.92 \times 10^{15}$ cm^{-2} case

such O_3 levels would require a very high O_2 inventory. It is most likely that attenuation from O_3 would have been negligible compared to that from CO_2 and/or H_2O.

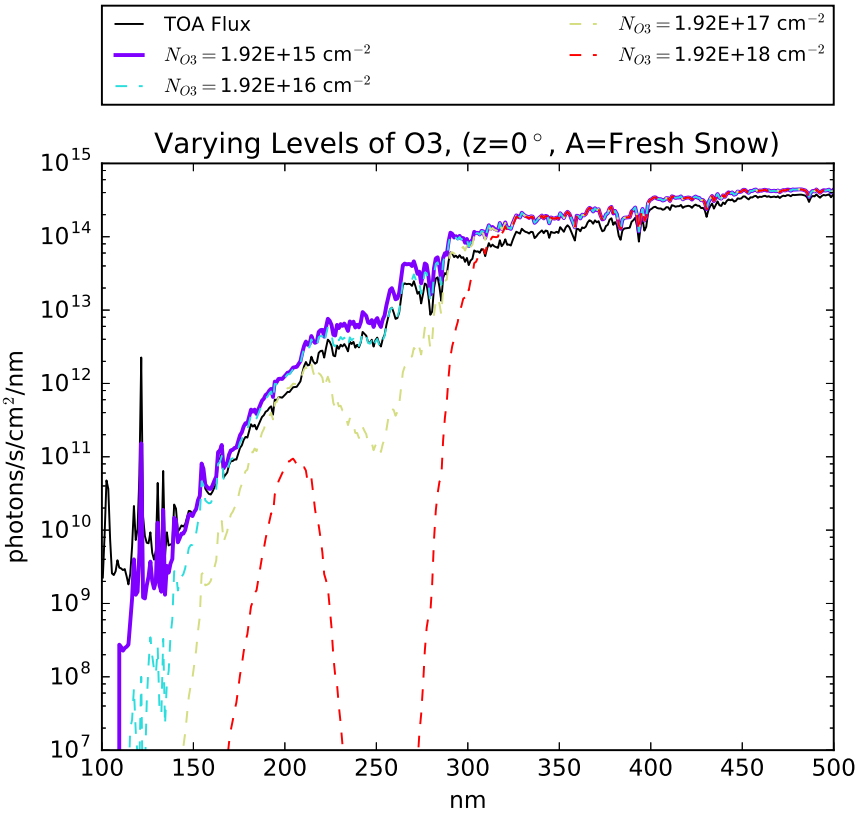

Figure 3.21: Surface radiances for an atmosphere with $N_{N_2} = 1.88 \times 10^{25}$ cm^{-2} and varying levels of O_3, for a surface albedo corresponding to new snow and SZA=0°. The line corresponding to the O_3 level calculated in the Rugheimer et al. (2015) model is presented as a solid, thicker line.

3.6 Conclusions

We have used a two-stream radiative transfer model to calculate the hemisphere-integrated surface radiance at UV wavelengths for different surface albedos, solar zenith angles, and atmospheric compositions for the 3.9 Ga Earth. To estimate the effect of these different variables on UV-sensitive prebiotic chemistry, we have convolved the surface radiance spectra with action spectra for glycosidic bond cleavage in UMP (a stressor for abiogenesis) and production of solvated electrons from photoionization of $CuCN_3^{2-}$ (an eustressor for abiogenesis) formed from absorption spectra and assumed QY curves, and integrated the result over wavelength to compute the biologically effective dose rate (BED).

Our findings demonstrate the importance of considering albedo and zenith angle in calculations of surface UV fluence. For the model atmosphere calculated by Rugheimer et al. (2015) for the 3.9 Ga Earth, variations in albedo (tundra vs new snow) can affect BEDs by a factor of 2.7-4.3, and variations in zenith angle ($0 - 66.5°$, corresponding to the range of minimum SZA available on Earth) can affect BEDs by a factor of 3.7-4.3, depending on the photoprocess and the assumptions we make about its quantum yield curve. Taken together, albedo and zenith angle can affect BEDs by a factor of 10.4-17.1, meaning that local conditions like latitude and surface type can drive variations in prebiotic photoreaction rate by an order of magnitude or more, independent of atmospheric composition.

While CO_2 levels on the 3.9 Ga Earth are debated, even minute amounts of CO_2 ($N_{CO_2} \geq 2.09 \times 10^{19}$ cm^{-2}) are enough to extinguish fluence shortward of 167 nm. Since $N_{CO_2} \geq 1.87 \times 10^{22}$ cm^{-2} based on proposed climate models in the literature, CO_2

extinction should have shielded prebiotic molecules from solar activity even if removed from the shortwave UV shield of liquid water (e.g. through drying cycles).

The BEDs vary by less than an order of magnitude as a function of CO_2 level for $N_{CO_2} \leq 9.76 \times 10^{25}$ cm^{-2} (the limit on CO_2 for conventional climate calculations), and less than two orders of magnitude for $N_{CO_2} \leq 9.82 \times 10^{26}$ cm^{-2} (the limit on CO_2 from the crustal carbon inventory). This implies prebiotic photoreaction rates are insensitive to CO_2 levels, assuming no other absorbers to be present.

For climatically reasonable levels of CO_2 ($N_{CO_2} \geq 1.87 \times 10^{22}$ cm^{-2}), plausible levels of CH_4, O_2, and O_3 do not significantly modify the UV surface fluence. CH_4 is a weak absorber. O_2 levels high enough to modify the surface UV fluence are ruled out by SMIF measurements, which means that O_3 is expected to be similarly low.

SO_2 and H_2S also do not impact the UV surface fluence at concentrations derived assuming modern levels of volcanism. However, it has been hypothesized that SO_2 and H_2S could have built up to higher (1-100 ppm in a 1-bar atmosphere) levels during epochs of high sustained volcanism. If this scenario occurred, such epochs were low-UV eras in Earth's history. At SO_2 levels of $N_{SO_2} \geq 7.05 \times 10^{19}$ cm^{-2} and H_2S levels of $N_{H_2S} = 1.41 \times 10^{21}$ cm^{-2}, corresponding to mixing ratios of 3 and 70 ppm respectively in a 1-bar N_2/CO_2 atmosphere, the photoreactions considered in our study are suppressed by multiple orders of magnitude relative to $N_{CO_2} = 2.09 \times 10^{24}$ cm^{-2}. If considering high SO_2/H_2S atmospheres, it is important to characterize the dependence of hypothesized prebiotic pathways on fluence levels to ensure they will not be quenched. It is possible that high-SO_2/H_2S atmospheres might be more clement environments for abiogenesis as measured by the change in tricyanocuprate photoionization rates compared to UMP

glycosidic bond cleavage as a function of SO_2/H_2S level, but further measurements of the action spectra of these photoprocesses are required to assess this possibility.

At the lowest CO_2 level proposed in the literature from climate constraints ($N_{CO_2} = 1.87 \times 10^{22}$ cm^{-2}) atmospheric CO_2 admits light to the surface at wavelengths as short as 190 nm. This raises the question whether sources like ArF eximer lasers (primary emission 193 nm) might be viable for the study of prebiotic chemistry. However, it transpires that H_2O vapor is a strong UV shield; at levels as low as $N_{H_2O} = 9.96 \times 10^{21}$ cm^{-2} (10% of that computed by Rugheimer et al. (2015)), it blocks fluence shortward of 198 nm. Therefore, such shortwave sources remain unsuitable for prebiotic chemistry studies, unless assuming exceptionally cold, dry environments (e.g. polar deserts, snowball Earths) with no other major UV absorbers in the atmosphere.

Conversely, water vapor does not absorb at 254 nm, and for $N_{CO_2} \lesssim 9.76 \times 10^{25}$ cm^{-2}, fluence at 254 nm remains available. Therefore, photochemical mechanisms isolated by laboratory studies using mercury lamps should have been extant on the prebiotic Earth across a wide range of CO_2 and H_2O abundances, though characterizing the wavelength dependence of these processes remains key to understanding whether they could function on the early Earth as well as they do in the lab.

In summary, variations in surface albedo and solar zenith angle can, taken together, affect prebiotically relevant photochemical reaction rates by an order of magnitude or more. Surficial prebiotic photochemistry is insensitive to the precise levels of CO_2, H_2O, O_2, O_3, and CH_4, across the levels of these gases permitted by available constraints. However, it is sensitive to the inventories of SO_2 and H_2S, if these gases are able to build up to the ppm levels (e.g. during epochs of enhanced volcanism). Surface fluence

shortward of 198 nm is available only for a very narrow range of parameter space. However, fluence at 254 nm is available across most of parameter space, meaning that mercury lamps are good candidates for initial studies of prebiotic chemistry (though with the caveat that their use might miss wavelength-dependent effects).

Acknowledgements

We thank Sarah Rugheimer for providing model metadata for testing, for insightful discussion, and for comments on this article. We thank C. Magnani and Z. Todd for helpful comments and discussion. We thank R. Ramirez, E. Schwieterman, R. Wordsworth, T. Laakso, A. Segura, F. Violotev, J. Szostak, A. Gonzalo, R. Kelley, R. Spurr, I. Cnossen, and L. Zhu for sharing their insights and knowledge with us in discussions. We thank two anonymous referees for comments which greatly improved this article.

This research has made use of NASA's Astrophysics Data System Bibliographic Services, and the MPI-Mainz UV-VIS Spectral Atlas of Gaseous Molecules.

S. R. and D. D. S. gratefully acknowledge support from the Simons Foundation, grant no. 290360.

3.7 Appendix A: Extinction And Rayleigh Scattering Cross-Sections

This Appendix specifies the sources of the total extinction and Rayleigh scattering cross-sections for the gases used in the surface UV environment model. Total extinction cross-sections were taken from literature measurements, while Rayleigh scattering cross-sections were computed from theoretical formalisms. Unless otherwise stated, all measurements were collected near room temperature ($\sim$ 295 K) and 1 bar of atmospheric pressure, and the digitized data files of the empirical measurements were taken from the MPI-Mainz UV/Vis Spectral Atlas. As discussed in Section 3.3, when the Rayleigh scattering cross-sections exceeded the total measured cross-section from a literature source, the total cross-section was set equal to the Rayleigh scattering value, and the absorption cross-section was set equal to zero. When integrating the cross-sections over a wavelength bin, we linearly interpolated within a given dataset when computing the integral.

3.7.1 N_2

We compute the Rayleigh scattering cross-section of N_2 using the formalism of Vardavas & Carver (1984): $\sigma = 4.577 \times 10^{-21} \times KCF \times [A(1 + B/\lambda^2)]/\lambda^4$, where λ is in μ m and KCF is the King correction factor, where $KCF = (6 + 3\delta)/(6 - 7\delta)$, where δ is the depolarization factor. This approach accounts for the wavelength dependence of the index of refraction but assumes a constant depolarization factor. We take the values of the coefficients A and B from Keady & Kilcrease (2000), and the depolarization factor

of $\delta = 0.0305$ from Penndorf (1957).

We take empirically measured N_2 extinction cross-sections shortward of 108 nm from Chan et al. (1993b), who measure the extinction cross-section from 6.2-113 nm ($\leq$ 5 nm resolution). No absorption is detected longward of 108 nm (Huffman 1969; Chan et al. 1993b), hence we take Rayleigh scattering to account for the extinction for $\lambda > 108$ nm. Figure 3.22 presents the total and Rayleigh scattering cross-sections for N_2 from 100-900 nm.

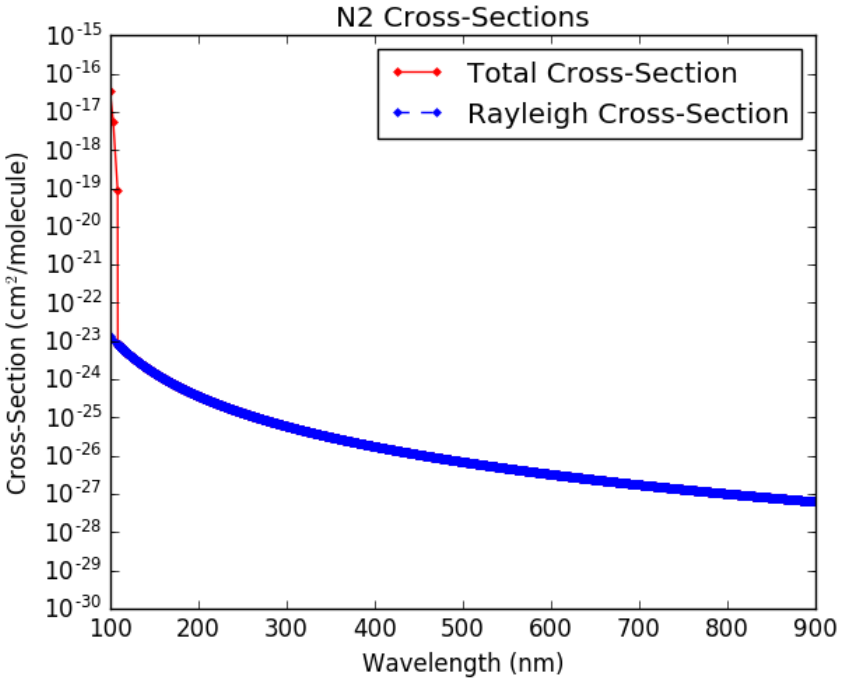

Figure 3.22: Total extinction and Rayleigh scattering cross-sections for N_2.

3.7.2 CO_2

We compute the Rayleigh scattering cross-section of CO_2 using the formalism of Vardavas & Carver (1984): $\sigma = 4.577 \times 10^{-21} \times KCF \times [A(1 + B/\lambda^2)]/\lambda^4$, where λ is in μ m

and KCF is the King correction factor, where $KCF = (6 + 3\delta)/(6 - 7\delta)$, where δ is the depolarization factor. This approach accounts for the wavelength dependence of the index of refraction but assumes a constant depolarization factor. We take the values of the coefficients A and B from Keady & Kilcrease (2000), and the depolarization factor of $\delta = 0.0774$ from Shemansky (1972).

We take empirically measured cross-sections shortward of 201.6 nm from Huestis & Berkowitz (2010). Huestis & Berkowitz (2010) review existing measurements of extinction cross-sections for CO_2, and aggregate the most reliable ones into a single spectrum (< 1 nm resolution). They test their composite spectrum with an electron-sum rule, and find it to agree with the theoretical expectation to 0.33%. From 201.75-300 nm, the measurements of Shemansky (1972) provide coverage. However, the resolution of these data ranges from 0.25 nm from 201.75-203.75 nm, to 12-25 nm from 210-300 nm. Further, Shemansky (1972) finds that essentially all extinction at wavelengths longer than 203.5 nm is due to Rayleigh scattering (Ityaksov et al. 2008 derive similar results) . Therefore, we adopt the measurements of Shemansky (1972) from 201.75-203.75 nm, and take Rayleigh scattering to describe CO_2 extinction at longer wavelengths. Figure 3.23 presents the total and Rayleigh scattering cross-sections for CO_2 from 100-900 nm.

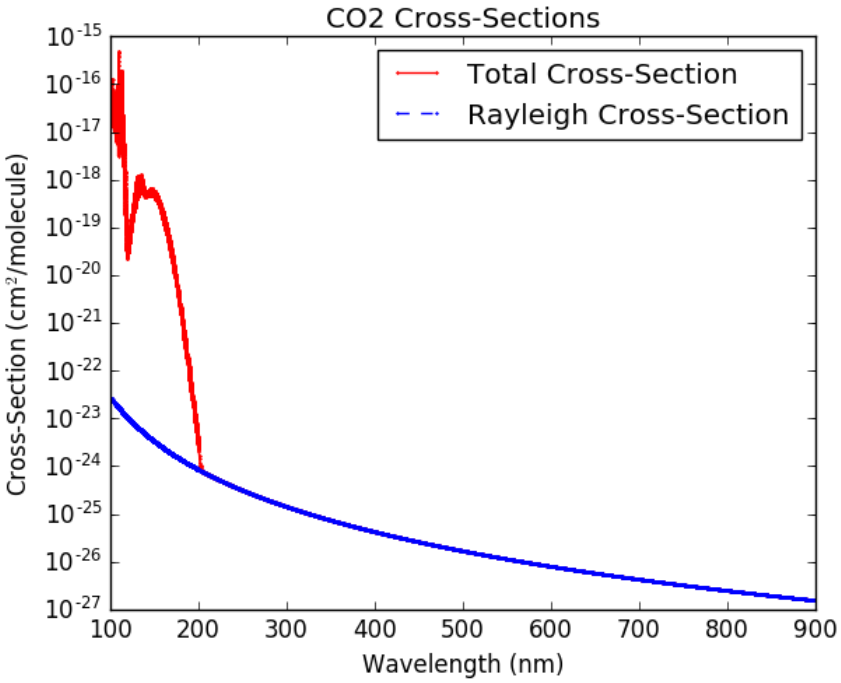

Figure 3.23: Total extinction and Rayleigh scattering cross-sections for CO_2.

3.7.3 H_2O

We compute the Rayleigh scattering cross-section of H_2O following the methodology of von Paris et al. (2010) and Kopparapu (2013). We compute the wavelength-dependent index of refraction of water vapor using the observation by Edlén (1966) that the refractivity of water vapor is 15% less than that of air (itself 1-2% water vapor by volume). We compute the refractivity of standard air from the formulae of Bucholtz (1995). von Paris et al. (2010) and Kopparapu (2013) used a value for the depolarization factor of 0.17, based on the work of Marshall & Smith (1990); however, this value was measured for liquid water. We instead adopt $\delta = 0.000299$ from the work of Murphy (1977). We note that the equations of Bucholtz (1995) have a singularity at 0.15946 μm

(159.46 nm) due to a $39.32957 - 1/\lambda^2$ (λ in μm) term in the denominator, which causes the Rayleigh scattering cross-section to go to infinity at that value. To circumvent this problem, in this term only we adopt $\lambda = 0.140\mu$m for $0.140\mu\text{m} < \lambda < 0.15946\mu$m, and $\lambda = 0.180\mu$m for $0.15946\mu\text{m} < \lambda < 0.180\mu$m. This removes the singularity from the Rayleigh scattering curve (see Figure 3.24).

We take empirically measured cross-sections shortward of 121 nm from the dipole (e,e) spectroscopy measurements of Chan et al. (1993a) ($\leq$ 6 nm resolution). From 121-198 nm, we use the compilation of Sander et al. (2011), who surveyed the measurements of H_2O vapor cross-section data to arrived at a recommended tabulation of cross-sections for planetary science studies ($<$ 1 nm resolution). From 396-755 nm we use the gas-cell absorption results of Coheur et al. (2002) and Fally et al. (2003), as combined by the MPI Atlas (mode of 0.0073 nm resolution). From 775-1081 nm, we use the measurements of Merienne et al. (2003) (mode of 0.0077 nm resolution). At all wavelengths not covered by these datasets, we take the extinction to be due to Rayleigh scattering. Figure 3.24 presents the total and Rayleigh scattering cross-sections for H_2O from 100-900 nm.

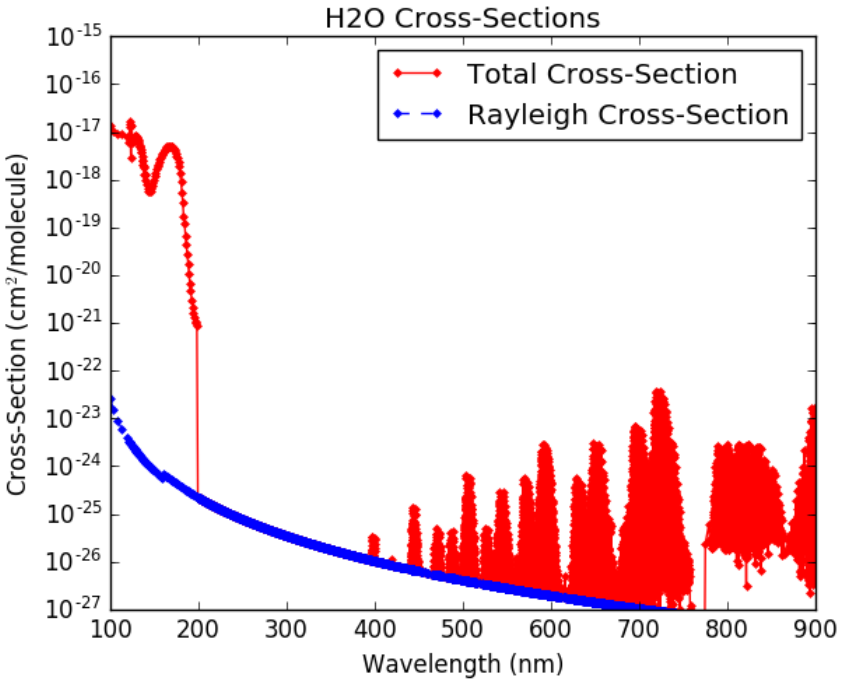

Figure 3.24: Total extinction and Rayleigh scattering cross-sections for H_2O.

3.7.4 CH_4

We compute the Rayleigh scattering cross-section of CH_4 using the formalism of Sneep & Ubachs (2005). This method accounts for the wavelength dependence of the index of refraction, and assumes a constant depolarization factor of 0.0002 which is equal to the depolarization factor of CCl_4, which has a similar structure. Comparing their computations to data, Sneep & Ubachs (2005) find their formalism overestimates the absorption cross-section of CH_4 at 532.5 nm by 15%; therefore, we follow Kopparapu (2013) in scaling down the Sneep & Ubachs (2005) estimate by 15% at all wavelengths.

We take empirically measured cross-sections shortward of 165 nm from the dipole (e,e) spectroscopy measurements of Au et al. (1993) ($<$ 5 nm resolution for $\lambda < 113$

nm, 6-10 nm resolution thereafter). Absorption due to CH_4has not been detected from 165-400 nm (Mount et al. 1977; Chen & Wu 2004). Rayleigh scattering is taken to account for extinction at wavelengths longer than 165 nm. Figure 3.25 presents the total and Rayleigh scattering cross-sections for CH_4 from 100-900 nm.

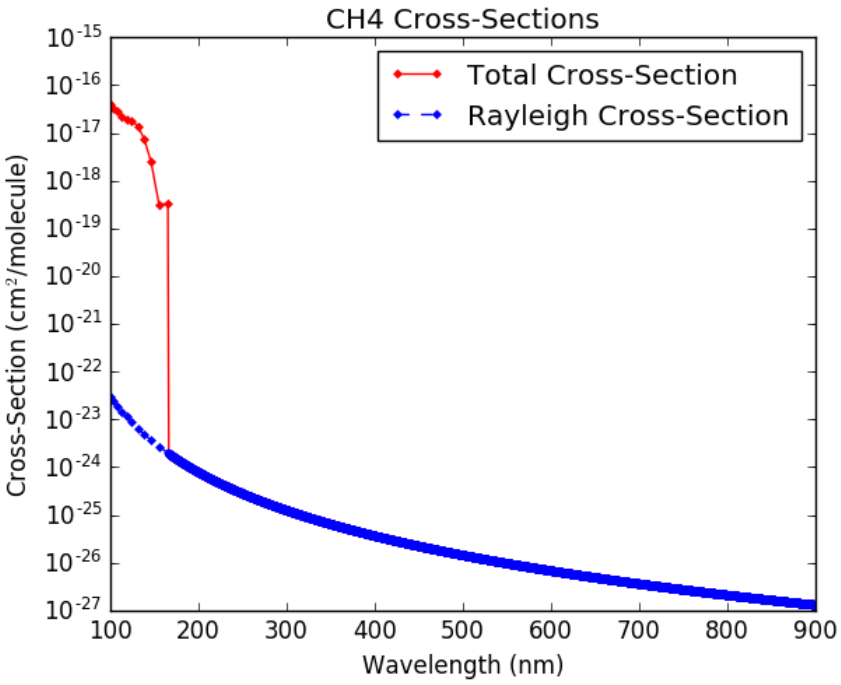

Figure 3.25: Total extinction and Rayleigh scattering cross-sections for CH_4.

3.7.5 SO_2

We compute the Rayleigh scattering cross-section of O_3 using the formalism of Keady & Kilcrease (2000): $\sigma = 1.306 \times 10^{20} \times KCF \times \alpha^2/\lambda^4$, where σ is in cm^2 and λ is in μm, and where KCF refers to the King correction factor, $KCF = (6 + 3.\delta)/(6 - 7\delta)$ (Sneep & Ubachs 2005), and α refers to the polarizability of the molecule and δ is the depolarization factor. Bogaard et al. (1978) list the polarizability α and depolarization

ratio δ for SO_2 at 488, 514.5, and 632.8 nm. We use α_{488nm} and δ_{488nm} for $\lambda < 501.25$ nm, $\alpha_{514.5nm}$ and $\delta_{514.5nm}$ for $501.25 < \lambda < 573.65$ nm, and $\alpha_{632.8nm}$ and $\delta_{632.8nm}$ for 573.65nm$< \lambda$ nm.

We take empirically measured cross-sections of SO_2 shortward of 106.1 nm from the dipole (e,e) spectroscopy measurements of Feng et al. (1999) (< 5 nm resolution). From 106.1-403.7 nm, we take the cross-sections for SO_2 extinction from the compendium of SO_2 cross-sections of Manatt & Lane (1993) (0.1 nm resolution). Manatt & Lane (1993) evaluate extant UV cross-sections for SO_2 extinction, and aggregate the most reliable into a single compendium covering this wavelength range at 293 $\pm$ 10 K. From 403.7-416.7 nm, we take the Fourier transform spectrometer measurements of Vandaele et al. (2009) (< 1 nm resolution). Many of the cross-sections reported in this dataset are negative, corresponding to an increase in flux from traversing an gas-filled cell. These cross-sections are deemed unphysical and removed from our model. Figure 3.26 presents the total and Rayleigh scattering cross-sections for SO_2 from 100-900 nm.

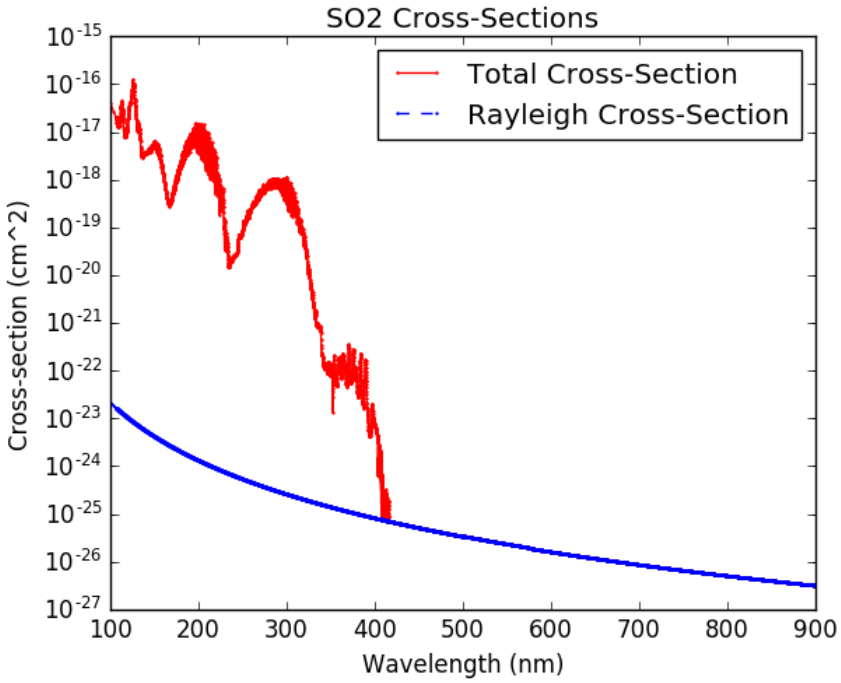

Figure 3.26: Total extinction and Rayleigh scattering cross-sections for SO_2.

3.7.6 H_2S

We compute the Rayleigh scattering cross-section of H_2S using the formalism of Keady & Kilcrease (2000): $\sigma = 1.306 \times 10^{20} \times KCF \times \alpha^2/\lambda^4$, where σ is in cm^2 and λ is in μm, and where KCF refers to the King correction factor, $KCF = (6 + 3.\delta)/(6 - 7\delta)$ (Sneep & Ubachs 2005), and α refers to the polarizability of the molecule and δ is the depolarization factor. Bogaard et al. (1978) list the polarizability α and depolarization ratio δ for H_2S at 488, 514.5, and 632.8 nm. We use α_{488nm} and δ_{488nm} for $\lambda < 501.25$ nm, $\alpha_{514.5nm}$ and $\delta_{514.5nm}$ for $501.25 < \lambda < 573.65$ nm, and $\alpha_{632.8nm}$ and $\delta_{632.8nm}$ for 573.65nm$< \lambda$ nm.

We take empirically measured cross-sections of H_2S shortward of 159.465 nm from

the dipole (e,e) spectroscopy measurements of Feng et al. (1999) (< 10 nm resolution). From 159.465-259.460 nm, we take the cross-sections for H_2S extinction from the gas cell absorption measurements of Wu & Chen (1998) (0.06 nm resolution), as recommended by Sander et al. (2011). From 259.460-370.007 nm, we take the gas cell absorption measurements of Grosch et al. (2015) (0.018 nm resolution). Many of the cross-sections reported in this dataset are negative, corresponding to an increase in flux from traversing an gas-filled cell. These cross-sections are deemed unphysical and removed from our model. Figure 3.27 presents the total and Rayleigh scattering cross-sections for H_2S from 100-900 nm.

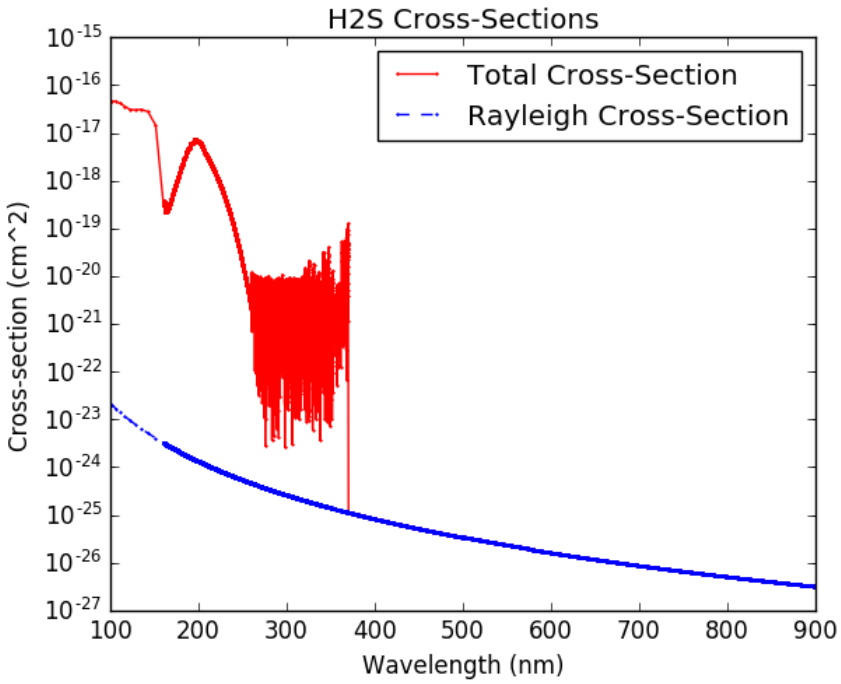

Figure 3.27: Total extinction and Rayleigh scattering cross-sections for H_2S.

3.7.7 O_2

We compute the Rayleigh scattering cross-section of O_2 using the formalism of Vardavas & Carver (1984): $\sigma = 4.577 \times 10^{-21} \times KCF \times [A(1 + B/\lambda^2)]/\lambda^4$, where λ is in μ m and KCF is the King correction factor, where $KCF = (6 + 3\delta)/(6 - 7\delta)$, where δ is the depolarization factor. This approach accounts for the wavelength dependence of the index of refraction but assumes a constant depolarization factor. We take the values of the coefficients A and B from Keady & Kilcrease (2000), and the depolarization factor of $\delta = 0.054$ from Penndorf (1957).

We take extinction cross-sections of O_2 shortward of 108.75 nm from the work of Huffman (1969) ($<$ 12.6 nm resolution). Huffman (1969) reviews previous literature measurements of VUV extinction cross-sections of O_2 and provides recommended values for aeronomic studies. From 108.75-130.0 nm, we use the gas absorption cell measurements for ground-state O_2 of Ogawa & Ogawa (1975) ($<$ 0.2 nm resolution). From 130.04-175.24 nm, we use the absorption cell measurements of Yoshino et al. (2005) ($<$ 0.42 nm resolution). From 179.2-202.6 nm, we use the gas absorption cell measurements of Yoshino et al. (1992) (300 K, 0.01 nm resolution). Duplicate values in this database (presumably due to rounding error) were removed. From 205-245 nm, we use the compilation of Sander et al. (2011), recommended by JPL for use in planetary atmospheres studies ($<$ 1 nm resolution). From 245-294 nm, we use the gas absorption cell extinction cross-sections measured by Fally et al. (2000) ($<$ 0.008 nm resolution.) From 650-799.6, we use the gas-cell absorption measurements of the SCIAMACHY calibration data from Bogumil et al. (2003) ($<$ 0.21 nm resolution,). As in the case of SO_2, several of the cross-sections reported for this dataset are negative;

these cross-sections are rejected as unphysical and removed from the model. Figure 3.28 presents the total and Rayleigh scattering cross-sections for O_2 from 100-900 nm. We note that the cross-sections presented here are for O_2 extinction only. Extinction due to molecular complexes, e.g. the O_2-O_2 complexes observed by Greenblatt et al. (1990), are not included in our parametrization. This does not materially impact the fidelity of our model since the cross-sections associated with these complexes are small at relevant partial pressures of O_2 ($< 3 \times 10^{-26}$ cm^2 for 1 atm of O_2).

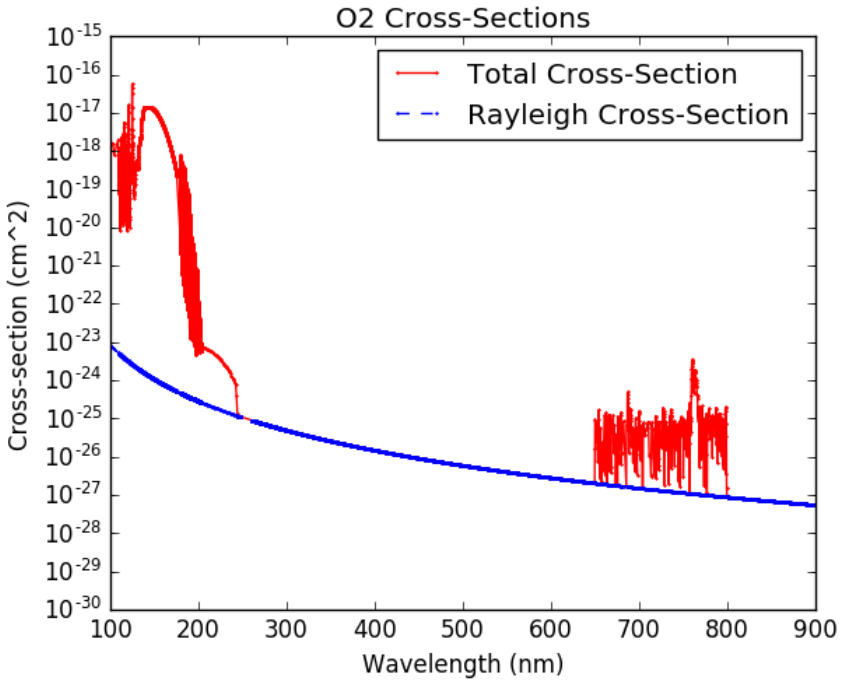

Figure 3.28: Total extinction and Rayleigh scattering cross-sections for O_2.

3.7.8 O_3

We take the Rayleigh scattering cross-section of O_3 using the formalism of Keady & Kilcrease (2000): $\sigma = 1.306 \times 10^{20} \times KCF \times \alpha^2/\lambda^4$, where σ is in cm^2 and λ is in μm,

and where KCF refers to the King correction factor, $KCF = (6 + 3.\delta)/(6 - 7\delta)$ (Sneep & Ubachs 2005), and α refers to the polarizability of the molecule. From Brasseur & De Rudder (1986), $KCF = 1.06$ for ozone. We adopt $\alpha = 3.21 \times 10^{-24}$ cm^3 based on the average electric dipole polarizability listed for ground state O_3 in Miller (2009). This formulation assumes constant polarizability (index of refraction) and depolarization factor.

We take empirically measured cross-sections of O_3 shortward of 110 nm from the gas cell absorption measurements of Ogawa & Cook (1958) ($<$ 9.5 nm resolution). We take cross-sections from 110-172 nm from the gas cell absorption measurements of Mason et al. (1996) ($<$ 2 nm resolution for $\lambda \leq 139.31$, 3-17 nm resolution for $\lambda = 139.31 - 172$ nm). Following the recommendations of Sander et al. (2011), we take cross-sections from 185-213 nm from the gas cell absorption measurements of Molina & Molina (1986) (0.5 nm resolution). Finally, we take the cross-sections for 213-1100 nm from the gas cell absorption measurements recently published in joint papers by Serdyuchenko et al. (2014) and Gorshelev et al. (2014) (0.02-0.06 nm resolution, interpolated to 0.01 nm; 293 K). Gorshelev et al. (2014) compares this dataset to previous measurements and finds good agreement. Figure 3.29 presents the total and Rayleigh scattering cross-sections for O_3 from 100-900 nm.

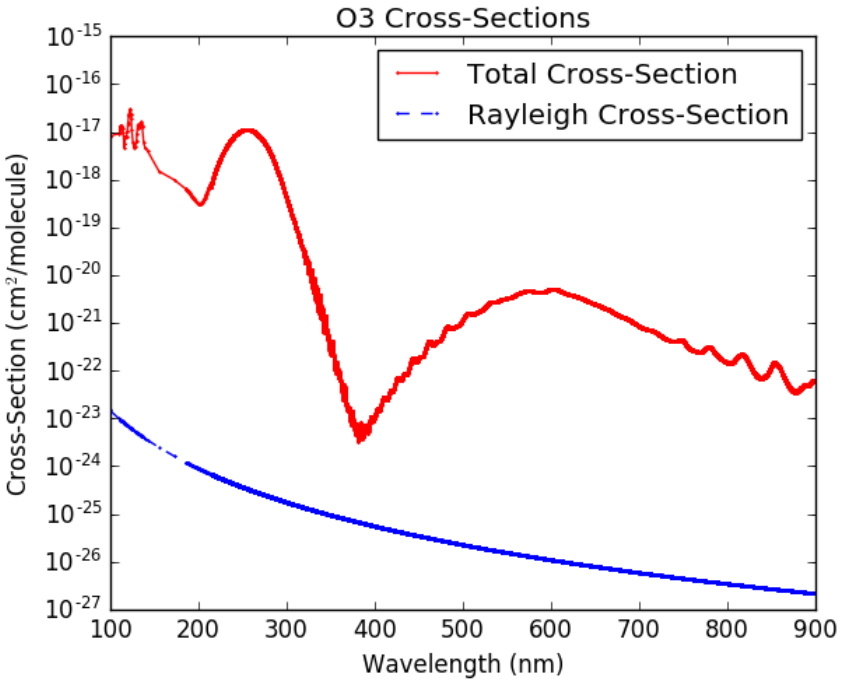

Figure 3.29: Total extinction and Rayleigh scattering cross-sections for O_3.

3.8 Appendix B: Spectral Albedos

This section describes the sources for the direct and diffuse spectral albedos, α_{dir} and α_{dif}, corresponding to different surface environments used in this study. In this section, $\mu = \cos(\theta_0)$ refers to the cosine of the solar zenith angle. For all albedos, we enforce a physical albedo range of 0-1 by setting any negative albedos to 0 and any albedos greater than 1 to 1.

3.8.1 Ocean

We approximate the albedo of pure (ice- and land-free) ocean via the methodology of Briegleb et al. (1986), who in turn rely upon Payne (1972). Briegleb et al. (1986) take $\alpha_{dif} = 0.06$ and $\alpha_{dir} = 2.6/(\mu^{1.7} + 0.065) + 15(\mu - 0.1)(\mu - 0.5)(\mu - 1.0)$.

Payne (1972) measured the reflectance of the ocean surface under a variety of conditions using a spectrometer with uniform sensitivity coverage from 280-2800 nm. Hence, albedos calculated from this work represent a fit to the mean albedo integrated 280-2800 nm, which includes 98% of solar flux. Briegleb et al. (1986) argue that the variation in ocean albedo as a function of wavelength is modest, due to the modesty of variations of the index of refraction of water across this wavelength range. Briegleb et al. (1986) modeled this variation and found the spectral corrections to the oceanic albedo due to the wavelength dependence of the optical properties of water to be +0.02 for 200-500 nm, -0.003 for 500-700 nm, -0.007 for 700-850 nm, and -0.007 for 850 nm-4 μm. They calculated these corrections to have minimal impact on the TOA broadband albedo, and hence ignored them.

However, for our applications (computing the spectra radiance over different surface environments), these corrections can be significant, especially in the case of diffuse radiation, where the shortwave correction is 1/3 of the diffuse albedo. Hence, we include these corrections by adding a correction term α_{corr} to α_{dir} and α_{dif}. Lacking any better assumption, we extend the 200-500 nm value to all wavelengths < 500 nm. Hence $\alpha_{corr} = 0.02$ for $\lambda < 500$ nm, $\alpha_{corr} = -0.003$ for $\lambda = 500 - 700$ nm, and $\alpha_{corr} = -0.007$ for $\lambda > 700$ nm.

3.8.2 Snow

We approximate the albedo of pure snow using the methodology outlined by Briegleb & Ramanathan (1982) and reviewed by Coakley (2003). This methodology treats new-fallen and old snow separately (new-fallen snow is brighter).

From Table 1 of Briegleb & Ramanathan (1982), for new fallen snow:

$$\alpha_{dif}(\lambda = 200 - 500\texttt{nm}) = 0.95$$

$$\alpha_{dif}(\lambda = 500 - 700\texttt{nm})) = 0.95$$

$$\alpha_{dif}(\lambda = 700 - 4000\texttt{nm})) = 0.65$$

Whereas for old snow:

$$\alpha_{dif}(\lambda = 200 - 500\texttt{nm})) = 0.76$$

$$\alpha_{dif}(\lambda = 500 - 700\texttt{nm})) = 0.76$$

$$\alpha_{dif}(\lambda = 700 - 4000\texttt{nm})) = 0.325$$

As before, we extend the 200-500 nm value to all $\lambda < 200$.

To compute the direct albedo, we follow Briegleb & Ramanathan (1982) in using the formalism of Dickinson et al. (1981) to account for zenith angle dependence: $\alpha_{dir} = \alpha_{dif} + (1 - \alpha_{dif}) \times 0.5 \times [3/(1 + 4\mu) - 1)$ for $\mu \leq 0.5$, and $\alpha_{dir} = \alpha_{dif}$ for $\mu > 0.5$.

3.8.3 Desert

We approximate the albedo of desert environments following the methods of Briegleb et al. (1986), as reviewed by Coakley (2003). Following Tables 1 and 2 of Briegleb et al.

(1986),

$$\alpha_{dif}(\lambda < 500\mathtt{nm})) = 0.5 \times 0.28 + 0.5 \times 0.15 = 0.22$$

$$\alpha_{dif}(\lambda = 500 - 700\mathtt{nm})) = 0.5 \times 0.42 + 0.5 \times 0.25 = 0.34$$

$$\alpha_{dif}(\lambda = 700 - 850\mathtt{nm})) = 0.5 \times 0.50 + 0.5 \times 0.35 = 0.43$$

$$\alpha_{dif}(\lambda = 850 - 4000\mathtt{nm})) = 0.5 \times 0.50 + 0.5 \times 0.40 = 0.45$$

Where we have again extended the Briegleb et al. (1986) 200-500 nm albedos to all wavelengths < 200 nm.

To compute the direct albedo, we follow Briegleb et al. (1986) in including zenith angle dependence by writing $\alpha_{dir} = \alpha_{dif} \times (1 + d)/(1 + 2d\mu)$, where d is a parameter derived from a fit to data for different terrain types. For desert, $d = 0.4$.

3.8.4 Tundra

We approximate the albedo of tundra environments following the methods of Briegleb et al. (1986), as reviewed by Coakley (2003).

$$\alpha_{dif}(\lambda < 500\mathtt{nm})) = 0.5 \times 0.04 + 0.5 \times 0.07 = 0.06$$

$$\alpha_{dif}(\lambda = 500 - 700\mathtt{nm})) = 0.5 \times 0.10 + 0.5 \times 0.13 = 0.12$$

$$\alpha_{dif}(\lambda = 700 - 850\mathtt{nm})) = 0.5 \times 0.25 + 0.5 \times 0.19 = 0.22$$

$$\alpha_{dif}(\lambda = 850 - 4000\mathtt{nm})) = 0.5 \times 0.25 + 0.5 \times 0.28 = 0.27$$

Where we have again extended the Briegleb et al. (1986) 200-500 nm albedos to all wavelengths < 200 nm.

To compute the direct albedo, we follow Briegleb et al. (1986) in including zenith angle dependence by writing $\alpha_{dir} = \alpha_{dif} \times (1 + d)/(1 + 2d\mu)$, where d is a parameter derived from a fit to data for different terrain types. For tundra, $d = 0.1$.

3.9 Appendix C: Enhancement of Upwelling Intensity in the Discrete Ordinates & Two Stream Approximations

In this section, we construct a detailed example to demonstrate that under the discrete ordinates approximation to atmospheric radiative transfer, of which the two-stream approximation is the $n = 2$ special case, the total upwelling intensity through the atmosphere can exceed the total downwelling intensity if the planet surface is an Lambertian (isotropic) reflector. In outlining this example, we follow closely the DISORT User's Guide (DUG, Stamnes et al. 2000). The DUG outlines the formalism behind the DISORT code (Stamnes et al. 1988), one of the best-known implementations of plane-parallel discrete-ordinates radiative transfer.

Consider a planet with a homogenous atmosphere illuminated from above by the Sun. Let the Sun be located at direction (μ_0, ϕ_0), where μ is the cosine of the solar zenith angle and ϕ is the azimuth, with incident intensity $I(\mu, \phi) = I_0\delta(\mu - \mu_0)\delta(\phi - \phi_0)$. Suppose thermal emission from the atmosphere and planet is negligible (i.e. solar forcing

is the only source of photons to the system). Further, let the atmosphere have negligible optical depth $\tau_0/\mu_0 << 1$ (transparent atmosphere approximation). Then atmospheric scattering and absorption have negligible effect on the planetary radiation field, the upwelling and downwelling intensity fields are essentially uncoupled, and the upward and downward fluxes and the mean intensity are constant throughout the atmosphere. Let the surface be a Lambertian reflector, with albedo $A = F^+/F^-$, where F^+ is the upwelling flux and F^- is the downwelling flux.

The hemispherically-integrated upwelling and downwelling intensities I^+ and I^- may be defined, following DUG equation 9c, by:

$$I^+ = 2\pi\overline{I^+} = 2\pi \int_0^1 I^0(\tau, +\mu)d\mu$$

$$I^- = 2\pi\overline{I^-} = I_0 \exp(-\tau_0/\mu_0) + 2\pi \int_0^1 I^0(\tau, -\mu)d\mu$$

Where $I^0(\tau, \mu)$ is the intensity at a depth τ in the atmosphere arriving from a direction μ. Since $\tau_0/\mu_0 << 1$, $I_0 \exp(-\tau_0/\mu_0) \approx I_0(1 - \tau_0/\mu_0)$. Further, since the atmosphere is optically very thin and noninteracting, essentially no flux is scattered out of the direct stream into the downward diffuse intensity, nor out of the upward diffuse intensity into the downward diffuse intensity (or vice versa). Therefore, we can further approximate that $I^0(\tau, -\mu) \approx 0$. We can then simplify

$$I^- \approx I_0(1 - \tau_0/\mu_0)$$

Next, from DUG equation 39, we can write the boundary condition at the planetary surface (i.e. the reflection condition):

$$I^0(\tau, +\mu) = \epsilon(\mu)B(T_g) + \frac{1}{\pi}\mu_0 I_0 \exp(-\tau_0/\mu_0)\rho_0(\mu, \mu_0) + 2\int_0^1 \mu' d\mu' I^0(\tau_0, -\mu)\rho_0(\mu, -\mu')$$

where $\epsilon(\mu)$ is the surface emissivity as a function of angle, $B(T_g)$ is the blackbody emission of the planet at temperature T_g, and. $\rho_0(\mu, -\mu')$ is the bidirectional reflection function. $B(T_g) \approx 0$ by assumption of negligible blackbody emission at UV wavelengths. $\rho_0(\mu_i, \mu_j) = A$ for a Lambertian surface (see, e.g., Spurr 2001, equation 2.19). $I^0(\tau, -\mu) \approx 0$ as above. We can therefore simplify:

$$I^0(\tau, +\mu) \approx \frac{1}{\pi}\mu_0 I_0(1 - \tau_0/\mu_0)A$$

Substituting for $I^0(\tau, +\mu)$ in our expression for I^+, we can then conclude

$$\begin{aligned} I^+ &\approx 2\pi \int_0^1 (\frac{1}{\pi}\mu_0 I_0(1 - \tau_0/\mu_0)A)d\mu \\ &= 2\int_0^1 (\mu_0 I_0(1 - \tau_0/\mu_0)A)d\mu \\ &= 2A\mu_0 I_0(1 - \tau_0/\mu_0) \end{aligned}$$

Therefore,

$$I^+/I^- = 2A\mu_0$$

.

For $A\mu_0 > 0.5$, $I^+ > I^-$, with a maximum value of $2I^-$. This condition is physically plausible. One example satisfying this condition is the equator of a snowball Earth at

noon on the equinox. At noon on the equinox, $\mu_0 = 1$ (SZA= 0), and snow approximates a Lambertian scatterer(Coakley 2003) with a UV albedo of 0.95 (Briegleb & Ramanathan 1982). Under these conditions, $A\mu_0 = 0.95 > 0.5$, and $I^+ = 1.9I^-$.

This example demonstrates that it is possible for the upwelling intensity to exceed the downwelling intensity. This result may be understood intuitively as a consequence of requiring flux conservation during reflection from a Lambertian surface. Consider the $\mu_0 = 1$, $A = 1$ case in the transparent atmosphere approximation. In this case, all downward photons are arriving from the direction μ_0, and the downwelling intensity and flux are both I_0. Since $A = 1$, all the flux must be reflected, so the upwelling flux $F^+ = I_0$ as well. But, since the surface is a Lambertian scatterer, the downward intensity was scattered uniformly in all directions. $I^+(\tau) = \int_0^1 d\mu I^0(\tau, +\mu) \geq \int_0^1 d\mu I^0(\tau, +\mu)\mu = F^+(\tau)$ since $1 \geq \mu$, so $I^+ \geq I_0 = I^-$.

For another discussion of this phenomenon, see Madronich (1987), their Section 2.3.

Chapter 4

Atmospheric Constraints on the Surface UV Environment of Mars at 3.9 Ga Relevant to Prebiotic Chemistry

This thesis chapter is in press as:

S. Ranjan, R. Wordsworth, and D. Sasselov. Accepted to *Astrobiology* on 10 January 2017.

Abstract

Recent findings suggest Mars may have been a clement environment for the emergence of life, and may even have compared favorably to Earth in this regard. These findings have revived interest in the hypothesis that prebiotically important molecules or even nascent life may have formed on Mars and been transferred to Earth. UV light plays a key role in prebiotic chemistry. Characterizing the early Martian surface UV environment is key to understanding how Mars compares to Earth as a venue for prebiotic chemistry.

Here, we present two-stream multi-layer calculations of the UV surface radiance on Mars at 3.9 Ga, to constrain the surface UV environment as a function of atmospheric state. We explore a wide range of atmospheric pressures, temperatures and compositions, corresponding to the diversity of Martian atmospheric states consistent with available constraints. We include the effects of clouds and dust. We calculate dose rates to quantify the effect of different atmospheric states on UV-sensitive prebiotic chemistry.

We find that for normative clear-sky CO_2-H_2O atmospheres, the UV environment on young Mars is comparable to young Earth. This similarity is robust to moderate cloud cover: thick clouds ($\tau_{cloud} \geq 100$) are required to significantly affect the Martian UV environment, because cloud absorption is degenerate with atmospheric CO_2. On the other hand, absorption from SO_2, H_2S, and dust is nondegenerate with CO_2, meaning if these constituents build up to significant levels, surface UV fluence can be suppressed. These absorbers have spectrally variable absorption, meaning that their presence affects prebiotic pathways in different ways. In particular, high SO_2 environments may admit UV fluence that favors pathways conducive to abiogenesis over pathways unfavorable to it. However, better measurements of the spectral quantum yields of these pathways are

required to evaluate this hypothesis definitively.

4.1 Introduction

Recent findings suggest that young Mars may have been a clement environment for the emergence of life. Analysis of Curiosity imaging of sedimentary rock strata deposited 3.2-3.6 Ga (Grotzinger et al. 2015) suggest individual lakes were stable on ancient Mars for 100-10,000 years, with fluvial features laid down over 10,000-10 million years assuming formation rates corresponding to modern Earth. Similarly, Curiosity measurements of olivine and magnetite at Yellowknife crater are consistent with aqueous conditions at near-neutral pH for thousands to hundreds of thousands of years in the Noachian, with an oxidant supply that could be an energy source (Bristow et al. 2015). In general, the geologic evidence is compelling that liquid water, a requirement for life as we know it, was present on Mars at least transiently in the Noachian (Wordsworth 2016).

The young Mars may also have been a favorable environment for prebiotic chemistry (chemistry relevant to the origin of life). Meteorite analysis has detected boron in Martian clays, important for abiogenesis since borate minerals can stabilize ribose and catalyze other prebiotic chemistry reactions (see Stephenson et al. 2013 and sources therein). Mars may also have enjoyed greater availability of prebiotically important phosphate than Earth (Adcock et al. 2013). Climate models suggest liquid water was transient on Mars (Wordsworth et al. 2013b), which suggests the evidence of wet/dry cycles. Such cycles are useful for prebiotic chemistry: aqueous eras are beneficial for the formation of biotic monomers, while dry eras tend to concentrate feedstock molecules and aid monomer polymerization (Benner & Kim 2015), relevant to the formation of

nucleotides and amino acids (Patel et al. 2015). Finally, the putative dryness of Mars and the potential acidity of its early aqueous environment owing to dissolved carbonic acid from a CO_2-dominated atmosphere, suggest molybdate, which is suggested to catalyze formation of prebiotically important sugars such as ribose, may have been stable on Mars (Benner & Kim 2015; Benner et al. 2010). Hence, there is growing interest in the possibility that prebiotically important molecules may have been produced on Mars (Benner 2013), and even the hypothesis that life may have originated on Mars and been seeded to Earth (Kirschvink & Weiss 2002; Gollihar et al. 2014; Benner & Kim 2015).

Ultraviolet (UV) light plays a key role in prebiotic chemistry. UV photons can dissociate molecular bonds, produce ionic species, and excite molecules. These properties mean that UV light can stress prebiotic molecules (Sagan 1973), but also that UV light can power synthetic prebiotic photochemistry. UV light has been invoked in prebiotic chemistry as diverse as the origin of chirality (Rosenberg et al. 2008), the synthesis of amino acid precursors (Sarker et al. 2013), and the polymerization of RNA (Mulkidjanian et al. 2003).

The last decade has seen breakthroughs in long-standing problems in prebiotic chemistry such as the discovery of plausible mechanisms for the abiotic formation of activated pyrimidine ribonucleotides (Powner et al. 2009), the synthesis of short (2- and 3-carbon) sugars (Ritson & Sutherland 2012), and a reaction network generating precursors for a range of prebiotically important molecules including lipids, amino acids, and ribonucleotides (Patel et al. 2015). These pathways all require UV light to function. In experiments, line sources such as low-pressure mercury lamps with monochromatic 254 nm emission are often used to simulate the incident UV radiation. However, prebiotic UV radiance in CO_2-dominated terrestrial-type atmospheres should instead be

characterized by access to broadband fluence (Ranjan & Sasselov 2017). The difference can have a significant impact on prebiotic chemistry (Ranjan & Sasselov 2017), and there is a growing awareness in the prebiotic community of the importance of characterizing the wavelength dependence of proposed prebiotic pathways and/or using broadband sources in simulations (Rapf & Vaida 2016). Consequently, it is important to constrain the UV environment on the surface of Mars at epochs relevant to potential prebiotic chemistry on a spectral (wavelength-dependent) basis.

In this work, we use a two-stream multilayer radiative transfer model to constrain the surface UV environment on young Mars (3.9 Ga). We calculate the surface radiance as a function of solar zenith angle (SZA), surface albedo (A), and atmospheric composition. Our model can calculate absorption and scattering due to 8 gaseous species (CO_2, H_2O, CH_4, SO_2, H_2S, O_2, and O_3) and 3 particulate species (H_2O ice, CO_2 ice, and Martian dust). Earlier analyses have focused on clear-sky "case studies" for the atmospheric composition; we instead explore the full range of Martian atmospheric states consistent with available geological data and climate/photochemical modelling for the Martian atmosphere. We convolve the calculated surface radiance spectra against action spectra corresponding to two different simple photochemical reactions (one useful to prebiotic chemistry, and one detrimental) that may have been important during the era of abiogenesis, and integrate the result to compute the biologically effective dose rate (BED) and estimate the impact of these parameters on prebiotic chemistry.

In Section 4.2, we discuss previous work on this topic. In Section 4.3, we describe our radiative transfer model and its inputs and assumptions. Section 4.4 presents the surface radiances calculated from our model as a function of Martian atmospheric state, and Section 4.5 discusses the implications for prebiotic chemistry. Section 4.6 summarizes

our findings.

4.2 Background

Recognizing the importance of UV light to life (though mostly in the context of a stressor), previous workers have placed constraints on the primitive Martian surface UV environment. In this section, we present a review of previous work on this topic, and discuss how our work differs from them.

Cockell (2000b) calculate the Martian surface flux at 3.5 Ga assuming solar input of 0.75× modern, and an atmosphere composed of 1 bar CO_2 and 0.1 bar N_2. They compute their radiative transfer in a cloud-free atmosphere using a monolayer two-stream approximation with Delta-Eddington closure. They ignore water absorption, but a dust optical depth of 0.1 is assumed, as is a Lambertian surface with surface albedo $A = 0.1$. Cockell (2000b) report the total irradiance as a function of solar time (equator at equinox) as well as the biologically-weighted[1] irradiance for DNA inactivation and photosystem damage, but not the spectral irradiance (for the early Mars case). They find the DNA inactivation-weighted irradiance to be comparable for their models of Early Mars and Early Earth, leading them to suggest that from a UV perspective the two worlds were comparably habitable.

Rontó et al. (2003) calculate the Martian surface flux at 3.5 Ga from 200-400 nm. They assume a 1-bar CO_2 atmosphere overlying volatilizable surface H_2O, and ran it through the PHOEBE photochemical model to generate atmospheric profiles for

[1] A measure of reaction rate; see Section 4.3.4

the other molecules that would be generated. They found a significant population of spectrally absorbing O_2, O_3, and NO_2 would be generated, including an ozone shield comparable to the modern Earth. They evaluated radiative transfer for both a pure CO_2 atmosphere, as well as for an atmosphere with the trace species calculated in their photochemical model. Their UV radiative transfer models assumes pure absorption and ignores scattering. In this formulation, Rontó et al. (2003) calculated Rayleigh scattering cross-sections but treated them as absorption cross-sections. This approach strongly overestimates attenuation at scattering wavelengths. It is consequently unsurprising that Rontó et al. (2003) report strong attenuation of surface UV fluence for both model atmosphere cases. in the full photochemical model case, fluence shortward of 290 nm is completely removed, due to the buildup of an ozone layer from CO_2 photolysis. However, Segura et al. (2007) note that this photochemical model neglects supply of reducing gases to the atmosphere due to volcanism and sinks of oxic gases due to processes involving rainout, and including either of these effects prevents the formation of an ozone layer. Geological evidence (e.g. the Tharsis plateau) indicates that young Mars had significant volcanism, which would have prevented formation of an ozone layer of the type calculated by Rontó et al. (2003).

Cnossen et al. (2007) calculate the Martian surface flux from $\sim 3.5 - 4$ Ga assuming a 5-bar CO_2, 0.8 bar N_2 clear-sky atmosphere. They used shortwave observations of the solar analog κ^1 ceti combined with a scaled solar spectrum at longer wavelengths as their top-of-atmosphere (TOA) solar input. To calculate radiative transfer, they partition the atmosphere into 40 layers. They compute absorption using the Beer-Lambert law. To account for scattering, they compute the flux scattered in each layer, assume half of it proceeds downwards and half of it proceeds upwards, and iterate this process to

the surface. This approach implicitly neglects multiple scattering and assumes a surface albedo of 0, and hence tends to overestimate atmospheric attenuation of incoming radiation. Hence, Cnossen et al. (2007) report broadband suppression of the TOA flux by multiple orders of magnitude.

Our work builds on these previous efforts. Like Cockell (2000b), Rontó et al. (2003), and Cnossen et al. (2007), we consider the effects of a denser CO_2 atmosphere; however, we consider a broader range of surface atmospheric pressures permitted by available constraints, ranging from $2 \times 10^{-5} - 2$ bar. We build on Cockell (2000b)'s use of a monolayer two-stream approach to radiative transfer by using a multiple-layer two stream model, which consequently accounts for the effects of multiple scattering. Such a treatment is essential because of the unique radiative transfer regime unveiled in thick anoxic atmospheres (e.g. multibar CO_2 atmospheres) at UV wavelengths, characterized by the atmosphere being simultaneously optically thick and scattering-dominated. In this regime, multiple-scattering dominates and it is critical to account for its effects in order to accurately compute surface radiation environments. As a corollary, the radiative transfer treatments of Rontó et al. (2003) and Cnossen et al. (2007) are not valid in this regime[2].

In addition to varying levels of CO_2, our work also explores the impact of other potential atmospheric constituents on the surface UV environment. In particular, we focus on the effect of enhanced concentrations of volcanogenic gases (e.g., SO_2, H_2S), which may have been present at elevated levels on the young Mars (Halevy et al. 2007; Halevy & Head 2014) and if present could have had a dramatic effect on the surface

[2]This regime is not available on the modern Earth or Mars, due to oxic absorption in the former and a thin atmosphere in the latter.

fluence (Ranjan & Sasselov 2017). We also explore the radiative impact of varying levels of dust and CO_2 and H_2O clouds in the Martian atmosphere, which may have been abundant (Wordsworth et al. 2013b; Halevy & Head 2014). Finally, previous workers reported the surface flux. However, as pointed out by other workers, while the flux is the relevant quantity when computing energy deposition, when computing molecular reaction rates the spherically integrated intensity, or actinic flux, is the more relevant quantity (Madronich 1987; Kylling et al. 1995). For a particle lying at the planet surface, fluence below the horizon is blocked by the surface. Therefore, we report instead the integral of the intensity field at the planet surface over the hemisphere defined by elevations > 0 (i.e. that part of the sky not blocked by the planet surface). We term this quantity the *surface radiance*. For more details, see Ranjan & Sasselov (2017).

4.3 Methods

In this section, we describe the methods used to calculate the surface UV environment of early Mars. All software associated with this project is available for validation and extension at `https://github.com/sukritranjan/ranjanwordsworthsasselov2016`.

4.3.1 Radiative Transfer Model

We use a multilayer two-stream approximation to compute the 1D radiative transfer of UV light through the early Martian atmosphere. Our code is based on the radiative transfer model of Ranjan & Sasselov (2017). In brief, we follow the two-stream treatment of Toon et al. (1989), and we use Gaussian (single) quadrature to connect the diffuse

intensity to the diffuse flux, since Toon et al. (1989) find Gaussian quadrature closure to be more reliable than Eddington or hemispheric mean closure at short (solar) wavelengths. We include absorption and scattering due to N_2, CO_2, H_2O, CH_4, O_2, O_3, SO_2, and H_2S. For reasons of numerical stability, we assign a ceiling on the per-layer single-scattering albedo ω_0 of $1 - 10^{-12}$. In Ranjan & Sasselov (2017), we included thermal emission from the atmosphere and surface, to enable application of our code to situations where planetary UV emission might be important. Early Mars is not such a case, so here we omit these features.

Our model requires the user to specify the partition of the atmosphere into homogenous layers, and to provide the temperature, pressure, and composition (gaseous molar concentrations) as a function of altitude. Section 4.3.2 describes our calculation of these quantities. Our model also requires the user to specify the wavelength bins over which the radiative transfer is to be computed; all spectral parameters are integrated over these wavelength bins using linear interpolation in conjunction with numerical quadrature. The user also must specify the solar zenith angle (SZA) and albedo. The albedo may be specified as either a fixed value (e.g. Rugheimer et al. 2015), or as a wavelength- and SZA-dependent user-determined mix of the albedos corresponding to different terrestrial physical surface media (new snow, old snow, desert, tundra, ocean).

We take the top-of-atmosphere (TOA) flux to be the solar flux at 3.9 Ga, computed at 0.1 nm resolution from the model of Claire et al. (2012) and scaled to the Martian semimajor axis of 1.524 AU. We choose 3.9 Ga for the prebiotically-relevant era 1) because of evidence for at least transient liquid water on Mars around this time (Bristow et al. 2015; Grotzinger et al. 2015; Wordsworth 2016), 2) it postdates the potentially-sterilizing Late Heavy Bombardment (Maher & Stevenson 1988; Sleep et al.

1989), and 3) it predates the bulk of the evidence for the earliest terrestrial life (see Ranjan & Sasselov 2016 and sources therein). If one hypothesizes terrestrial abiogenesis was aided by transfer of prebiotically relevant compounds from Mars (Benner 2013; Gollihar et al. 2014; Benner & Kim 2015), then the synthesis of these molecules and their transfer must have occurred concomitantly with the origin of life on Earth. We note that, unlike the XUV, solar output varies only modestly (within a factor of 2) from 3.5-4.1 Ga in the > 180 nm wavelength range unshielded by atmospheric CO_2 or H_2O. Therefore, our results are insensitive to the precise choice of epoch for abiogenesis.

In Ranjan & Sasselov (2017), we did not include scattering and absorption due to atmospheric particulates. However, clouds have been suggested to play a major role in Martian paleoclimate (Forget & Pierrehumbert 1997; Colaprete & Toon 2003; Wordsworth et al. 2013b). Therefore, we updated our model to allow the user to emplace CO_2 and H_2O cloud decks of user-specified optical depth (at 500 nm) in the atmosphere. The cloud decks are assumed to uniformly span the atmospheric layers into which they are emplaced. Section 4.3.3 discusses the calculation of the particulate optical parameters (per-particle cross-section σ, asymmetry parameter g, and ω_0). We use delta-scaling with Henyey-Greenstein closure (Joseph et al. 1976) to correct for the effects of highly forward-peaked particulate scattering phase functions.

The fundamental output of our code is the surface radiance as a function of wavelength. The surface radiance is the integral of the intensity field at the planet surface over the unit hemisphere defined by elevations greater than zero, i.e. the intensity field integrated over all parts of the sky not blocked by the planet surface. As we argue in Ranjan & Sasselov (2017), this is the relevant quantity for calculating reaction rates of molecules at planet surfaces (as compared to the actinic fluxes for molecules suspended

in the atmosphere, see Madronich 1987). In the two-stream formalism, this quantity is

$$I_{surf} = F_N^{\downarrow}/\mu_1 + F_N^{dir}/\mu_0,$$

where $F_N^{\downarrow}$ is the downward diffuse flux at the planet surface, F_N^{dir} is the direct flux at the planet surface, and $\mu_0 = \cos(SZA)$ is the cosine of the solar zenith angle. In Gaussian quadrature for the $n = 1$ (two-stream) case, $\mu_1 = 1/\sqrt{3}$ (Toon et al. 1989); it can be interpreted as the effective zenith angle for the diffuse flux.

4.3.2 Atmospheric Profile

We assume a CO_2-dominated Martian atmosphere at 3.9 Ga. We take the atmosphere to be fully saturated with H_2O. Typical calculations of Noachian climate call for steady-state local surface temperatures of $T_0 \lesssim 273$K across the planetary surface, and more typically $T_0 \sim 210 - 250$K (Forget et al. 2013; Wordsworth et al. 2013b).Both one- and three-dimensional calculations of Noachian climate produce global mean surface temperatures of 240 K or less (Forget et al. 2013; Wordsworth et al. 2013b; Ramirez et al. 2014). At such cold temperatures, the H_2O saturation pressure is very low, and H_2O is a trace gas in the atmosphere. Therefore, we approximate the thermodynamic properties of the Martian atmosphere by the thermodynamic properties of CO_2. We take $c_p = c_{p,CO_2}$ and $R = R_{CO_2}$, where c_p and R are the heat capacity at constant pressure and the specific gas constant respectively. We assume the heat capacity to be constant, with $c_p = c_p(T_0)$, where T_0 is the surface temperature. We calculate $c_p = c_{p,CO_2}$ from the Shomate relation, taking the coefficients from Pierrehumbert (2010, page 115). We tested the effects of permitting the heat capacity to vary with temperature, and found minimal impact on our results.

Martian paleoclimate models have been proposed that invoke effects like enhanced volcanism (Halevy & Head 2014) and high H_2 abundance (Ramirez et al. 2014) to argue for global mean temperatures in excess of 273K. However, these models also require pCO_2 in excess of 1 bar, meaning that H_2O remains a trace atmospheric constituent. Regardless, our results are insensitive to the precise thermal properties of the atmosphere because of the modest variation of the absorption cross-sections of the gases in our model with temperature at UV wavelengths.

For a given surface pressure, surface temperature (P_0, T_0), we let the temperature decrease as a dry adiabat until it reaches the CO_2 saturation temperature, at which point it follows the CO_2 saturation curve. We use the empirical saturation curve of Fanale et al. (1982), as in Wordsworth et al. (2013b). To avoid the need for a full radiative-convective climate model, which is tangential to our objectives in this paper, we assume a stratosphere starting at 0.1 bar, following the observation of Robinson & Catling (2014) that atmospheres dominated by triatomic gases tend to become optically thin and hence radiatively dominated around that pressure. We follow other workers (e.g. Kasting 1991; Hu et al. 2012; Halevy & Head 2014) assuming the stratosphere to be isothermal; we conduct sensitivity studies demonstrating our results are not sensitive to this assumption.

To calculate the H_2O saturation pressure, we use the empirical formulation of Wagner et al. (1994) via Wagner & Pruß (2002) for the vapor pressure of water overlying a solid reservoir (as would be the case for $T_0 < 273$ K). We assume the atmosphere to be fully saturated in H_2O until the tropopause, and we assumed the molar concentration of water in the stratosphere to be equal to its concentration at the tropopause throughout.

Our model requires temperature, pressure, and molar concentrations as functions of altitude. To obtain a mapping between pressure and altitude, we approximate the atmosphere as a series of 1000 layers, each individually isothermal, evenly spanning $P_0 - P_0 \times \exp(-10)$. We then use the equation for an isothermal atmosphere in hydrostatic equilibrium,

$$P(z)/P(z_0) = \exp(-(z - z_0)/H),$$

to calculate the change in altitude across each pressure layer, and sum to obtain a mapping between z and P. Here, P is pressure, z is the altitude of the layer top, z_0 is the altitude of the layer bottom, and $H = kT/(\mu g)$ is the scale height of the layer, with T being the layer temperature, μ the mean molecular weight of the atmospheric layer, and g the acceleration due to Martian gravity. We also considered numerically integrating the hydrostatic equilibrium equation,

$$dP/dz = -\rho g,$$

where the density $\rho = \mu P/(kT)$ for an ideal gas, directly to obtain $z(P)$. We found this approach to agree within 1%; we consequently elected to use the simpler isothermal partition approach for our calculation. Section 4.7 presents sample atmospheric profiles derived using our methods.

4.3.3 Particulate Optical Parameters

In this section, we discuss our calculation of the optical parameters (σ, ω_0, and g) associated with interaction of radiation with the CO_2 and H_2O ice particles that constitute clouds.

We approximate the particles as spherical, and compute their optical parameters using Mie theory at 0.1 nm resolution, following the treatment outlined in Hansen & Travis (1974). At each wavelength, we compute ω_0, g, and the scattering efficiency Q_s. We numerically integrate these parameters over a log normal size distribution with effective radius r_{eff} and effective variance v_{eff}, weighted by $\pi r^2 n(r)$, where r is the particle radius and n(r) is the size distribution, and demand a precision of 1% in the distribution-averaged mean values. We obtain the per-particle total extinction cross-section by

$$\sigma = (\overline{Q_s}/\overline{\omega_0})G,$$

where $\overline{Q_s}$ is the distribution-averaged mean value of Q_s, ω_0 is the distribution-averaged mean value of ω_0, and

$$G = \int_{r_1}^{r_2} \pi r^2 n(r) dr$$

is the "geometric cross-sectional area of particles per unit volume" (Hansen & Travis 1974) computed at 1 ppm precision. For our numerical integral, we integrated from $r_1 = r_{eff} 10^{-10 v_{eff}}$ to $r_2 = r_{eff} 10^{4 v_{eff}}$; we found $n(r) < 10^{-4}$ beyond these limits.

We take the index of refraction for H_2O ice from the compendium of Warren & Brandt (2008) [3]. We take the index of refraction for CO_2 ice from the compendium given in Pierrehumbert (2010)[4]. This compendium was formed by G. Hansen by subjecting the absorption spectra of Hansen (1997) and Hansen (2005) to Kramers-Kronig analysis to obtain self-consistent spectra of real and imaginary indices of refraction (S. Warren, private communication). We take the index of refraction for Martian dust from Wolff

[3]accessed via `http://www.atmos.washington.edu/ice_optical_constants`

[4]accessed via `http://geosci.uchicago.edu/~rtp1/PrinciplesPlanetaryClimate/Data/WorkbookDatasets/Chapter5Data/co2i4a.rfi.txt`

et al. (2009) [5]. The data of Wolff et al. (2009) truncate at 263 nm. Measurements of the imaginary index of refraction down to 194 nm are available from Pang & Ajello (1977). We adopt the values of Pang & Ajello (1977) for wavelengths < 263 nm. Zurek (1978) present a compendia of the real index of refraction of Martian dust. Their study indicates that the index of refraction changes by only ~ 0.1 from $\sim 200 - 263$ nm. Their values at 263 nm are 0.4 higher than Wolff et al. (2009); to avoid a discontinuity, we subtract 0.4 from the real indices of refraction of Zurek (1978).

Figure 4.1 presents the CO_2 and H_2O ice optical parameters as a function of wavelength for size distributions with $v_{eff} = 0.1$ and $r_{eff} = 1, 10, 100$ microns. Previous work has assumed CO_2 cloud particle sizes to be in the 1-100 μm range (e.g., Forget & Pierrehumbert 1997). Microphysical modelling by Colaprete & Toon (2003) suggests that primitive Martian CO_2 clouds may have been characterized by large particle sizes, as high as $r_{eff} = 100\mu$m. The optical properties of CO_2 and H_2O ice particles for $r_{eff} \geq 10\mu$m are insensitive to r_{eff}; we attribute this to size parameter $x = 2\pi r_{eff}/\lambda$ being large in this regime, meaning such particles approach the large-particle limit. ($x > 12$ for $r_{eff} \geq 10\mu$m and $\lambda \leq 500$ nm). For wavelengths satisfying $195 < \lambda < 500$ nm, CO_2 and H_2O ice are characterized by $\omega_0 \approx 1$. This means that CO_2 and H_2O clouds do not significantly absorb at wavelengths unshielded by H_2O (< 198 nm) or CO_2 (< 204 nm). By contrast, dust absorbs across $100 - 500$ nm, meaning dust particles can supply absorption at wavelengths not shielded by CO_2 or H_2O.

[5] accessed via `http://spacescience.arc.nasa.gov/mars-climate-modeling-group/documents/Dust_Refractive_Indicies.txt`

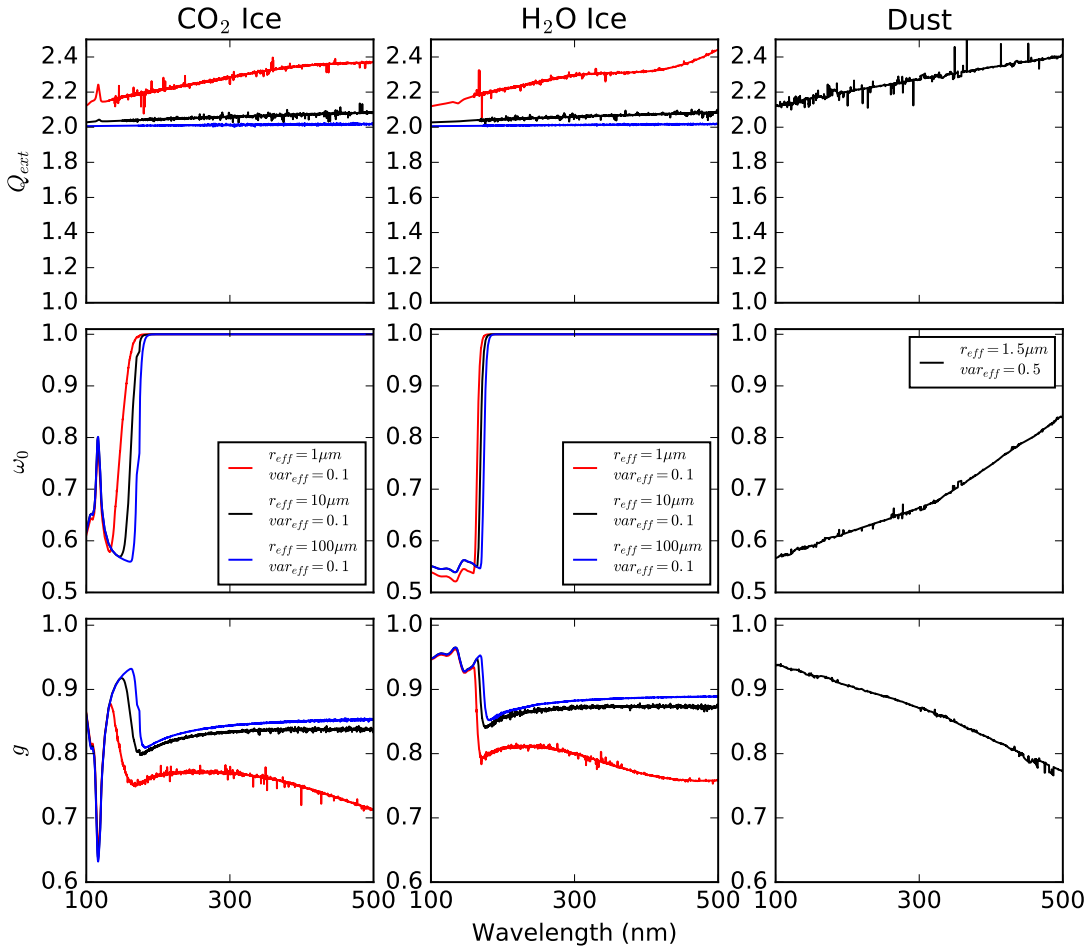

Figure 4.1: Scattering efficiency Q_{ext}, single-scattering albedo ω_0, and asymmetry parameter g as a function of wavelength for CO_2 ice, H_2O ice, and modern Martian dust, integrated over the specified log-normal size distributions.

4.3.4 Action Spectra and Calculation of Dose Rates

To quantify the impact of different surface UV radiation environments on prebiotic chemistry, we follow the approach of Cockell (1999), Rontó et al. (2003), and Rugheimer et al. (2015) in computing Biologically Effective Dose rates (BEDs). Specifically, we

compute

$$D = (\int_{\lambda_0}^{\lambda_1} d\lambda \mathcal{A}(\lambda) I_{surf}(\lambda)),$$

where $\mathcal{A}(\lambda)$ is an action spectrum, λ_0 and λ_1 are the limits over which $\mathcal{A}(\lambda)$ is defined, and $I_{surf}(\lambda)$ is the UV surface radiance. An action spectrum parametrizes the relative impact of radiation on a given photoprocess as a function of wavelength, with a higher value of $\mathcal{A}$ meaning that a higher fraction of the incident photons are being used in the photoprocess. Hence, D is proportional to the reaction rate rate of a given photoprocess for a single molecule at the surface of a planet.

As D is a relative measure of reaction rate, a normalization is required to assign a physical interpretation to its value. In this paper, we report

$$\overline{D} = D/D_{\oplus},$$

where $D_{\oplus}$ is the dose rate on 3.9 Ga Earth. The atmospheric model for 3.9 Ga Earth is taken from Rugheimer et al. (2015), who use a 1D coupled climate-photochemistry model to compute the atmospheric profile (T, P, composition) for the Earth at 3.9 Ga, assuming modern abiotic outgassing rates and a background atmosphere of 0.9 bar N_2, 0.1 bar CO_2, with SZA=60° and $A = 0.2$. Consequently, $\overline{D} > 1$ means that the photoprocess is proceeding faster on the Martian surface under the specified atmosphere than it would on the surface of the Rugheimer et al. (2015) fiducial Earth. Note this normalization is different from what we chose in Ranjan & Sasselov (2017), because here we are trying to assess how Mars compares to the Earth as a venue for prebiotic chemistry.

Previous workers used action spectra of UV stress on modern biology (e.g. the DNA inactivation action spectrum) (Cockell 2000b, 2002; Cnossen et al. 2007; Rugheimer et al. 2015) as a gauge of the level of stress imposed by UV fluence on the prebiotic

environment. However, these action spectra are based on modern life. Modern organisms have evolved sophisticated methods to deal with environmental stress, including UV exposure, that would not have been available to the first life. Further, this approach presupposes that UV light is solely a stressor, and ignores its potential role as a eustressor for abiogenesis. In this work, we follow the reasoning of our previous efforts in Ranjan & Sasselov (2017) in formulating action spectra corresponding to simple photoreactions that are expected to have played major roles in prebiotic chemistry. We consider two reactions: a stressor process, to capture the stress UV light places on nascent biology, and an eustressor process, to capture the role of UV light in promoting prebiotic chemistry. A detailed description of these processes and their corresponding action spectra is given in Ranjan & Sasselov (2017); a brief outline is presented below.

Stressor Process: Cleavage of N-Glycosidic Bond of UMP

For our stressor process, we chose the cleavage of the N-glycosidic bond in the RNA monomer uridine monophospate (UMP). UV radiation can cleave the N-glyocosidic bond which joins the sugar to the nucleobase (Gurzadyan & Görner 1994), irreversibly destroying this molecule. Hence, this process represents a stressor to abiogenesis.

The action spectrum is equal to the product of the absorption spectrum (fraction of incident photons absorbed) and the quantum yield curve (QY, fraction of absorbed photons that lead to the photoreaction). We take our UMP absorption spectrum from the work of (Voet et al. 1963) (pH=7.6). Detailed spectral measurements of the QY of glyocosidic bond cleavage have not been obtained. However, Gurzadyan & Görner (1994) found the QY of N-glycosidic bond cleavage in UMP in neutral aqueous solution

saturated with Ar (i.e. anoxic) to be 4.3×10^{-3} at 193 nm and $(2-3) \times 10^{-5}$ for 254 nm. We therefore represent the QY curve as a step function with value 4.3×10^{-3} for $\lambda \leq \lambda_0$ and 2.5×10^{-5} for $\lambda > \lambda_0$. We consider λ_0 values of 193 and 254 nm, corresponding to the empirical limits from Gurzadyan & Görner (1994). We also consider $\lambda_0 = 230$ nm, which corresponds to the end of the broad absorption feature centered near 260 nm corresponding to the $\pi - \pi^*$ transition and also to the transition to irreversible decomposition suggested by Sinsheimer & Hastings (1949). As shorthand, we refer to this photoprocess under the assumption that λ_0 =X nm by UMP-X. Figure 4.2 presents these action spectra.

The absorption spectra of the other RNA monomers are structurally similar to UMP (Voet et al. 1963), and the quantum yield of N-glycosidic bond cleavage in adenosine monophospate (AMP) increases at short wavelengths like UMP's does (Gurzadyan & Görner 1994), leading us to argue that action spectra for N-glycosidic bond cleavage of the other RNA monomers should be broadly similar to that for UMP. Therefore, results derived using the action spectrum for UMP N-glycosidic bond cleavage should be broadly applicable to the other RNA monomers: if a UV environment is destructive for UMP, it should be bad for the other RNA monomers, and hence for abiogenesis in the RNA world hypothesis, as well.

Eustressor Process: Production of Aquated Electrons from Photoionization of Cyanocuprate

For our eustressor process, we choose the production of aquated electrons from the irradiation of a tricyanocuprate ($CuCN_3^{2-}$) complex. We chose this process because

it underlies the selective 2- and 3-carbon sugar (glycolaldehyde and glyceraldehyde) synthesis pathway of Ritson & Sutherland (2012), which is the best candidate proposed so far for a selective prebiotic synthesis of these sugars. These sugars are required for the synthesis of RNA, and hence abiogenesis in the RNA world hypothesis. This process is also important to the prebiotic reaction network of Patel et al. (2015). More generally, aquated electrons are useful for a broad range of reductive prebiotic chemistry, e.g., the reduction of nitriles to amines, aldehydes to hydroxyls, and hydroxyls to alkyls[6]. Therefore, this process represents a eustressor to abiogenesis. While other UV-sensitive processes conducive to abiogenesis doubtless exist, we argue this process is of particular interest because of its unique role in the most promising plausibly prebiotic pathways to the RNA monomers.

We again form the action spectrum by multiplying the absorption spectrum and the quantum yield curve. We take the cyanocuprate absorption spectrum from the work of Magnani (2015), via Ranjan & Sasselov (2016). The spectral QY of aquated electron production from cyanocuprate irradiation is not known. However, Horváth et al. (1984) measure a QY of 0.06 for this process at 254 nm. Following Ritson & Sutherland (2012)'s hypothesis that photoionization of the complex drives aquated electron production, we assume the QY to be characterized by a step function with value 0.06 for $\lambda \leq \lambda_0$ and 0 otherwise. We empirically know $\lambda_0 \geq 254$ nm. To explore a range of λ_0, we consider $\lambda_0 = 254$ nm and $\lambda_0 = 300$ nm. As shorthand, we refer to this photoprocess under the assumption that $\lambda_0 =$Y nm by CuCN3-Y. Figure 4.2 presents these action spectra.

Action spectra typically encode information about relative, not absolute, reaction

[6]J. Szostak, private communication, 2/5/16

rates. Consequently, they are generally arbitrarily normalized to 1 at some wavelength (see, e.g., Cockell 1999 and Rugheimer et al. 2015). We normalize these spectra to 1 at 190 nm.

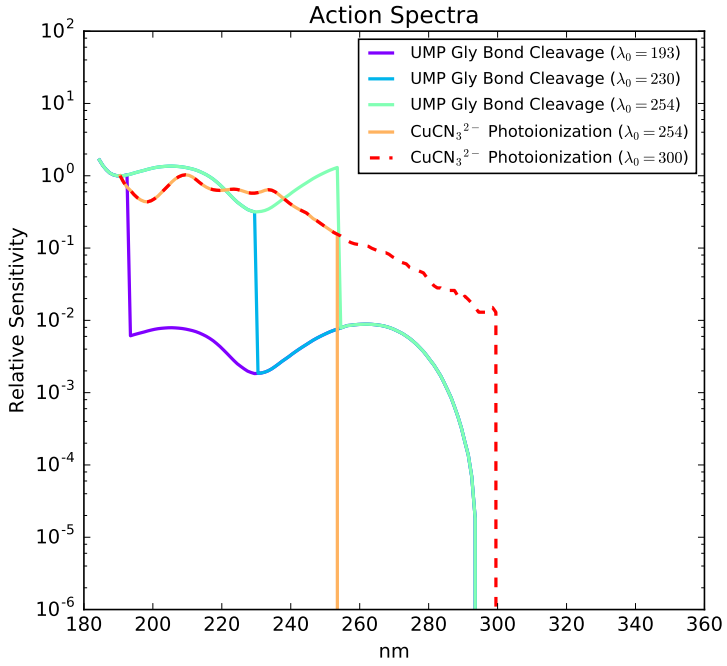

Figure 4.2: Action spectra for photolysis of UMP$-\lambda_0$ and photoionization of CuCN3 $-\lambda_0$, assuming a step-function form to the QE for both processes with step at λ_0. The spectra are arbitrarily normalized to 1 at 190 nm.

4.4 Results

4.4.1 Clear-Sky H_2O-CO_2 Atmospheres

We evaluated the UV surface radiance for a range of (pCO_2 , T_0) for pure H_2O-CO_2 atmospheres in the clear-sky case (no clouds, dust or other particulates). We considered

$pCO_2 = 0.02 - 2$ bar, corresponding to the range of surface pressure for which Wordsworth et al. 2013a reported at least transient local temperatures above 273 K, and $T_0 = 210 - 300$ K. We took an SZA of 0, corresponding to noon at equatorial latitudes. We took the surface albedo to correspond to desert (diffuse albedo of 0.22); we adopted this albedo because young Mars is thought to have been dry and desert-like in conventional climate models. Modern Mars has a UV albedo an order of magnitude lower (Fox et al. 1997), likely due to formation of UV-absorbing metal oxides on the planet's basaltic surface over geologic time; sensitivity tests indicate our results are robust to choices of surface albedo down to A 0.02. Taken together, variations in surface albedo and SZA can drive variations in the spectral surface radiance of up to a factor of ~ 20, and overall variations in prebiotically-relevant reaction rates of a factor of $\gtrsim 10$ (Ranjan & Sasselov 2017). These surface radiances are shown in Figure 4.3.

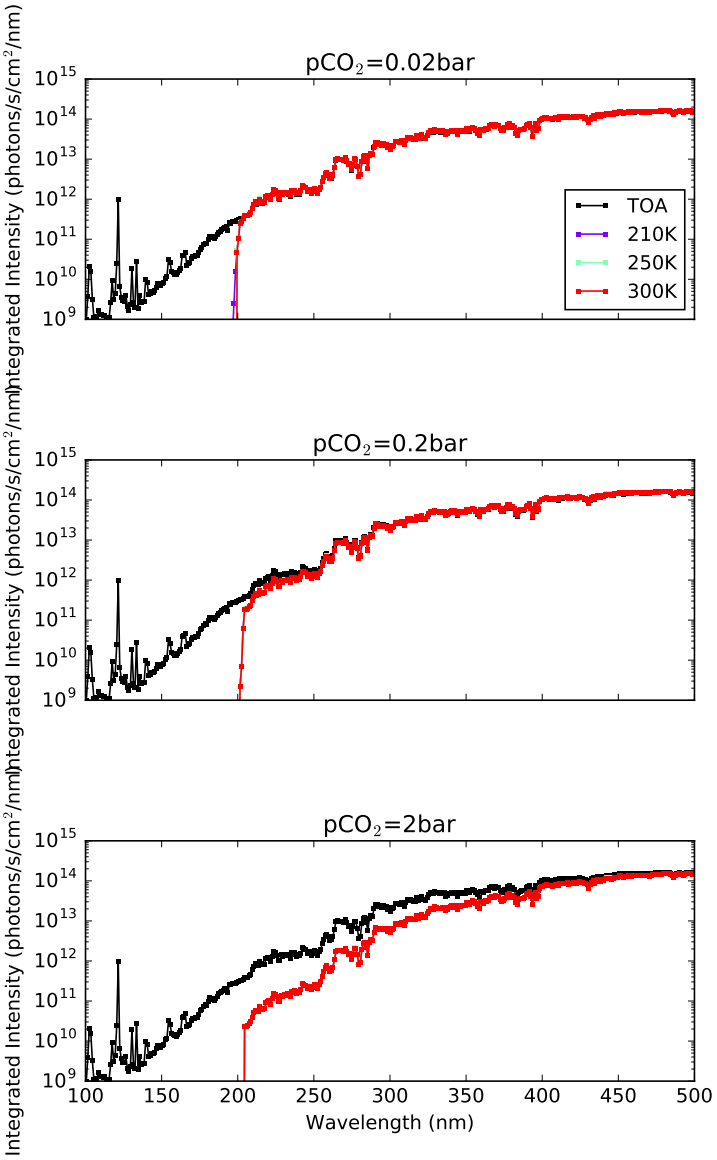

Figure 4.3: Surface radiance as a function of wavelength for varying pCO_2 and T_0, for SZA=0 and albedo corresponding to desert. Also plotted for scale is the TOA solar flux. The surface radiance is insensitive to atmospheric and surface temperature.

In the scattering regime ($\lambda > 204$ nm), our surface radiances fall off only slowly with pCO_2. This is a consequence of random walk statistics in the context of multiple scattering: transmission through purely scattering media go as $1/\tau$ (see, e.g., Bohren

1987 for a discussion with application to clouds). This result stands in contrast to the calculations of Cnossen et al. (2007) and Rontó et al. (2003), who ignore multiple scattering in their radiative transfer treatments, and illustrates the importance of self-consistently including this phenomenon when considering dense, highly scattering atmospheres.

We find our surface radiance calculations to be insensitive to T_0. This is because 1) the total atmospheric column is set by P_0 and independent of T_0, 2) the rapid increase of CO_2 cross-sections for $\lambda < 204$ nm, which means that the the atmosphere rapidly becomes optically thick in the UV, and 3) increased water vapor abundance with increasing T_0 does not drive an increase in opacity because water vapor absorption is degenerate with CO_2 absorption in the UV (Ranjan & Sasselov 2017).

We considered the hypothesis that including the effect of variations in CO_2 cross-section with temperature might impact our results. We followed the approach of Hu et al. (2012) in interpolating between cold ($\sim$ 195 K) and room-temperature datasets for CO_2 absorption to estimate the effects of temperature dependence on CO_2 cross-section. We used the dataset of Stark et al. (2007) from 106.5-118.7 nm, Yoshino et al. (1996) from 118.7-163 nm, and Parkinson et al. (2003) from 163-192.5 nm. We did not find cold-temperature cross-sections for CO_2 at longer wavelengths. We found our results were not altered by including temperature-dependence of CO_2 cross-sections for $pCO_2 = 0.02 - 2$ bar, because the CO_2 UV absorption is already saturated by 192.5 nm, where our temperature dependence kicks in. We considered lower values of $pCO_2 = 2 \times 10^{-3} - 2 \times 10^{-5}$ bar (below PAL), where the CO_2 absorption does not saturate until wavelengths shorter than 192.5 nm. Even in the low pCO_2 case, including temperature-dependence only changed the onsite of CO_2 absorption saturation by $1 - 2$

nm. We attribute this to the rapidity of the rise in CO_2 absorption cross section with decreasing wavelength for $\lambda \lesssim 204$ nm. We conclude that even including the effects of temperature on CO_2 UV cross-section, the UV surface fluence is insensitive to T_0. We consequently elected to ignore the temperature dependence of CO_2 cross-sections in the remainder of this study.

Figure 4.4 presents the surface radiances in the $pCO_2 = 2 \times 10^{-5}$ bar cases, calculated for SZA=0, A corresponding to desert, and $T_0 = T_{eq} \approx 200$K, with and without CO_2 cross-sections included. Such low atmospheric pressures have been suggested based on atmospheric escape arguments (Tian et al. 2009), followed by a buildup of the atmosphere after escape rates subsided with shortwave solar output. In such a case, aqueous prebiotic chemistry could only have proceeded in environments kept warm by non-climatological means, e.g. geothermal reservoirs. Even for such low pCO_2, EUV fluence shortward of 185 nm is shielded out by atmospheric CO_2.

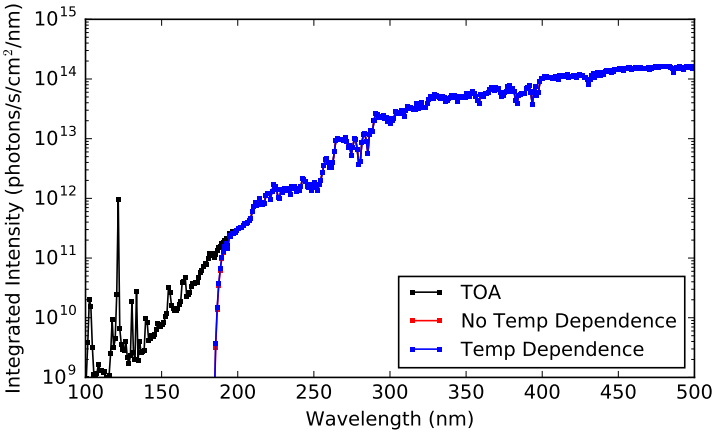

Figure 4.4: Surface radiance as a function of wavelength for $pCO_2 = 2 \times 10^{-5}$ bar , $T_0 = 200$K, SZA=0, A corresponding to desert, with and without temperature dependence of the CO_2 cross-sections included. Also plotted for scale is the TOA solar flux. The surface radiance is insensitive to inclusion of temperature dependence of the CO_2 cross-sections, even for very low pCO_2.

4.4.2 Effect of CO_2 and H_2O Clouds

We considered the effect of CO_2 and H_2O clouds in a CO_2-H_2O atmosphere. Such clouds have been detected on modern Mars (see, e.g., Vincendon et al. 2011), and GCM results suggest they should have been present on early Mars as well(Wordsworth et al. 2013b). Figure 4.5 presents the UV surface fluence for a 0.02-bar CO_2-H_2O atmosphere with H_2O and CO_2 cloud decks of varying optical depths emplaced in the atmosphere. This low surface pressure is chosen in order to isolate the effects of the clouds as opposed to atmospheric CO_2. The surface albedo corresponds to desert, and SZA=0. The optical depths are specified at 500 nm. The H_2O and CO_2 cloud decks are emplaced from 3-4 km and 20-21 km of altitude, respectively, corresponding approximately to the altitudes of

peak cloud formation identified in Wordsworth et al. (2013a). For both types of clouds, we varied the cloud deck altitudes between 0.5-60.5 km, and found the surface fluence to be insensitive to the cloud deck altitude. We also experimented with partitioning the clouds into two decks, and found the surface fluence to be insensitive to the partition.

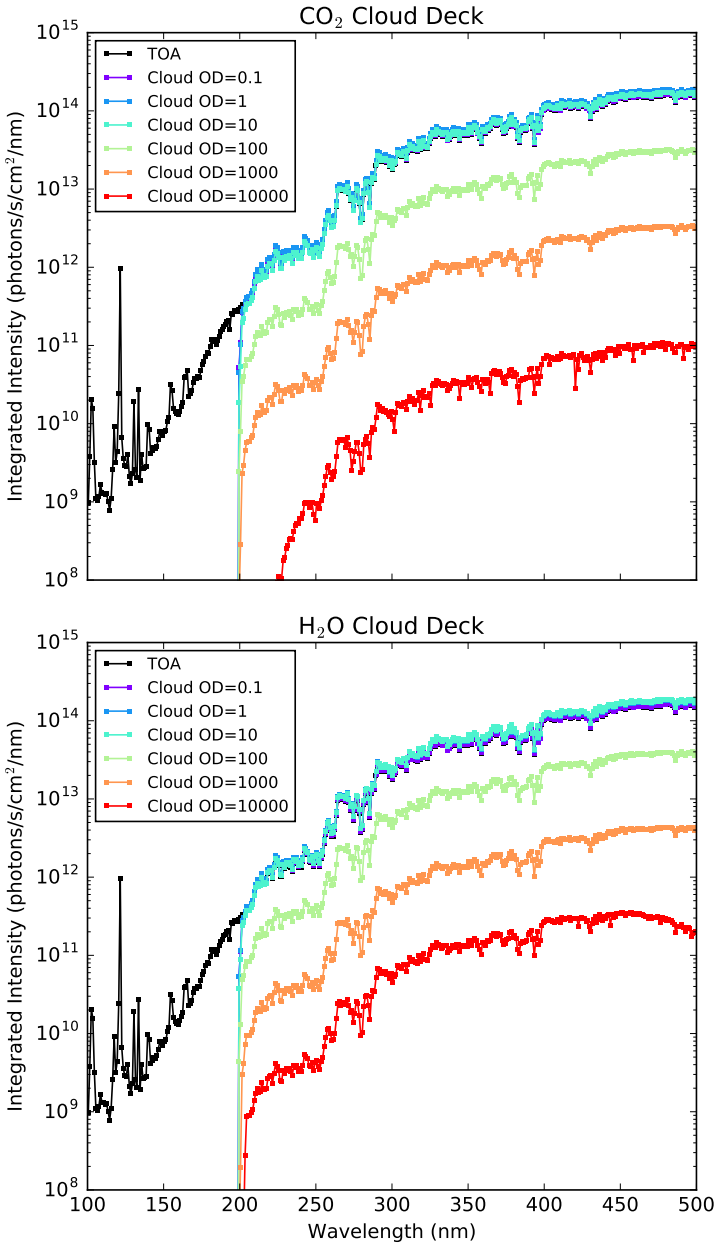

Figure 4.5: Surface radiance as a function of wavelength for $pCO_2 = 0.02$ bar, $T_0 = 250$K, SZA=0, A corresponding to desert, and CO_2 and H_2O cloud decks of varying thicknesses inserted from 20-21 and 3-4 km respectively. Also plotted for scale is the TOA solar flux.

CO_2 and H_2O ice clouds have similar impact on the surface fluence. This is because both types of ice have similar optical parameters for $195 < \lambda < 500$ nm and $r_{eff} \geq 1\mu$m. The $\lambda < 195$ nm regime, where they have different optical parameters, is shielded out by gaseous CO_2 absorption.

CO_2 and H_2O ice particles are pure scatterers for $195 < \lambda < 500$ nm and $r_{eff} \geq 1\mu$m. Consequently, it is unsurprising that surface fluence falls off only slowly with increasing optical depth. In fact, the transmission of a purely scattering cloud layer varies as $\sim 1/\tau^*$, where τ^* is the delta-scaled optical depth of the cloud layer (Bohren 1987). This is a consequence of the random-walk nature of radiative transfer in the optically-thick purely-scattering limit.

The particle size r_{eff} can have an impact on surface radiance. For $r_{eff} = 1\mu$m, the surface fluence at 500 nm is $\sim 40\%$ lower compared to $r_{eff} = 100\mu$m (A corresponding to desert, SZA=0). This is because as r_{eff} decreases in this regime, so does g, meaning that the rescaled optical depth in the delta-scaling formalism $\tau^* = \tau \times (1 - g^2)$ is higher for small particles than large particles.

Suppressing surface radiance to 10% or less of TOA flux requires cloud optical depths of $\gtrsim 100$. This is comparable to the optical depth of a terrestrial thunderstorm (Mayer et al. 1998). We can compute the mass column of ice particle required to achieve this optical depth by

$$u = (\frac{\tau}{\pi r^2 Q_{ext}})(\frac{4\pi}{3} r^3 \rho),$$

where ρ is the mass density of the ice, r is the ice particle radius, τ is the cloud optical depth, and Q_{ext} is the extinction efficiency. For CO_2 ice, $\rho = 1.5$ g/cm^3 [7], $r = 10\mu$m,

[7] http://terpconnect.umd.edu/~choi/MSDS/Airgas/CARBON\%20DIOXIDE.pdf

and approximating $Q_{ext} = 2$, we find $\tau = 100$ corresponds to $u = 1$ kg/m^2. Wordsworth et al. (2013b) find in their 3D simulation CO_2 ice columns of up to 0.6 kg/m^2 in patches, suggesting CO_2 clouds may have significantly affected the surface UV environment. For water ice, taking $\rho = 0.92$ g/cm^3 (Miller 2009), $r = 10\mu$m, and approximating $Q_{ext} \approx 2$, we find $\tau = 100$ corresponds to $u = 6 \times 10^{-1}$ kg/m^2. By contrast, Wordsworth et al. (2013b) finds expected ice columns of $\lesssim 2 \times 10^{-3}$ kg/m^2. Consequently, barring a mechanism which can increase the H_2O cloud levels above that considered by Wordsworth et al. (2013b), H_2O ice clouds by themselves are unlikely to significantly alter the surface radiance environment on early Mars.

4.4.3 Effect of Elevated Levels of Volcanogenic Gases

So far, we have considered pure CO_2-H_2O atmospheres. However, other gases may have been present in the early Martian atmosphere. In particular, Mars at ~ 3.9 Ga was characterized by volcanic activity, which emplaced features like the Tharsis igneous province (Halevy & Head 2014). Such volcanism could have injected elevated levels of volcanogenic gases like SO_2 and H_2S into the atmosphere. SO_2 and H_2S are also strong and broad UV absorbers, and at elevated levels they can completely reshape the surface UV environment (Ranjan & Sasselov 2017). Consequently, we consider the impact of elevated levels of SO_2 and H_2S on the surface UV environment.

We consider SO_2 levels up to 2×10^{-5} bar. For scale, Halevy & Head (2014) compute that an SO_2 level of 1×10^{-5} bar in a 1 bar CO_2-dominated atmosphere requires volcanic outgassing at 100$\times$ the current terrestrial outgassing. Figure 4.6 presents the surface radiance for varying pSO_2 and $pCO_2 = 0.02 - 2$ bar (SZA=0, A corresponding to desert,

and $T_0 = 250$ K).

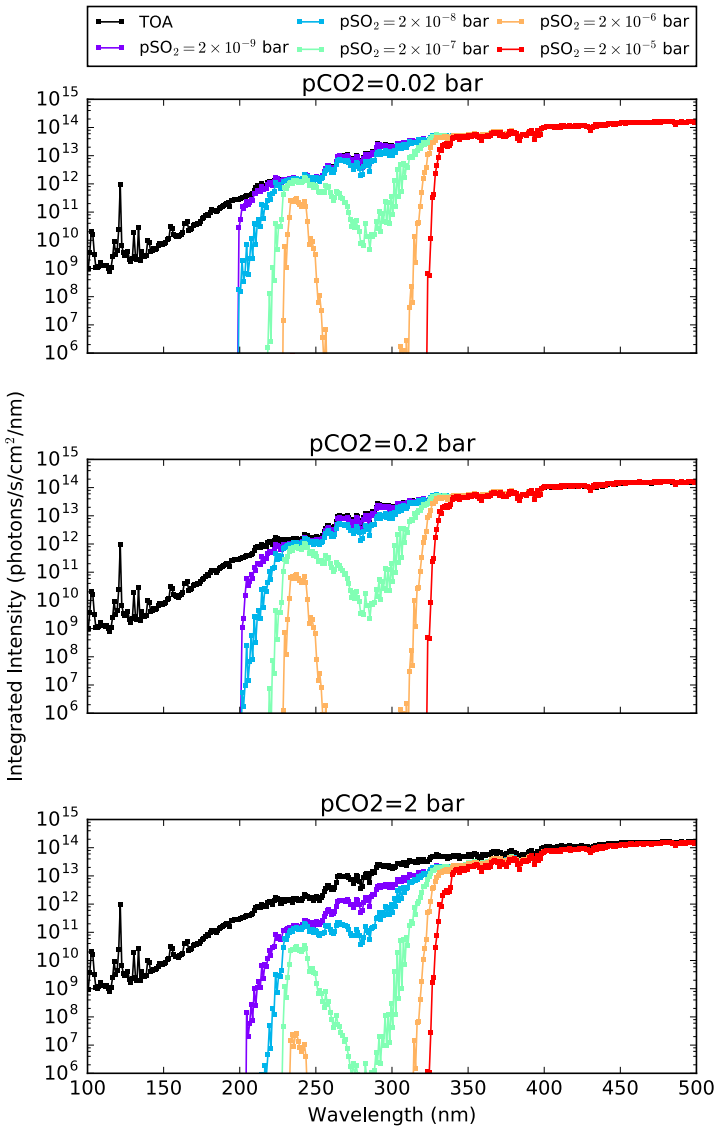

Figure 4.6: Surface radiance as a function of wavelength for $T_0 = 250$K, SZA=0, A corresponding to desert, $\mathrm{pCO_2} = 0.02 - 2$ bar, and $\mathrm{pSO_2} = 2 \times 10^{-9} - 2 \times 10^{-5}$ bar. Also plotted for scale is the TOA solar flux.

Note that for the same $\mathrm{pSO_2}$, the surface radiance varies as a function of $\mathrm{pCO_2}$. This is because at high $\mathrm{pCO_2}$, the scattering optical depth of the atmosphere exceeds

unity. In such a regime, the impact of trace absorbers is amplified due to higher effective path length caused by multiple scattering events (Bohren 1987). This effect has been seen in studies of UV transmittance through thick clouds on Earth as well (Mayer et al. 1998). Consequently, the surface UV environment is a feature of both pCO_2 and pSO_2. For $pSO_2 \geq \times 10^{-5}$ bar, UV fluence < 330 nm is strongly suppressed.

H_2S is also a major volcanogenic gas that may have been emitted at rates greater than or equal to SO_2 on young Mars, based on studies of the oxidation state of Martian basalts (Herd et al. 2002; Halevy et al. 2007). While Halevy & Head (2014) do not calculate the H_2S abundance as a function of volcanic outgassing, the calculations of Hu et al. (2013) (T_0=288K, modern solar irradiance) suggest that pH_2S>pSO_2 in a CO_2 dominated atmosphere. Consequently, we also consider the impact of elevated levels of H_2S, up to $pH_2S = 2 \times 10^{-4}$ bar in atmospheres with $pCO_2 = 0.02 - 2$ bar. Figure 4.7 presents the surface radiance calculated over this range of atmospheres (SZA=0, A corresponding to desert, and $T_0 = 250$ K). For $pH_2S \geq \times 10^{-4}$ bar, UV fluence < 370 nm is strongly suppressed.

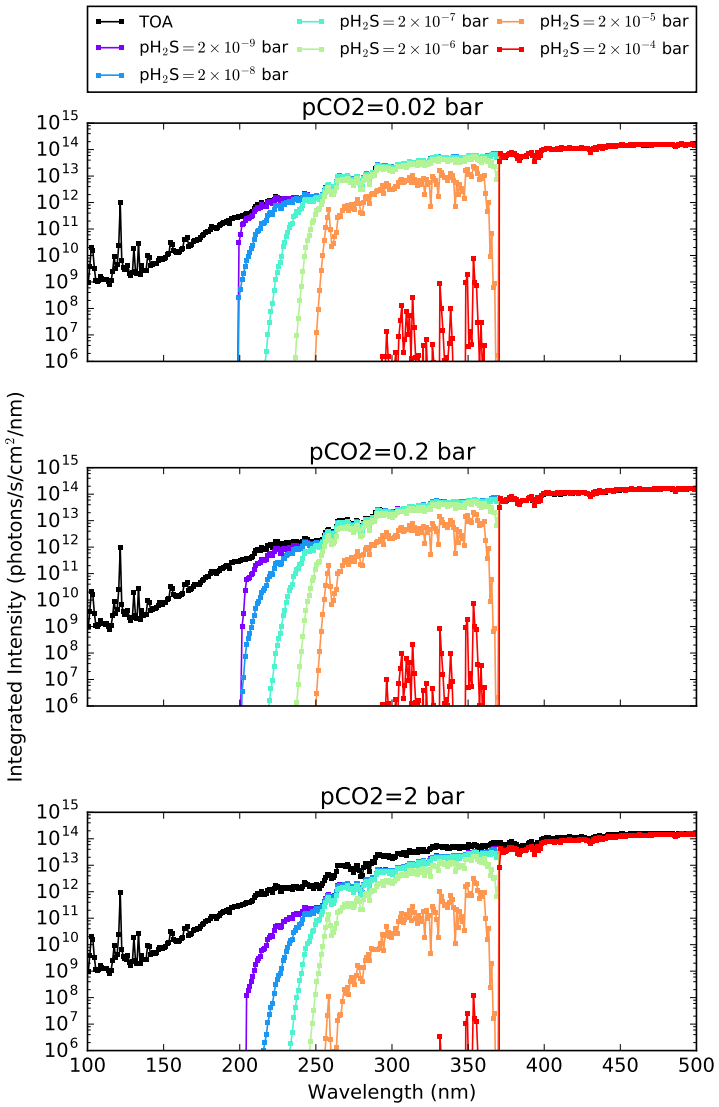

Figure 4.7: Surface radiance as a function of wavelength for T_0 = 250K, SZA=0, A corresponding to desert, $pCO_2 = 0.02 - 2$ bar, and $pH_2S = 2 \times 10^{-9} - 2 \times 10^{-4}$ bar. Also plotted for scale is the TOA solar flux.

Scattering due to thick cloud decks can also enhance absorption by trace pSO_2 and pH_2S. For $pSO_2 = 2 \times 10^{-7}$ bar and pCO_2=0.02 bar[8] (SZA=0, A corresponding

[8]At pCO_2=0.02 bar, the gaseous scattering optical depth is less than unity for wave-

to new snow (near 1), $T_0 = 250$ K, $r_{eff} = 10\mu$m), inclusion of CO_2 clouds with optical depth of 1000 amplifies attenuation by a factor of 10 at 236.5 nm (optically thin in SO_2 absorption) and by a factor of 10^5 at 281.5 nm (optically thick in SO_2 absorption) compared to what one would calculate by multiplying the transmission from the SO_2 and cloud deck individually. This effect is weaker for low-albedo cases, because there are fewer passes of radiation through the atmosphere due to bouncing between the surface and cloud deck. This nonlinear variance in transmission due to multiple scattering effects illustrates the need to specify surface albedo, cloud thickness and absorber level when calculating surface radiances. Figure 4.8 and Figure 4.9 present the surface radiance at the base of a pCO_2=0.02 bar atmosphere with varying levels of SO_2 and H_2S respectively, with CO_2 cloud decks of optical depths $1 - 1000$ emplaced from 20-21 km (SZA=0, A corresponding to desert, $T_0 = 250$ K, $r_{eff} = 10\mu$m).

---

lengths longer than 204 nm, meaning that we can attribute this amplification primarily to the cloud deck (as opposed to gaseous scattering).

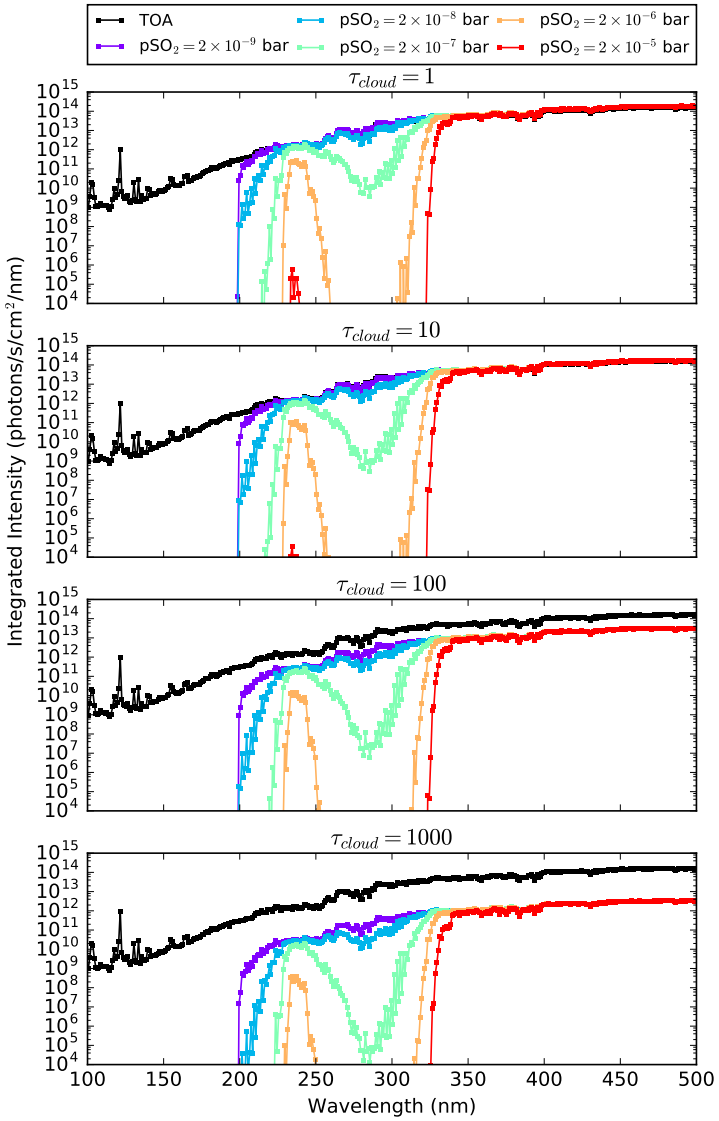

Figure 4.8: Surface radiance as a function of wavelength for T_0 = 250K, SZA=0, A corresponding to desert, pCO_2 = 0.02 bar, $pSO_2 = 2 \times 10^{-9} - 2 \times 10^{-5}$ bar, and CO_2 cloud decks of varying optical thickness emplaced from 20-21 km altitude. Also plotted for scale is the TOA solar flux.

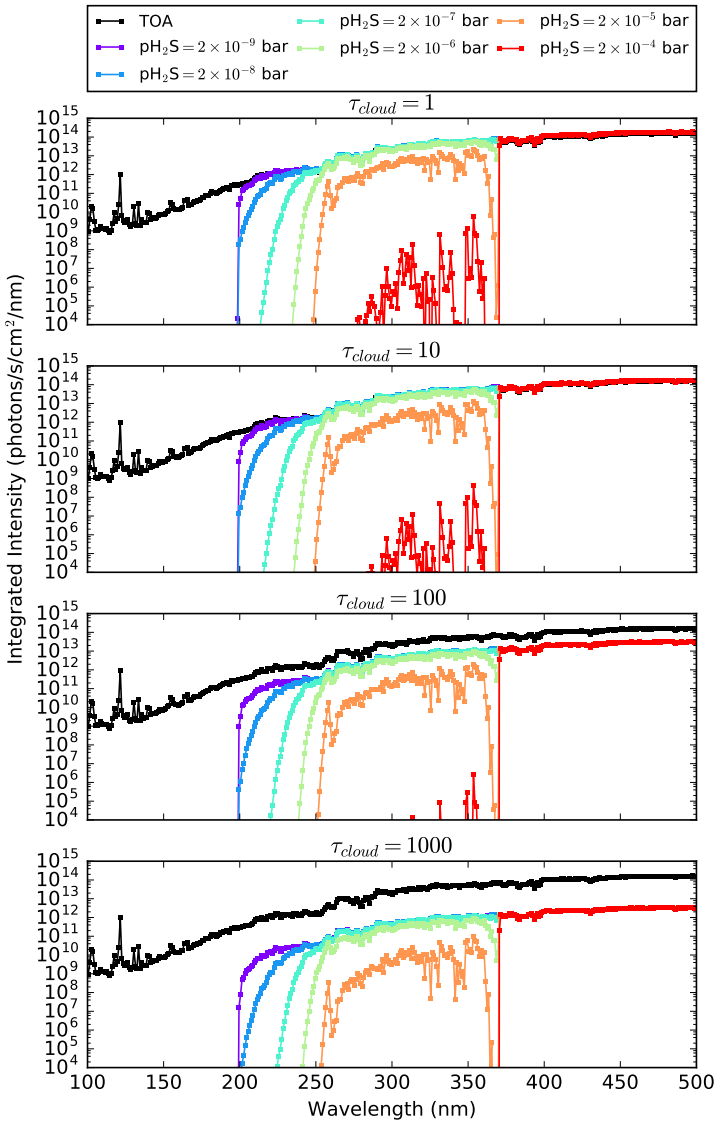

Figure 4.9: Surface radiance as a function of wavelength for T_0 = 250K, SZA=0, A corresponding to desert, pCO_2 = 0.02 bar, pH_2S= $2 \times 10^{-9} - 2 \times 10^{-4}$ bar, and CO_2 cloud decks of varying optical thickness emplaced from 20-21 km altitude. Also plotted for scale is the TOA solar flux.

4.4.4 Effect of Dust

The atmosphere of modern Mars is dusty, with typical dust optical depths varying from $\tau_d \sim 0.2 - 2$ at solar wavelengths (Smith et al. 2002; Lemmon et al. 2015), with the higher values achieved during global dust storms. Mars's dryness contributes to its dustiness, through the availability of desiccated surface to supply dust and the lack of a hydrologic cycle to quickly scrub it from the atmosphere. If one assumes that Mars were similarly dry in the past, dust levels in the Martian atmosphere may have been significant. We may speculate that if the atmosphere were thicker, it could have hosted even more dust than the modern Martian atmosphere due to slower sedimentation times. However, detailed study of atmospheric dust dynamics, including analysis of how dust lofting scales with pCO_2, is required to constrain this possibility. Dust absorbs at UV wavelengths (see Figure 4.1), so dust could play a role similar to volcanogenic gases in scrubbing UV radiative from the UV surface environment.

We explored the impact of including dust in our calculation of surface UV fluence. We assumed that, similar to the modern Mars, the dust followed an exponential profile with scale height height $H_d = 11$ km, similar to the atmospheric pressure scale height (Hoekzema et al. 2010; Mishra et al. 2016). For surface temperatures (and hence scale heights) comparable to modern Mars, this corresponds to the assumption by previous workers that the dust mixing ratio is constant in the lower atmosphere (Forget et al. 1999). Then, the dust optical depth across each atmospheric layer of width Δz is

$$C \exp\left[-z/H_d\right],$$

where z is the altitude of the layer center. The parameter

$$C = \tau_d(\exp\left[\Delta z/(2H_d)\right])(1 - \exp\left[-\Delta z/H_d\right])$$

is chosen such that the column-integrated dust optical depth is τ_d.

Figure 4.10 presents the surface radiance for varying τ_d and $pCO_2 = 0.02 - 2$ bar (SZA=0, A corresponding to desert, and $T_0 = 250$ K). As for SO_2 and H_2S, highly scattering atmospheres amplify the impact of trace absorbers. $\tau_d = 1$ only marginally suppresses UV fluence for $pCO_2 = 0.02$ bar, but for $pCO_2 = 2$ bar shortwave fluence is suppressed due to enhanced Rayleigh scattering. In the absence of scattering amplification, $\tau_d \gtrsim 10$ is required to strongly suppress UV fluence.

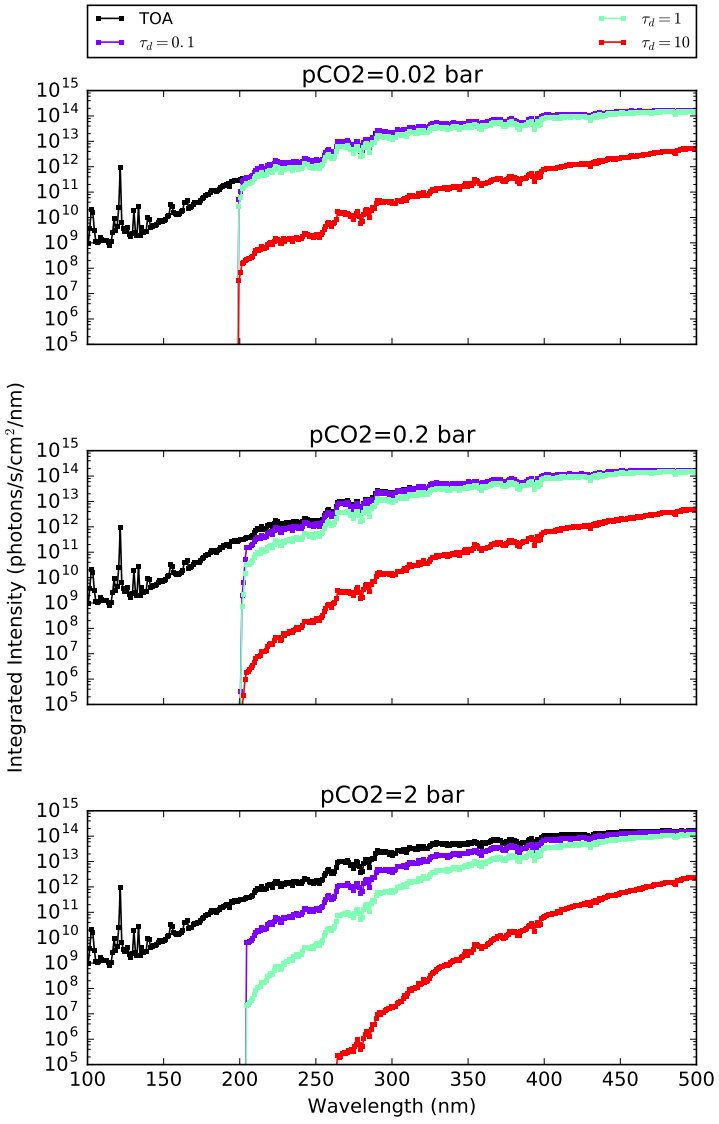

Figure 4.10: Surface radiance as a function of wavelength for T_0 = 250K, SZA=0, A corresponding to desert, $\mathrm{pCO_2} = 0.02 - 2$ bar, and $\tau_d = 0.1 - 10$. Also plotted for scale is the TOA solar flux.

Figure 4.11 presents the surface radiance at the base of a $\mathrm{pCO_2}$=0.02 bar atmosphere with varying τ_d, with $\mathrm{CO_2}$ cloud decks of optical depths $1 - 1000$ emplaced from 20-21 km (SZA=0, A corresponding to desert, T_0 = 250 K, $r_{eff} = 10\mu$m). The impact of a

cloud deck is less than the impact of increasing overall atmospheric pressure, because of the limited column of absorber contained within the cloud itself. If the cloud deck is extended, then the surface fluence is reduced (for the same total cloud and dust optical depth).

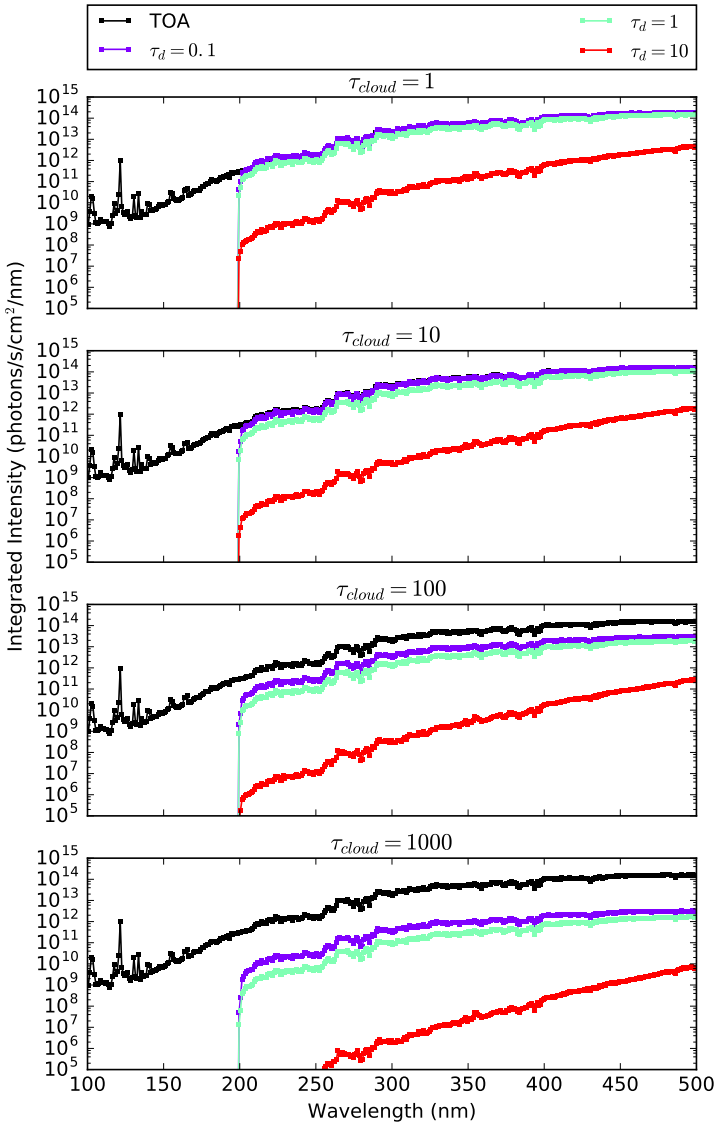

Figure 4.11: Surface radiance as a function of wavelength for T_0 = 250K, SZA=0, A corresponding to desert, $pCO_2 = 0.02$ bar, $\tau_d = 0.1 - 10$, and CO_2 cloud decks of varying optical thickness emplaced from 20-21 km altitude. Also plotted for scale is the TOA solar flux.

4.5 Discussion

4.5.1 CO_2-H_2O Atmosphere

Normative CO_2-H_2O climate models predict the steady-state early Martian climate to have been cold, with global mean temperatures below freezing (Forget et al. 2013; Wordsworth et al. 2013b, 2015). In this scenario, aqueous prebiotic chemistry would proceed in meltwater pools, which could have occurred transiently during midday due to the diurnal cycle, during summer during a seasonal cycle, or a combination of both. Aqueous prebiotic chemistry could also have proceeded in geothermally heated pools, which may have been abundant during the more volcanically active Noachian.

Figure 4.12 presents the dose rates $\overline{D}_i$ corresponding to irradiation of prebiotically relevant molecules through a clear-sky CO_2-H_2O atmosphere with SZA=0 and A corresponding to desert. The dose rates $\overline{D}_i$ decline by only an order of magnitude across 5 orders of magnitude of $pCO_2 \leq 2$ bar, meaning that the prebiotic photochemistry dose rates are only weakly sensitive to pCO_2 across this range. $\overline{D}_i$ is within an order of magnitude of unity across this range, meaning that the Martian dose rates are comparable to the terrestrial rates. This is consistent with the results of Cockell (2000b), who found that UV stress as measured by DNA damage were comparable for 3.5 Ga Earth and Mars.

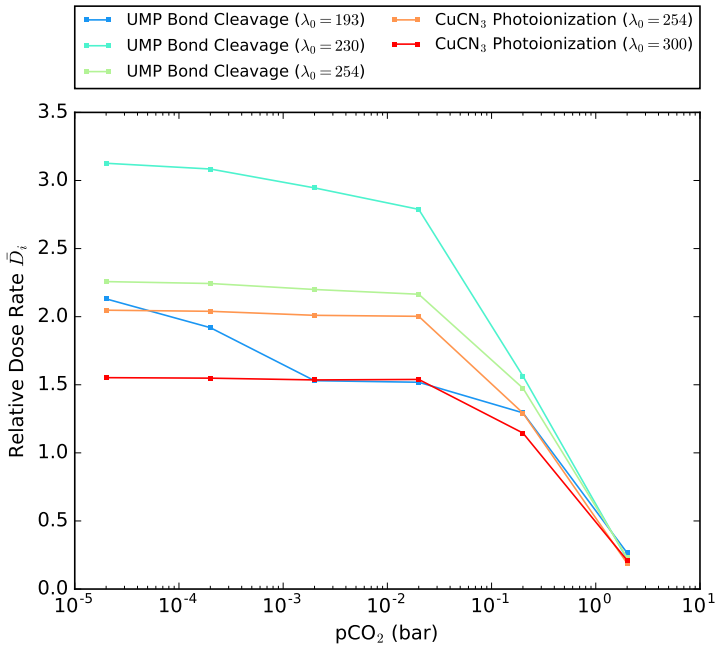

Figure 4.12: UV dose rates $\overline{D}_i$ for clear-sky CO_2-H_2O atmospheres as a function of pCO_2 ($T_0 = 250$K, SZA=0, A corresponding to desert).

However, the sky was not necessarily clear during this epoch. In fact, formation of H_2O and CO_2 clouds are expected based on GCM studies (Wordsworth et al. 2013b). Thick (though patchy) CO_2 cloud decks in particular are expected for thick CO_2 atmospheres. Figure 4.13 presents the dose rates $\overline{D}_i$ as a function of CO_2 cloud optical depth for pCO_2=0.02 bar, SZA=0, and A corresponding to desert. As we might expect from Figure 4.5, the dose rate drops off only modestly with τ_{cloud}. $\tau_{cloud} \gtrsim 1000$ is required to suppress dose rates by more than an order of magnitude. For $r_{eff} = 10\mu m$, this corresponds to 20× the maximum cloud column calculated by Wordsworth et al. (2013b). Overall, the impact of clouds on their own on UV-sensitive photochemistry is expected to be modest.

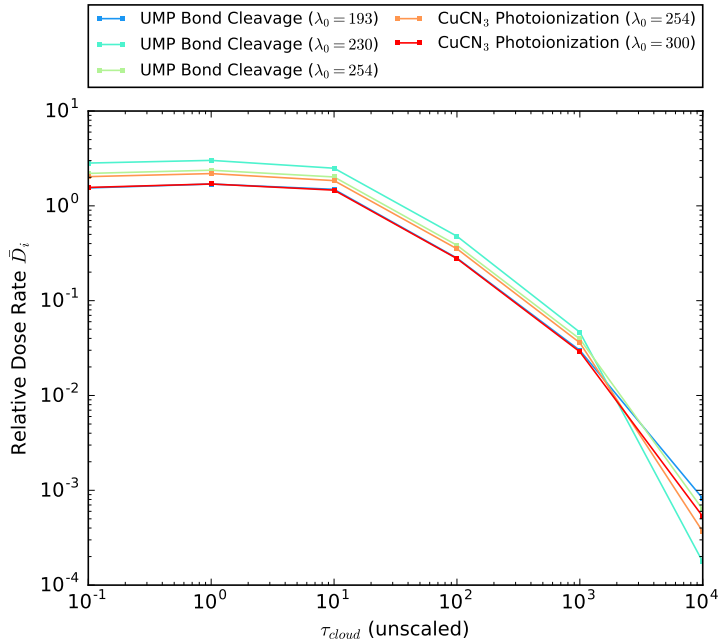

Figure 4.13: UV dose rates $\overline{D}_i$ for CO_2-H_2O atmospheres with a CO_2 cloud deck emplaced from 20-21 km altitude, as a function of cloud deck optical depth (T_0 = 250K, pCO_2=0.02 bar, SZA=0, A corresponding to desert).

If young Mars were indeed cold and dry, then one might expect it to have been dusty, as it is today. The modern Martian dust optical depth ranges from $\tau_d \sim 0.2 - 2$, with higher values achieved during dust storms (Smith et al. 2002; Lemmon et al. 2015). Higher dust loadings may have been possible when the atmosphere was thicker. Figure 4.14 presents the dose rates as a function of τ_d and pCO_2, for SZA=0 and A corresponding to desert. Figure 4.15 presents the dose rates as a function of τ_d and CO_2 cloud optical depth, for SZA=0 and A corresponding to desert.

Unlike CO_2 and H_2O ice and gas, dust absorbs across the UV waveband. Further, this absorption can be dramatically increased in highly scattering atmospheres due to

enhanced effective path length due to multiple scattering effects. Consequently, dust can dramatically suppress UV fluence and hence photochemistry, especially for thick and/or cloudy atmospheres. For $\tau_d \geq 10$, dose rates are suppressed by 2-10 orders of magnitude, depending on atmospheric pressure and cloud thickness. Dust of thickness $\tau_d = 1$ provides minimal suppression for $pCO_2 \leq 0.2$ bar or $\tau_{cloud} < 100$, but for $pCO_2 \geq 2$ bar or $\tau_{cloud} \geq 1000$, can suppress dose rates by orders of magnitude. Dust of thickness $\tau_d \leq 0.1$ does not significantly alter dose rates across the explored parameter space. Overall, dust can significantly alter dose rates if it is present at high levels (greater than that seen for modern Martian dust storms) or if it is present at levels comparable to the modern average, but embedded in a thick atmosphere or underlying thick clouds.

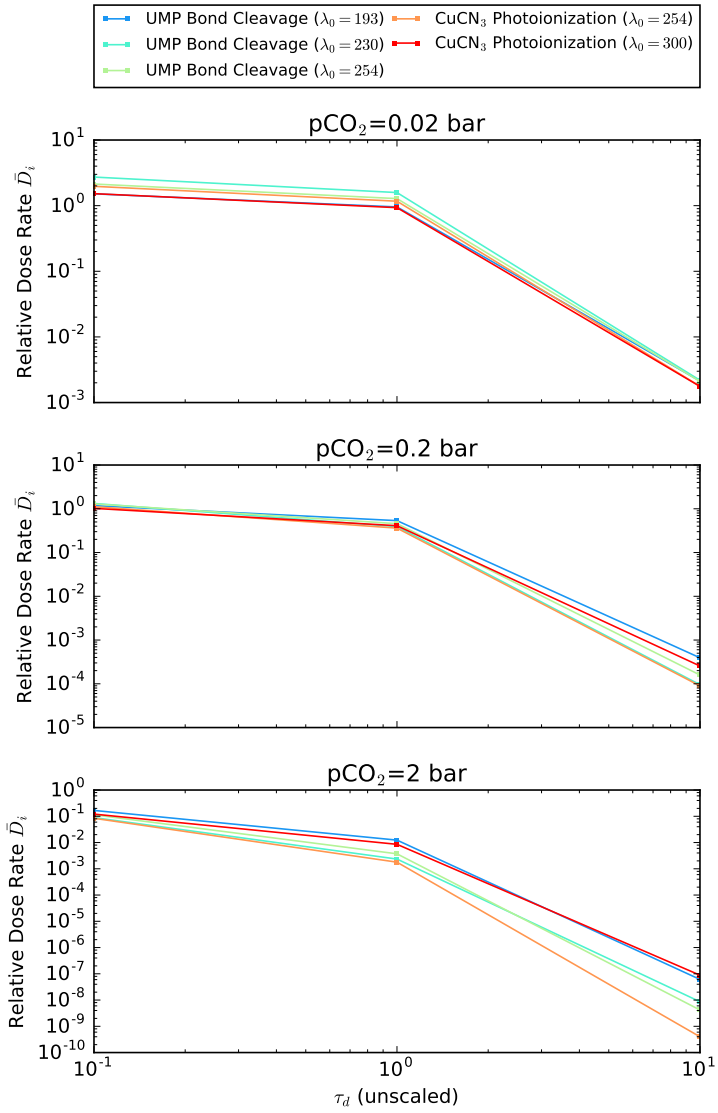

Figure 4.14: UV dose rates $\overline{D}_i$ for dusty CO_2-H_2O atmospheres as a function of pCO_2 and τ_d ($T_0 = 250$K, SZA=0, A corresponding to desert).

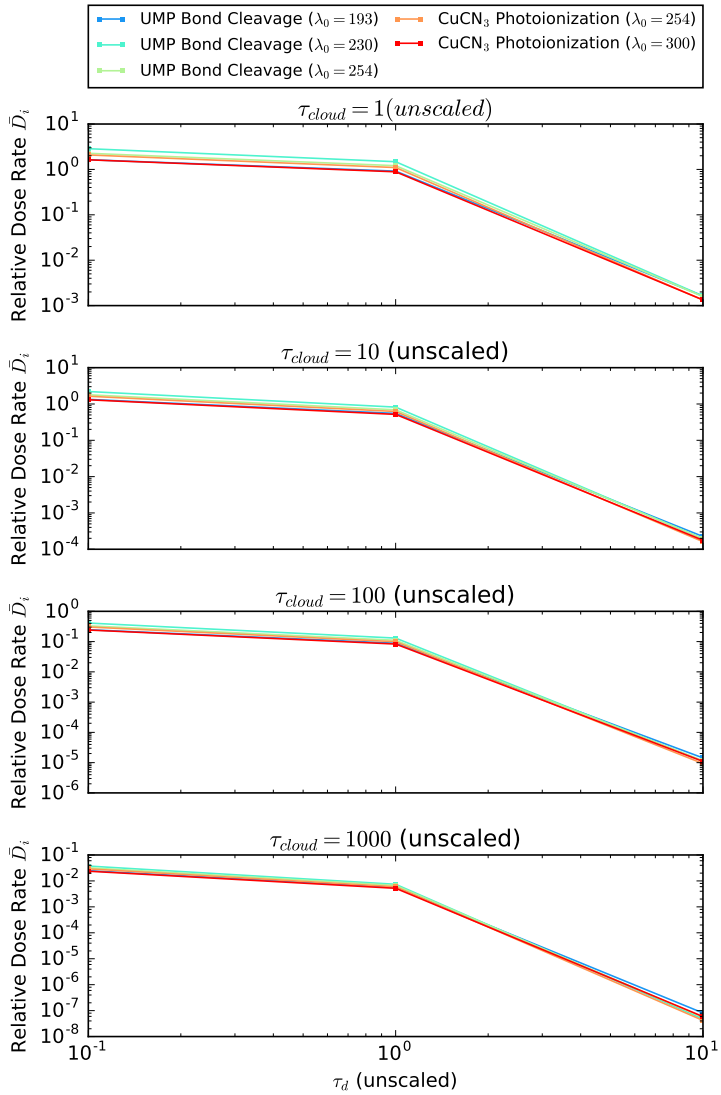

Figure 4.15: UV dose rates $\overline{D}_i$ for dusty CO_2-H_2O atmospheres with a CO_2 cloud deck emplaced, as a function of τ_d and τ_{cloud} (T_0 = 250K, pCO_2=0.02, SZA=0, A corresponding to desert).

We considered the hypothesis that attenuation due to dust might differentially affect the stressor and eustressor pathways. That is, we considered the possibility that the eustressor reaction rates might fall off faster (or slower) than the stressor reaction

rates with attenuation due to dust. Since the stressor pathway measures destruction of RNA monomers and the eustressor pathway measures a process important to the synthesis of key RNA precursors, this means that environments that favor the eustressor pathway over the stressor pathway are a more favorable venue for abiogenesis than the reverse, in the RNA world hypothesis. This argument assumes that these particular stressor and eustressor processes were important in the prebiotic world. They might not have been. However, we expect other photochemical stressor and eustressor processes to behave in generally similar ways to these processes. For example, we generally expect the quantum yield of prebiotic molecular destruction to decrease with increasing wavelength because of decreased photon energy compared to bond strength. Similarly, regardless of the solvated electron source (e.g. HS^- as opposed to tricyanocuprate), we expect the quantum yield to go approximately as a step function in wavelength. We therefore suggest that results derived from these pathways may generalize to other processes, though a detailed comparison is required to rule on this hypothesis.

To assess the hypothesis that a dusty Mars might be less (or more) clement for abiogenesis than a non-dusty Mars as measured by our stressor (UMP-X) and eustressor (CuCN3-Y) pathways, we calculated $\overline{D}_{UMP-X}/\overline{D}_{CuCN3-Y}$. We calculated this quantity for $pCO_2 = 2$ bar (no clouds) and $\tau_{cloud} = 1000$ (pCO_2=0.02 bar) for $\tau_d = 0.1 - 1$. If these ratios rise with τ_d, it means that the stressor pathway is relatively favored by dusty atmospheres; if they fall, it means that the stressor pathway is relatively disfavored by dusty atmospheres.

Figure 4.16 presents these calculations. Dust attenuation on its own is relatively flat at CO_2-scattering wavelengths, as is cloud attenuation. Consequently dusty/cloudy atmospheres tend to reduce UV fluence in a spectrally flat manner, and favor neither

the stressor nor the eustressor pathway. On the other hand, in a thick CO_2 atmosphere, the scattering optical depth, and hence amplification of dust absorption, increases as wavelength decreases. Consequently, the dose rate ratio does change with increasing τ_d. However, the direction of the change is sensitive to the value of λ_0, the ionization threshold for the tricyanocuprate ionization process, and the magnitude is further sensitive to the value of λ_0 for the UMP cleavage process. We consequently conclude it is possible that thick, dusty atmospheres might be more or less clement for abiogenesis than non-dusty atmospheres, but determining which requires wavelength-dependent measurements of the QYs of these chemical processes in the laboratory.

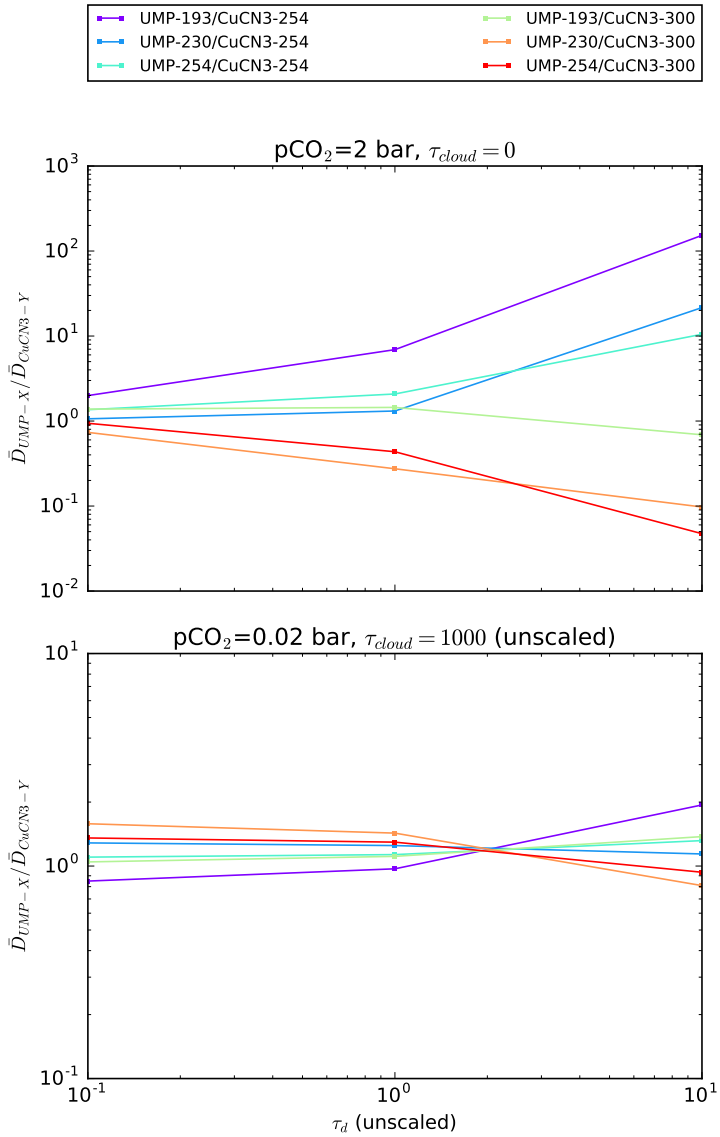

Figure 4.16: Ratio of stressor dose rates UMP-X divided by eustressor dose rates UMP-Y for dusty CO_2-H_2O atmospheres, as a function of τ_d ($T_0 = 250$K, SZA=0, A corresponding to desert). The atmospheres are highly scattering, either because of high pCO_2 or thick CO_2 clouds. Lower ratios imply a more favorable environment for abiogenesis as measured by these two photoprocesses.

4.5.2 Highly Reducing Atmospheres

Recent work suggests that if the reduced gases H_2 and/or CH_4 were present at elevated levels in a thick ($\sim$ 1 bar) atmosphere, collision-induced absorption (CIA) due to the interaction of these gases with CO_2 might provide enough greenhouse warming to elevate mean Noachian temperatures above freezing (Ramirez et al. 2014; Wordsworth et al. 2017). Ramirez et al. (2014) found that global mean surface temperatures exceeded 273K for $P_0 \geq 3$ bar and $[H_2] \geq 0.05$, with higher concentrations of H_2 required for lower P_0. More recently, Wordsworth et al. (2017) used new ab initio calculations of H_2-CO_2 and CH_4-CO_2 CIA to show earlier estimates of the CIA were underestimated, and that 2-10% levels of CH_4 or H_2 in a > 1.25 bar atmosphere could elevate planetary mean temperatures over freezing. While it is unclear if such high reducing conditions can be sustained in the steady state, this scenario remains an intriguing avenue to a Noachian Mars with conditions at least transiently globally clement for liquid water and prebiotic chemistry (Batalha et al. 2015; Wordsworth et al. 2017).

H_2 is spectrally inert at UV wavelengths compared to CO_2. Based on the constraints on H_2 absorption we found (Backx et al. 1976; Victor & Dalgarno 1969), the contribution of H_2 to atmospheric absorption and scattering are negligible for H_2 mixing ratios of $0 - 0.1$. Similarly, CH_4 does not absorb at wavelengths longer than 165 nm (Au et al. 1993; Chen & Wu 2004). Hence, its absorption is highly degenerate with CO_2, and its presence at the levels suggested in Wordsworth et al. (2017) does not impact the UV surface environment. Photochemically-generated hydrocarbon hazes require CH_4/CO_2 ratios of > 0.1, and are consequently expected to be thin or nonexistent in this scenario (DeWitt et al. 2009). Consequently, the UV surface environment in an H_2 or CH_4-rich

atmosphere should be similar to the pCO_2=2 bar case discussed in Section 4.5.1.

4.5.3 Highly-Volcanic Mars (CO_2-H_2O-SO_2/H_2S Atmosphere)

We have so far considered atmospheres with CO_2 and H_2O as their dominant photoactive gaseous species. However, other gases have been proposed as significant constituents of the Martian atmosphere. In particular, Halevy et al. (2007) suggest that the lack of massive carbonate deposits on Mars could have been explained if, during epochs of high volcanism on young Mars, SO_2 built up to the $\sim 1 - 100$ ppm level. At such levels, Halevy et al. (2007) find that SO_2 would supplant CO_2 as the agent regulating global chemistry and climate, inhibiting massive carbonate precipitation in the process. Halevy & Head (2014) further argue that enhanced radiative forcing from high SO_2 levels could transiently raise mean surface temperatures at the subsolar point (assuming no horizontal heat transport) above the freezing point of water, explaining the observed fluvial features. Halevy & Head (2014) calculate that SO_2 mixing ratios $\gtrsim$ 10 ppm (1 bar atmosphere) could have been possible during, e.g., the emplacement of the Martian volcanic plains. While the impact of SO_2 on Martian carbonates and climate remains debated (e.g., Niles et al. 2013, Kerber et al. 2015), it remains plausible that Noachian Mars may have been characterized by at least transiently high SO_2 levels due to higher volcanic outgassing rates.

We consequently sought to explore the impact of elevated levels of SO_2 on the UV surface environment and hence prebiotic chemistry. Figure 4.17 presents the dose rates calculated for a clear-sky atmosphere with varying pSO_2 and pCO_2. Figure 4.18 presents the dose rates calculated for an atmosphere with pCO_2=0.02 bar (optically thin at

scattering wavelengths), but varying levels of CO_2 clouds. In both cases, SZA=0 and A corresponds to desert.

SO_2 is a far broader, stronger UV absorber than either CO_2 or H_2O, and consequently its presence can exert a dramatic impact on UV surface radiance and photochemistry rates. As with dust, multiple scattering from other atmospheric constituents can amplify SO_2 absorption. For $pCO_2 \leq 0.2$ bar, $pSO_2 \geq 2 \times 10^{-6}$ bar is required to suppress dose rates to $\overline{D}_i < 0.1$, whereas for $pCO_2 \geq 2$ bar, $pSO_2 \geq 2 \times 10^{-7}$ bar is sufficient. Similarly, for $\tau_{cloud} \leq 10$, $pSO_2 \geq 2 \times 10^{-6}$ bar is required to suppress dose rates to $\overline{D}_i < 0.1$, whereas for $\tau_{cloud} \geq 100$, $pSO_2 \geq 2 \times 10^{-7}$ bar is sufficient. For $pSO_2 \geq 2 \times 10^{-5}$ bar, UV-sensitive prebiotic photochemistry is strongly quenched.

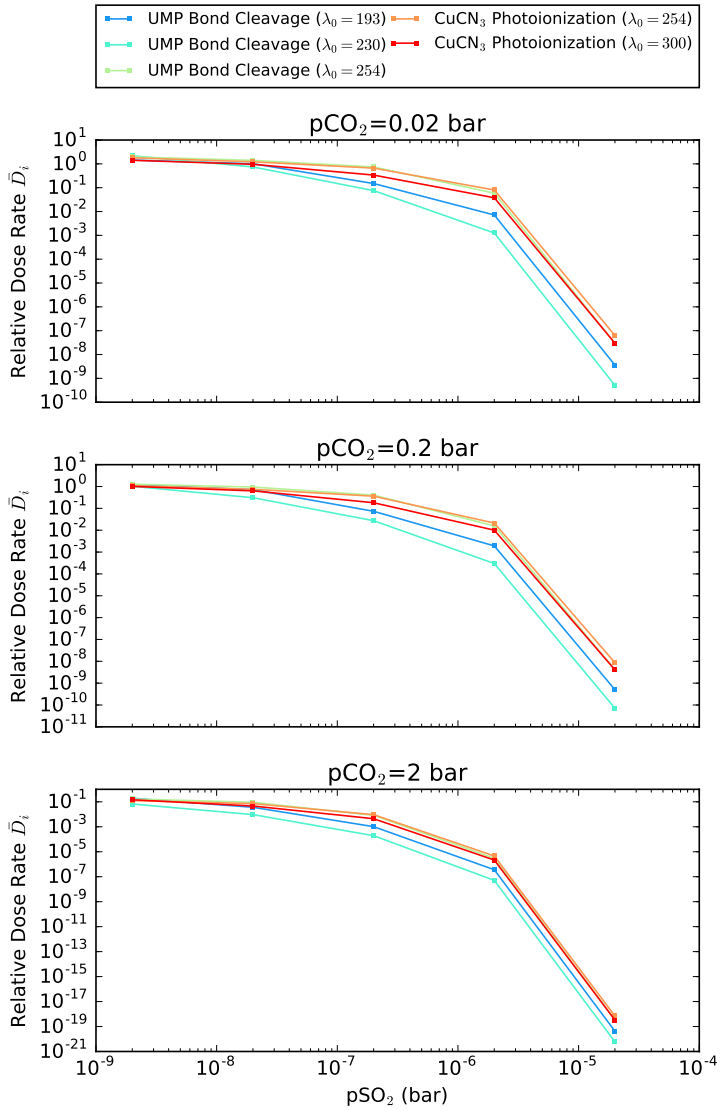

Figure 4.17: UV dose rates $\overline{D}_i$ for CO_2-H_2O-SO_2 atmospheres as a function of pCO_2 and pSO_2 ($T_0 = 250$K, SZA=0, A corresponding to desert).

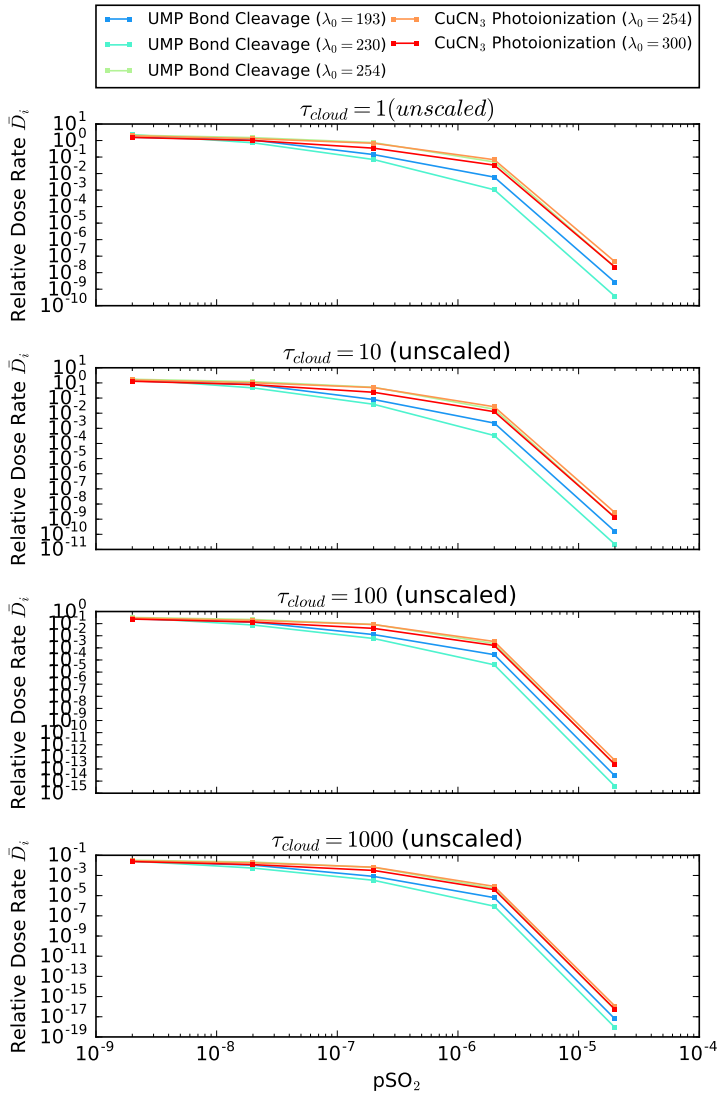

Figure 4.18: UV dose rates $\overline{D}_i$ for CO_2-H_2O-SO_2 atmospheres with a CO_2 cloud deck emplaced, as a function of pSO_2 and τ_{cloud} (T_0 = 250K, pCO_2=0.02SZA=0, A corresponding to desert).

As with dust, we considered the hypothesis that attenuation from SO_2 might have a differential impact on the eustressor and stressor pathways. We calculated $\overline{D}_{UMP-X}/\overline{D}_{CuCN3-Y}$ for pCO_2 = 2 bar (no clouds) and τ_{cloud} = 1000 (pCO_2=0.02

bar) for a broad range of pSO_2. This calculation is presented in Figure 4.19. We note that regardless of assumption on λ_0, as pSO_2 increases from $2 \times 10^{-7} - 2 \times 10^{-5}$ bar, the eustressor pathway is favored over the stressor pathways, by as much as 2 orders of magnitude (dependent on λ_0). We conclude that it seems plausible that high-SO_2 planetary atmospheres have a UV throughput more clement for abiogensis compared to low-SO_2 atmospheres under the assumption that the stressor and eustressor pathways we have identified were important. However, better measurements of the spectral QY of these photoprocesses is required to confirm and quantify the magnitude of this effect.

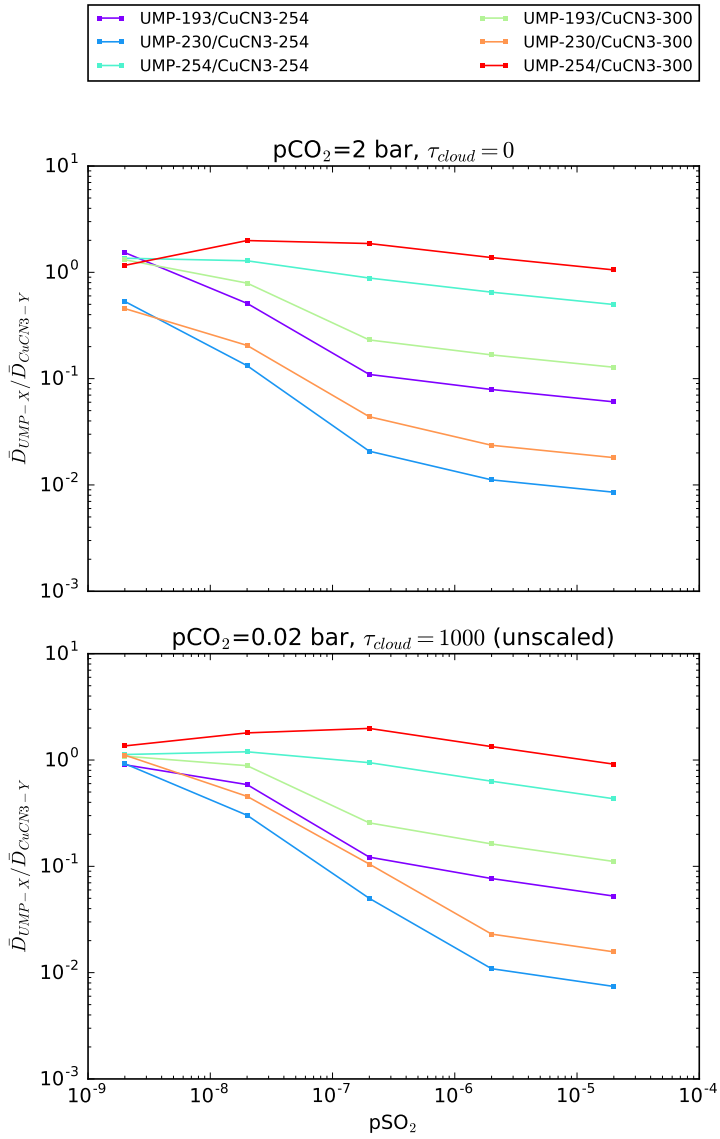

Figure 4.19: Ratio of stressor dose rates UMP-X divided by eustressor dose rates UMP-Y for CO_2-H_2O-SO_2 atmospheres, as a function of pSO_2 (T_0 = 250K, SZA=0, A corresponding to desert). The atmospheres are highly scattering, either because of high pCO_2 or thick CO_2 clouds. Lower ratios imply a more favorable environment for abiogenesis as measured by these two photoprocesses.

While Halevy & Head (2014) focused on the abundance of SO_2 in the Martian

atmosphere, H_2S is emitted in equal proportion by the more reduced Martian mantle (Halevy et al. 2007). Hu et al. (2013) model the atmospheric composition as a function of sulfur emission rate for a 1-bar CO_2 atmosphere assuming equipartition of the outgassed sulfur between SO_2 and H_2S, irradiated by a G2V star at a distance of 1.3 AU. They find H_2S concentrations to be even higher than SO_2 concentrations, by over an order of magnitude at high S emission rates. H_2S is also a stronger, broader UV absorber than CO_2 or H_2O. Consequently, we sought to explore the impact of elevated levels of H_2S on the UV surface environment and prebiotic photochemistry.

Figure 4.20 presents the dose rates calculated for a clear-sky atmosphere with varying pH_2S and pCO_2. Figure 4.21 presents the dose rates calculated for an atmosphere with pCO_2=0.02 bar (optically thin at scattering wavelengths), but varying levels of CO_2 clouds. In both cases, SZA=0 and A corresponding to desert. As with SO_2 and dust, highly scattering atmospheres can amplify H_2S absorption. For $pCO_2 \leq 0.2$ bar, $\overline{D}_i < 0.1$ for $pH_2S \geq 2 \times 10^{-5}$ bar, but for $pCO_2 \geq 2$ bar, $\overline{D}_i < 0.1$ for $pH_2S \geq 2 \times 10^{-6}$ bar. Similarly, for $\tau_{cloud} \leq 10$, $\overline{D}_i < 0.1$ for $pH_2S \geq 2 \times 10^{-5}$ bar, but for $\tau_{cloud} \geq 100$, $\overline{D}_i \lesssim 0.1$ for $pH_2S \geq 2 \times 10^{-6}$ bar. For $pH_2S \geq 2 \times 10^{-4}$ bar, surface photochemistry is strongly quenched regardless of atmospheric state.

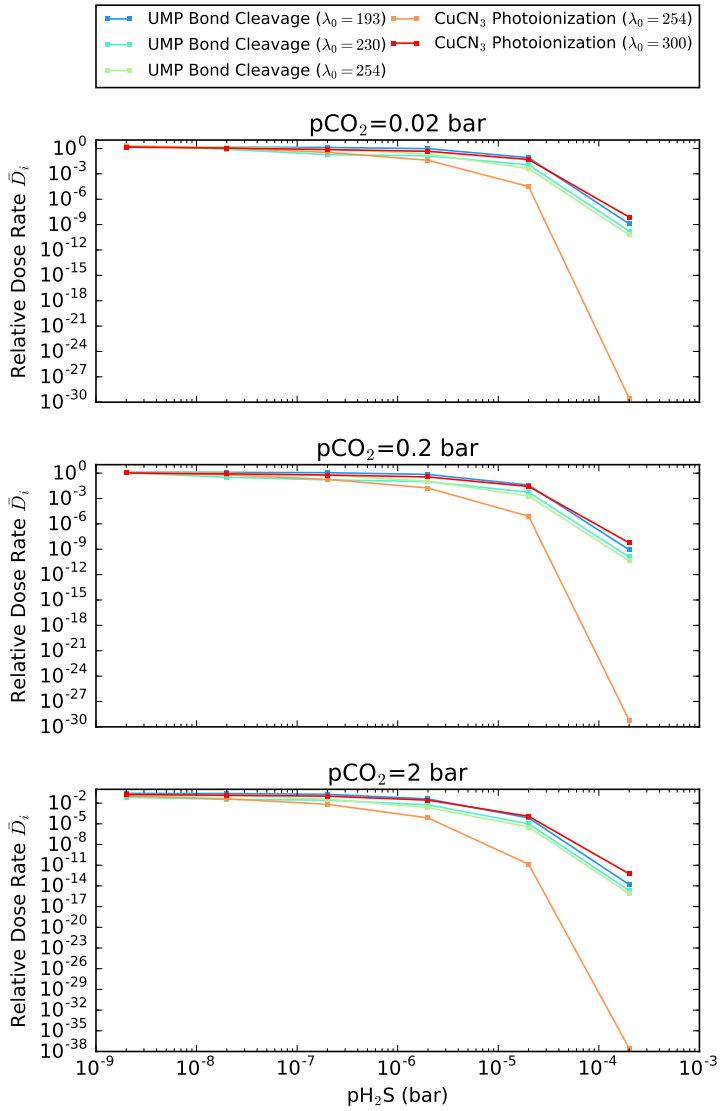

Figure 4.20: UV dose rates $\overline{D}_i$ for CO_2-H_2O-H_2S atmospheres as a function of pCO_2 and pH_2S ($T_0 = 250$K, SZA=0, A corresponding to desert).

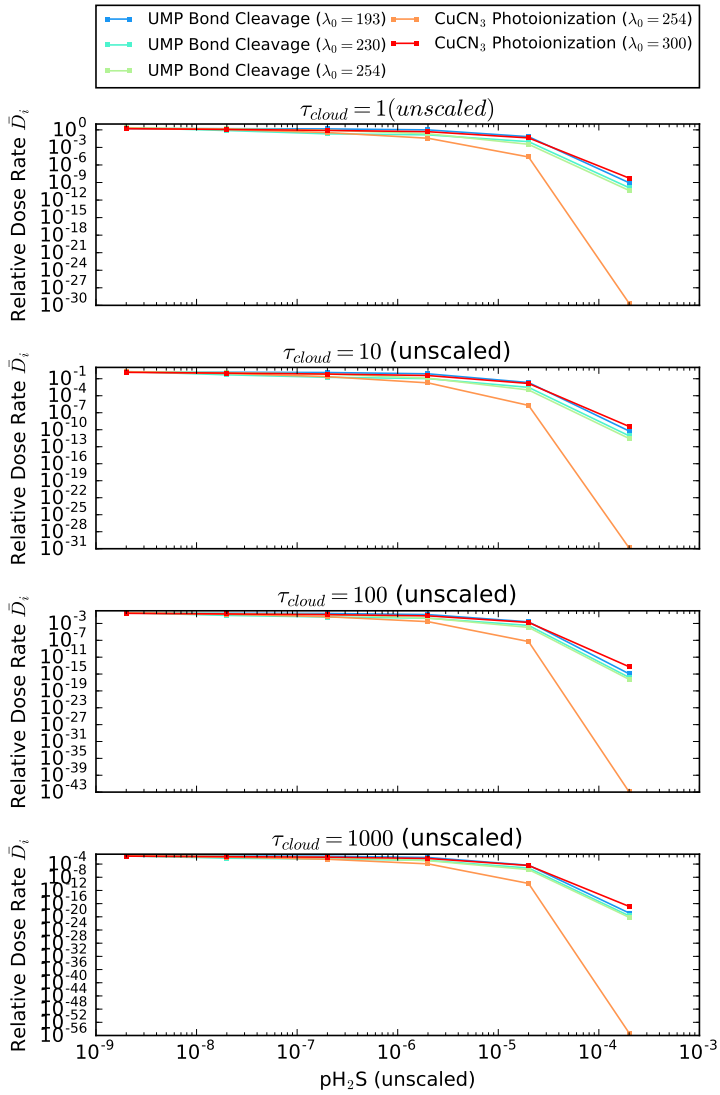

Figure 4.21: UV dose rates $\overline{D}_i$ for CO_2-H_2O-H_2S atmospheres with a CO_2 cloud deck emplaced, as a function of pH_2S and τ_{cloud} (T_0 = 250K, pCO_2=0.02 bar, SZA=0, A corresponding to desert).

We again considered the hypothesis that H_2S attenuation might have a differential impact on the stressor and eustressor dose rates. We calculated $\overline{D}_{UMP-X}/\overline{D}_{CuCN3-Y}$ for pCO_2 = 2 bar (no clouds) and τ_{cloud} = 1000 (pCO_2=0.02 bar) for a broad range of

pH_2S. This calculation is presented in Figure 4.22. As in the case of dust in a dense CO_2 atmosphere, the ratios diverge from 1, but in opposite directions depending on the value assumed for λ_0 for photoionization of tricyanocuprate. We conclude that attenuation from H_2S may well have a differential impact on the stressor and eustressor dose rates, but that assessing which it favors requires better constraints on the QYs of the photoprocesses, especially the photoionization of tricyanocuprate.

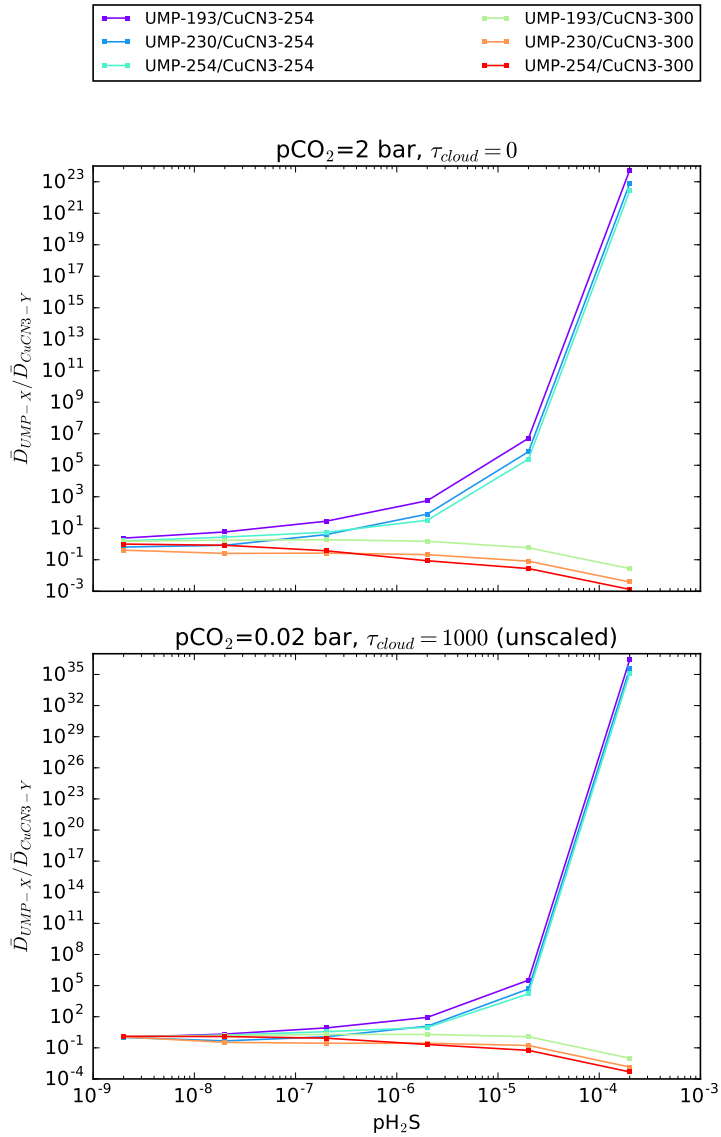

Figure 4.22: Ratio of stressor dose rates UMP-X divided by eustressor dose rates UMP-Y for CO_2-H_2O-H_2S atmospheres, as a function of pH_2S (T_0 = 250K, SZA=0, A corresponding to desert). The atmospheres are highly scattering, either because of high pCO_2 or thick CO_2 clouds. Lower ratios imply a more favorable environment for abiogenesis as measured by these two photoprocesses.

4.6 Conclusion

We have used a two-stream multi-layer radiative transfer model to estimate the UV surface environment on the surface of 3.9 Ga Mars as a function of atmospheric composition, and explored the implications for prebiotic chemistry. Prebiotic photoreaction rates are within an order of magnitude of the terrestrial values for normative clear-sky CO_2-H_2O atmospheres, in agreement with past work (e.g., Cockell 2000b) suggesting early Martian and terrestrial atmospheres featured comparable UV environments. In agreement with prior work, we find shortwave radiation to be effectively attenuated by CO_2 absorption, with fluence $\lesssim 185$ nm removed for $pCO_2 \geq 2 \times 10^{-5}$ bar and fluence < 204 nm removed for $pCO_2 \geq 0.2$ bar. Fluence drops off more slowly in the > 204 nm regime, where neither CO_2 nor H_2O absorb. This is a consequence of random walk statistics in highly scattering regimes, and stands in contrast to prior studies(Rontó et al. 2003; Cnossen et al. 2007) which did not account for multiple scattering. The impact of CO_2 and H_2O clouds on their own is similarly muted because they too are pure scatterers in the > 204 nm regime; $\tau_{cloud} \geq 100$ is required to significantly affect surficial reaction rates, comparable to but in excess of the highest patchy cloud optical depths predicted by some 3D GCM studies (e.g., Wordsworth et al. 2013b).

While dense atmospheres and cloud decks only modest reduce surface fluence on their own, in concert with other absorbers (dust, SO_2, H_2S) they can have a dramatic effect on surface fluence and reaction rates, though amplification of the effects of these absorbers. Dust levels of $\tau_d = 1$, only a factor of a few higher than that sustained in the modern atmosphere, could suppress prebiotic reaction rates by orders of magnitude for $pCO_2 \geq 2$bar or $\tau_{cloud} \geq 1000$, and dust levels of $\tau_d = 10$ would sharply reduce

reaction rates independent of the atmospheric state. Similarly, $pSO_2 \geq 10^{-7}$ bar or $pH_2S \geq 2 \times 10^{-6}$ bars are required to significantly reduce reaction rates for $pCO_2 \geq 2$bar or $\tau_{cloud} \geq 100$, but for less scattering atmospheres, $pSO_2 \geq 10^{-6}$ bar or $pH_2S \geq 2 \times 10^{-5}$ bar is required. $pSO_2 \geq 10^{-5}$ bars or $pH_2S \geq 2 \times 10^{-4}$ bars quenches UV-sensitive photochemistry by many orders of magnitude regardless of other atmospheric conditions.

The absorbers described above have spectrally variable absorption, and prebiotic photochemistry is wavelength-dependent, leading us to speculate whether high abundances of these absorbers, despite suppressing UV-sensitive chemistry generally, might not favor or disfavor eustressor photoprocesses conducive to the origin of life compared to stressor processes that impede life's formation. We compare the relative impact of absorption from dust, SO_2, and H_2S attenuation on two such stressor (cleavage of the N-glycosidic bond of UMP) and eustressor photoprocesses (production of aquated electrons from $CuCN_3^{2-}$). We find that it is possible for high levels of these absorbers to disproportionately favor one or the other of these photoprocesses. In particular, high SO_2 levels may create an especially favorable environment for abiogenesis, under the assumption that these photoprocesses were important to abiogenesis (so long as enough fluence reaches the ground to power these reactions). However, the magnitude and direction of this effect is sensitive to assumptions about the QY of these processes. Better characterization of the spectral quantum yields of these processes are required to rule definitively on this question.

Acknowledgements

We thank C. Magnani and S. Rugheimer for sharing their data with us, and for many insightful conversations. We thank J. Sutherland and J. Szostak for sharing their insights into prebiotic chemistry. We thank two anonymous referees, whose comments improved this manuscript.

This research has made use of NASA's Astrophysics Data System Bibliographic Services, and the MPI-Mainz UV-VIS Spectral Atlas of Gaseous Molecules.

S. R. and D. D. S. gratefully acknowledge support from the Simons Foundation, grant no. 290360.

4.7 Appendix A: Sample Atmospheric Profiles

This appendix presents sample atmospheric profiles calculated using the methods in Section 4.3.2, to illustrate the application of these methods. Figure 4.23 shows the T/P profiles associated with a sample atmosphere with varying (pCO_2, T_0), where pCO_2 is the surface partial pressure of CO_2. Figure 4.24 shows the pressure, temperature, and H_2O molar concentration altitude provides associated with an atmosphere with $T_0 = 250$ K and varying pCO_2.

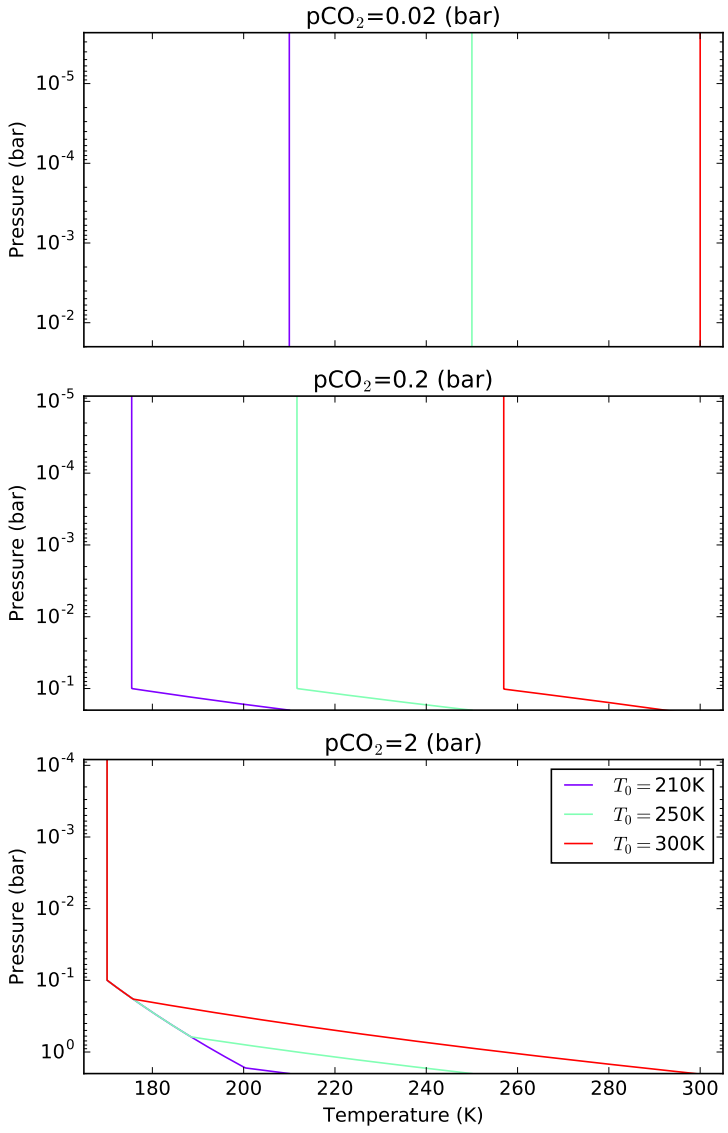

Figure 4.23: Sample T/P profiles for CO_2-dominated CO_2-H_2O atmospheres using the methodology in Section 4.3.2 for $T_0 = 210, 250, 300$K and $pCO_2 = 0.02, 0.2, 2$ bar. The pressure is the total atmospheric pressure (CO_2 and H_2O).

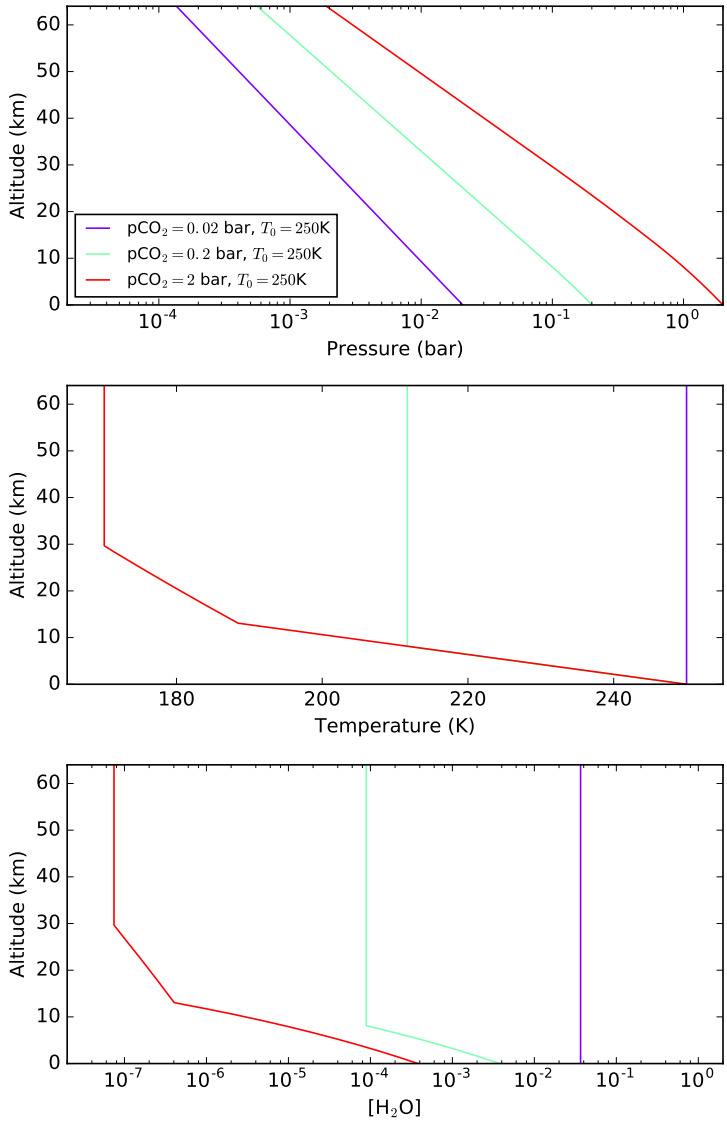

Figure 4.24: Temperature, pressure, and molar concentration of H_2O for atmospheres with $pCO_2 = 0.02, 0.2, 2$ bar and $T_0 = 250$K.

Chapter 5

The Surface UV Environment on Planets Orbiting M-Dwarfs: Implications for Prebiotic Chemistry & Need for Experimental Follow-Up

This thesis chapter has been submitted as:

S. Ranjan, R. Wordsworth, and D. Sasselov. Submitted to the Astrophysical Journal on 14 March 2017.

Abstract

Potentially-habitable planets orbiting M-dwarfs are of intense astrobiological interest because they are the only rocky worlds accessible to biosignature search over the next 10+ years due to a confluence of observational effects. Simultaneously, recent experimental and theoretical work suggests that UV light may have played a key role in the origin of life on Earth, and especially the origin of RNA. Characterizing the UV environment on M-dwarfs planets is important to understanding whether life as we know it could emerge on such worlds. In this work, we couple radiative transfer models to observed M-dwarf spectra to determine the UV environment on prebiotic Earth-analog planets orbiting M-dwarfs. We calculate dose rates to quantify the impact of different host stars on prebiotically-important photoprocesses. We find that M-dwarf planets have access to 100-1000 times less bioactive fluence than the young Earth. It is unclear whether UV-sensitive prebiotic chemistry that may have been important to abiogenesis, such as the only known prebiotically plausible pathways for pyrimidine ribonucleotide synthesis, could function on M-dwarf planets. This uncertainty affects objects like the recently-discovered habitable-zone planets orbiting Proxima Centauri and TRAPPIST-1. Laboratory studies of the sensitivity of putative prebiotic pathways to irradiation level are required to resolve this uncertainty. If steady-state M-dwarf UV output is insufficient to power these pathways, transient elevated UV irradiation due to flares may suffice; laboratory studies can constrain this possibility as well.

5.1 Introduction

Planets orbiting M-dwarfs are the most compelling targets for the search for life beyond the solar system. M-dwarfs are the most common type of star in the Galaxy, and exoplanet population studies suggest potentially habitable[1] planets orbiting these stars are common (Dressing & Charbonneau 2015). Indeed, Proxima Centauri, the closest star to our Solar System and an M-dwarf, has recently been shown to host a potentially habitable world (Anglada-Escudé et al. 2016), and the late M-dwarf TRAPPIST-1 (Gillon et al. 2017). Perhaps most importantly, due to a confluence of observational effects, M-dwarf terrestrial planets (and *only* M-dwarf terrestrial planets) will be accessible to atmospheric characterization and hence biosignature search with the flagship telescopes[2] due to come online over the next decade (Seager 2014; Rodler & López-Morales 2014; Batalha et al. 2015; Cowan et al. 2015). Such observations will require tens to hundreds of hours of observation time on the best telescopes in the world, a very large investment. Consequently, it is crucial to understand whether life can emerge and endure on such worlds.

Extensive work has been done on M-dwarf planet habitability, i.e., whether life as we know it could endure on these worlds; see, e.g., Tarter et al. (2007), Scalo et al. (2007), and Shields et al. (2016b) for reviews of work on this topic. However, far fewer investigations have been conducted as to the favorability of M-dwarf planets for abiogenesis (the origin of life), i.e., whether life as we know it could emerge on

[1] i.e. Earth-sized planets receiving instellation compatible with surface liquid water

[2] e.g. the James Webb Space Telescope, JWST, and the Extremely Large Telescopes, ELTs

these worlds. In part, the paucity of work on this question is due to limitations in our understanding of the origin of life. For example, much of the work on exoplanet habitability has been motivated by the biological fact that life as we know it today requires liquid water, and has focused on understanding the availability of this key requirement for life in different planetary environments (e.g., Kasting et al. 1993). Such certainty does not exist in our understanding of the origin of life on Earth, making it challenging to compare the clemency of planetary environments for abiogenesis scenarios.

Recent advances in prebiotic chemistry (chemistry relevant to the origin of life) are changing this situation. The last decade has seen breakthroughs in long-standing problems in prebiotic chemistry, perhaps most remarkably in the discovery of plausible mechanisms for the prebiotic synthesis of activated pyrimidine ribonucleotides (Powner et al. 2009; Xu et al. 2016), the selective synthesis of short (2- and 3-carbon) sugars (Ritson & Sutherland 2012), and a reaction network generating precursors for each of the four fundamental classes of biomolecule (lipids, amino acids, carbohydrates, and nucleotides) (Patel et al. 2015). These advances represent major progress towards the solution of critical problems in prebiotic chemistry, including the asphaltization problem in sugar synthesis (Benner et al. 2012) and the N-glcosylation of ribose with the nucleobases to make ribonucleosides and ribonucleotides[3] (Šponer et al. 2016). These problems are decades-to-centuries old, and their solution is required for the abiotic origin of RNA, and hence the origin of life in the RNA world hypothesis (Gilbert 1986).

UV light plays a key role in these recently proposed prebiotic pathways. While UV light can destroy nascent biomolecules (Sagan 1973), it can also power synthetic prebiotic

[3]The monomers of RNA

photochemistry. In addition to the pathways discussed above, UV light is invoked in prebiotic chemistry as diverse as the origin of chirality (Rosenberg et al. 2008), the synthesis of amino acid precursors (Sarker et al. 2013), and the polymerization of RNA (Mulkidjanian et al. 2003). Measurements of nucleobase photostability suggest that the biogenic nucleobases (the informational components of the RNA and DNA monomers) are exceptionally stable to UV irradiation compared to structurally similar molecules with comparable thermal properties, suggesting they evolved in a UV-rich environment (Rios & Tor 2013; Beckstead et al. 2016; Pollum et al. 2016). This scenario is consistent with our understanding of conditions on prebiotic Earth: UV light is thought to have been abundant on young Earth due to the absence of a biogenic ozone layer (Cockell 2000b,a; Ranjan & Sasselov 2016). Prebiotic photochemistry interacts with UV radiation in ways that are sensitive to its spectral shape and overall intensity (Ranjan & Sasselov 2016). Consequently, it is important to constrain the UV environment on the surface of planets orbiting M-dwarfs, to understand if UV-sensitive prebiotic chemistry pathways that could have lead to the origin of life on Earth could function on such worlds. This represents a new criterion for planetary inhabitability, motivated by specific empirical advances in prebiotic syntheses and by an emergent theoretical understanding of the likely importance of high-energy radiation in origin-of-life scenarios (Pascal 2012).

In this work, we use a two-stream multilayer radiative transfer model to constrain the surface UV environment on planets analogous to prebiotic Earth orbiting M-dwarf stars. Our model includes the effects of absorption and multiple scattering from the surface and from atmospheric gases, and uses recently-measured high-quality UV observations of M-dwarf stars (e.g., France et al. 2016) to provide realistic top-of-atmosphere (TOA) stellar irradiation spectra. We convolve the calculated surface radiance spectra against action

spectra corresponding to two fundamental, simple photochemical reactions (one useful to prebiotic chemistry, and one detrimental) that may have been important during the era of abiogenesis, integrate the results to compute measures of prebiotically-important reaction rates, and discuss the implications for the emergence of life on planets orbiting M-dwarfs. Our work suggests the need for specific experimental tests that must be done to determine whether the UV-sensitive prebiotic chemistry that may have powered the origin of life on Earth could function on planets orbiting M-dwarf stars.

5.2 Background: Previous Studies of M-dwarf Planet UV

Most habitability studies of M-dwarfs treat UV radiation as a negative for habitability (Heath et al. 1999; Tarter et al. 2007; Lammer et al. 2009; Shields et al. 2016b; Meadows et al. 2016), motivated by the observation that UV radiation has deleterious effects on modern life (Setlow 1974). Extensive work has been done to explore mechanisms that might protect surface life from the UV output of M-dwarfs in quiescence and in flare, such as ozone layers (Segura et al. 2005, 2010; Rugheimer et al. 2015), oceans (Kiang et al. 2007), and bioflourescence (O'Malley-James & Kaltenegger 2016). Overall, these works show that UV irradiance at the surface of modern-Earth analog M-dwarf planets should be suppressed to levels below those of modern Earth itself, due to lower M-dwarf near-UV (NUV) output and due to favorable ozone-generating atmospheric photochemistry. Similarly, the UV levels on M-dwarf planets analogous to young Earth (i.e. with anoxic atmospheres) should be lower than on young Earth itself, due to lower

M-dwarf NUV emission. Hence, these works in aggregate conclude that UV radiation environment on terrestrial planets orbiting M-dwarf stars should be clement for life, with potential caveats for very active stars [4]. In this work, we consider in addition the possible positive roles of UV irradiation, motivated by recent experimental advances in prebiotic chemistry that require UV light.

Some previous workers have considered possible positive roles for UV radiation for early life. Scalo et al. (2007) hypothesize that highly variable M-dwarf UV emission could drive variations in mutation rates on orbiting planets, which might enhance the rate of evolution. Buccino et al. (2007) argue based on the "Principle of Mediocrity" [5] that habitable planets should receive stellar irradiance similar to Archaean Earth in order to power potential prebiotic chemistry, and use it to suggest life cannot arise on planets orbiting inactive, low-UV M-dwarfs because in order to receive Earthlike UV instellation, planets will need to orbit within the inner edge of the habitable zone. Buccino et al. (2007) suggest that moderately active M-dwarfs may consequently be better candidates for habitability due to enhanced UV output during flares. These works are abstract in their arguments, and neither links their discussion of UV environment to specific prebiotic photochemistry. Our work is differentiated from these works in coupling the M-dwarf

[4]These arguments presume that planetary atmospheres can be retained despite XUV-powered escape processes, which has been demonstrated for super-Earths ($M_{planet} \geq 6M_{\oplus}$, Tian 2009). However, escape calculations for young Mars ($M = 0.1M_{\oplus}$)suggest its atmosphere would have been unstable to escape powered by higher XUV emission from the young Sun (Tian et al. 2009). It is therefore unclear whether the atmospheres Earth-mass planets orbiting M-dwarfs should be stable to escape, particularly in light of M-dwarf's enhanced fractional XUV emission relative to solar-type stars. Further modelling is required to constrain this possibility.

[5]The hypothesis that Earth's properties should be typical of inhabited planets

UV environment to specific prebiotic photoreactions through their action spectra. Our work is also differentiated from Buccino et al. (2007) in computing spectrally resolved radiation environments, considering the role of atmospheric attenuation, and using a larger, higher-quality sample of M-dwarf UV radiation fields.

5.3 Methods

In this section, we describe our methods. In brief, we calculated the attenuation of empirically measured M-dwarf UV emission by the atmosphere to compute the spectral surface radiance, and coupled the spectral radiance to prebiotically relevant action spectra to evaluate the implications for prebiotic chemistry. We chose a two-stream approach to radiative transfer to correctly account for the role of multiple scattering in atmospheric attenuation (Ranjan et al. 2017), thought our results are ultimately insensitive to inclusion of this effect. All code associated with this project is available for validation and extension at `https://github.com/sukritranjan/ranjanwordsworthsasselov2017b`.

5.3.1 Radiative Transfer

Our radiative transfer formalism is described in detail in Ranjan & Sasselov (2017). Briefly, we partition the atmosphere into 64 1-km homogenous layers and use a two-stream formalism with Gaussian (single) quadrature closure to compute propagation of UV light through the atmosphere (Toon et al. 1989). Two-stream radiative transfer is monochromatic; we partition our spectra into wavelength bins of 4 nm width[6], and

[6]chosen to avoid negative fluxes in low-SNR input spectra, see Section 5.3.3

integrate all optical parameters over these bins. For numerical stability, we assign a ceiling on the per-layer single-scattering albedo ω_0 of $1-1^{-12}$. We take the surface albedo to be 0.2, a representative value for rocky planets and consistent with past 1D modelling for Earth and Mars(Kasting 1991; Segura et al. 2003; Wordsworth et al. 2015). We take the solar zenith angle (SZA) to be 48.2°, corresponding to the insolation-weighted global mean value (Cronin 2014). These parameter value correspond to global mean conditions; variations in surface albedo and solar zenith angle can generally be expected to drive changes in band-averaged fluence of approximately 1 order of magnitude (Ranjan & Sasselov 2017). As in Ranjan & Sasselov (2017) and Ranjan et al. (2017), the fundamental quantity our code calculates is the surface radiance, i.e. the integral of the intensity field at the planet surface for elevations > 0. This is the relevant radiative quantity for calculating photoreaction rates at planet surfaces, and in the two-stream formalism can be calculated as

$$I_{surf} = F_N^{\downarrow}/\mu_1 + F_N^{dir}/\mu_0,$$

where I_{surf} is the surface radiance, $F_N^{\downarrow}$ is the downward diffuse flux at the planet surface, F_N^{dir} is the direct flux at the planet surface, $\mu_0 = \cos(SZA)$ is the cosine of the solar zenith angle, and $\mu_1 = 1/\sqrt{3}$ for Gaussian quadrature (Toon et al. 1989).

5.3.2 Atmospheric Model

Following Rugheimer et al. (2015), we take the planetary atmosphere to be cloud-free, with a surface pressure of 1 bar composed of 0.9 bar N_2 and 0.1 bar CO_2. Our results are insensitive to these assumptions on atmospheric state, because CO_2 absorption (< 204

nm) saturates for $p_{CO_2} > 0.072$ bar[7]. The absorption of most major atmospheric gases (e.g., N_2, H_2O, CH_4) is degenerate with this CO_2 absorption, meaning that surface UV is insensitive to their abundances (Ranjan & Sasselov 2017). Trace gases whose UV absorption is nondegenerate with CO_2 (e.g., O_3, SO_2) do not build up to levels high enough to affect surface UV for atmospheric boundary conditions corresponding to the modern abiotic Earth, according to the photochemical calculations of Rugheimer et al. (2015)[8]. Similarly, the absorption of both CO_2 and H_2O clouds are degenerate with gaseous CO_2 absorption, and for Earthlike global mean cloud optical depths of 4-10 (Stubenrauch et al. 2013), the surface UV environment is insensitive to the presence of clouds (Ranjan et al. 2017). Finally, because the thermal emission of the atmosphere is negligible at UV wavelengths, the UV surface radiance is insensitive to the atmospheric temperature/pressure profile. Consequently, we approximate the atmosphere by a simple exponential model, with $T = T_{surf} = 288K$ throughout. We experimented with a more realistic atmospheric model with dry adiabatic evolution in the troposphere and an isothermal stratosphere, and obtained conclusions identical to the exponential atmosphere; consequently, we elected to use the simpler exponential model in this work.

[7]Such high levels of CO_2 are expected for abiotic Earth-analogs because CO_2 is emitted in bulk from volcanos for planets with Earthlike mantle oxidation states.

[8]For atmospheric boundary conditions not corresponding to the modern abiotic Earth, it is possible for elevated levels of O_3 and O_2 to build up on M-dwarf planets, e.g., Harman et al. (2015). Section 5.5.1 discusses this phenomenon and its implications in more detail.

5.3.3 Stellar Fluxes

We used empirically measured UV spectra of M-dwarfs as top-of-atmosphere (TOA) fluxes to input into our radiative transfer model. Comparatively few such measurements are available, due to low M-dwarf luminosity and high telluric opacity in the UV. We relied primarily on spectra collected by the MUSCLES project, which obtained high-quality spectra of 7 M-dwarfs with the Hubble Space Telescope (France et al. 2016; Loyd et al. 2016) and combined them with measurements from other instruments and stellar models to aggregate broadband emission spectra; we use all M-dwarf stars in their sample[9]. The MUSCLES team also aggregated HST and XMM-Newton measurements and a PHOENIX stellar model to create a spectrum for Proxima Centauri, which we also use. Segura et al. (2005) aggregated IUE and HST observations to compile a UV spectrum of AD Leo in quiescence; we used this spectrum as well[10]. Because of their low luminosities, no spectra of M-dwarfs of stellar type later than M5 are available. To obtain coverage of late-type M-dwarfs, we use the M8 "active" model of Rugheimer et al. (2015), which is formed by scaling a spectrum of AD Leo using emission lines and concatenating it to a PHOENIX model. This may be taken to correspond to the spectrum of a highly active M8 star.

M-dwarfs are known for their frequent and energetic flares (Osten 2016). Few spectral measurements of M-dwarf flares in the prebiotically relevant 150-300 nm regime are available. The exception is AD Leo; the Great Flare of 1985 on this star

[9]Accessed via `https://archive.stsci.edu/prepds/muscles/`, 2016 December 16

[10]Accessed via `http://vpl.astro.washington.edu/spectra/stellar/mstar.htm`, 2016 December 16.

was measured by space- and ground-based instruments, and Segura et al. (2010) have synthesized these measurements to compile spectra of this flare at different time points from 100-444 nm. We use these flare spectra of AD Leo to understand the impact of M-dwarf flares on the surface UV environment and on prebiotic chemistry. We note that the Great Flare on AD Leo may not be representative of all M-dwarf flares, as it was an exceptionally energetic flare (U-band emission of $10^{33.8}$ erg, Hawley & Pettersen 1991) on one of the most active known M-dwarfs. However, it is the only full-coverage spectrally resolved measurement of M-dwarf flares we are aware of, and hence remains the focus of our investigation. Results derived from this flare may be interpreted as a limiting case of the impact of M-dwarf flares on the surface UV environment.

We bin all data to a resolution of 4 nm, to eliminate negative fluxes. Such a coarse resolution is acceptable when working with biological action spectra, which have spectral features with widths on the order of $\gtrsim$ 10 nm (see, e.g., Setlow (1974), Rontó et al. 2003, Cnossen et al. 2007). Following Segura et al. (2005), we scale all M-dwarf emission spectra to a distance a such that the flux at distance a is equal to the modern Solar constant, including the factor of 0.9 correction for the redshifted SEDs of M-dwarfs:

$$a = \sqrt{\frac{L/L_{\odot}}{0.9}} * 1AU$$

Table 5.1 provides these distances and also summarizes other relevant properties of the M-dwarfs in our sample.

To establish a basis of comparison between M-dwarfs and Sunlike stars, we use the model of Claire et al. (2012) to calculate the spectra of the young Sun at 3.9 Ga. We choose this age because it is consistent with available evidence for the origin of life on Earth (see, e.g., Ranjan & Sasselov 2016, Appendix A); our results are insensitive to the

choice of solar age, and are unaffected for solar ages from 3.5-4.1 Ga.

Table 5.1:: Stars Used in This Study & Associated Properties.

Star	$T_{eff}(K)$	Spectral Class	d (pc)	$a(AU)$	Reference	Note
GJ 1214	2953	M4.5	14.6	0.064	1 & sources therein	
Proxima Centauri	3042	M5.5	1.3	0.042	2, 3, & sources therein	Flare star
GJ 876	3062	M5	4.7	0.12	1 & sources therein	
GJ 436	3281	M3.5	10.1	0.17	1 & sources therein	
GJ 581	3295	M5	6.2	0.11	1 & sources therein	
GJ 667C	3327	M1.5	6.8	0.11	1 & sources therein	
AD Leo	3400	M4.5	4.9	0.16	4 & sources therein	Very active star
GJ 176	3416	M2.5	9.3	0.19	1 & sources therein	
GJ 832	3816	M1.5	5.0	0.14	1 & sources therein	

5.3.4 Action Spectra and Calculation of Dose Rates

To quantify the impact of different UV surface radiation environments on prebiotic photochemistry, we compute Biologically Effective Dose rates (BEDs), which measure the reaction rates of specific prebiotically important photoprocesses (Cockell 1999; Rontó et al. 2003; Rugheimer et al. 2015). Our method is described in detail in Ranjan &

Sasselov (2017) and Ranjan et al. (2017). Briefly, we compute

$$D = (\int_{\lambda_0}^{\lambda_1} d\lambda \mathcal{A}(\lambda) I_{surf}(\lambda)).$$

$I_{surf}(\lambda)$ is the UV surface radiance, computed from our model. $\mathcal{A}(\lambda)$ corresponds to the action spectrum, which parametrizes the wavelength dependence of a given photoprocess; higher values of $\mathcal{A}$ mean that a higher fraction of the incident photons are being used in the photoprocess. $\lambda_0 - \lambda_1$ is the wavelength range over which $\mathcal{A}(\lambda)$ and $I_{surf}(\lambda)$ are defined. Since D is a relative measure of reaction rate, a normalization is required to assign a physical interpretation to its value. In this paper, we report

$$\overline{D} = D/D_{\oplus},$$

where $D_{\oplus}$ is the dose rate on 3.9 Ga Earth. $\overline{D} > 1$ means the reaction is proceeding faster than it would have on young Earth; $\overline{D} < 1$, the reverse.

We use action spectra corresponding to simple, prebiotically relevant photoprocesses to measure the impact of UV light on nascent life. This differentiates our work from previous works (Cockell 2000b, 2002; Cnossen et al. 2007; Rugheimer et al. 2015) which used action spectra corresponding to DNA damage in modern organisms. Focus on DNA damage is inappropriate for prebiotic chemistry because 1) DNA is not thought to have been the primordial biomolecule, 2) modern organisms have evolved sophisticated methods to deal with environmental stress, including UV exposure, that would not have been available to the first life, and 3) this approach ignores the role of UV light as a eustressor[11] for abiogenesis. We consider two photochemical reactions: a stressor process and a eustressor process. We also compute the band-integrated NUV radiation, which is a pathway-independent measure of the abundance of prebiotically useful radiation.

[11]i.e., beneficial for the origin of life

For our stressor process, we use the cleavage of the N-glycosidic bond in the RNA monomer uridine monophospate (UMP) by UV light, which irreversibly destroys this key biomolecule. We take the action spectrum as the product of the UMP absorption spectrum (Voet et al. 1963) and the quantum yield curve. We assume a step function form to the quantum yield curve, with value 4.3×10^{-3} for $\lambda \leq \lambda_0$ and 2.5×10^{-5} for $\lambda > \lambda_0$, and we consider λ_0 values of 193, 254, and 230 nm, consistent with the measurements of Gurzadyan & Görner (1994). The absorption spectra of the other RNA monomers are structurally similar to UMP and the molecules share many photochemical properties[12]. Therefore, if a UV environment is destructive for UMP, it should be destructive for the other RNA monomers, and hence for abiogenesis in the RNA world hypothesis, as well. As shorthand, we refer to this photoprocess under the assumption that λ_0 =X nm by UMP-X.

For our eustressor process, we use the production of solvated electrons from the irradiation of a tricyanocuprate ($CuCN_3^{2-}$) complex, which was invoked by Ritson & Sutherland (2012) in their pathway for the selective synthesis of the short sugars (glycolaldehyde, gylceraldehyde) that are key for the synthesis of RNA, and which are generally useful in a wide range of reductive prebiotic chemistry. We again take the action spectrum to be the product of the absorption spectrum (Magnani 2015; Ranjan & Sasselov 2016) and the quantum yield curve. Following Ritson & Sutherland (2012)'s hypothesis that photoionization of the cyanocuprate drives solvated electron production, we assume the QY to be characterized by a step function with value 0.06 for $\lambda \leq \lambda_0$ and 0 otherwise, and we consider $\lambda_0 = 254$ and 300 nm, consistent with the empirical

[12]e.g, the quantum yield of N-glycosidic bond cleavage in adenosine monophospate (AMP) increases at short wavelengths like UMP's does (Gurzadyan & Görner 1994)

constraints of Ritson & Sutherland (2012). Laboratory measurements of the spectral quantum yield of this process are forthcoming (Todd et al. 2017a); preliminary results suggest a step occurring at ~ 250 nm. As shorthand, we refer to this photoprocess under the assumption that $\lambda_0 =$Y nm by CuCN3-Y.

Action spectra typically encode information about relative, not absolute, reaction rates. Consequently, they are generally arbitrarily normalized to 1 at some wavelength (see, e.g., Cockell 1999 and Rugheimer et al. 2015). We normalize these spectra to 1 at 190 nm. We were unable to located absorption cross-section data for tricyanocuprate for $\lambda < 190$ nm, nor for UMP for $\lambda < 184$ nm; for wavelengths below these cutoffs, we padded the absorption spectra with the shortest wavelength data available. Since $\lambda < 190$ nm is shielded out by even modest amounts of CO_2 in the atmosphere, this padding only comes into play when considering nonexistent or tenuous atmospheres, as we briefly consider in Section 5.5. Figure 5.1 presents the action spectra.

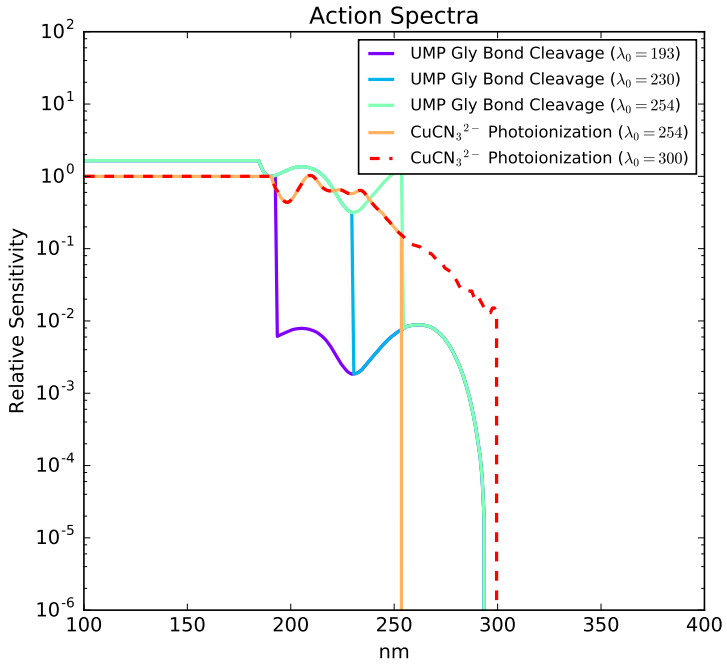

Figure 5.1: Action spectra for photolysis of UMP$-\lambda_0$ and photoionization of CuCN3 $-\lambda_0$, assuming a step-function form to the QE for both processes with step at λ_0. The spectra are arbitrarily normalized to 1 at 190 nm. Data shortward of 184 nm for UMP$-\lambda_0$ and CuCN3$-\lambda_0$ are padded.

The action spectra discussed above correspond to specific prebiotically relevant photochemical processes. In addition, we calculate the band-integrated surface radiance for $\lambda = 200 - 300$ nm, which we term the "NUV radiance". This is based on emerging studies of the wavelength-dependence of a number of prebiotically important photoprocesses, which suggest that radiation in the 200-300 nm regime can be useful to prebiotic chemistry, while radiation at wavelengths < 200 nm seems to be solely destructive (Todd et al. 2017a). We use the NUV radiance as a process-independent measure of the abundance of prebiotically useful UV radiation; the dose rate for the

NUV radiance tracks those of the specific prebiotic photoprocesses, as expected for a generalized measure.

5.4 Results

5.4.1 Steady-State M-dwarf Emission

Figure 5.2 presents the TOA fluxes for the M-dwarfs in our study and the corresponding surface radiances on prebiotic Earth-analog planets shielded by a 1 bar atmosphere (0.9 bar N_2, 0.1 bar CO_2, matching Rugheimer et al. 2015). As noted by Rugheimer et al. (2015), the surface conditions are defined by a cutoff at 204 nm imposed by atmospheric CO_2, and minimal attenuation at longer wavelengths. Notably, young-Earth-analog planets orbiting M-dwarf planets are exposed to far less UV radiation than those orbiting Sunlike stars, because of the cooler photosphere and hence lower NUV emission of M-dwarfs. At short wavelengths, M-dwarfs emit proportionately more radiation than the young Sun, but fluence at these wavelengths is robustly blocked by a range of atmospheric absorbers, including CO_2 and H_2O, which shield out < 200 nm radiation. Consequently, M-dwarf planets, so long as they can retain their atmospheres, are low-UV environments.

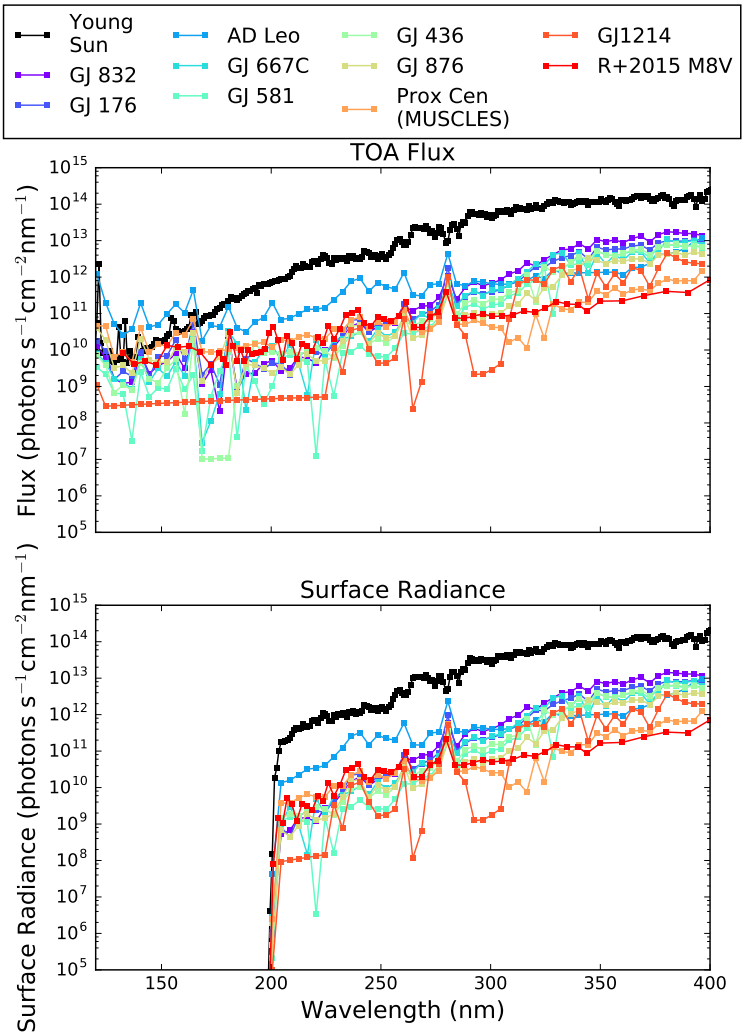

Figure 5.2: TOA fluxes (top) and corresponding surface radiances as a function of wavelength for prebiotic Earth-analog planets with 1-bar N_2-CO_2 atmospheres orbiting a range of M-dwarfs. The young Sun and Earth case (3.9 Ga) is also shown for comparison.

We quantify this observation by computing the relative dose rates $\overline{D}$ for each of the stars in our sample. These dose rates are presented in Figure 5.3. The stars are ordered by decreasing T_{eff}. We observe that with the exception of the exceptionally active star

AD Leo and the Rugheimer et al. (2015) M8V "Active" model, which is a scaled AD Leo, all dose rates are suppressed by $>$ 2 orders of magnitude relative to the young Earth. Putative UV-dependent prebiotic chemistry will proceed at rates 2-4 orders of magnitude slower on planets orbiting non-active M-dwarfs compared to the young Earth. Active stars like AD Leo emit more UV radiation, so bioactive fluence on planets orbiting such active stars will only be suppressed by 1-2 orders of magnitude.

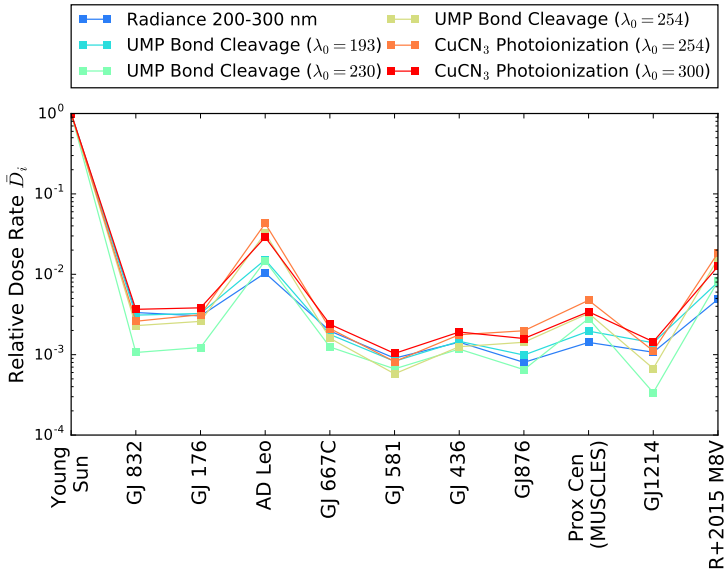

Figure 5.3: UV dose rates $\overline{D}_i$ for UMP-X and CuCN3-Y at the surfaces of prebiotic Earth-analog planets with 1-bar N_2-CO_2 atmospheres orbiting a range of M-dwarfs. Dose rates corresponding to the 3.9 Ga Earth are also shown for comparison.

We considered the hypothesis that different host stars might affect the stressor and eustressor pathways in different ways. Specifically, we considered the possibility that the eustressor reaction rates might fall off slower or faster than the stressor reaction rates due to variations in the shape of the Spectral Energy Distributions (SEDs) between the different host stars, which would imply more or less favorable venues for abiogenesis,

respectively. To test this hypothesis, we calculated $\overline{D}_{UMP-X}/\overline{D}_{CuCN3-Y}$ for all X and Y. If this ratio is < 1, the stressor pathway is disfavored over the eustressor pathway relative to Earth, and the environment compares favorably to Earth as a venue for abiogenesis; if this ratio is > 1, the reverse is true. Figure 5.4 presents these calculations. In aggregate, the dose rate ratios does not vary much as a function of host star, remaining within an order of magnitude of unity for all stars in this study, and no clear aggregate trends are visible. We attribute this to the fact that the SEDs of the M-dwarf stars considered here are broadly similar in shape to the Sun's SED at the NUV wavelengths that makes it to the planet surface. We conclude that M-dwarf planets are comparable to early Earth in terms of how much their UV environments favor stressor processes over eustressor processes.

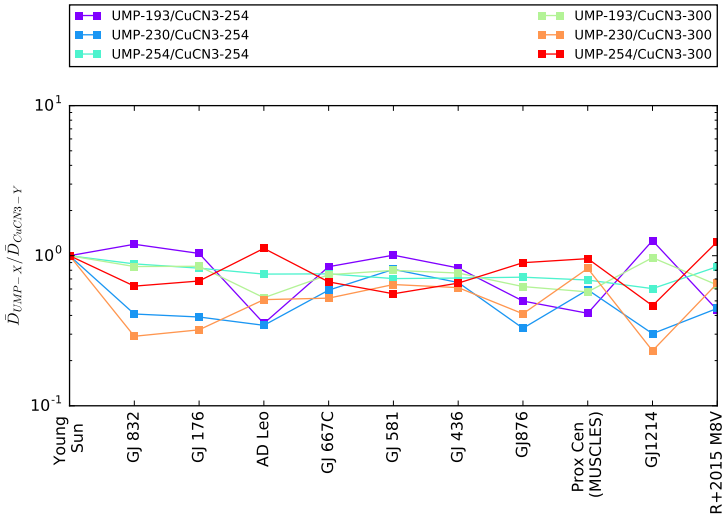

Figure 5.4: Ratio of stressor dose rates UMP-X divided by eustressor dose rates UMP-Y for dusty CO_2-H_2O atmospheres, as a function of host star. Lower ratios imply a more favorable environment for abiogenesis as measured by these two photoprocesses.

5.4.2 M-dwarf Flares

Figure 5.5 presents the TOA fluxes for AD Leo in quiescence and at the peak of the Great Flare (912s, Segura et al. 2010), and the corresponding surface radiances on a young-Earth-analog planet orbiting it. In flare, AD Leo's UV output rises by orders of magnitude, and the increase in fluence is not confined to line emission as it was for the young Sun in the study of Cnossen et al. (2007). Rather, the increase is across the UV spectrum, including the continuum.

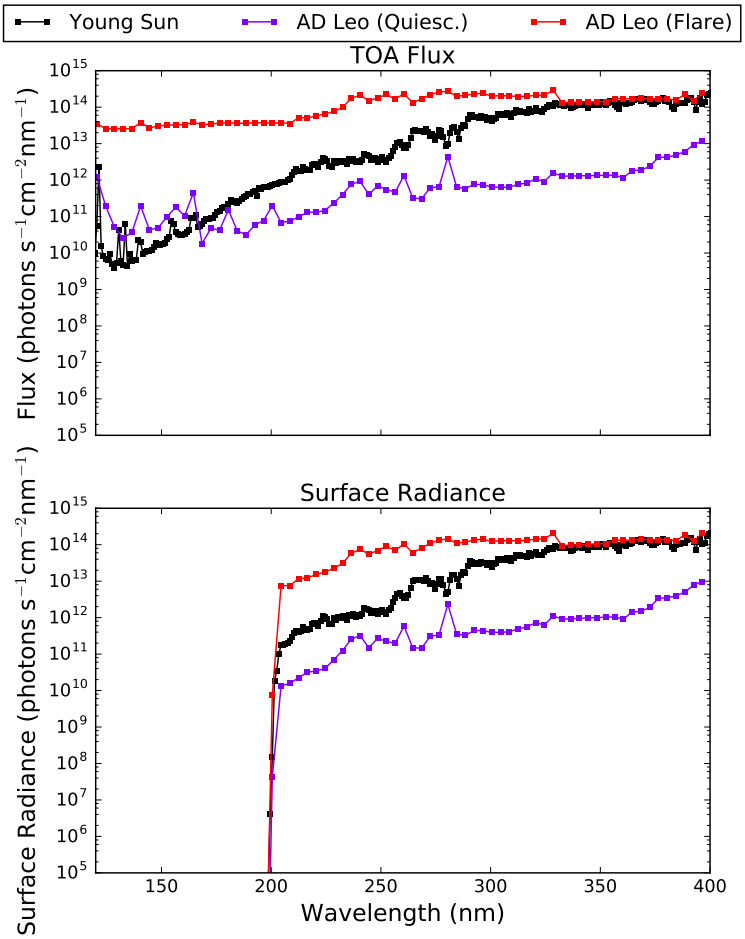

Figure 5.5: TOA fluxes (top) and corresponding surface radiances as a function of wavelength for a prebiotic Earth-analog planet with a 1-bar N_2-CO_2 atmosphere orbiting AD Leo in quiescence and during the Great Flare of 1985. The young Sun and Earth case (3.9 Ga) is also shown for comparison.

This increase in fluence drives a dramatic increase in reaction rates. Figure 5.6 shows the dose rates for a young-Earth analog orbiting AD Leo in and out of flare, compared to the young Earth. While in quiescence prebiotically relevant reaction rates are suppressed

by 1-2 orders of magnitude relative to the young Earth, in flare the reaction rates are enhanced, by up to 1 order of magnitude relative to young Earth. The increase in UV fluence is relatively spectrally flat across the NUV regime that penetrates the atmosphere to the planet surface, and the flare does not deliver radiation that particularly favors or disfavors stressor processes versus eustressor processes relative to quiescence.

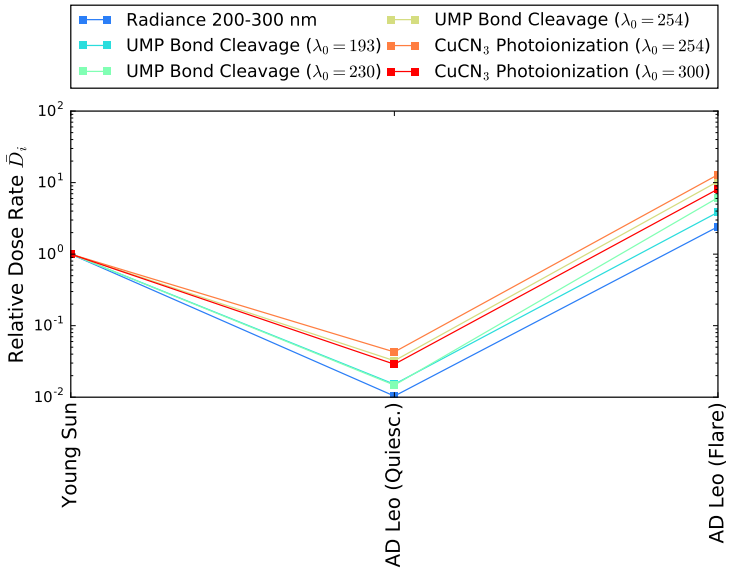

Figure 5.6: UV dose rates $\overline{D}_i$ for UMP-X and CuCN3-Y at the surfaces of a prebiotic Earth-analog planet with a 1-bar N_2-CO_2 atmosphere orbiting AD Leo in quiescence and during the Great Flare of 1985. Dose rates corresponding to the 3.9 Ga Earth are also shown for comparison.

5.5 Discussion

5.5.1 Low-UV on M-dwarfs: A Challenge for Abiogenesis?

Prebiotic chemistry on planet orbiting M-dwarfs has access to orders of magnitude less UV radiation than prebiotic chemistry on planets orbiting Solar-type stars, due to lower NUV emission by the cooler M-dwarfs. This poses a challenge for some origin-of-life scenarios on such worlds. As discussed in Section 5.1, UV light is a key requirement of several proposed prebotic pathways, including the only known pathways for prebiotic syntheses of ribonucleotides (Powner et al. 2009; Ritson & Sutherland 2012; Patel et al. 2015; Xu et al. 2016). It is possible that these pathways will still function under a low-UV regime, albeit at lower rates. However, it is equally possible that they will not, due to interference or competition with thermal reactions. For example, the core of the sugar synthesis pathway of Ritson & Sutherland (2012) and Patel et al. (2015) involves the reduction of glycolonitrile to glycolaldehyde imine by a photochemically-produced solvated electron, which then hydrolyzes to give the desired glycolaldehyde sugar. However, glycolonitrile can also react with H_2S[13] to produce its alpha-hydroxy thioamide form, which subsequently hydrolyzes to its alpha-hydroxy acid form. If the UV irradiance is low enough, the latter pathway will dominate over the former, and the sugar synthesis pathway will not proceed[14]. Similarly, the efficacy of UV light at selecting and amplifying the population of biogenic ribonucleotides and generating uridine from cytidine in Powner et al. (2009) will be functions of the

[13]Required for the synthesis scenario outlined in Patel et al. (2015)

[14]J. Szostak, private communication, 2016 November 6

irradiation level. These examples illustrates the need to characterize the sensitivity of putative prebiotic pathways to the amplitude of irradiation, to understand whether they can proceed under the lower-UV conditions on planets orbiting M-dwarfs. In sum, it is unclear whether UV-dependent prebiotic pathways that may have been important to the origin of life on Earth can proceed in the low-UV environment on planets orbiting M-dwarfs, such as the recently-discovered habitable zone planet Proxima Centauri b (Anglada-Escudé et al. 2016) or the habitable-zone planets orbiting TRAPPIST-1 (Gillon et al. 2017).

Even if these pathways do proceed at lower irradiance levels, their reaction rates will likely be orders of magnitude lower than on planets around Sunlike stars. If UV-dependent pathways like the RNA monomer synthesis pathways of Patel et al. (2015) were a rate-limiting step in the origin of life on Earth, then lower M-dwarf NUV radiation could delay the origin of life on planets orbiting M-stars by orders of magnitude. If abiogenesis is fast, this is not a problem. However, if abiogenesis is slow, this could pose a challenge. For example, if abiogenesis took 100 Ma on Earth and UV photochemistry was the rate-limiting step, then it would take $\gtrsim 10$ Ga around M-dwarfs, meaning that only old M-dwarfs could host planets with native life. In the worst-case scenario, the Universe might be too young for M-dwarf-orbiting life to have evolved at all.

The UV-scarcity problem may be exacerbated by atmospheric photochemistry, depending on planet history and surface conditions. Luger & Barnes (2015) show that terrestrial planets with significant initial water inventories orbiting in the current habitable zones of main-sequence M-dwarfs may have undergone a runaway greenhouse and suffered massive loss of water due to enhanced M-dwarf luminosity in their extended pre-main sequence phase, which could have generated high levels of UV-shielding O_2 and

O_3 if not balanced by loss to the mantle and crust. Similarly, Harman et al. (2015) show that Earthlike planets with significant CO_2 inventories[15] orbiting M-dwarfs can build up abiotic ozone layers comparable in strength to modern Earth's if sinks of O_2 and CO are small, because the greater FUV/NUV ratio of M-dwarfs means that O_3 production rates are higher and dissociation rates are lower. Gao et al. (2015) demonstrate that CO_2-rich, H_2O-poor planets orbiting M-dwarfs can also build up abiotic ozone layers comparable to modern Earth's, and for high H levels can also build up H_2O_2 which can also act as a UV shield at elevated levels. Wordsworth & Pierrehumbert (2014) showed that water-rich planets with low inventories of non-condensible gases like N_2 may also abiotically oxygenate. In sum, planets orbiting M-dwarfs with inefficient sinks of O_2 and CO, with desiccated CO_2 rich atmospheres, or lacking non-condensible background gases, may photochemically produce atmospheric UV shields like O_3 that can further block the already low M-dwarf UV from the planet surface.

One might argue that our focus on UV light is unwarranted because it is not certain that UV light played a role in the origin of life on Earth, let alone on other planets; indeed, UV light would be altogether absent in the deep-sea hydrothermal vent hypothesis for the origin of life, one of the leading paradigms in origin of life studies (e.g., Martin et al. 2008). Our rationale for focusing on UV light is threefold. First, the nucleotides of RNA show evidence of selection pressure from UV irradiation, suggesting they arose in a UV-rich environment (Rios & Tor 2013; Beckstead et al. 2016; Pollum et al. 2016). If one assumes RNA were the primordial autocatalytic replicator, as is the paradigm in the RNA world hypothesis (Gilbert 1986), this implies UV light was abundant during abiogenesis on Earth. Second, only UV light has been empirically

[15]Expected for Earthlike volcanic outgassing

demonstrated to drive the only known prebiotically plausible pathways for the origin of the pyrimidine RNA monomers and for the selective sugar synthesis pathway that sidesteps the asphaltization problem (Patel et al. 2015; Benner et al. 2012). It is possible that a different energy source could substitute for UV, but this has not yet been demonstrated in the laboratory. Third, It is difficult to envision sources of free energy that can substitute for UV light in general. The energetic nature of UV light means that it is capable of directly affecting or altering molecular electronic structure, permitting it to effect irreversible changes in the entropic states of molecular systems. To effect similar changes thermally requires sources with temperatures on the orders of thousands of degrees Kelvin, coupled to quenching mechanisms to prevent thermal relaxation to the equilibrium state (Pascal 2012). Two such high-temperature planetary sources are lightning and impacts, which have been contemplated as energy sources for prebiotic molecular synthesis (Chyba & Sagan 1992; Nava-Sedeño et al. 2016). However, these sources face the problem of abundance: lightning and impact-driven shockwaves are estimated to have delivered three orders of magnitude less energy than UV photons (< 300 nm) to the young Earth (Ferris & Chen 1975). Hence, it is difficult to avoid the conclusion that a paucity of UV light could pose a problem for abiogenesis scenarios on M-dwarf planets like Proxima Centauri b or the TRAPPIST-1 planets. Conversely, if life is found on an M-dwarf planet it might imply a pathway to the origin of life very different from what seems to have played out on Earth.

5.5.2 Possible Mechanisms to Compensate for Low M-dwarf UV

We considered whether the UV paucity problem could be solved with thinner atmospheres that block less UV light. We might imagine elevated young M-dwarf EUV emission could strip the atmosphere from a low-mass planet, similar to the scenario Tian et al. (2009) calculated for the young Mars due to elevated early solar EUV emission. We repeated our study for a tenous, 1-microbar N_2-CO_2 atmosphere which provided essentially no attenuation of incoming fluence. Relative dose rates did rise by 1-2 orders of magnitude. However, the strongest increases in reaction rates were for destructive reactions (i.e. UMP photolysis), which is unsurprising: the new fluence admitted by the thinner atmosphere were primarily the destructive FUV (< 200 nm) wavelengths, making the environment less clement for abiogenesis. In addition, such low atmospheric pressures pose other problems for prebiotic chemistry: for example, liquid water is not stable at pressures below the triple point, i.e. $P_0 < 6 \times 10^{-3}$ bar (Miller 2009), meaning aqueous phase prebiotic chemistry would face challenges on an airless world. We conclude that atmospheric stripping cannot solve the UV paucity problem for prebiotic chemistry.

Our analysis has focused on main-sequence M-dwarfs. Young M-dwarfs, especially pre-main-sequence M-dwarfs emit a larger fraction of their bolometric luminosity as NUV radiation compared to their main sequence phase (Shkolnik & Barman 2014). The lowest-mass M-dwarfs remain in this state for up to ~ 1 Gyr timescales, and one might speculate whether planets orbiting such stars might receive NUV irradiation more comparable to planets orbiting Sunlike stars. However, the bolometric luminosity of such stars is also higher; planets in the main-sequence habitable zones of such stars are

liable to be in a runaway greenhouse state during their pre-main-sequence evolution, with temperatures globally above the boiling point of water and possibly as high as $\gtrsim$ 1000K (Ramirez & Kaltenegger 2014; Luger et al. 2015; Luger & Barnes 2015; Schaefer et al. 2016). Hence, these objects will lack clement conditions for aqueous-phase prebiotic chemistry, and are unlikely to be habitable during this phase. Planets orbiting farther out, in the pre-main-sequence habitable zone, may remain habitable for up to gigayear timescales (Ramirez & Kaltenegger 2014), and will on average experience NUV irradiation (175-275 nm) up to 1 order of magnitude (OOM) higher than planets orbiting at equivalent bolometric instellations during the star's main sequence phase (Shkolnik & Barman 2014). However, these objects will exit the habitable zone when their host star joins the main sequence and reduce their bolometric luminosity. Unless global temperatures are subsequently elevated by mechanisms not considered in the traditional Earth-analog habitable zone calculation, e.g. greenhouse warming due to elevated levels of atmospheric H_2 (Stevenson 1999; Pierrehumbert & Gaidos 2011; Wordsworth & Pierrehumbert 2013; Wordsworth et al. 2017; Ramirez & Kaltenegger 2017), liquid water will freeze at the planet surface and life will be confined to volcanic or subsurface reservoirs, whose ability to produce global atmospheric biosignatures is unclear. More critically, it is uncertain whether a 1-OOM enhancement in 175-275 nm fluence is adequate to compensate for the $\sim$2-4 OOM suppression in bioactive NUV fluence on M-dwarf planets compared to the early Earth; experimental characterization of the fluence dependence of UV-sensitive putative prebiotic chemistry remains necessary to answer this question. Nevertheless, planets orbiting in the habitable zones of late-type (low-mass) pre-main-sequence M-dwarfs remain of special interest from the perspective of UV-sensitive prebiotic chemistry.

We considered whether M-dwarf flares, which are typically considered barriers to habitability (Segura et al. 2010), might provide a partial solution to the problem of UV paucity on M-dwarf planets (Buccino et al. 2007). During the Great Flare of 1985, AD Leo's NUV output increased dramatically, delivering more NUV radiation to the surface of a young-Earth-analog planet than the young Sun for a period of at least 0.7 hour and possibly longer[16]. Flare frequency studies of AD Leo suggest that flares of this strength occur with frequency 0.1 day^{-1} Pettersen et al. (1984) [17]. For comparison, the typical irradiation time used in laboratory studies of UV-sensitive prebiotic pathways like C-to-U conversion and glycolaldehyde/glyceraldehyde formation at fluence levels comparable with the young Sun is on the order of 4 hours (Todd et al. 2017a), a duration comparable to strong M-dwarf flares. One might imagine a scenario whereby photosensitive prebiotic chemistry proceeds during the high-UV flares and ceases during stellar quiescence, providing an activity-powered analog to the terrestrial day/night cycle that would be absent on tidally-locked habitable zone M-dwarf planets. Experimental studies are required to constrain whether shorter duration but higher intensity irradiation corresponding to an M-dwarf flare is sufficient to power putative prebiotic chemistry. Theoretical studies are also required to understand whether the enhanced UV radiation these flares provide also strip the atmosphere, which would negatively impact planetary habitability and obviate this solution. We note that this mechanism could best solve the UV-paucity problem for planets orbiting the most active M-stars, like AD Leo. Planets orbiting active stars would experience much lower flare rates; for example,

[16]The flare lasted 4 hours but we located NUV observations for only the first 0.7 hours; see Segura et al. 2010

[17]Lower-energy flares occur more frequently but emit substantially less UV radiation, and are likely also shorter in duration (c.f. the study of Hawley et al. 2014 for GJ 1243)

extrapolation of white-light flare frequency studies for Proxima Centauri suggest that Proxima Centauri b would experience UV instellation comparable the Great Flare of AD Leo only ~ 8 year^{-1}, $5\times$ less frequently than an Earth-analog planet orbiting AD Leo(Davenport et al. 2016).

5.5.3 Laboratory Follow-Up

Our work suggests a critical need for laboratory studies to determine whether putative UV-dependent prebiotic pathways (e.g., Powner et al. 2009, Ritson & Sutherland 2012, Patel et al. 2015, Xu et al. 2016) could function at the $10 - 1000\times$ lower UV irradiation accessible on planets orbiting M-dwarfs compared to the young Earth. First, the fluence dependence of these pathways should be determined: How do their rates vary as a function of irradiation level, and at which minimum fluence do they shut down? These questions should be probed down to fluence levels as low as $10^{-3} - 10^{-4}$ of that accessible on early Earth, corresponding to the fluence available on quiet M-dwarfs. Integrated from 200-300 nm, prebiotic chemistry on early Earth would have been exposed to $6 \sim 10^{14}$ photons s^{-1}cm^{-2}, implying the need to probe down to photon fluxes as low as $6 \sim 10^{11}$ photons s^{-1}cm^{-2} (5 erg s^{-1}cm^{-2} at the 254 nm line generally used in prebiotic chemistry studies).

If such studies determine that one or more of these pathways fail at M-dwarf irradiation levels, experiments should be done to determine whether transient high UV irradiation due to flares can substitute for steady-state irradiation. The best-established case to simulate is the Great Flare on AD Leo; this event delivered 2×10^{15} photons/s/cm^2 (2×10^4 erg s^{-1}cm^{-2} at 254 nm) to the surface of an orbiting young-Earth analog,

integrated from 200-300 nm. Such fluence levels would have been available for periods of 0.7-4 hours at intervals of ≈ 240 hours according to the power-law presented in Pettersen et al. (1984). If such intense flares are too infrequent to power prebiotic chemistry, then the influence of lower-intensity, higher-frequency flares may be considered. For example, flares 1/10 as energetic as the Great Flare occur every 60 hours (see Section 5.7). If flare frequencies $\sim 5\times$ less than that of AD Leo are found to be sufficient to power UV-dependent prebiotic chemistry, then flare instellation could solve the potential UV paucity problem for Proxima Centauri b.

5.6 Conclusions

Recent laboratory studies suggest that UV light played a critical role in the origin of life on Earth. We have used a radiative transfer model to evaluate the UV surface environment on planets analogous to prebiotic Earth (N_2-CO_2 atmosphere) orbiting M-dwarfs, and used action spectra to calculate dose rates and quantify the implications for prebiotic chemistry on such worlds. Such planets are the most compelling target for biosignature searches over at least the next decade.

We find the UV surface environment on M-dwarf planets is chiefly differentiated from planets orbiting Sunlike stars in that they have access to orders of magnitude less prebiotically-useful NUV radiation, due to the lower emission of M-dwarfs at these wavelengths. Planets orbiting in the transient habitable zones of pre-main-sequence late-type M-dwarfs should experience more NUV irradiation, but only transiently, and not enough to close the deficit with planets orbiting Sunlike stars. This raises uncertainty over whether the UV-dependent prebiotic pathways that may have lead to

the origin of life on Earth could function on planets orbiting M-dwarfs, such as the recently-discovered habitable-zone planets orbiting Proxima Centauri and TRAPPIST-1. Even if the pathways proceed, their reaction rates will likely be orders of magnitude lower than for planets around Sunlike stars, potentially slowing abiogenesis.

These scenarios can be tested empirically, through laboratory studies to measure the reaction rate of putative UV-dependent prebiotic pathways (e.g. Ritson & Sutherland 2012, Patel et al. 2015, Xu et al. 2016) to the amplitude of irradiation. Such laboratory studies are urgently needed, in order to identify the most compelling targets for biosignature search with next-generation near-term instruments like JWST and the ELTs. If such laboratory studies reveal that near-solar levels of NUV fluence are required to move forward UV-sensitive prebiotic chemistry, they will raise questions regarding the prospects for the emergence of life on M-dwarf planets. Interestingly, in this case planets orbiting active M-dwarfs may be more compelling candidates for abiogenesis scenarios, due to both the higher quiescent emission of such stars and the frequent flares from such stars, which will periodically illuminate the planet with elevated levels of UV that may power prebiotic photochemistry. Laboratory experiments are required to understand whether burst of brief (∼hours), high-intensity radiation separated by long intervals ($\sim$ 10 days) can substitute for steady-state solar emission. Theoretical studies are required to ensure that enhanced UV and particle fluxes from such flares would not also strip the planetary atmosphere, obviating this solution.

Acknowledgements

We thank Z. Todd, J. Szostak, and A. Beckstead for their insight regarding prebiotic chemistry and its interaction with UV light. We thank S. Rugheimer, A. Segura, K. France, S. Engle, C. Johns-Krull, R. Osten, and C. Bonfio for sharing their data with us, and for their answers to our questions. We thank L. Walkowicz, V. Meadows, O. Venot, and R. Loyd for insightful discussions.

This research has made use of NASA's Astrophysics Data System Bibliographic Services, and the MPI-Mainz UV-VIS Spectral Atlas of Gaseous Molecules.

S. R. and D. D. S. gratefully acknowledge support from the Simons Foundation, grant no. 290360.

5.7 Appendix A: Flare Frequency Distribution Calculation

In this section, we calculate explicitly the flare frequencies alluded to in Section 5.5

For AD Leo: Pettersen et al. (1984) find the flare frequency distribution to be fit by

$$\log[\nu(E_{U_0})] = \alpha - \beta \log[E_{U_0}],$$

where ν is the frequency of flares with integrated U-band energy $E_U \geq E_{U_0}$ in units of s^{-1}, $\alpha = 15.0 \pm 2.1$, and $\beta = 0.62 \pm 0.09$. The AD Leo Great Flare of 1985 had a U-band energy of $10^{33.8}$ erg (Hawley & Pettersen 1991, Table 8), corresponding to a frequency of $\nu = 10^{\alpha - \beta \times 33.8} s^{-1} = 1.1 \times 10^{-6} s^{-1} = 0.1 day^{-1}$. Lower energy flares occur

more frequently: A flare with 1/10 the Great Flare's U-band energy would occur with frequency $\nu = 10^{\alpha-\beta\times32.8}s^{-1} = 4.6 \times 10^{-6}s^{-1} = 0.4$ day^{-1}.

Chapter 6

Cyanosulfidic Origins of Life Chemistry: Planetary Sources for Reducing Sulfur Compounds

This thesis chapter is in preparation for submission as:

S. Ranjan, Z. Todd, J. Sutherland, and D. Sasselov.

Abstract

Cyanosulfidic prebiotic reaction networks (e.g., Patel et al. (2015), are building a tantalizing picture of sustained abiotic synthesis of activated ribonucleotides, amino acids and lipid precursors. The lab experiments indicate planetary conditions in concordance with what we know of early Earth. Sulfur-bearing anions under midrange UV irradiation play important roles, but their planetary sources via outgassing of SO_2 and H_2S and

dissolution into water reservoirs have been uncertain. In this paper we place constraints on the partial pressures of each gas required for reaching at least 1 μM concentrations. We conclude that epochs of high volcanism could have been characterized by access to both the midrange UV radiation and sulfurous anions required for the cyanosulfidic chemistry, and by lower levels of potentially-damaging far-UV radiation. The only exception is the HS^- anion, which seems to reach only sub-micromolar levels from atmospheric sources. In general, epochs of high volcanism may have been uniquely conducive to cyanosulfidic prebiotic chemistry.

6.1 Introduction

The past decade has witnessed a number of breakthroughs in prebiotic chemistry, and especially in the origin of RNA. In particular, Powner et al. (2009) demonstrated a plausibly abiotic synthesis of the activated pyrimidine ribonucleotides (cytidine monophospate, CMP and uridine monophospate, UMP), and Ritson & Sutherland (2012) discovered a mechanism for abiotic synthesis of the 2- and 3-carbon sugars glycolaldehyde and glyceraldehyde that avoided the asphaltization problem (Benner et al. 2012). Patel et al. (2015) unified these discoveries into a cyanosulfidic prebiotic reaction network starting with a limited set of feedstock molecules in aqueous solution and UV irradiation (at 254 nm) to generate activated ribonucleotides, amino acids and lipid precursors. In this reaction network the requirements for the UV light are very specific in terms of wavelength range. Recent indications from both theory (Ranjan & Sasselov 2016, 2017) and experiments (Todd et al. 2017a,b) seem to point to the need for the open UV window from 200-to-300 nm afforded by the cutoffs from water and atmospheric CO_2

below 200 nm and the lack of any viable absorbers like ozone or H_2S above 200 nm.

The reaction network of Patel et al. (2015) requires sulfide[1] (HS^-) as both a feedstock and as a photoreductant; recent work by the same group suggests that bisulfite (HSO_3^-) or sulfite (SO_3^{2-})[2] may play a similar role. Patel et al. (2015) invoke interaction of water with impact-delivered metallosulfides as a source for HS^-. While an impactor-derived source of sulfide is possible, especially in light of elevated impactor flux early in Earth's history, this mechanism does impose an additional local requirement for the cyanosulfidic reaction network of Patel et al. (2015). A planetary source for the sulfidic feedstock would reduce the requirements for this reaction network to function, and would make it a more compelling candidate for the prebiotic chemistry that ultimately lead to the origin of life.

In this work, we explore a planetary source the atmosphere, for the sulfidic photoreductants required by the cyanosulfidic chemistry proposed by Patel et al. (2015). The prebiotic Earth's atmosphere is thought to have been more reducing than modern Earth (Kasting 2014), and volcanism levels have been hypothesized to have been higher (Richter 1985). If so, then the abundance of atmospheric H_2S and especially SO_2 should have been higher compared to modern day levels, and aqueous reservoirs in equilibrium with the atmosphere would have dissolved some of these gases in accordance with Henry's Law. Would that provide high enough concentrations of HS^-, HSO_3^- and SO_3^{2-}? Conversely, would the required high atmospheric levels absorb the UV light in the 200-300 nm window, which is required by the prebiotic chemistry? In this paper, we

[1]derived from dissolving H_2S in water

[2]derived from dissolving SO_2 in water in the absence of oxygen

provide estimates of the speciation of S-bearing photoreductants in aqueous solution as a function of pSO_2 and pH_2S, governed by Henry's Law. We evaluate the plausibility of an atmospheric source of sulfidic compounds for prebiotic chemistry, and discuss implications for future work.

6.2 Background

6.2.1 Plausible Prebiotic Levels of H_2S and SO_2

The abundances of H_2S and SO_2 in the Earth's atmosphere are set by photochemistry, and are sensitive to a variety of factors. One of the most important of these factors is the outgassing rate of these compounds from volcanoes into the atmosphere. Absent biogenic sources, atmospheric photochemistry models typically assume abiotic SO_2 outgassing rates of $1 - 3 \times 10^9$ $cm^{-2}s^{-1}$ (Kasting et al. 1989; Zahnle et al. 2006; Hu et al. 2013; Claire et al. 2014), consistent with the measured mean volcanogenic SO_2 outgassing rate of $1.7 - 2.4 \times 10^9$ $cm^{-2}s^{-1}$ (Halmer et al. 2002). H_2S emission rates are indirectly estimated and much less certain; they range from $3.1 \times 10^8 - 7.7 \times 10^9$ $cm^{-2}s^{-1}$. A common assumption in atmospheric modelling is that SO_2 and H_2S are outgassed in a 10:1 ratio (e.g., Zahnle et al. 2006; Claire et al. 2014).

The early Earth is often hypothesized to have been characterized by higher levels of volcanic outgassing compared to the modern Earth due to presumed higher levels of internal heat and tectonic activity; models often assume Archaean SO_2 outgassing rates were $\sim 3\times$ modern (Richter 1985; Kasting et al. 1989; Zahnle et al. 2006). However, Halevy & Head (2014) point out that during the emplacement of major volcanogenic

features such as the terrestrial basaltic plains, sulfur outgassing rates as high as $10^{10} - 10^{11.5}$ $cm^{-2}s^{-1}$ are possible.

No firm constraints exist for SO_2 and H_2S levels on the prebiotic Earth. Kasting et al. (1989) modeled a plausibly prebiotic atmosphere of 2 bars CO_2, 0.8 bar N_2 atmosphere under 0.75× solar irradiation to account for the effects of the faint young Sun 3.9 Ga. Kasting et al. (1989) assumed that sulfur was outgassed entirely as SO_2 at a total sulfur outgassing flux of $\phi_S = 3 \times 10^9$ $cm^{-2}s^{-1}$ into an atmosphere overlying an ocean saturated in SO_2; these conditions favor accumulation of SO_2. Claire et al. (2014) modeled an atmosphere of 0.99 bar N_2 and 0.01 bar CO_2, under irradiation by the 2.5 Ga Sun, with an SO_2:H_2S outgassing ratio of 10:1, for $\phi_S = 1 \times 10^8 - 1 \times 10^{10}$ $cm^{-2}s^{-1}$. Hu et al. (2013) modeled an atmosphere consisting of 0.9 bar CO_2 and 0.1 bar N_2 under irradiation by the modern Sun, with an SO_2:H_2S emission ratio of 2, for $\phi_S = 3 \times 10^9 - 1 \times 10^{13}$ $cm^{-2}s^{-1}$. The SO_2 and H_2S mixing ratios calculated by these models are shown in Table 6.1. Note that the Claire et al. (2014) and Kasting et al. (1989) values are surface mixing ratios, while the Hu et al. (2013) values are column-integrated mixing ratios. Since H_2S and SO_2 levels tend to decrease with altitude due to losses from photochemistry, column-integrated mixing ratios should be understood as lower bounds on the surface mixing ratio. However, since density also decreases with altitude, mixing ratios at lower altitudes are more strongly weighted in the calculation of column-integrated mixing ratios, so the column-integrated mixing ratio tends to be close to the surface mixing ratio.

Table 6.1:: Mixing ratios of H_2S and SO_2 for different early Earth models in the literature and different ϕ_S. a=surface mixing ratio, b=column-integrated mixing ratio.

Reference & assumed ϕ_S	r_{H_2S}	r_{SO_2}
Kasting et al. (1989)^a, $\phi_S = 3 \times 10^9$ cm^{-2}s^{-1}	2×10^{-10}	2×10^{-9}
Claire et al. (2014)^a, $\phi_S = 3 \times 10^9$ cm^{-2}s^{-1}	1×10^{-11}	5×10^{-11}
Hu et al. (2013)^b, $\phi_S = 3 \times 10^9$ cm^{-2}s^{-1}	4×10^{-10}	3×10^{-10}
Claire et al. (2014)^a, $\phi_S = 1 \times 10^{10}$ cm^{-2}s^{-1}	3×10^{-11}	1×10^{-10}
Hu et al. (2013)^b, $\phi_S = 1 \times 10^{10}$ cm^{-2}s^{-1}	1×10^{-9}	9×10^{-10}

These models broadly agree that SO_2 and H_2S levels were low and increase with sulfur emission rate, but their estimates for r_{SO_2} and r_{H_2S} are in tension with each other by up to a factor of 400. The variation in these abundances demonstrates the sensitivity of SO_2 and H_2S levels to atmospheric parameters such as composition and deposition velocities. Of these models, we feel Hu et al. (2013) best matches current understanding of conditions on early Earth: a CO_2-N_2 atmosphere, with volcanic outgassing of both SO_2 and H_2S, with oceans not saturated in SO_2 (as compared to early Mars; see Halevy et al. 2007). Hu et al. (2013) also has the advantage of calculating atmospheric composition at higher values of sulfur outgassing flux than Kasting (1993) and Claire et al. (2014), encompassing the $1 \times 10^{11.5}$ cm^{-2}s^{-1} flux which is the upper limit of what Halevy & Head (2014) suggest possible for the emplacement of terrestrial basaltic plains. We therefore use Hu et al. (2013) as a guide when estimating H_2S and SO_2 levels as a function of sulfur outgassing flux, with the understanding that further, prebiotic-Earth specific modelling is required to constrain this relation with certainty. Table 6.2 presents

H_2S and SO_2 mixing ratios as a function of ϕ_S from Hu et al. (2013) (their Figure 5, CO_2-dominated atmosphere case). We will use this transformation in the rest of this paper.

Table 6.2:: Column-integrated mixing ratios of H_2S and SO_2 as a function of ϕ_S from Hu et al. (2013) (Figure 5, CO_2-dominated case).

ϕ_S ($cm^{-2}s^{-1}$)	r_{H_2S}	r_{SO_2}
3×10^9	4×10^{-10}	3×10^{-10}
1×10^{10}	1×10^{-9}	9×10^{-10}
3×10^{10}	9×10^{-9}	3×10^{-9}
1×10^{11}	5×10^{-8}	7×10^{-9}
3×10^{11}	2×10^{-7}	1×10^{-8}
1×10^{12}	7×10^{-7}	3×10^{-8}
3×10^{12}	2×10^{-6}	8×10^{-8}
1×10^{13}	9×10^{-6}	3×10^{-7}

6.3 Methods

In accordance with the geochemical scenario outlined by Patel et al. (2015), we consider a gas G dissolving into an aqueous reservoir such as a shallow lake or stream (< 10 m deep), through which the UV light required for prebiotic biomolecules synthesis can penetrate (Ranjan & Sasselov 2016). Henry's Law states that the concentration of G,

[G], in aqueous solution at the air/water interface is proportional to the partial pressure of the gas at that interface. We assume the aqueous reservoir to be well-mixed, such that the dissolved gas concentration throughout the solution matches that set by Henry's Law at the interface. If the reservoir is not well-mixed, then the dissolved gas concentration will decrease deeper into the reservoir. Consequently, our calculation provides an upper bound on [G].

In aqueous solution, H_2S undergoes the reactions

$$H_2S \rightarrow HS^- + H^+, pKa_{H_2S,1} = 7.05 \tag{6.1}$$

$$HS^- \rightarrow S^{2-} + H^+, pKa_{H_2S,2} = 19 \tag{6.2}$$

Where the pKa values are taken from Miller (2009), and can be related to the corresponding equilbrium constants by $Ka_X = 10^{-pKa_X}$. Similarly, SO_2 undergoes the reactions

$$SO_2 + H_2O \rightarrow HSO_3^- + H^+, pKa_{SO_2,1} = 1.86 \tag{6.3}$$

$$HSO_3^- \rightarrow SO_3^{2-} + H^+, pKa_{SO_2,2} = 7.2 \tag{6.4}$$

$$HSO_3^- + SO_2 \rightarrow HS_2O_5^-, pKa_{SO_2,3} = 1.5 \tag{6.5}$$

Where the pKa values are from Neta & Huie (1985).

To compute the abundances of these different sulfur-bearing compounds as a function of [G], we must make assumptions as to the background chemistry of the aqueous reservoir they are dissolved in. We can assume they are buffered to a fixed

pH, meaning that the relative speciation of sulfur compounds is independent of [G]. Alternately, we can assume that the reservoir is unbuffered; in this case, the pH of the solution (and hence the speciation of S-bearing compounds) will evolve with [G]. We explore both assumptions below.

6.3.1 Henry's Law Calculation

Henry's Law states that for a species G,

$$[G] = H_G pG, \tag{6.6}$$

where H_G is the gas-specific Henry's Law constant and pG is the partial pressure of G. At $T_0 = 298.15$ K, the Henry's Law constants for H_2S and SO_2 dissolving in pure water are $H_{H_2S} = 0.101$ M/bar and $H_{SO_2} = 1.34$ M/bar, respectively. Increasing salinity tends to decrease H_G, a process known as salting out. Similarly, increasing temperature also tends to decrease H_G. The magnitudes of these effects are modest, and our results are insensitive to variations in temperature of 20K from T_0 and $0 \leq$[NaCl]≤ 1; see Section 6.9. For simplicity, we therefore neglect the temperature- and salinity-dependence of Henry's Law.

6.3.2 Unbuffered Solution

Consider an unbuffered solution with dissolved G, whose properties are determined entirely by the reactions G and its products undergo. From the definition of equilibrium constant, we can use the H_2S and SO_2 speciation reactions to write:

$$\frac{A_{HS^-}A_{H^+}}{A_{H_2S}} = Ka_{H_2S,1} \tag{6.7}$$

$$\frac{A_{S^{2-}}A_{H^+}}{A_{HS^-}} = Ka_{H_2S,2} \tag{6.8}$$

and

$$\frac{A_{HSO3^-}A_{H^+}}{A_{SO_2}} = Ka_{SO_2,1} \tag{6.9}$$

$$\frac{A_{SO3^{2-}}A_{H^+}}{A_{HSO3^-}} = Ka_{SO_2,2} \tag{6.10}$$

$$\frac{A_{HS_2O_5^-}}{A_{SO_2}A_{H^+}} = Ka_{SO_2,3} \tag{6.11}$$

Where A_X is the activity of species X. A_X is related to the concentration of X, $[X]$, by $A_X = \gamma_X[X]$, where γ_X is the activity coefficient (Misra 2012). The use of activities instead of concentrations accounts for ion-ion and ion-H_2O interactions which cause some fraction of the ions to be unavailable for the equilibrium chemistry. $\gamma = 1$ for a solution with an ionic strength of $I = 0$; $\gamma \to 0$ as I increases. For ionic strengths of 0-0.1 M, we calculate the activity coefficients for each species as a function of solution ionic strength using Extended Debye-Huckel theory (Debye & Huckel 1923). For ionic strengths of 0.1-1 M, we calculate the activity coefficients as a function of solution ionic strength by Truesdell-Jones theory.(Truesdell & Jones 1974). The activity coefficients in this regime are calculated by:

$$log(\gamma_X) = -Az_X^2 \frac{I^{0.5}}{1 + B\alpha_X I^{0.5}} \tag{6.12}$$

Here, I is the ionic strength of the solution, A and B are constants that depend on

the temperature and dielectric constant of the solvent (in this case, water), and α_X is ion-specific, with values obtained from Misra (2012); see Section 6.7 for details.

We can combine these equations with the equation for water dissociation:

$$H_2O \rightarrow OH^- + H^+,\ pK_w = 14 \tag{6.13}$$

$$A_{H^+}A_{OH^-} = K_w \tag{6.14}$$

and the requirement for charge conservation:

$$\Sigma_i z_i [X_i] = 0 \tag{6.15}$$

where $[X_i]$ is the concentration of species i and z_i is the charge of species i. With [G] specified by Henry's Law and our assumption of a well-mixed reservoir, this system is fully determined, and we can numerically solve it to determine the concentration of each of the species above as a function of pG and I. A wide range of ionic strengths are possible for natural waters; modern freshwater systems like rivers have typical ionic strengths of order $1 \times 10^{-3}M$ (Lerman et al. 1995), whereas modern terrestrial oceans have typical ionic strengths of $0.72M$[3]. The concentrations of divalent cations, especially Mg^{2+} and Ca^{2+} in early oceans has been suggested to be near 10mM (Deamer & Dworkin 2005), leading to an ionic strength near 20mM. A more fundamental constrain comes from vesicle formation, which is known to be inhibited at high salt concentrations and hence ionic strengths: Maurer & Nguyen (2016) report that lipid vesicle formation is impeded in solutions with $I > 0.1M$.

[3] `http://www.aqion.de/site/69`, accessed 29 November 2016

We calculate the speciation of sulfur-bearing species from dissolved H_2S and SO_2 for $I = 0$, $I = 0.1M$, and $I = 1M$; the results are shown in Figures 6.1 and 6.2. $I = 0$ is the lowest possible ionic strength; $I = 0.1M$ corresponds to the limit from vesicle formation; and $I = 1$ corresponds approximately to the ionic strength of modern oceans.

6.3.3 Buffered Solution

Consider now an aqueous reservoir that is buffered to a given pH. For example, the pH of the oceans is buffered by calcium carbonate to a global mean value of $8.1 - 8.2$ (Hall-Spencer et al. 2008). Then, we know $[H^+]$, and can hence calculate the speciation of dissolved H_2S and SO_2 from the equilibrium constant equations 6.7-6.8 and 6.9-6.11 individually. The geochemical scenario of Patel et al. (2015) invokes lakes and rivers, not oceans, motivating us to focus on low-ionic strength environments. For $I \leq 1 \times 10^{-3}$, $\gamma_X \geq 0.8577$ for the species we consider (Section 6.7). We therefore take $I = 0$ for simplicity for this calculation. Our results are insensitive to ionic strength for $I \leq 1$M (see Figures 6.1 and 6.2), and $I < 1$M is required for vesicle formation and other prebiotic chemistry (Maurer & Nguyen 2016), justifying this simplification.

With Henry's Law and our assumption of a well-mixed reservoir, we can readily calculate the concentration of the above species as a function of pH_2S/pSO_2 and pH. The results of this calculation are presented in Figures 6.1 and 6.2 for 3 representative pHs. We selected pH=8.2, corresponding to modern ocean; pH=7, corresponding to the near-neutral phospate-buffered conditions in which Patel et al. (2015) conducted their experiments; and pH=4.25, corresponding to raindrops in a $pCO_2 \sim 0.1$ bar (Halevy et al. 2007). Such high CO_2 levels are hypothesized for the young Earth in order to power

a greenhouse effect large enough to keep surface conditions clement (Kasting 1993).

6.4 Results

6.4.1 H_2S vs SO_2

Figure 6.1 shows the speciation of sulfur-bearing compounds from dissolved H_2S for an unbuffered reservoir, and reservoirs buffered to various pHs. Over the range of ionic strengths considered, HS^- is the dominant anion, and S^{2-} is present at negligible concentrations. As pH_2S increases, the pH of the unbuffered reservoir drops, but slowly. This is expected, since H_2S is a weak acid.

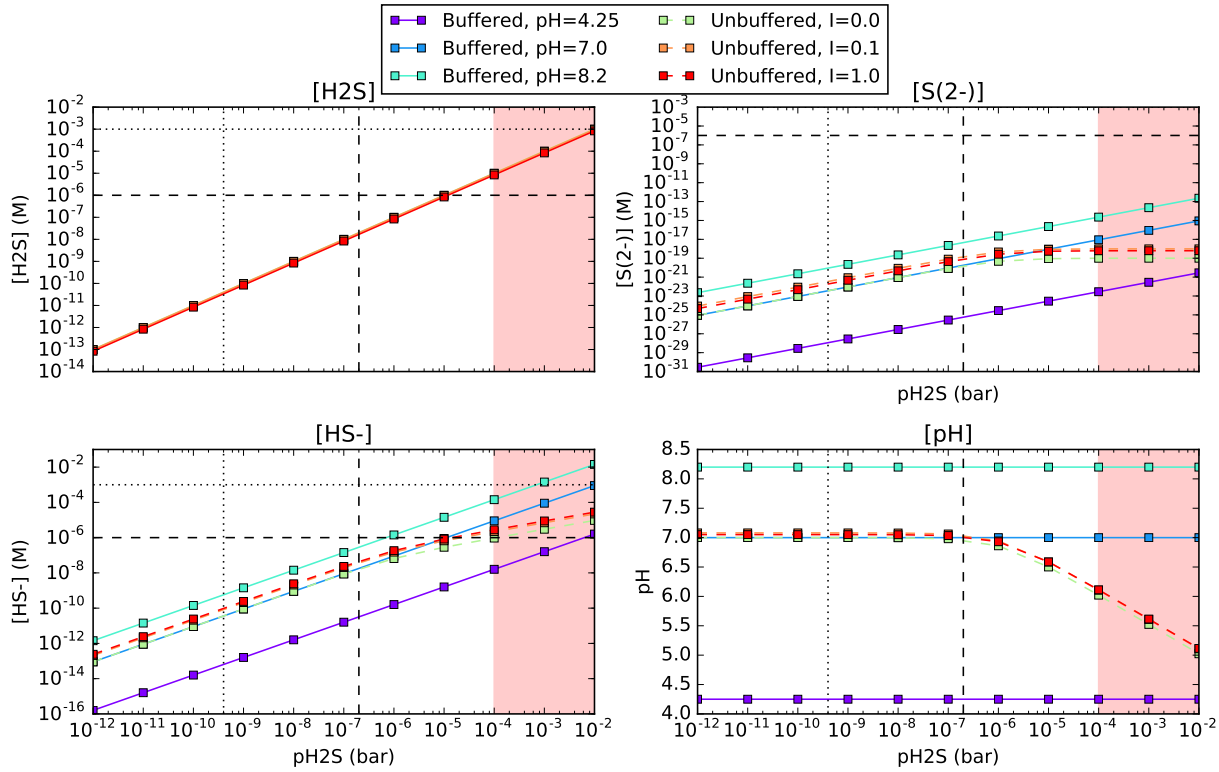

Figure 6.1: Concentrations of sulfur bearing compounds and pH as a function of pH_2S for a well-mixed aqueous reservoir. $[H_2S]$ is calculated from Henry's Law; the concentrations of HS^- and S^{2-} are calculated from equilbrium chemistry for 1) solutions buffered to various pHs, and 2) unbuffered solutions with varying ionic strengths. The vertical dotted line demarcates the expected pH_2S for an abiotic Earth with a weakly reducing CO_2-N_2 atmosphere with modern levels of sulfur outgassing, from Hu et al. (2013). The vertical dashed line demarcates the expected pH_2S for the same model, but with outgassing levels of sulfur corresponding to the upper limit of the estimate for the emplacement of the terrestrial flood basalts. In the red shaded area, pH_2S is so high it blocks UV light from the planet surface, meaning the prebiotic pathways of, e.g., Patel et al. (2015) cannot function (see Section 6.4.3 for details). The horizontal dashed and dotted lines demarcate micromolar and millimolar concentrations, respectively. The cyanosulfidic chemistry of Patel et al. (2015) has been demonstrated at millimolar S-bearing photoreductant concentrations, and at least micromolar levels of these compounds are thought to be required for high-yield prebiotic chemistry

Figure 6.2 shows the speciation of sulfur-bearing compounds from dissolved SO_2 for an unbuffered reservoir, and reservoirs buffered to various pHs. HSO_3^- and SO_3^{2-} are

present at comparable levels; $HS_2O_5^-$ is negligible. As pSO_2 increases, the pH of the unbuffered reservoir falls off rapidly; this is expected since SO_2 is a strong acid.

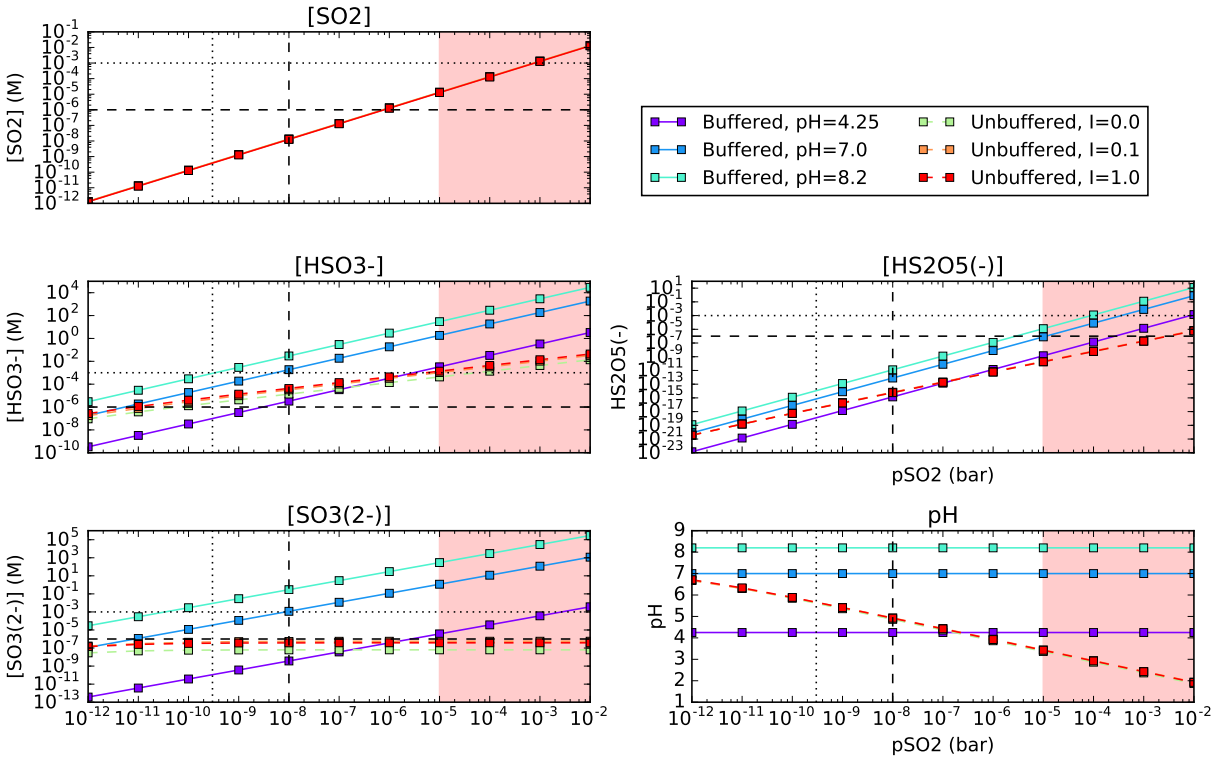

Figure 6.2: Concentrations of sulfur bearing compounds and pH as a function of pSO_2 for a well-mixed aqueous reservoir. $[SO_2]$ is calculated from Henry's Law; the concentrations of HSO_3^-, SO_3^{2-}, and $HS_2O_5^-$ are calculated from equilbrium chemistry for 1) solutions buffered to various pHs, and 2) unbuffered solutions with varying ionic strengths. The vertical dotted line demarcates the expected pSO_2 for an abiotic Earth with a weakly reducing CO_2-N_2 atmosphere with modern levels of sulfur outgassing, from Hu et al. (2013). The vertical dashed line demarcates the expected pH_2S for the same model, but with outgassing levels of sulfur corresponding to the upper limit of the estimate for the emplacement of the terrestrial flood basalts. In the red shaded area, $pSO_2$is so high it blocks UV light from the planet surface, meaning the prebiotic pathways of, e.g., Patel et al. (2015) cannot function (see Section 6.4.3 for details). The horizontal dashed and dotted lines demarcate micromolar and millimolar concentrations, respectively. The cyanosulfidic chemistry of Patel et al. (2015) has been demonstrated at millimolar S-bearing photoreductant concentrations, and at least micromolar levels of these compounds are thought to be required for high-yield prebiotic chemistry

SO_2 is an order of magnitude more soluble than H_2S, and its first dissociation is much more strongly favored ($pKa_{SO_2,1} = 1.86$ vs $pKa_{H_2S,1} = 7.05$). Consequently, far lower concentrations of sulfurous anions can be sustained for a given H_2S than for the same pSO_2 (see Figures 6.1 and 6.2). Maintaining micromolar concentrations of HS^- requires $pH_2S \geq 1 \times 10^{-6}$ bar at pH=8.2 (modern ocean), and $pH_2S \geq 1 \times 10^{-5}$ for more neutral pHs. Maintaining millimolar concentrations of S^{2-} ($pKa_{H_2S,2} = 19$) is impossible over the pH ranges considered. The concentration of sulfurous anions could be increased by going to higher pH and salinity, but these scenarios pose their own challenges to prebiotic chemistry.

By contrast, dissolved SO_2 gives rise to comparatively high concentrations of sulfurous anions due to higher solubility and a more favorable first ionization. Micromolar concentrations of HSO_3^- are possible for $pSO_2 > 10^{-11}$ bar for all but very acidic solutions; micromolar concentrations of SO_3^{2-} are possible for solutions buffered to pH$\geq$ 7 over the same range. *Millimolar* levels of HSO_3^- and SO_3^{2-} are possible for solutions buffered to pH$\geq$ 8.2 for $pSO_2 \gtrsim 10^{-10}$ bar, and for pH$\geq$ 7 solutions for $pSO_2 \gtrsim 10^{-8}$ bar. $pSO_2 \geq 3 \times 10^{-10}$ bar is expected for even modern outgassing rates according to the model of Hu et al. (2013), and outgassing rates on early Earth are generally thought to have been higher than the modern day. During transient epochs of intense volcanism such as the emplacement of basaltic plains, emission rates could rise as high as $\phi_S = 10^{11.5}$ cm^{-2}s^{-1} (Halevy & Head 2014; Self et al. 2006), corresponding to $pSO_2 = 1 \times 10^{-8}$ bar. We note that estimates based on Hu et al. (2013) are for column-integrated abundances, and hence are lower bounds on the surface abundances. Hence, it seems likely that the atmosphere could have supplied micromolar-levels of SO_2-derived anions for prebiotic chemistry, and perhaps even millimolar concentrations

if the solution were buffered to slightly alkaline pH (e.g., the ocean today).

6.4.2 H_2S and SO_2

In Section 6.4.1 we evaluated the prospects for buildup of sulfur-bearing anions from dissolved atmospheric H_2S and SO_2 in isolation. However, H_2S and SO_2 are injected simultaneously into the atmosphere by volcanism, and would have been present at the same time. Figure 6.3 presents the speciation of sulfur-bearing molecules from dissolved atmospheric H_2S and SO_2 in a solution buffered to a pH of 7 as a function of total sulfur outgassing rate, ϕ_S.

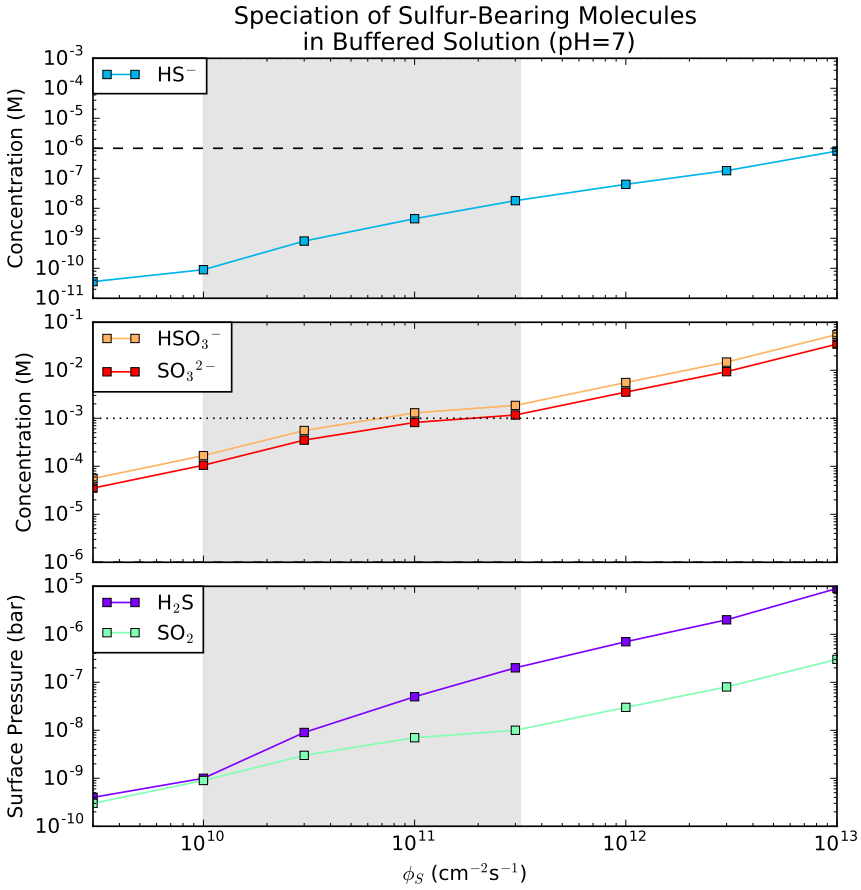

Figure 6.3: Speciation of sulfur-bearing molecules in an aqueous reservoir buffered to pH=7 as a function of total sulfur emission flux ϕ_S. The range of ϕ_S highlighted by Halevy & Head (2014) for emplacement of basaltic plains on Earth is shaded in grey. Horizontal dashed and dotted lines demarcate micromolar and millimolar concentrations, respectively.

This pH corresponds to the phospate-buffered conditions in which the chemistry of Powner et al. (2009) and Patel et al. (2015) proceeded. $\phi_S = 1 - 3 \times 10^9$ cm^{-2}s^{-1} for modern Earth, and $\phi_S = 10^{10} - 10^{11.5}$ cm^{-2}s^{-1} have been suggested on a transient (1-10 year) basis for major volcanic episodes like the emplacement of basaltic plains on Earth

(Halevy & Head 2014; Self et al. 2006). We took the surface mixing ratio of these gases to equal the column-integrated mixing ratio. In practice, the surface mixing ratio should be slightly higher than the column-integrated mixing ratio. Consequently, the pH_2S and pSO_2 we use here are lower bounds. As discussed in Section 6.4.1, SO_2-derived anions can build to micromolar levels at modern outgassing rates, and can build to millimolar levels during volcanic episodes like the emplacement of basaltic plains, while H_2S-derived anions cannot.

6.4.3 Coupling to the UV Surface Environment

The cyanosulfidic chemistry of Patel et al. (2015) critically requires ultraviolet (UV) radiation to power photoreduction and to amplify the population of biogenic ribonucleotides (Powner et al. 2009). H_2S and SO_2 are robust UV shields, and at elevated levels their presence can have a dramatic impact on the surface UV environment (Ranjan & Sasselov 2017). Figure 6.4 presents the attenuation of incoming UV radiation due solely to atmospheric H_2S and SO_2 as a function of ϕ_S, with the H_2S and SO_2 abundances connected to ϕ_S from the work of Hu et al. (2013) as before. Scattering effects due to background gases like CO_2 and N_2 are ignored for simplicity and because of the considerable uncertainty in their abundances. If the prebiotic atmosphere were high scattering (e.g. due to high surface pressure, high CO_2 abundance, or thick clouds), the radiative impact of atmospheric absorbers would be amplified. This would decrease transmission, especially at shorter wavelengths where Rayleigh scattering is stronger. This calculation also ignores the radiative impact of aerosols; Hu et al. (2013) predict significant aerosol formation for $\phi_S > 3 \times 10^{11}$ cm^{-2}s^{-1}. At such levels, these

aerosols would also make the atmosphere more scattering and amplify atmospheric absorption. Therefore, the transmissions show in Figure 6.4 are upper bounds. However, for conventional thin, N_2-dominated atmospheres with $\phi_S < 3 \times 10^{11}$ cm^{-2}s^{-1}, they are reasonable approximations.

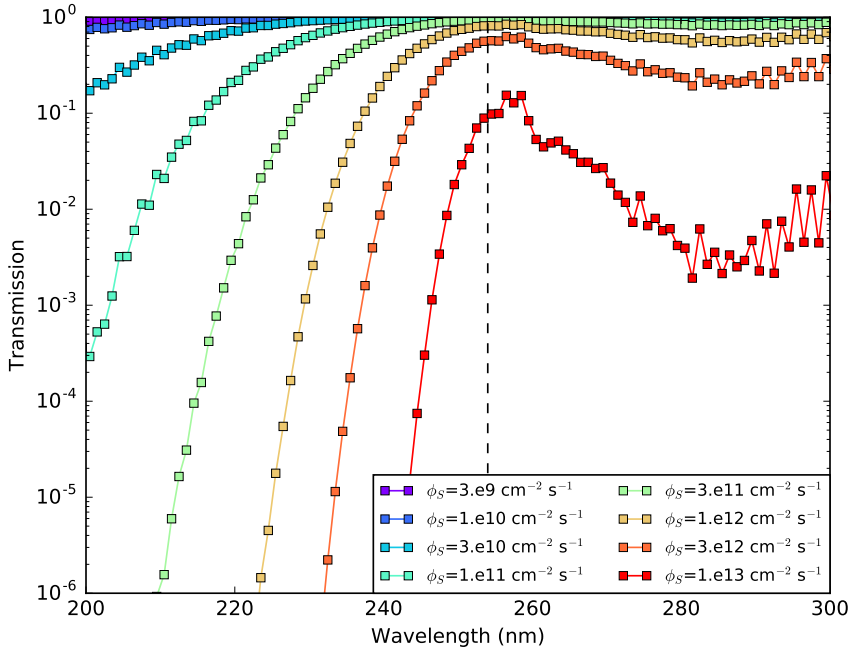

Figure 6.4: Atmospheric spectral transmission as a function of ϕ_S due to SO_2 and H_2S. The black line demarcates 254 nm, the wavelength at which the low pressure mercury lamps commonly used in prebiotic chemistry experiments emit. This clear-sky calculation ignores the radiative impact of background gases and of aerosols, and hence must be considered an upper bound on available fluence.

While atmospheric H_2S and SO_2 can attenuate shortwave UV radiation, transmission of longer-wavelength UV radiation remains high over the plausible range of ϕ_S. In particular, radiation near the 254 nm emission peak of the low pressure mercury lamps

commonly used in prebiotic chemistry studies, including Powner et al. (2009), Ritson & Sutherland (2012), and Patel et al. (2015), is available across the plausible range of $\phi_S < 3 \times 10^{11}$ cm^{-2}s^{-1}. Indeed, these gases have an absorption window near 254 nm, meaning the radiation used by such prebiotic chemistry experiments is available at even higher ϕ_S. Consequently, volcanism could supply up to millimolar levels of SO_3^{2-} and HSO_3^- for prebiotic chemistry without blocking off the UV radiation required by UV-sensitive prebiotic pathways. Figures 6.1 and 6.2 illustrate these UV cutoff limits.

6.5 Discussion

The cyanosulfidic prebiotic chemistry of Patel et al. (2015) requires sulfur-bearing anions, both as feedstocks and as photoreductants (e.g. through donation of solvated electrons through UV-powered photoionization). We have shown that terrestrial volcanism could have supplied two such compounds, SO_3^{2-} and HSO_3^{2-}, derived from the dissolution of SO_2 into aqueous solution. These compounds would have been available at micromolar levels for volcanic outgassing rates lower than the modern day, and even higher levels at the elevated outgassing rates hypothesized for early Earth. During episodes of high volcanism such as those responsible for emplacement of basaltic plains ($\phi_S \approx 3 \times 10^{11}$ cm^{-2} s^{-1}), these compounds could have built up to the millimolar levels for pH$\geq$ 7. Such concentrations of sulfurous anions and such pH's (due to phospate buffering) are invoked by the Sutherland team in their cyanosulfidic prebiotic chemistry (Patel et al. 2015).

Due to its lower solubility and unfavorable first dissociation, sulfurous anions derived from H_2S can only be supplied at low concentrations (sub-micromolar) across the plausible range of pH_2S. Therefore, non-atmospheric mechanisms must be invoked

for supply of such anions, if required by a proposed prebiotic chemical pathway.

H_2S and SO_2 are strong UV absorbers, and if present at high enough levels could suppress UV-sensitive prebiotic chemistry (Ranjan & Sasselov 2017). However, over the expected range of sulfur outgassing fluxes, including during epochs of intense volcanism, these gases are not present at high enough levels to extinguish prebiotic chemistry. Indeed, these gases have an an absorption window near 254 nm, the emission wavelength for the mercury lamps commonly used in prebiotic chemistry. Rather, H_2S and SO_2 preferentially attenuate shortwave radiation that is expected to be more damaging to nascent biomolecules and less prebiotically useful. This is an intriguing coincidence: epochs of high volcanism should have been characterized by access to both the midrange UV radiation and sulfurous anions required for cyanosulfidic chemistry, and by lower levels of potentially-damaging FUV radiation. Volcanism can also be a source of reducing gases like CH_4, which would have been photochemically processed into HCN and rained out (Zahnle 1986), providing both key feedstock molecules required by the cyanosulfidic chemistry of Patel et al. (2015). Hence, epochs of high volcanism may have been uniquely conducive to cyanosulfidic prebiotic chemistry.

6.6 Conclusions

Cyanosulfidic prebiotic reaction networks like those of Patel et al. (2015) require reduced sulfidic anions at elevated levels (micromolar-millimolar) to proceed. Here, we show that such levels of certain sulfidic anions are globally available in shallow, well-mixed aqueous reservoirs due to dissolution of sulfur-bearing gases that are volcanically injected into the atmosphere. In particular, anions derived from SO_2 are available at $\geq 1\mu$M levels

in non-acidic reservoirs for SO_2 outgassing rates corresponding to the modern Earth and higher. During episodes of intense volcanism, like the emplacement of basaltic fields like the Deccan Traps, SO_2-derived anions may be available at $\geq 1m$M levels for reservoirs buffered to pH$\geq$ 7 (e.g., the modern ocean at pH= 8.2). Atmospheric modelling suggests that during these episodes, atmospheric SO_2 and H_2S will not the block the NUV radiation also required by these pathways (Powner et al. 2009; Ritson & Sutherland 2012; Patel et al. 2015), though further modelling is required to ensure that photochemically-generated aerosols will not build to levels sufficient to quench UV. Coupled with generation of the feedstock molecule HCN from photochemical reprocessing of volcanically outgassed CH_4 (Zahnle 1986), it appears that episodes of intense volcanism might have been especially clement for cyanosulfidic prebiotic chemistry which exploits SO_2-derived anions (e.g., HSO_3^-). On the other hand, anions derived from H_2S would not have been available at micromolar levels across the plausible range of volcanic outgassing due to low solubility of H_2S and an unfavorable dissociation constant, and prebiotic chemistry invoking such anions must invoke local, specialized sources.

Acknowledgements

We thank Amit Levi for extensive discussions and guidance on aqueous-phase equilibrium chemistry. We thank Trista Vick-Majors for helpful discussions.

This research has made use of NASA's Astrophysics Data System Bibliographic Services, and the MPI-Mainz UV-VIS Spectral Atlas of Gaseous Molecules.

S. R. and D. D. S. gratefully acknowledge support from the Simons Foundation, grant no. 290360.

6.7 Appendix A: Activity Coefficient Calculation

This appendix describes the calculation of the activity coefficients of the ions involved in equilibria reactions for SO_2 and H_2S.

We use the Extended Debye-Huckel Theory to calculate activity coefficients (γ_i) for ions at comparatively lower ionic strengths. Extended Debye-Huckel theory is valid for ionic strengths up to 0.1M. Beyond this ionic strength, other theories have to be used. We implement the Truesdell-Jones theory (valid up to I=1M) for higher ionic strengths. We don't consider ionic strengths beyond 1M, due to the general difficulties of other prebiotically relevant reactions at such high ionic strengths. For comparison, the Dead Sea has an ionic strength of 9M (Krumgalz 1997). Lipid vesicle formation, which is thought to be a necessary step in most formation of life scenarios, is generally not possible at ionic strengths above 0.1M Maurer & Nguyen (2016). Thus, our implementation of Extended Debye Huckel theory for lower ionic strengths should be sufficient for most conditions we consider. However, to test the trend of continuing to increase the ionic strength, we also provide a method for calculating activities up to an ionic strength of 1M.

Extended Debye Huckel theory states that:

$$log\gamma_i = -Az_i^2 \frac{I^{0.5}}{1 + B\alpha_i I^{0.5}} \tag{6.16}$$

where A and B depend on the temperature and dielectric constant of the solvent,

and α_i is an ion specific parameter.

Table 6.3 summarizes the values for these parameters used in our calculations, all of which are taken from Misra (2012).

Table 6.3:: Extended Debye-Huckel parameters used in this work

	HSO_3^-	SO_3^{2-}	HS^-	S^{2-}	OH^-	H^+
α_i	4.0	4.5	3.5	5.0	3.5	9.0
$A \times 10^{-8}$	0.5	0.0585	0.4960	0.5130	0.4966	0.5271
$B \times 10^{8}$	0.3262	0.3281	0.3258	0.3290	0.3258	0.3314

Truesdell-Jones theory modifies the Extended Debye-Huckel theory as follows:

$$log\gamma_i = -Az_i^2 \frac{I^{0.5}}{1 + B\alpha_i^0 I^{0.5}} + b_i I \tag{6.17}$$

where b_i is a parameter typically on the order of 0.1 and α_i^0 is the effective ion radius. We assume the effective radius is the same for Extended Debye Huckel theory and Truesdell Jones theory ($\alpha_i = \alpha_i^0$). We choose a value of $b_i = 0.2$.

In our calculation, we choose three values of ionic strength: I=0M, I=0.1M, and I=1M. Table 6.4 shows the activity coefficients for the relevant ions at the three ionic strengths.

Table 6.4:: Activity coefficients calcuated for the ions in this study.

	I=0 M	I=0.1 M	I=1M
HSO_3^-	1.0	0.773	0.607
SO_3^{2-}	1.0	0.227	0.00925
HS^-	1.0	0.697	0.319
S^{2-}	1.0	0.224	0.00887
OH^-	1.0	0.697	0.319
H^+	1.0	0.215	0.00779

6.8 Appendix B: Sensitivity of Equilibrium Constants to Temperature

This appendix summarizes our assessment of the temperature dependence of acid dissociation equilibrium constants used in this work.

In order to assess the temperature dependence of acid dissociation constants, we use the Van't Hoff Equation:

$$\frac{\partial[lnK]}{\partial T} = \frac{-\Delta H}{RT^2} \tag{6.18}$$

Solving this differential equation gives:

$$K_2 = K_1 exp\left[-\frac{\Delta H}{R}\left(\frac{1}{T_2} - \frac{1}{T_1}\right)\right] \tag{6.19}$$

With this equation, the acid dissociation constant can be calculated at any given

temperature, provided its value is known at a reference temperature, typically room temperature (298K). ΔH is the change in enthalpy of the reaction, given by:

$$\Delta H = \sum \Delta H_f^o(products) - \sum \Delta H_f^o(reactants) \tag{6.20}$$

The enthalpies of formation for the products and reactants of the reactions we are considering were tabulated from (Miller 2009), and are shown in Table 6.5.

Table 6.5:: Enthalpies of formation for products and reactants of the reactions we consider.

	ΔH_f^o (kJ/mol)
HSO_3^-	-626.2
SO_3^{2-}	-635.5
SO_2	-296.8
HS^-	-17.6
S^{2-}	33.1
H_2S	-20.6
H_2O	-285.8

Using these values and the Van't Hoff equation, we calculated the temperature dependence of the acid dissociation constants. Table 6.6 shows the pKa's for SO_2 and H_2S at three temperatures: 0, 25, and 50 degrees Celsius.

Table 6.6:: pKa for dissociations of aqueous sulfur-bearing gases as a function of temperature.

	$\lvert\frac{pKa_1(T=0°C)}{pKa_1(T=25°C)}-1\rvert$	$\lvert\frac{pKa_1(T=50°C)}{pKa_1(T=25°C)}-1\rvert$
SO_2, pKa_1	2.65×10^{-5}	2.24×10^{-5}
SO_2, pKa_2	1.16×10^{-4}	9.77×10^{-5}
H_2S, pKa_1	7.00×10^{-6}	5.90×10^{-6}
H_2S, pKa_2	4.38×10^{-5}	3.70×10^{-5}

Prebiotic environments are likely within the 0-50°C range we consider here, and Table 6.6 shows very small variation in the pKa's at temperatures over this range. Variations are typically on the order of hundreths to thousandths of pKa, which do not significantly affect our results. We thus conclude that our equilibrium chemistry calculations are insensitive to temperature.

6.9 Appendix C: Sensitivity of Henry's Law Constants to Salinity and Temperature

This appendix describes our assessment of the sensitivity of the Henry's Law coefficients for SO_2 and H_2S to temperature and salinity.

We account for the effect of salinity on H_G using the Schumpe-Sechenov method, as

outlined in Burkholder et al. (2015):

$$\log H_0/H = \Sigma_i(h_i + h_G) * c_i, \tag{6.21}$$

where H_0 is the Henry's Law constant in pure water, H is the Henry's law constant in saline solution, c_i is the concentration of the ion i, h_i is an ion-specific constant, and h_G is a gas-specific constant. h_G is temperature dependent, via $h_G = h_0 + h_T(T - 298.15K)$. NaCl is the dominant salt in Earth's oceans; we approximate NaCl as the sole source of salinity in our calculations. Table 6.7 summarizes the values of these parameters used for this study, all taken from the compendium of Burkholder et al. (2015).

Table 6.7:: Henry's law parameters used in this study.
[a]Value not found in literature search; assumed to be 0.

	H_2S	SO_2	Na^+	Cl^-
H_0 (M/bar)	0.101	1.34	–	–
h_0 (M^{-1})	-0.0333	-0.0607	–	–
h_T (M^{-1})	0[a]	0.000275	–	–
h_i (M^{-1})	–	–	0.1143	0.0318

The Henry's Law constants for these gases as a function of [NaCl] at $T = 298.15$K is show in Figure 6.5. In this study, we consider ionic strengths $I \leq 1$M, corresponding to [NaCl]$\leq$ 1M. At such levels, salinity has a negligible effect on Henry's Law solubility, and we consequently neglect it in our calculations.

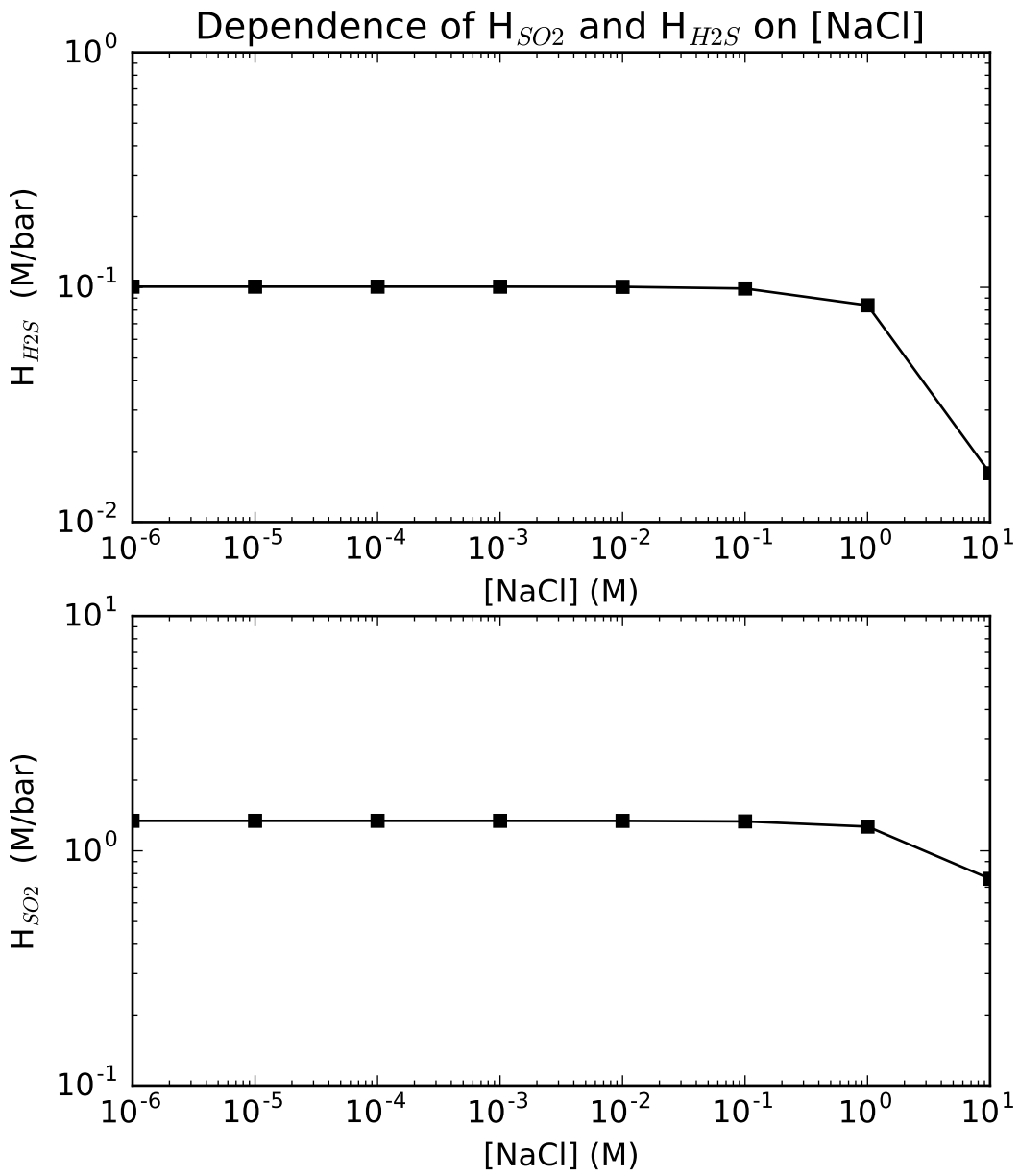

Figure 6.5: Dependence of Henry's Law constants for H_2S and SO_2 on [NaCl], calculated using the formalism from Burkholder et al. (2015). H_{H_2S} and H_{SO_2} are insensitive to [NaCl] for [NaCl]$<$ 1M.

We calculated the effect of temperature on Henry's Law using the three-term empirical fit outlined in Burkholder et al. (2015), i.e. $\ln(H) = A + B/T + C\ln(T)$, where H is in units of M/atm and A, B, and C are gas-specific coefficients of an empirical fit. The values of these coefficients for H_2S and SO_2 were taken from Burkholder et al. (2015) and are summarized in Table 6.8. $H(T)$ for H_2S and SO_2 is plotted in Figure 6.6. For temperatures ranging from $278 - 318$ K, the Henry's Law constants vary by less than a factor of 2. As we are concerned with order-of-magnitude variations in concentrations in this study, our conclusions are insensitive to such modest variations in gas solubility. We also estimated the temperature dependence using the van 't Hoff equation as outlined in Sander (2015), and obtained similar results.

Table 6.8:: Parameters used to calculate temperature dependence of Henry's law in this work.

Parameter	H_2S	SO_2
A	-145.2	-39.72
B	8120	4250
C	20.296	4.525

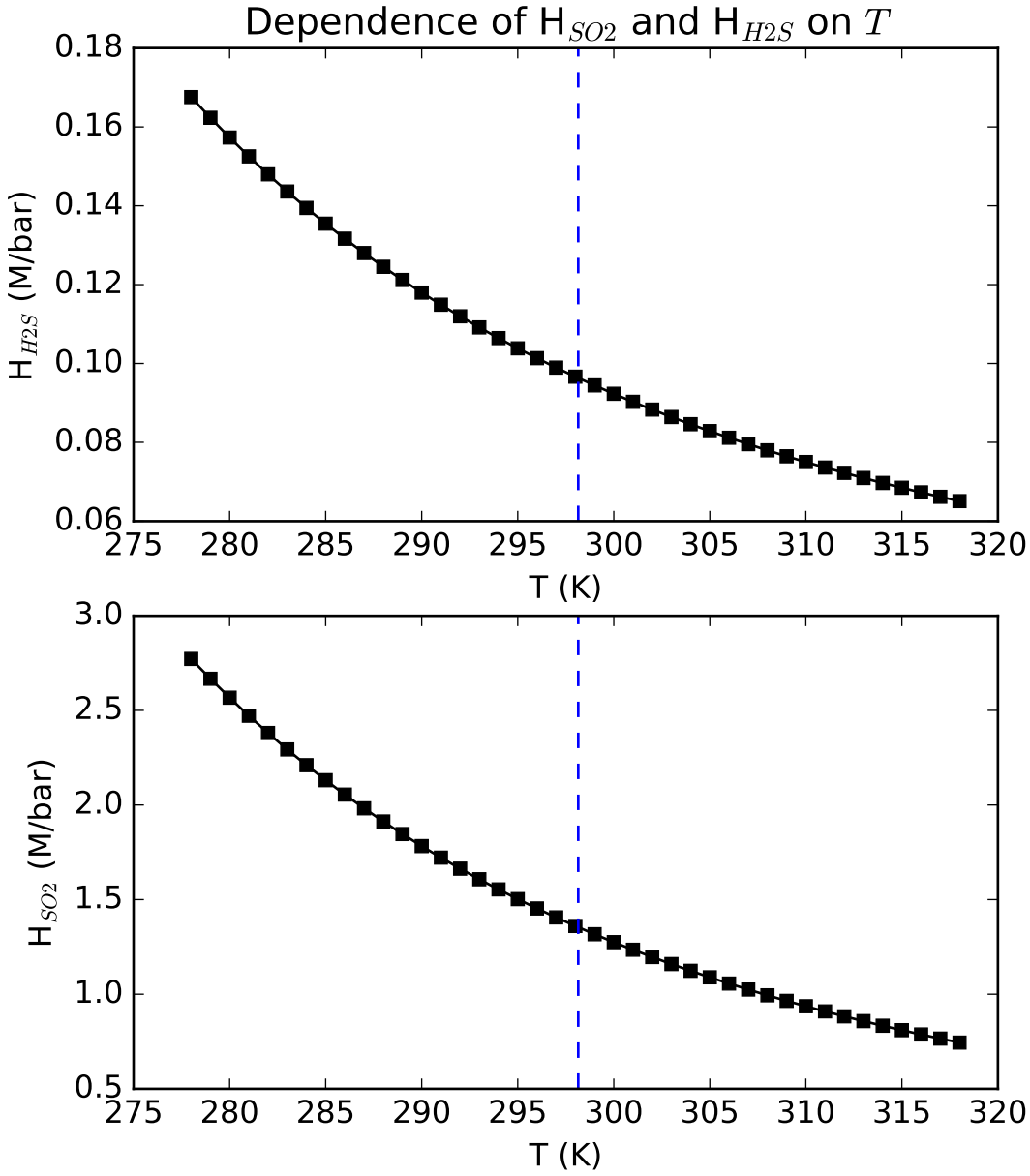

Figure 6.6: Temperature dependence of Henry's Law constants for H_2S and SO_2, calculated using the formalism from Burkholder et al. (2015). Varying the temperature by 20K relative to the reference temperature of 298.15K (blue line) affects the value of H_{H_2S} and H_{SO_2} by less than a factor of two. Our conclusions are insenstive to such variations.

6.10 Appendix D: H_2S and SO_2 Cross-Sections

We took our H_2S and SO_2 cross-sections as described in Ranjan & Sasselov (2017). In brief: SO_2 cross-sections from 200-300 nm came from the compilation of Manatt & Lane (1993). H_2S cross-sections from 200-259.460 nm were from Wu & Chen (1998), and from 259.460-300 nm were from Grosch et al. (2015). Figures 6.7 and 6.8 below present the total and Rayleigh scattering cross-sections for H_2S and SO_2 from 200-300 nm; scattering from these gases is negligible compared to absorption across this spectral range.

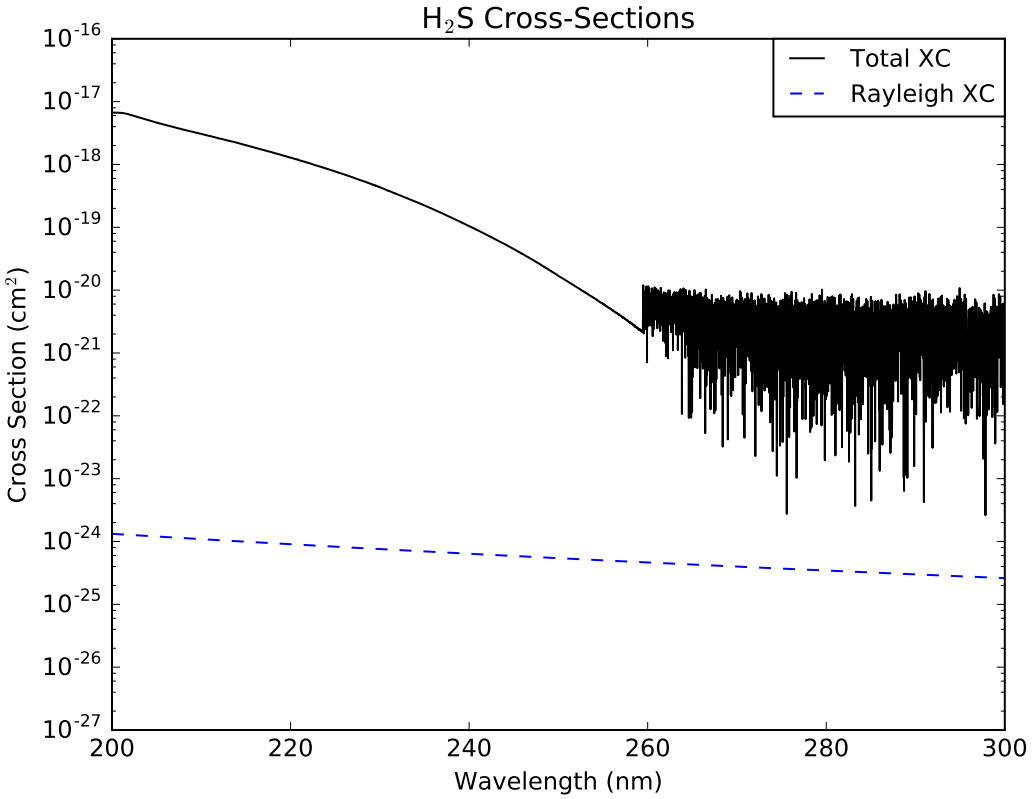

Figure 6.7: Total and scattering cross-sections for H_2S in the NUV range. .

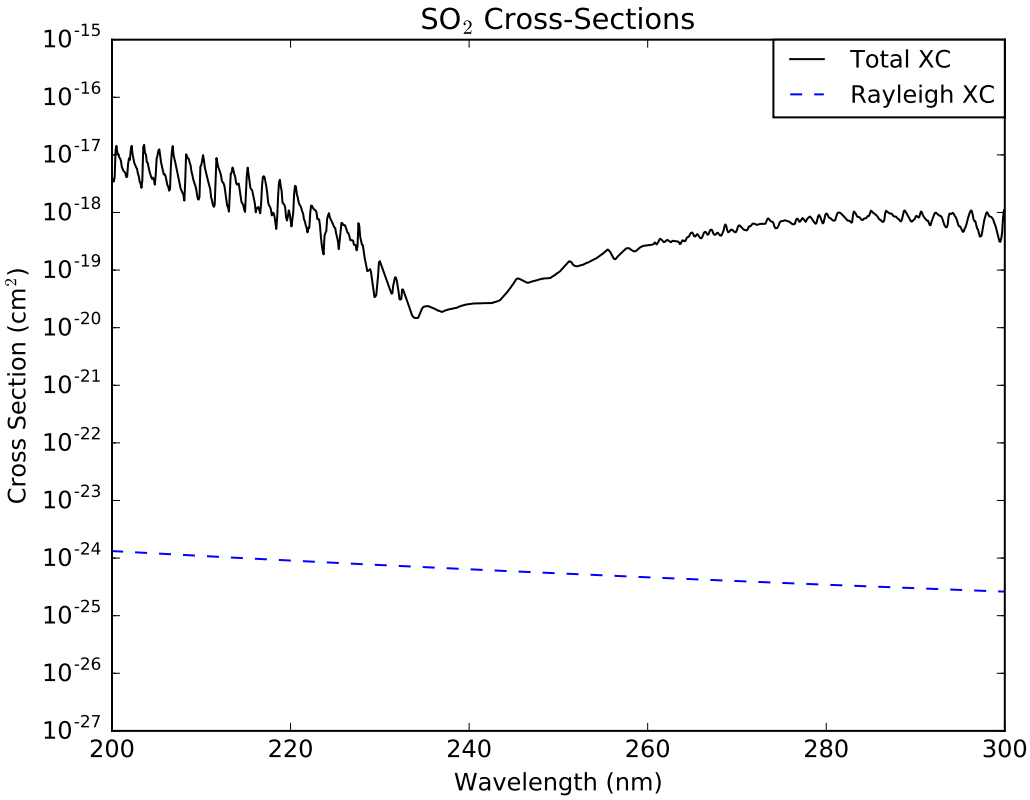

Figure 6.8: Total and scattering cross-sections for SO_2 in the NUV range.

Chapter 7

Conclusions and Future Directions

7.1 Conclusions

With the objectives of improving our understanding of abiogenesis, this thesis has identified environmental requirements for putative prebiotic chemistry, and explored their availability on Earth and on other worlds.

In Chapter 2, we have compared the monochromatic UV irradiation commonly used in laboratory simulations of prebiotic chemistry to the broadband surficial and aqueous UV environment on early Earth. We demonstrated that prebiotic chemistry is robustly shielded from solar activity and/or destructive FUV radiation by both water vapor and atmospheric absorbers, and discussed the constraints placed by photolysis on buildup of atmospheric HCN and CH_4. We showed that prebiotic photochemistry is sensitive to the spectral shape and amplitude of irradiation, and that reactions derived under monochromatic irradiation might fail under more realistic conditions.

Our work demonstrates the need to characterize the prebiotic UV environment in spectral shape and amplitude and to characterize the wavelength dependence of prebiotic photochemistry, to ensure that putative prebiotic pathways could have functioned in natural condition.

Motivated motivated by our work in Chapter 2, in Chapter 3 we explored the spectral shape and amplitude of UV irradiation on prebiotic Earth. Our work demonstrated that due to degeneracy of most major atmospheric absorbers with CO_2 absorption, the surface UV environment is robust to much of the considerable uncertainty in early Earth's atmospheric state. This enabled us to robustly constrain the prebiotic UV environment, a critical input for laboratory simulations of prebiotic chemistry. Our work affirms that NUV sources like Hg lamps are reasonable sources for initial simulations of prebiotic chemsitry because radiation at their emission wavelengths would have been available at Earth's surface largely independent of atmospheric state[1], while FUV sources like ArF eximer lasers are not (e.g., Pestunova et al. 2005).

In Chapter 4, we characterized the UV environment on early Mars. We found the early Martian UV environment to be similar to prebiotic Earth's under normative assumptions as to atmospheric state. However, if dust or volcanic gas levels were high on Mars, UV radiation would have been strongly suppressed. In these scenarios, Martian surface UV would have been strongly suppressed, and UV-sensitive prebiotic chemistry would have been quenched, including the most promising (and arguably only) pathway for the abiotic synthesis of the ribonucleotides, potentially disfavoring abiogenesis on Mars. Further modelling is required to constrain the plausibility of these scenarios.

[1]Though for very thick ($>$ 70 bar) atmospheres UV fluence would have been suppressed by 1-2 orders of magnitude.

In Chapter 5, we characterized the UV environment on prebiotic Earth-analog planets orbiting M-dwarfs, which for observational reasons are the most compelling targets for spectroscopic biosignature gas search. Regardless of atmospheric state, M-dwarf planets are low-UV environments due to low emission of prebiotically useful NUV radiation by these cooler stars. Prebiotic chemistry on such worlds would have access to $\geq 2-3$ orders of magnitude less bioactive fluence, and laboratory measurements are required to determine whether UV-dependent prebiotic chemistry can proceed under such conditions. Increased UV emission during M-dwarfs' frequent flares may offer a solution to this UV-paucity problem; laboratory measurements can also constrain this possibility.

In Chapter 6, we explored the global availability of reduced sulfidic anions in aqueous solution. Such molecules are critically required for cyanosulfidic reaction networks that remain the most promising prebiotic path to the ribonucleotides. Past prebiotic chemistry work has assumed the availability of H_2S-derived anions like HS^-. We show that while it is challenging to build up prebiotically-relevant levels of HS^- due to an unfavorable dissociation constant and rapid loss of H_2S to the atmosphere, elevated levels of SO_2-derived anions like HSO_3^- can be readily achieved, especially during episodes of volcanism like the emplacement of basaltic plains. Our work suggests that epochs of high volcanism might have been especially favorable for cyanosulfidic prebiotic chemistry if this chemistry can exploit SO_2-derived anions instead of H_2S-derived anions.

7.2 Future Work

This thesis motivates a number of paths for future work, spanning experiment, observation and theory.

Experimentally, there is a need for work to characterize the dependence of photosensitive prebiotic chemistry on the spectral shape and amplitude of irradiation. Characterization of the wavelength and intensity dependence is required to constrain whether pathways that function in the laboratory could have functioned on early Earth. Characterization of the intensity dependence is also required to determine whether putative prebiotic photochemistry could have functioned on planets orbiting M-dwarfs, and hence will directly impact assessments of the inhabitability of these objects. We are pleased to note that this realization is beginning to percolate the community, and has begun to impact research trajectories (Rapf & Vaida 2016; Todd et al. 2017a).

Observationally, there is a need for more observations of M-dwarfs in the NUV. Improved M-dwarf NUV flare statistics and spectral characterization can constrain whether M-dwarf flaring can compensate for their low NUV radiation. Additionally, while the median increase in NUV emission of pre-main-sequence (PMS) M-dwarfs is only an order of magnitude and insufficient to compensate for their reduced NUV outut relative to the Sun, it is possible some extremal objects show much higher fractional NUV output. A survey of PMS NUV emission can help constrain this possibility.

Theoretically, first, this work highlighted potential low-UV scenarios for Mars, whereby elevated levels of dust and/or volcanic emissions could suppress surface UV and dependent prebiotic chemistry. Atmospheric modelling can constrain if these scenarios

can occur and if so under what conditions and for how long. Second, in thick (highly scattering) atmospheres the radiative impact of absorbers like dust can be amplified, potentially suppressing UV. This effect is especially important to objects at the outer edge of the habitable zone, where thick atmospheres are required to sustain surface liquid water. Atmospheric modelling can constrain the impact of this effect, and its role in prebiotic chemistry. Third, while M-dwarf flares directly impact the surface UV environment due to elevated levels of stellar NUV emission, they also indirectly impact it thanks to the reprocessing and downshifting of higher-energy radiation, the so-called UV flash (Smith et al. 2004). This may further help solve the NUV paucity problem for M-dwarfs. Atmospheric modelling can constrain this effect as well. I plan to execute these three investigations during my postdoctoral fellowship.

References

Abramov, O., & Mojzsis, S. J. 2009, Nature, 459, 419

Adcock, C. T., Hausrath, E. M., & Forster, P. M. 2013, Nature Geoscience, 6, 824

Alizadeh, E., & Sanche, L. 2012, Chemical reviews, 112, 5578

Anglada-Escudé, G., Amado, P. J., Barnes, J., et al. 2016, Nature, 536, 437

Au, J. W., Cooper, G., Burton, G. R., Olney, T. N., & Brion, C. E. 1993, Chemical Physics, 173, 209

Ayres, T. R., & Linsky, J. L. 1980, ApJ, 235, 76

Backx, C., Wight, G. R., & Van der Wiel, M. J. 1976, Journal of Physics B Atomic Molecular Physics, 9, 315

Balavoine, G., Moradpour, A., & Kagan, H. 1974, Journal of the American Chemical Society, 96, 5152

Ban, N., Nissen, P., Hansen, J., Moore, P. B., & Steitz, T. A. 2000, Science, 289, 905

Banerjee, A., Ganguly, G., Tripathi, R., Nair, N. N., & Paul, A. 2014, Chemistry–A European Journal, 20, 6348

Barks, H. L., Buckley, R., Grieves, G. A., et al. 2010, ChemBioChem, 11, 1240

Barnes, R., Deitrick, R., Luger, R., et al. 2016, ArXiv e-prints, arXiv:1608.06919

Batalha, N., Domagal-Goldman, S. D., Ramirez, R., & Kasting, J. F. 2015, Icarus, 258, 337

Beckstead, A. A., Zhang, Y., de Vries, M. S., & Kohler, B. 2016, Physical Chemistry Chemical Physics, 18, 24228

Benner, S. A. 2013, Mineral Mag, 77, 686

Benner, S. A., & Kim, H.-J. 2015, in Proc. SPIE, Vol. 9606, Instruments, Methods, and Missions for Astrobiology XVII, 96060C

Benner, S. A., Kim, H.-J., & Carrigan, M. A. 2012, Accounts of chemical research, 45, 2025

Benner, S. A., Kim, H.-J., Kim, M.-J., & Ricardo, A. 2010, Cold Spring Harbor perspectives in biology, 2, a003467

Bernas, A., Ferradini, C., & Jay-Gerin, J.-P. 1997, Chemical physics, 222, 151

Bernstein, M., Sandford, S. A., Allamandola, L. J., et al. 2000, in Astronomical Society of the Pacific Conference Series, Vol. 213, Bioastronomy 99, ed. G. Lemarchand & K. Meech, 197

Bernstein, M. P., Dworkin, J. P., Sandford, S. A., Cooper, G. W., & Allamandola, L. J. 2002, Nature, 416, 401

Berta, Z. K., Irwin, J., & Charbonneau, D. 2013, ApJ, 775, 91

Blanksby, S. J., & Ellison, G. B. 2003, Accounts of chemical research, 36, 255

Bogaard, M. P., Buckingham, A. D., Pierens, R. K., & White, A. H. 1978, Journal of the Chemical Society, Faraday Transactions 1: Physical Chemistry in Condensed Phases, 74, 3008

Bogumil, K., Orphal, J., Homann, T., et al. 2003, Journal of Photochemistry and Photobiology A: Chemistry, 157, 167

Bohren, C. F. 1987, American Journal of Physics, 55, 524

Boston, P. J., Ivanov, M. V., & McKay, C. P. 1992, Icarus, 95, 300

Brasseur, G., & De Rudder, A. 1986, in Stratospheric Ozone Reduction, Solar Ultraviolet Radiation, and Plant Life (Springer), 1–29

Briegleb, B., & Ramanathan, V. 1982, Journal of Applied Meteorology, 21, 1160

Briegleb, B. P., Minnis, P., Ramanathan, V., & Harrison, E. 1986, Journal of Applied Meteorology, 25, 214

Bristow, T. F., Bish, D. L., Vaniman, D. T., et al. 2015, American Mineralogist, 100, 824

Buccino, A. P., Lemarchand, G. A., & Mauas, P. J. D. 2007, Icarus, 192, 582

Bucholtz, A. 1995, Applied Optics, 34, 2765

Buick, R. 2007, The Earliest Records of Life on Earth, ed. W. T. S. III & J. Baross (New York, NY: Cambridge University Press), 237–264

Burke, C. J., Christiansen, J. L., Mullally, F., et al. 2015, ApJ, 809, 8

Burkholder, J., Abbatt, J., Huie, R., et al. 2015, Chemical Kinetics and Photochemical Data for Use in Atmospheric Studies: Evaluation Number 18, Tech. rep., NASA Jet Propulsion Laboratory

Burroughs, E. R. 1917, A Princess of Mars (A.C. McClurg & Company)

Burton, A. S., Stern, J. C., Elsila, J. E., Glavin, D. P., & Dworkin, J. P. 2012, Chemical Society Reviews, 41, 5459

Butlerow, A. 1861, CR Acad. Sci, 53, 145

Calbó, J., PagèS, D., & GonzáLez, J.-A. 2005, Reviews of Geophysics, 43, RG2002

Callahan, M. P., Smith, K. E., Cleaves, H. J., et al. 2011, Proceedings of the National Academy of Science, 108, 13995

Canganella, F., & Wiegel, J. 2011, Naturwissenschaften, 98, 253

Caro, G. M. M., & Dartois, E. 2013, Chemical Society Reviews, 42, 2173

Catling, D., & Kasting, J. F. 2007, Planetary Atmospheres and Life, ed. W. T. S. III & J. Baross (New York, NY: Cambridge University Press), 91–116

Cavicchioli, R. 2002, Astrobiology, 2, 281

Cech, T. R. 2009, Cell, 136, 599

Cede, A., Blumthaler, M., Luccini, E., Piacentini, R. D., & Nuñez, L. 2002, Geophys. Res. Lett., 29, 76

Chan, W. F., Cooper, G., & Brion, C. E. 1993a, Chemical Physics, 178, 387

Chan, W. F., Cooper, G., Sodhi, R. N. S., & Brion, C. E. 1993b, Chemical Physics, 170, 81

Chapman, C. R., Cohen, B. A., & Grinspoon, D. H. 2007, Icarus, 189, 233

Charbonneau, D., Brown, T. M., Noyes, R. W., & Gilliland, R. L. 2002, ApJ, 568, 377

Charbonneau, D., Allen, L. E., Megeath, S. T., et al. 2005, ApJ, 626, 523

Chen, F. Z., & Wu, C. Y. R. 2004, J. Quant. Spec. Radiat. Transf., 85, 195

Chyba, C., & Sagan, C. 1992, Nature, 355, 125

Claire, M. W., Kasting, J. F., Domagal-Goldman, S. D., et al. 2014, Geochim. Cosmochim. Acta, 141, 365

Claire, M. W., Sheets, J., Cohen, M., et al. 2012, ApJ, 757, 95

Cleaves, H. J. 2008, Precambrian Research, 164, 111

Cleaves, H. J., Chalmers, J. H., Lazcano, A., Miller, S. L., & Bada, J. L. 2008, Origins of Life and Evolution of Biospheres, 38, 105. http://dx.doi.org/10.1007/s11084-007-9120-3

Cleaves, H. J., & Miller, S. L. 1998, Proceedings of the National Academy of Science, 95, 7260

Cnossen, I., Sanz-Forcada, J., Favata, F., et al. 2007, Journal of Geophysical Research (Planets), 112, 2008

Coakley, J. A. 2003, in Encyclopedia of atmospheric sciences (Elsevier), 1914–1923

Cockell, C. S. 1999, Icarus, 141, 399

Cockell, C. S. 2000a, Origins of Life and Evolution of the Biosphere, 30, 467

—. 2000b, Planet. Space Sci., 48, 203

—. 2002, International Journal of Astrobiology, 1, 31

Cockell, C. S., Bush, T., Bryce, C., et al. 2016, Astrobiology, 16, 89

Coheur, P.-F., Fally, S., Carleer, M., et al. 2002, Journal of Quantitative Spectroscopy and Radiative Transfer, 74, 493

Colaprete, A., & Toon, O. B. 2003, Journal of Geophysical Research (Planets), 108, 6

Copley, S. D., Smith, E., & Morowitz, H. J. 2007, Bioorganic Chemistry, 35, 430 . http://www.sciencedirect.com/science/article/pii/S004520680700051X

Court, R. W., & Sephton, M. A. 2012, Planet. Space Sci., 73, 233

Cowan, N. B., Greene, T., Angerhausen, D., et al. 2015, PASP, 127, 311

Cronin, T. W. 2014, Journal of Atmospheric Sciences, 71, 2994

Crooke, J. A., Roberge, A., Domagal-Goldman, S. D., et al. 2016, in Proc. SPIE, Vol. 9904, Society of Photo-Optical Instrumentation Engineers (SPIE) Conference Series, 99044R

Davenport, J. R. A., Kipping, D. M., Sasselov, D., Matthews, J. M., & Cameron, C. 2016, ApJL, 829, L31

de Wit, J., Wakeford, H. R., Gillon, M., et al. 2016, Nature, 537, 69

Deamer, D. 2007, The Origin of Cellular Life, ed. W. T. S. III & J. Baross (New York, NY: Cambridge University Press), 187–209

Deamer, D. W., & Dworkin, J, P. 2005, Prebiotic Chemistry, ed. P. Walde (Springer), 1–28

Debye, P., & Huckel, E. 1923, Physik Z, 24, 185

Delano, J. W. 2001, Origins of Life and Evolution of the Biosphere, 31, 311

Deming, D., Wilkins, A., McCullough, P., et al. 2013, ApJ, 774, 95

Des Marais, D. J., Harwit, M. O., Jucks, K. W., et al. 2002, Astrobiology, 2, 153

DeWitt, H. L., Trainer, M. G., Pavlov, A. A., et al. 2009, Astrobiology, 9, 447

Dickinson, R. E., Jaeger, J., Washington, W. M., & Wolski, R. 1981, Boundary subroutine for the NCAR global climate model (Atmospheric Analysis and Prediction Division, National Center for Atmospheric Research)

Dressing, C. D., & Charbonneau, D. 2015, ApJ, 807, 45

Edlén, B. 1966, Metrologia, 2, 71

Emmanuel, S., & Ague, J. J. 2007, Geophys. Res. Lett., 34, L15810

Fally, S., Vandaele, A. C., Carleer, M., et al. 2000, Journal of molecular spectroscopy, 204, 10

Fally, S., Coheur, P.-F., Carleer, M., et al. 2003, J. Quant. Spec. Radiat. Transf., 82, 119

Fanale, F. P., Salvail, J. R., Banerdt, W. B., & Saunders, R. S. 1982, Icarus, 50, 381

Farquhar, J., Bao, H., & Thiemens, M. 2000, Science, 289, 756

Farquhar, J., Savarino, J., Airieau, S., & Thiemens, M. H. 2001, J. Geophys. Res., 106, 32829

Feng, R., Cooper, G., & Brion, C. E. 1999, Chemical Physics, 244, 127

Feng, R., Cooper, G., Burton, G. R., Brion, C., & Avaldi, L. 1999, Chemical physics, 240, 371

Ferris, J., & Chen, C. 1975, Journal of the American Chemical Society, 97, 2962

Ferris, J., Tran, B., Joseph, J., et al. 2005, Advances in Space Research, 36, 251

Ferris, J. P. 1987, in Cold Spring Harbor symposia on quantitative biology, Vol. 52, Cold Spring Harbor Laboratory Press, 29–35

Ferris, J. P., & Hagan, W. J. 1984, Tetrahedron, 40, 1093

Ferris, J. P., Hill, A. R., Liu, R., & Orgel, L. E. 1996, Nature, 381, 59

Follmann, H., & Brownson, C. 2009, Naturwissenschaften, 96, 1265

Forget, F., & Pierrehumbert, R. T. 1997, Science, 278, 1273

Forget, F., Wordsworth, R., Millour, E., et al. 2013, Icarus, 222, 81

Forget, F., Hourdin, F., Fournier, R., et al. 1999, Journal of Geophysical Research: Planets, 104, 24155

Fox, G. K., Code, A. D., Anderson, C. M., et al. 1997, AJ, 113, 1152

France, K., Parke Loyd, R. O., Youngblood, A., et al. 2016, ApJ, 820, 89

Gao, P., Hu, R., Robinson, T. D., Li, C., & Yung, Y. L. 2015, ApJ, 806, 249

Gilbert, W. 1986, Nature, 319, 618

Gillon, M., Triaud, A. H. M. J., Demory, B.-O., et al. 2017, Nature, 542, 456

Glavin, D. P., Elsila, J. E., Burton, A. S., et al. 2012, Meteoritics and Planetary Science, 47, 1347

Goldblatt, C., Claire, M. W., Lenton, T. M., et al. 2009, Nature Geoscience, 2, 891

Gollihar, J., Levy, M., & Ellington, A. D. 2014, Science, 343, 259

Gorshelev, V., Serdyuchenko, A., Weber, M., Chehade, W., & Burrows, J. P. 2014, Atmospheric Measurement Techniques, 7, 609

Gough, D. 1981, in Physics of Solar Variations (Springer), 21–34

Greenblatt, G. D., Orlando, J. J., Burkholder, J. B., & Ravishankara, A. R. 1990, J. Geophys. Res., 95, 18577

Grosch, H., Fateev, A., & Clausen, S. 2015, Journal of Quantitative Spectroscopy and Radiative Transfer, 154, 28

Grotzinger, J. P., Gupta, S., Malin, M. C., et al. 2015, Science, 350, doi:10.1126/science.aac7575

Guillemin, J.-C., Bouyahyi, M., & Riague, E. H. 2004, Advances in Space Research, 33, 81

Gurzadyan, G. G., & Görner, H. 1994, Photochemistry and photobiology, 60, 323

Guzman, M. I., & Martin, S. T. 2008, International Journal of Astrobiology, 7, 271

Guzmán-Marmolejo, A., Segura, A., & Escobar-Briones, E. 2013, Astrobiology, 13, 550

Haldane, J. 1929, Rationalist Annual, 148, 3

Halevy, I., & Head, III, J. W. 2014, Nature Geoscience, 7, 865

Halevy, I., Zuber, M. T., & Schrag, D. P. 2007, Science, 318, 1903

Hall-Spencer, J. M., Rodolfo-Metalpa, R., Martin, S., et al. 2008, Nature, 454, 96

Halmer, M. M., Schmincke, H.-U., & Graf, H.-F. 2002, Journal of Volcanology and Geothermal Research, 115, 511

Hanczyc, M. M., Fujikawa, S. M., & Szostak, J. W. 2003, Science, 302, 618

Hansen, G. B. 1997, J. Geophys. Res., 102, 21569

—. 2005, Journal of Geophysical Research (Planets), 110, E11003

Hansen, J. E., & Travis, L. D. 1974, Space Sci. Rev., 16, 527

Haqq-Misra, J. D., Domagal-Goldman, S. D., Kasting, P. J., & Kasting, J. F. 2008, Astrobiology, 8, 1127

Harman, C. E., Schwieterman, E. W., Schottelkotte, J. C., & Kasting, J. F. 2015, ApJ, 812, 137

Hawley, S. L., Davenport, J. R. A., Kowalski, A. F., et al. 2014, ApJ, 797, 121

Hawley, S. L., & Pettersen, B. R. 1991, ApJ, 378, 725

Heath, M. J., Doyle, L. R., Joshi, M. M., & Haberle, R. M. 1999, Origins of Life and Evolution of the Biosphere, 29, 405

Herd, C. D. K., Borg, L. E., Jones, J. H., & Papike, J. J. 2002, Geochim. Cosmochim. Acta, 66, 2025

Higgs, P. G., & Lehman, N. 2015, Nature Reviews Genetics, 16, 7

Hoekzema, N. M., Garcia-Comas, M., Stenzel, O. J., et al. 2010, Earth and Planetary Science Letters, 294, 534

Hofmann, H. J., Grey, K., Hickman, A. H., & Thorpe, R. I. 1999, Geological Society of America Bulletin, 111, 1256

Holland, H. D. 1978, The Chemistry of the Atmospheres and Oceans (John Wiley and Sons)

Horváth, A., Papp, S., & Décsy, Z. 1984, Journal of photochemistry, 24, 331

Hu, R., Seager, S., & Bains, W. 2012, ApJ, 761, 166

—. 2013, ApJ, 769, 6

Huestis, D. L., & Berkowitz, J. 2010, Critical Evaluation of the Photoabsorption Cross Section of CO2 from 0.125 to 201.6 nm at Room Temperature (World Scientific Company), 229–242. http://books.google.com/books?hl=en&lr=&id=rrfz8ruDzxgC&oi=fnd&pg=PA229

Huffman, R. E. 1969, Canadian Journal of Chemistry, 47, 1823

Ityaksov, D., Linnartz, H., & Ubachs, W. 2008, Chemical Physics Letters, 462, 31

Javaux, E. J., Marshall, C. P., & Bekker, A. 2010, Nature, 463, 934

Johnson, A. P., Cleaves, H. J., Dworkin, J. P., et al. 2008, Science, 322, 404

Jonasz, M. 2007, data of: Querry M. R., Wieliczka D. M., Segelstein D. J. 1991. [Refractive index of] Water (H2O). In: Handbook of optical constants of solids. Palik, E. D. (ed.). Academic Press, New York, pp. 1059-1077. http://www.tpdsci.com/Tpc/AbsCfOfWaterQuerry1991.txt

Jonasz, M., & Fournier, G. R. 2007, Light Scattering by Particles in Water (Boston, MA: Academic Press)

Joseph, J. H., Wiscombe, W. J., & Weinman, J. A. 1976, Journal of Atmospheric Sciences, 33, 2452

Kaltenegger, L., Fridlund, M., & Kasting, J. 2002, in ESA Special Publication, Vol. 514, Earth-like Planets and Moons, ed. B. H. Foing & B. Battrick, 277–282

Kaltenegger, L., & Sasselov, D. 2010, ApJ, 708, 1162

Kaltenegger, L., Traub, W. A., & Jucks, K. W. 2007, ApJ, 658, 598

Kasting, J. F. 1982, J. Geophys. Res., 87, 3091

Kasting, J. F. 1987, Precambrian research, 34, 205

Kasting, J. F. 1991, Icarus, 94, 1

—. 1993, Science, 259, 920

—. 2010, Nature, 464, 687

Kasting, J. F. 2014, Geological Society of America Special Papers, 504, 19

Kasting, J. F., & Ackerman, T. P. 1986, Science, 234, 1383

Kasting, J. F., & Brown, L. L. 1998a, The Early Atmosphere As A Source of Biogenic Compounds, ed. A. Brack (Cambridge University Press), 35–56. http://books.google.com/books?hl=en&lr=&id=ElRpeoPAtWEC&oi=fnd&pg=PA35

—. 1998b, in The Molecular Origins of Life: Assembling Pieces of the Puzzle, ed. A. Brack (Cambridge University Press), 35–56

Kasting, J. F., Pollack, J. B., & Ackerman, T. P. 1984, Icarus, 57, 335

Kasting, J. F., Whitmire, D. P., & Reynolds, R. T. 1993, Icarus, 101, 108

Kasting, J. F., Zahnle, K. J., Pinto, J. P., & Young, A. T. 1989, Origins of Life and Evolution of the Biosphere, 19, 95

Keady, J. J., & Kilcrease, D. 2000, in Allen's Astrophysical Quantities, 4th edn., ed. A. N. Cox (New York, NY: Springer-Verlag)

Kerber, L., Forget, F., & Wordsworth, R. 2015, Icarus, 261, 133

Kerr, J., & Fioletov, V. 2008, Atmosphere-ocean, 46, 159

Kiang, N. Y., Segura, A., Tinetti, G., et al. 2007, Astrobiology, 7, 252

Kirschvink, J. L., & Weiss, B. P. 2002, Palaeontologia electronica, 4, 8

Klein, H. P. 1999, Origins of Life and Evolution of Biospheres, 29, 625

Knauth, L. P. 2005, Palaeogeography, Palaeoclimatology, Palaeoecology, 219, 53

Knutson, H. A., Charbonneau, D., Allen, L. E., et al. 2007, Nature, 447, 183

Kopparapu, R. K. 2013, ApJL, 767, L8

Krasnopolsky, V. A., Maillard, J. P., & Owen, T. C. 2004, Icarus, 172, 537

Kreidberg, L., Bean, J. L., Désert, J.-M., et al. 2014, Nature, 505, 69

Krumgalz, B. 1997, Ion Interaction Approach to Geochemical Aspects of Dead Sea, ed. TBD (TBD)

Kuzicheva, E. A., & Gontareva, N. B. 2001, Advances in Space Research, 28, 713

Kylling, A., Stamnes, K., & Tsay, S.-C. 1995, Journal of Atmospheric Chemistry, 21, 115

Lammer, H., Bredehöft, J. H., Coustenis, A., et al. 2009, A&A Rev., 17, 181

LaRowe, D. E., & Regnier, P. 2008, Origins of Life and Evolution of Biospheres, 38, 383

Laskar, J., Joutel, F., & Robutel, P. 1993, Nature, 361, 615

Latham, D. W., Stefanik, R. P., Mazeh, T., Mayor, M., & Burki, G. 1989, Nature, 339, 38

Lee, L. C. 1980, J. Chem. Phys., 72, 6414

Léger, A., Fontecave, M., Labeyrie, A., et al. 2011, Astrobiology, 11, 335

Leighton, R. B., Murray, B. C., Sharp, R. P., Denton Allen, J., & Sloan, R. K. 1965, Science, 149, 627

Lemmon, M. T., Wolff, M. J., Bell, III, J. F., et al. 2015, Icarus, 251, 96

Lerman, A., Imboden, D., & Gat, J., eds. 1995, Physics and Chemistry of Lakes, Second Edition (Springer-Verlag)

Li, W., Czaja, A. D., Van Kranendonk, M. J., et al. 2013, Geochim. Cosmochim. Acta, 120, 65

Lias, S. G., & Ausloos, P. 1978, Journal of the American Chemical Society, 100, 6027

Lin, H. W., Gonzalez Abad, G., & Loeb, A. 2014, ApJL, 792, L7

Lingam, M., & Loeb, A. 2017, ArXiv e-prints, arXiv:1702.05500

Liou, K.-N. 1973, Journal of Atmospheric Sciences, 30, 1303

—. 1974, Journal of Atmospheric Sciences, 31, 1473

Liou, K. N. 2002, An Introduction to Atmospheric Radiation (Elsevier Science)

Lovelock, J. E. 1965, Nature, 207, 568

Lowell, P. 1906, Mars and its canals (The Macmillan company; London: Macmillan & co., ltd.)

Loyd, R. O. P., France, K., Youngblood, A., et al. 2016, ApJ, 824, 102

Luger, R., & Barnes, R. 2015, Astrobiology, 15, 119

Luger, R., Barnes, R., Lopez, E., et al. 2015, Astrobiology, 15, 57

Madronich, S. 1987, J. Geophys. Res., 92, 9740

Magnani, C. J. 2015, A.B. Thesis, Harvard University

Maher, K. A., & Stevenson, D. J. 1988, Nature, 331, 612

Manatt, S. L., & Lane, A. L. 1993, J. Quant. Spec. Radiat. Transf., 50, 267

Mansy, S. S., Schrum, J. P., Krishnamurthy, M., et al. 2008, Nature, 454, 122

Marshall, B. R., & Smith, R. C. 1990, Appl. Opt., 29, 71

Martel, J., Young, D., Peng, H.-H., Wu, C.-Y., & Young, J. D. 2012, Annual Review of Earth and Planetary Sciences, 40, 167

Martin, W., Baross, J., Kelley, D., & Russell, M. J. 2008, Nature Reviews Microbiology, 6, 805

Marty, B., Zimmermann, L., Pujol, M., Burgess, R., & Philippot, P. 2013, Science, 342, 101

Mason, N., Gingell, J., Davies, J., et al. 1996, Journal of Physics B: Atomic, Molecular and Optical Physics, 29, 3075

Matsunaga, T., Hieda, K., & Nikaido, O. 1991, Photochemistry and photobiology, 54, 403

Maurer, S. E., & Nguyen, G. 2016, Origins of Life and Evolution of Biospheres, 46, 215

Mayer, B., Kylling, A., Madronich, S., & Seckmeyer, G. 1998, J. Geophys. Res., 103, 31

Mayor, M., & Queloz, D. 1995, Nature, 378, 355

McCollom, T. M. 2013, Annual Review of Earth and Planetary Sciences, 41, 207

McKay, C. P. 1997, in Planetary and Interstellar Processes Relevant to the Origins of Life (Springer), 263–289

McKay, D. S., Gibson, Jr., E. K., Thomas-Keprta, K. L., et al. 1996, Science, 273, 924

Meadows, V. S., Arney, G. N., Schwieterman, E. W., et al. 2016, ArXiv e-prints, arXiv:1608.08620

Mennesson, B., Gaudi, S., Seager, S., et al. 2016, in Proc. SPIE, Vol. 9904, Society of Photo-Optical Instrumentation Engineers (SPIE) Conference Series, 99040L

Menor-Salván, C., & Marín-Yaseli, M. R. 2013, Chemistry–A European Journal, 19, 6488

Merienne, M.-F., Jenouvrier, A., Hermans, C., et al. 2003, J. Quant. Spec. Radiat. Transf., 82, 99

Miller, S. L. 1953, Science, 117, 528

Miller, T. M. 2009, in CRC Handbook of Chemistry and Physics, 90th edn., ed. D. R. Lide (Boca Raton, FL: CRC Press)

Mishra, M. K., Chauhan, P., Singh, R., Moorthi, S. M., & Sarkar, S. S. 2016, Icarus, 265, 84

Misra, K. C. 2012, Introduction to Geochemistry (Wiley-Blackwell), 137

Mojzsis, S. J., Harrison, T. M., & Pidgeon, R. T. 2001, Nature, 409, 178

Molina, L. T., & Molina, M. J. 1986, J. Geophys. Res., 91, 14501

Morowitz, H., & Sagan, C. 1967, Nature, 215, 1259

Mota, R., Parafita, R., Giuliani, A., et al. 2005, Chemical Physics Letters, 416, 152

Mount, G. H., Warden, E. S., & Moos, H. W. 1977, ApJL, 214, L47

Mozumder, A. 2002, Phys. Chem. Chem. Phys., 4, 1451. http://dx.doi.org/10.1039/B106017C

Mulkidjanian, A. Y., Cherepanov, D. A., & Galperin, M. Y. 2003, BMC evolutionary biology, 3, 12

Mumma, M. J., Villanueva, G. L., Novak, R. E., et al. 2009, Science, 323, 1041

Murphy, W. F. 1977, The Journal of Chemical Physics, 67, 5877

Mustard, J., Adler, M., Allwood, A., et al. 2013, Report of the 2020 Mars Science Definition Team, Tech. rep., Mars Exploration Program Analysis Group. http://mepag.jpl.nasa.gov/reports/MEP/Mars_2020_SDT_Report_Final.pdf

Nava-Sedeño, J. M., Ortiz-Cervantes, A., Segura, A., & Domagal-Goldman, S. D. 2016, Astrobiology, 16, 744

Neta, P., & Huie, R. E. 1985, Environmental health perspectives, 64, 209

Niles, P. B., Catling, D. C., Berger, G., et al. 2013, Space Science Reviews, 174, 301

Nissen, P., Hansen, J., Ban, N., Moore, P. B., & Steitz, T. A. 2000, Science, 289, 920

Noffke, N., Christian, D., Wacey, D., & Hazen, R. M. 2013, Astrobiology, 13, 1103

Noffke, N., Eriksson, K. A., Hazen, R. M., & Simpson, E. L. 2006, Geology, 34, 253

Nuevo, M., Milam, S. N., & Sandford, S. A. 2012, Astrobiology, 12, 295

Nuth, J. A., & Glicker, S. 1982, J. Quant. Spec. Radiat. Transf., 28, 223

Öberg, K. I., Garrod, R. T., van Dishoeck, E. F., & Linnartz, H. 2009, Astronomy & Astrophysics, 504, 891

Ogawa, M., & Cook, G. R. 1958, J. Chem. Phys., 28, 173

Ogawa, S., & Ogawa, M. 1975, Canadian Journal of Physics, 53, 1845

Ohtomo, Y., Kakegawa, T., Ishida, A., Nagase, T., & Rosing, M. T. 2014, Nature Geoscience, 7, 25

Ojha, L., Wilhelm, M. B., Murchie, S. L., et al. 2015, Nature Geoscience, 8, 829

O'Malley-James, J. T., & Kaltenegger, L. 2016, ArXiv e-prints, arXiv:1608.06930

Oparin, A. 1924, Proiskhodenie Zhisni, Moscovky Rabotchii, Moscow

Orgel, L. E. 2004, Critical reviews in biochemistry and molecular biology, 39, 99

Oró, J., & Kimball, A. 1961, Archives of biochemistry and biophysics, 94, 217

Osten, R. 2016, Heliophysics: Active Stars, their Astrospheres, and Impacts on Planetary Environments, ed. C. J. Schrijver, F. Bagenal, & J. J. Sojka (Cambridge University Press)

Pang, K., & Ajello, J. M. 1977, Icarus, 30, 63

Pappalardo, R., Senske, D., Prockter, L., et al. 2015, in EGU General Assembly Conference Abstracts, Vol. 17, EGU General Assembly Conference Abstracts, 8155

Parker, E. T., Cleaves, H. J., Dworkin, J. P., et al. 2011, Proceedings of the National Academy of Sciences, 108, 5526

Parkinson, W. H., Rufus, J., & Yoshino, K. 2003, Chemical Physics, 290, 251

Pascal, R. 2012, Journal of Systems Chemistry, 3, 1

Patel, B. H., Percivalle, C., Ritson, D. J., Duffy, C. D., & Sutherland, J. D. 2015, Nature Chemistry, 7, 301

Patel, M., Zarnecki, J., & Catling, D. 2002, Planetary and Space Science, 50, 915

Pavlov, A. A., & Kasting, J. F. 2002, Astrobiology, 2, 27

Pavlov, A. A., Kasting, J. F., Brown, L. L., Rages, K. A., & Freedman, R. 2000, J. Geophys. Res., 105, 11981

Payne, R. E. 1972, Journal of Atmospheric Sciences, 29, 959

Peng, W., & Shaw, B. R. 1996, Biochemistry, 35, 10172. `http://pubs.acs.org/doi/pdf/10.1021/bi960001x`

Penndorf, R. 1957, Journal of the Optical Society of America (1917-1983), 47, 176

Pestunova, O., Simonov, A., Snytnikov, V., Stoyanovsky, V., & Parmon, V. 2005, Advances in Space Research, 36, 214

Petigura, E. A., Howard, A. W., & Marcy, G. W. 2013, Proceedings of the National Academy of Science, 110, 19273

Pettersen, B. R., Coleman, L. A., & Evans, D. S. 1984, ApJS, 54, 375

Pierrehumbert, R., & Gaidos, E. 2011, ApJL, 734, L13

Pierrehumbert, R. T. 2010, Principles of planetary climate (Cambridge University Press)

Pollum, M., Ashwood, B., Jockusch, S., Lam, M., & Crespo-Hernández, C. E. 2016, Journal of the American Chemical Society, 138, 11457

Powner, M. W., Anastasi, C., Crowe, M. A., et al. 2007, ChemBioChem, 8, 1170

Powner, M. W., Gerland, B., & Sutherland, J. D. 2009, Nature, 459, 239

Powner, M. W., Sutherland, J. D., & Szostak, J. W. 2010, Journal of the American Chemical Society, 132, 16677, pMID: 21043502. `http://dx.doi.org/10.1021/ja108197s`

Querry, M. R., Wieliczka, D. M., & Segelstain, D. J. 1991, Handbook of Optical Constants of Solids II, ed. E. D. Palik (San Diego, CA: Academic Press, Inc), 1059–1077

Ramirez, R., & Kaltenegger, L. 2017, ArXiv e-prints, arXiv:1702.08618

Ramirez, R. M., & Kaltenegger, L. 2014, ApJL, 797, L25

Ramirez, R. M., Kopparapu, R., Zugger, M. E., et al. 2014, Nature Geoscience, 7, 59

Ranjan, S., Charbonneau, D., Désert, J.-M., et al. 2014, ApJ, 785, 148

Ranjan, S., & Sasselov, D. D. 2016, Astrobiology, 16, 68

—. 2017, Astrobiology, 17, 169

Ranjan, S., Wordsworth, R. D., & Sasselov, D. D. 2017, ArXiv e-prints, arXiv:1701.01373

Rapf, R. J., & Vaida, V. 2016, Phys. Chem. Chem. Phys., 18, 20067. `http://dx.doi.org/10.1039/C6CP00980H`

Reinhard, C. T., Olson, S. L., Schwieterman, E. W., & Lyons, T. W. 2017, ArXiv e-prints, arXiv:1702.01137

Ribas, I., Porto de Mello, G. F., Ferreira, L. D., et al. 2010, ApJ, 714, 384

Ribas, I., Bolmont, E., Selsis, F., et al. 2016, A&A, 596, A111

Richter, F. M. 1985, Earth and Planetary Science Letters, 73, 350

Rios, A. C., & Tor, Y. 2013, Israel journal of chemistry, 53, 469

Ritson, D., & Sutherland, J. D. 2012, Nature Chemistry, 4, 895

Robinson, T. D., & Catling, D. C. 2014, Nature Geoscience, 7, 12

Robinson, T. D., Stapelfeldt, K. R., & Marley, M. S. 2016, PASP, 128, 025003

Rodler, F., & López-Morales, M. 2014, ApJ, 781, 54

Rogers, L. A. 2015, ApJ, 801, 41

Romanzin, C., Gazeau, M.-C., Bénilan, Y., et al. 2005, Advances in Space Research, 36, 258

Ronov, A. B., & Yaroshevsky, A. A. 1969, The Earth's Crust and Upper Mantle, ed. P. J. Hart (Washington, D.C.: American Geophysical Union)

Rontó, G., Bérces, A., Lammer, H., et al. 2003, Photochemistry and Photobiology, 77, 34. http://dx.doi.org/10.1562/0031-8655(2003)0770034SUICOT2.0.CO2

Rosenberg, R. A., Abu Haija, M., & Ryan, P. J. 2008, Physical Review Letters, 101, 178301

Rothschild, L. J., & Mancinelli, R. L. 2001, Nature, 409, 1092

Rugheimer, S., Kaltenegger, L., Zsom, A., Segura, A., & Sasselov, D. 2013, Astrobiology, 13, 251

Rugheimer, S., Segura, A., Kaltenegger, L., & Sasselov, D. 2015, ApJ, 806, 137

Ruiz-Mirazo, K., Briones, C., & de la Escosura, A. 2014, Chem. Rev, 114, 285

Sagan, C. 1973, Journal of Theoretical Biology, 39, 195

Sagan, C., & Khare, B. N. 1971, Science, 173, 417

Sagan, C., Thompson, W. R., Carlson, R., Gurnett, D., & Hord, C. 1993, Nature, 365, 715

Sanchez, R. A., & Orgel, L. E. 1970, Journal of molecular biology, 47, 531

Sander, R. 2015, Atmospheric Chemistry & Physics, 15, 4399

Sander, S. P., Friedl, R. R., Barker, J. R., et al. 2011, Chemical Kinetics and Photochemical Data for Use in Atmospheric Studies Evaluation Number 17, Tech. Rep. 17, NASA JPL. http://jpldataeval.jpl.nasa.gov/

Sankaran, N. 2016, Journal of molecular evolution, 83, 169

Sarker, P. K., Takahashi, J.-i., Obayashi, Y., Kaneko, T., & Kobayashi, K. 2013, Advances in Space Research, 51, 2235

Scalo, J., Kaltenegger, L., Segura, A. G., et al. 2007, Astrobiology, 7, 85

Schaefer, L., Wordsworth, R. D., Berta-Thompson, Z., & Sasselov, D. 2016, ApJ, 829, 63

Schwieterman, E. W., Meadows, V. S., Domagal-Goldman, S. D., et al. 2016, ApJL, 819, L13

Seager, S. 2014, Proceedings of the National Academy of Science, 111, 12634

Seager, S., Bains, W., & Hu, R. 2013, ApJ, 775, 104

Seager, S., Turner, E. L., Schafer, J., & Ford, E. B. 2005, Astrobiology, 5, 372

Segelstein, D. J. 1981, Master's thesis, University of Missouri – Kansas City, Kansas City, MO

Segura, A., Kasting, J. F., Meadows, V., et al. 2005, Astrobiology, 5, 706

Segura, A., Krelove, K., Kasting, J. F., et al. 2003, Astrobiology, 3, 689

Segura, A., Meadows, V. S., Kasting, J. F., Crisp, D., & Cohen, M. 2007, A&A, 472, 665

Segura, A., Walkowicz, L. M., Meadows, V., Kasting, J., & Hawley, S. 2010, Astrobiology, 10, 751

Self, S., Widdowson, M., Thordarson, T., & Jay, A. E. 2006, Earth and Planetary Science Letters, 248, 518

Serdyuchenko, A., Gorshelev, V., Weber, M., Chehade, W., & Burrows, J. P. 2014, Atmospheric Measurement Techniques, 7, 625

Setlow, R. B. 1974, Proceedings of the National Academy of Sciences, 71, 3363

Shapiro, R. 1987, Origins: A skeptic's guide to the creation of life on earth (Bantam Dell Pub Group)

Shapiro, R., & Schulze-Makuch, D. 2009, Astrobiology, 9, 335

Shaw, G. 2008, Chemie der Erde / Geochemistry, 68, 235

Shemansky, D. E. 1972, J. Chem. Phys., 56, 1582

Shettle, E. P., & Weinman, J. A. 1970, Journal of Atmospheric Sciences, 27, 1048

Shields, A. L., Ballard, S., & Johnson, J. A. 2016a, ArXiv e-prints, arXiv:1610.05765

Shields, A. L., Barnes, R., Agol, E., et al. 2016b, Astrobiology, 16, 443

Shklovskii, I. S., & Sagan, C. 1966, Intelligent Life in the Universe (Holden-Day, Inc.)

Shkolnik, E. L., & Barman, T. S. 2014, AJ, 148, 64

Simonov, A. N., Pestunova, O. P., Matvienko, L. G., et al. 2007, Advances in Space Research, 40, 1634

Singer, D. W. 1950, Giordano Bruno: His Life and Thought (H. Wolff Book Manufacturing Co.), 323

Sinsheimer, R. L. 1954, Radiation Research, 1, 505

Sinsheimer, R. L., & Hastings, R. 1949, Science, 110, 525

Sisson, C. H. 2003, De Rerum Natura: The Poem on Nature (Routledge), 74

Sleep, N. H., & Zahnle, K. 2001, J. Geophys. Res., 106, 1373

Sleep, N. H., Zahnle, K. J., Kasting, J. F., & Morowitz, H. J. 1989, Nature, 342, 139

Smith, D. S., Scalo, J., & Wheeler, J. C. 2004, Icarus, 171, 229

Smith, M. D., Conrath, B. J., Pearl, J. C., & Christensen, P. R. 2002, Icarus, 157, 259

Sneep, M., & Ubachs, W. 2005, J. Quant. Spec. Radiat. Transf., 92, 293

Snellen, I. A. G., de Kok, R. J., de Mooij, E. J. W., & Albrecht, S. 2010, Nature, 465, 1049

Šponer, J. E., Szabla, R., Góra, R. W., et al. 2016, Physical Chemistry Chemical Physics

Springsteen, G. 2015, ChemBioChem, 16, 1411

Spurr, R. J. D. 2001, PhD thesis, Technische Universiteit Eindhoven

Squyres, S. W., Grotzinger, J. P., Arvidson, R. E., et al. 2004, Science, 306, 1709

Srinivasan, P. 1976, Social Scientist, 3

Stamnes, K., Tsay, S., & Istvan, L. 2000, DISORT, a General-Purpose Fortran Program for Discrete-Ordinate-Method Radiative Transfer in Scattering and Emitting Layered Media: Documentation of Methodology (version 1.1), Tech. rep. `ftp://gs613-climate1.gsfc.nasa.gov/wiscombe/Multiple{\_}Scatt/DISORTReport1.1.pdf`

Stamnes, K., Tsay, S.-C., Jayaweera, K., & Wiscombe, W. 1988, Appl. Opt., 27, 2502

Stark, G., Yoshino, K., Smith, P. L., & Ito, K. 2007, J. Quant. Spec. Radiat. Transf., 103, 67

Steitz, T. A., & Moore, P. B. 2003, Trends in biochemical sciences, 28, 411

Stephenson, J. D., Hallis, L. J., Nagashima, K., & Freeland, S. J. 2013, PLoS ONE, 8, e64624

Stevenson, D. J. 1999, Nature, 400, 32

Stubenrauch, C. J., Rossow, W. B., Kinne, S., et al. 2013, Bulletin of the American Meteorological Society, 94, 1031

Sullivan, P. W., Winn, J. N., Berta-Thompson, Z. K., et al. 2015, ApJ, 809, 77

Sullivan, W. 1964, We Are Not Alone (McGraw-Hill Book Company)

Summers, D. P., Basa, R. C. B., Khare, B., & Rodoni, D. 2012, Astrobiology, 12, 107

Tarter, J. C., Backus, P. R., Mancinelli, R. L., et al. 2007, Astrobiology, 7, 30

Thomas, B. C., Neale, P. J., & Snyder, II, B. R. 2015, Astrobiology, 15, 207

Thuillier, G., Floyd, L., Woods, T. N., et al. 2004, in Washington DC American Geophysical Union Geophysical Monograph Series, Vol. 141, Solar Variability and its Effects on Climate. Geophysical Monograph 141, ed. J. M. Pap, P. Fox, C. Frohlich, H. S. Hudson, J. Kuhn, J. McCormack, G. North, W. Sprigg, & S. T. Wu, 171

Tian, F. 2009, ApJ, 703, 905

Tian, F., Claire, M. W., Haqq-Misra, J. D., et al. 2010, Earth and Planetary Science Letters, 295, 412

Tian, F., Kasting, J. F., & Solomon, S. C. 2009, Geophys. Res. Lett., 36, L02205

Todd, Z., Fahrenbach, A., Sasselov, D., Magnani, C., & Ranjan, S. 2017a, in preparation for submission to Angewandte Chemie

—. 2017b, in prep

Toon, O. B., McKay, C. P., Ackerman, T. P., & Santhanam, K. 1989, J. Geophys. Res., 94, 16287

Trail, D., Watson, E. B., & Tailby, N. D. 2011, Nature, 480, 79

Truesdell, A. H., & Jones, B. F. 1974, Journal Research U.S. Geological Survey, 2, 233

Vandaele, A. C., Hermans, C., & Fally, S. 2009, J. Quant. Spec. Radiat. Transf., 110, 2115

Vardavas, I. M., & Carver, J. H. 1984, Planet. Space Sci., 32, 1307

Victor, G. A., & Dalgarno, A. 1969, J. Chem. Phys., 50, 2535

Vincendon, M., Pilorget, C., Gondet, B., Murchie, S., & Bibring, J.-P. 2011, Journal of Geophysical Research (Planets), 116, E00J02

Voet, D., Gratzer, W., Cox, R., & Doty, P. 1963, Biopolymers, 1, 193

von Paris, P., Rauer, H., Lee Grenfell, J., et al. 2008, Planet. Space Sci., 56, 1244

von Paris, P., Gebauer, S., Godolt, M., et al. 2010, A&A, 522, A23

Wagner, W., & Pruß, A. 2002, Journal of Physical and Chemical Reference Data, 31, 387

Wagner, W., Saul, A., & Pruss, A. 1994, Journal of Physical and Chemical Reference Data, 23, 515

Walker, J. C. 1985, Origins of Life and Evolution of the Biosphere, 16, 117

Warren, S. G., & Brandt, R. E. 2008, Journal of Geophysical Research (Atmospheres), 113, D14220

Way, M. J., Del Genio, A. D., Kiang, N. Y., et al. 2016, Geophys. Res. Lett., 43, 8376

Webster, C. R., Mahaffy, P. R., Atreya, S. K., et al. 2015, Science, 347, 415

Weiss, B. P., Kirschvink, J. L., Baudenbacher, F. J., et al. 2000, Science, 290, 791

Wilde, S. A., Valley, J. W., Peck, W. H., & Graham, C. M. 2001, Nature, 409, 175

Wohler, F. 1828, On the artificial production of urea (Wm. Benton)

Wolf, E. T., & Toon, O. B. 2010, Science, 328, 1266

Wolff, M. J., Smith, M. D., Clancy, R. T., et al. 2009, Journal of Geophysical Research (Planets), 114, E00D04

Wordsworth, R., Forget, F., Millour, E., et al. 2013a, Icarus, 222, 1

—. 2013b, Icarus, 222, 1

Wordsworth, R., Kalugina, Y., Lokshtanov, S., et al. 2017, Geophys. Res. Lett., 44, 665

Wordsworth, R., & Pierrehumbert, R. 2013, Science, 339, 64

—. 2014, ApJL, 785, L20

Wordsworth, R. D. 2016, Annual Review of Earth and Planetary Sciences, 44, 381

Wordsworth, R. D., Kerber, L., Pierrehumbert, R. T., Forget, F., & Head, J. W. 2015, Journal of Geophysical Research (Planets), 120, 1201

Worth, R. J., Sigurdsson, S., & House, C. H. 2013, Astrobiology, 13, 1155

Wozniak, B., & Dera, J. 2007, Atmospheric and Oceanographic Sciences Library, Vol. 33, Light Absorption In Sea Water (New York, NY: Springer Science+Business Media, LLC)

Wu, C. R., & Chen, F. 1998, Journal of Quantitative Spectroscopy and Radiative Transfer, 60, 17

Wuttke, S., & Seckmeyer, G. 2006, Theoretical and applied climatology, 85, 131

Xu, J., Tsanakopoulou, M., Magnani, C. J., et al. 2016, Nature Chemistry

Yamagata, Y., Watanabe, H., et al. 1991, Nature, 352, 516

Yang, J., Cowan, N. B., & Abbot, D. S. 2013, ApJL, 771, L45

Yoshino, K., Esmond, J. R., Cheung, A. S.-C., Freeman, D. E., & Parkinson, W. H. 1992, Planet. Space Sci., 40, 185

Yoshino, K., Esmond, J. R., Sun, Y., et al. 1996, J. Quant. Spec. Radiat. Transf., 55, 53

Yoshino, K., Parkinson, W. H., Ito, K., & Matsui, T. 2005, Journal of molecular spectroscopy, 229, 238

Yu, H., Zhang, S., Dunn, M. R., & Chaput, J. C. 2013, Journal of the American Chemical Society, 135, 3583. `http://pubs.acs.org/doi/abs/10.1021/ja3118703`

Zahnle, K. 2015, Science, 347, 370

Zahnle, K., Claire, M., & Catling, D. 2006, Geobiology, 4, 271

Zahnle, K., Freedman, R. S., & Catling, D. C. 2011, Icarus, 212, 493

Zahnle, K. J. 1986, J. Geophys. Res., 91, 2819

Zolotov, M. Y., & Shock, E. L. 2000, J. Geophys. Res., 105, 539

Zurek, R. W. 1978, Icarus, 35, 196